Ultrasonic Measurement of Longitudinal Stress in Rail Tracks

Joe Hill

A thesis submitted in partial fulfilment of the requirements for the degree of

Doctor of Philosophy

The University of Sheffield

Faculty of Engineering

Department of Mechanical Engineering

Submission Date

2024

This was an uphill struggle.
Thank you to Marina, Mel, Lizzie & Roger, without whom I would never have been able to overcome the red tape and gain acceptance to this programme.

Acknowledgements

I owe thanks to many of my friends and colleagues, without whom this thesis could not have been written.

Dr Henry Brunskill and Dr Giorgios Tyreas - who manufactured the very first wedge sensor assembly that provided a springboard to develop the angled wedge method

Dr Art Gower - for support with understanding the mathematics and for developing the sensitivity analysis models.

Dr Gary Nicholas - for his efforts in our collaborations in the area of rail stress measurement, his support in providing data analysis code for this thesis and processing of some experimental results.

Dr Will Gray - for support with testing and development of a data capture system

Abstract

This thesis details the investigation of the use of a novel stress relation identity, using pairs of guided bulk ultrasonic waves travelling through a highly incompressible isotropic material, to return a non-destructive and calibration-free measurement of Rail Neutral Temperature, an essential measurement in railway safety maintenance.

The angled-wedge method is developed alongside a birefringence method, allowing comparison of accuracy and repeatability.

Several iterations of testing platform are undertaken, and testing conducted on dog-bone tensile specimens in the laboratory and on full rail sections on a test bed. Both methods show some improvement during the course of the investigation, but both techniques encounter significant experimental and material dependant errors.

While the birefringence method returns greater accuracy, the constant need for external calibration limits its usefulness in the rail industry.

The angled wedge method shows initial promise, however, the overall sensitivity of the measurement technique results in experimental noise that exceeds the desired measurement range.

Significant further work would be required to bring either technique to a technology readiness level suitable for deployment in the rail maintenance industry.

Contents

Abbreviations

AEC Acousto-Elastic Constant.

AMTRAK The National Railroad Passenger Corporation.

AREMA American Railway Engineering and Maintenance-of-Way Association.

CAD Computer Aided Design.

CNC Computer Numerical Control.

CWR Continuously Welded Rail.

DAQ Data Acquisition.

EDM Electrical Discharge Machining.

EI Electromechanical Impedance.

EMAT Electro-magnetic Acoustic Transmission.

EMI Electromagnetic interference.

EU European Union.

FE Finite Element.

FRA Federal Railroad Administration.

HSDQ High-Speed Data Acquisition system.

IPCC Intergovernmental Panel on Climate Change.

LCR Longitudinal critically refracted.

LDV Laser Doppler Vibrometer.

LS Longitudinal Stress.

MMM-MBN Metal Magnetic Memory-Magnetic Barkhausen Noise.

NDT Non Destructive Testing.

NR Network Rail.

NRT Neutral Rail Temperature.

OTS Off the Shelf.

PZT Lead zirconate titanate.

SDGs Sustainable Development Goals.

SNR Signal-to-Noise ratio.

SoS Speed of Sound.

TEN-T Trans-European Transport Network.

ToF Time of Flight.

TRL Technology Readiness Level.

TTCI Transportation Technology Centre Inc..

UK United Kingdom.

UN United Nations.

US The United States of North America.

Volpe United States Department of Transportation Volpe Centre.

Chapter 1

Introduction

1.1 Background

Rail networks are a vital part of national and international infrastructure. Millions of kilometers of track must be serviced and maintained, across vast areas, spanning dramatically different terrains and climates.

Traditional railway construction, using bolted plates to join rails and leaving expansion gaps between them, has made way for Continuously Welded Rail (CWR), with modern installations using single lengths of CWR in excess of 500m that are themselves welded together into many uninterrupted kilometers of rail.

When fixed to their ties/sleepers, these lengths of rail are constrained. Without the traditional expansion joints, this constrained rail cannot freely expand or contract longitudinally with changes in temperature, causing thermally induced Longitudinal Stress (LS).

The stability of a section of railway track relies on a complex set of interactions and interrelations, such as the condition of the ballast and regularity of ballast consolidation, the presence or lack of fixed structures such as bridges or crossings, the type and age of sleepers and fixings. If the system reaches a point of instability, then a potentially catastrophic track failure could occur, such as track buckling. A primary cause of track buckling is the thermally induced LS exceeding the threshold of stability provided by the entire track supporting structure, and these events occur during periods of extreme temperature.

To combat this, when installing or repairing CWR, engineering teams must ensure the installed rail has the correct Neutral Rail Temperature (NRT) (23 °C for most of the UK). This means that CWR that is in ideal conditions will be in tension when the ambient temperature is below 23 °C, be free from any longitudinal stress at 23 °C exactly, and will be in compression should the temperature climb higher.

Rail infrastructure stakeholders have the unenviable task of managing the LS across their networks. The task is made all the more challenging, not only by how the above-mentioned stability factors change over time, passage of rail traffic or other maintenance activities, but the NRT of the track at any location can also change due to these factors, even changing during the day or from month to month based on how daily and seasonal environmental trends affect each element of the track structure to a difference extent. In addition, NRT can change over time in specific locales by the accelerating or braking or rail traffic, such as before and after bends. This means that the only time an asset manager can be sure that the rail is at the correct tension is right after the last cut and weld operation at that location.

Rail maintenance stakeholders, therefore, have a need to accurately measure the NRT at any point in the network to maintain the correct parameters. This is a significant safety and financial concern, as a derailment could cost lives and track downtime is costly.

Currently the best available measurement techniques are time consuming, disruptive and costly. They require track closure, significant time and labour to conduct a single measurement and results are not always reliable. The railway industry considers the development of a quick, non-destructive and non-disruptive measurement of this key safety parameter to be a 'Holy Grail' of rail maintenance and condition monitoring measurements.

As such, the University of Sheffield has received, to date, a total of nearly £450,000 in project grants from stakeholders in both the U.S.A. and Europe Federal Railroad Administration (FRA) & Network Rail (NR)) in order to develop a novel and fundamentally important technique for measuring LS in railway track.

While the applications of the work are truly global, this thesis will focus on European Union (EU) and North American (US) rail markets for the assessment of potential value and impact.

1.1.1 The rail market

The United States has the largest rail transport network size of any country in the world [1]. About 700 railroad companies (operators) operate carrier freight services in the United States along a well-integrated network of about 257,722 km (160,141 mi) of standard gauge private freight railroads extending well into Canada and Mexico [2]. These operators move 40% of US freight [3].

US passenger services, operated by The National Railroad Passenger Corporation (AMTRAK), are limited mainly to mass transit and commuter rail in major cities. With the rise of the car, intercity passenger service, once a large and vital part of the nation's passenger transportation network, has severely declined, culminating in the removal of requirements for rail companies to provide passenger services in 1970 [4].

In contrast, European railways are an integrated network spanning all members of the Schengen area, comprising 217,000km of track (including nearly 9000km of High Speed Rail network [5]). Overall the EU moved 15-18% of it's freight via railway in 2020 [6] [7] though the percentage for each member state varies dramatically (Figure 1.1). European and North American rail networks are compared in Table 1.1.

Table 1.1: Overview of North American and EU rail markets

	Track (km)	Rail Freight (%)	Locomotives	Freight Cars
North America [2] [8]	257,722	38	31,875	1,471,736
Europe [5] [6] [7]	217,000	15 - 18		

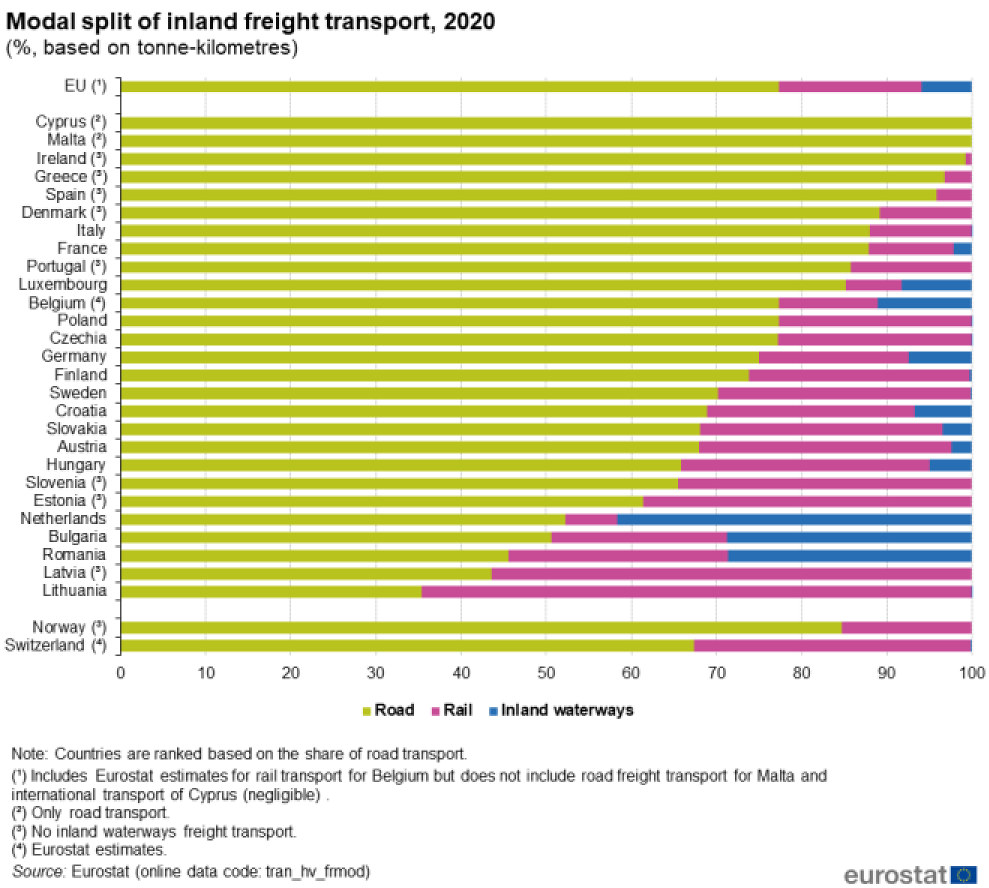

Figure 1.1: Modal split of freight transport by percentage in the EU member states for 2020 [6]

1.1.2 The future for rail

The number of planned government and industry initiatives is too large to be adequately covered in this text. There is also a complicated picture of rail, both passenger and freight, as it interacts with and responds to economic and political trends.

1.1.2.1 Recent trends

Yearly ridership across all modes of US public transit increased by 17% from 2022 to 2023 [9]. While still recovering from the shock of the Covid 19 pandemic, AMTRAK's ridership figures increased by 25% for 2023 with 29 million unlinked passenger journeys [10], recovering some 80% of its lost ridership in that year and going on to post record ridership of 30.8 million in the 2024 fiscal year [11].

US rail freight volumes are linked to the economy they serve. Notable correlations include significant drops in freight volumes of building materials in 2018 and the continuing decline in coal volumes across the network [12]. Overall volumes of US rail freight have declined from over 1.3 million carloads in 2008 to 934,000 in 2024 [13], though figures have remained relatively stable since 2022. Intermodal shipping has been gradually increasing in recent years and looks to remain an important growth area for the US rail network [14].

In Europe, rail freight has never represented as large a proportion of freight transport as in the US. Overall figures show a gradual decline in recent decades. Europe saw an annual drop in rail freight of 4.9% from 2022 to 2023 [15] and UK railways' share of freight volumes dropped from 5% to 4% 2015 and 2022 [16]. Similar trends in coal and intermodal freight are also identified [17].

Rail passenger ridership in the UK has yet to recover completely from the pandemic, though in 2024 it had climbed back to 60.1 billion passenger kilometers, 90% of pre-pandemic levels and a 13% increase on the previous year [18].

1.1.2.2 The near future

Despite the Covid challenges and recent trends in rail freight, rail freight industry forecasts are still bullish. EU Rail freight is predicted to at least double its market share by 2050 [7] and in the North American freight market, growth of 30% is predicted by 2040 [19]. Even if growth is limited, rail forms an essential part of European and US economics, and will remain a vital part of national and international infrastructure.

Governments have shown great appetite for investment in rail infrastructure. 2024 saw $100 billion of federal funds promised to the public transport infrastructure [9]. In Europe a combination cost of living increases and green transport considerations resulted in some countries in the EU significantly reducing the price for traveling on public transport [20]. Germany reduced the cost of a trans-national ticket to €9 for the summer of 2022 and some cities cut the costs of rail tickets by more than 90%. The use of trains increased so significantly that "ticket websites have crashed upon the release of the tickets" [5].

In the medium term, geopolitical considerations such as the Russian war in Ukraine have resulted in sanctions on Russian oil and gas imports, placing pressure on European states to become more self-sufficient and reduce their reliance on fossil fuels. Transport initiatives are core components of these policies [20].

1.1.2.3 Net-Zero 2050 & United Nations Sustainable Development Goals

In the longer term, with the ongoing implementation of global plans to reduce carbon emissions and the United Nations' focus on Sustainable Development Goals, the rail industry will have a growing part to play in the transport infrastructure.

The European transport sector is responsible for 25% of the CO_2 emissions in the EU [7], and with the European Green Deals gaining momentum there is a large role for the rail industry to play in reducing transport emissions and developing a more robust, safer rail network to support the ongoing political changes.

Carbon emissions per tonne of freight from rail transport are 3-4 times lower than those from road transportation. In the US, railroads account for 40% of freight volume but only 2.1% of transport related greenhouse gas emissions [3]. The EU has indicated that to meet the aims of the Green Deals, a 'forceful shift from road to rail transport is necessary' [21]. Improvements to railway infrastructure will also contribute to nearly half of the UN's 17 SDGs.

1.1.2.4 (Re)Investment in rail networks

In Europe the Trans-European Transport Network (TEN-T) projects consist of significant infrastructure improvements with the aim of creating 9 rail corridors. "TEN-T envisages coordinated improvements to primary roads, railways, inland waterways, airports, seaports, inland ports and traffic management systems, providing integrated and intermodal long-distance, high-speed routes" [22]. The completion target for the 9 corridors is 2030 [23].

Sadly for the United Kingdom (UK) rail, following Brexit, plans to integrate the UK into these corridors (Figure 1.2) were dropped and the corridors have since been significantly expanded in Spain, France, Scandinavia and South-Eastern Europe (Figure 1.3).

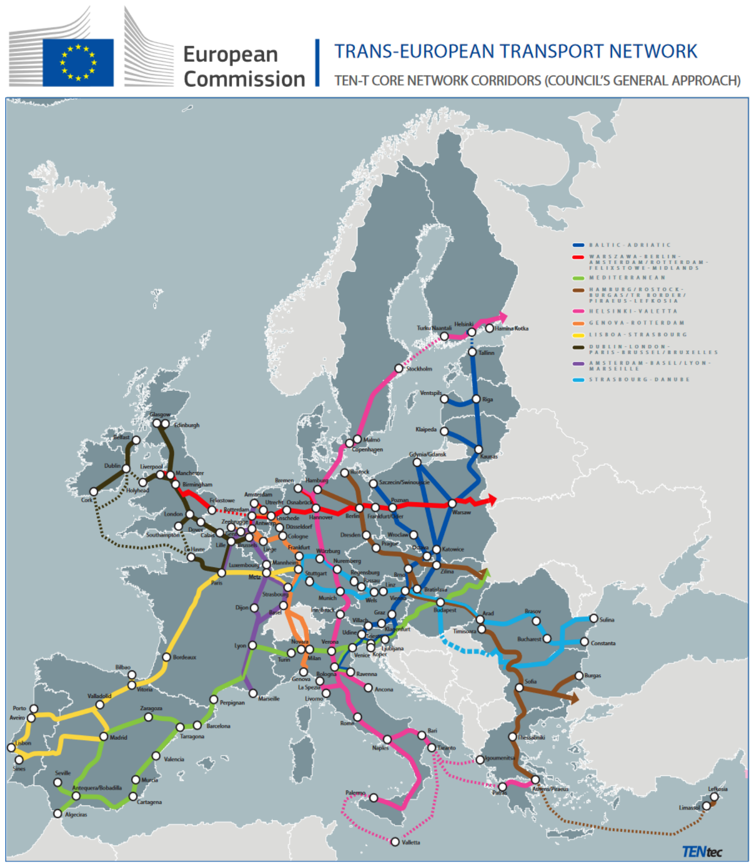

Figure 1.2: Plans for the 9 TEN-T corridors pre-Brexit [24]

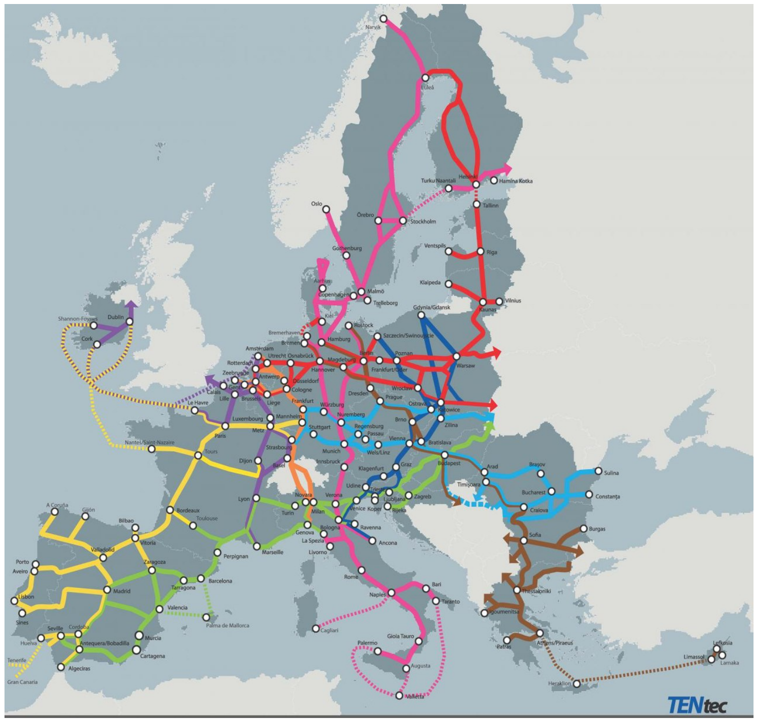

Figure 1.3: Plans for the 9 TEN-T corridors Post-Brexit [25]

In North America, Class I freight railroads spent approximately $740bn on capital expenditures and maintenance expenses between 1980 and 2020. Maintenance expenses account for 21% of their revenue [19] and in 2020 the capital expenditure for Class 1 operators was in excess of US$26bn a year [26]. Reductions to the maintenance potions of these costs are strongly desired.

AMTRAK, the largest passenger operator in North America, has proposed plans of a package of US$75bn of federal capital investment in rail infrastructure over the next 15 years [27] and has itself committed US$3.4bn in contracts for new greener train sets [28].

1.2 The problem

As discussed earlier in this introduction, we need a huge increase in uptake and efficiency of rail and intermodal transport to achieve our existentially important climate goals.

The existing momentum in the climate will result in significant increases to global average temperatures regardless of our short and medium-term achievements in reducing our climate change impacts. In the sixth Intergovernmental Panel on Climate Change (IPCC) Climate Change Assessment report [29], every single scenario predicts a global average temperature rise higher than the 1.5°C climate limit mandated by the 2015 Paris Agreement (Figure 1.4).

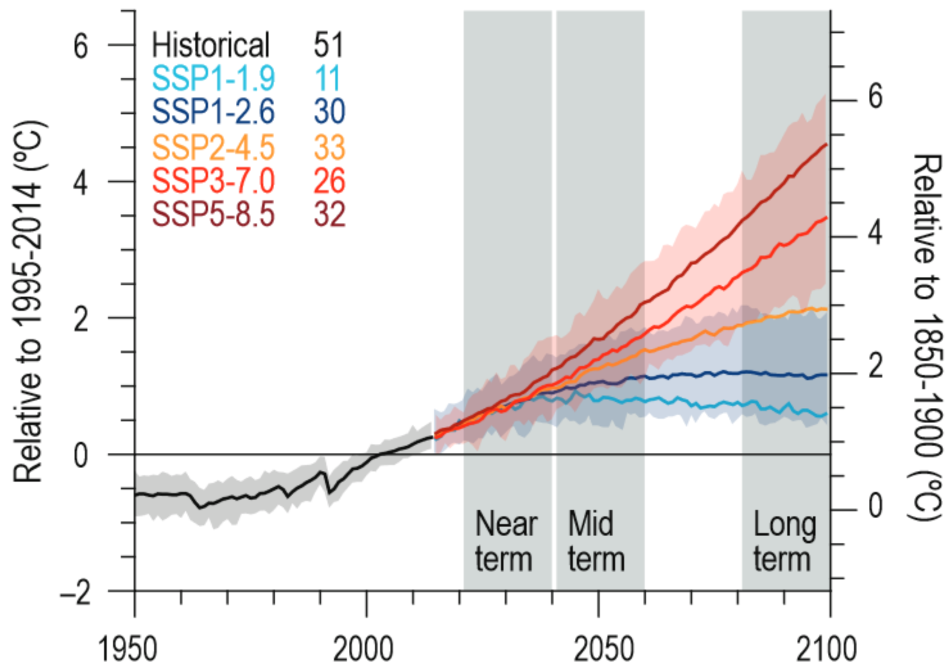

Figure 1.4: IPCC predictions for global temperature change [29]

The costs from temperature-related track issues are significant. The two-day heatwave of 2015 cost the UK economy an estimated £16 million and caused 220,000 delay minutes [30]. Instances of track failure from buckling, a direct result of improperly or ineffectively managed LS in rail, will increase as we experience more and more high temperature weather events.

To combat this we need to better manage LS in our networks. This requires a faster, cheaper and less disruptive technique to be developed to measure the stresses on in-situ rail tracks. This is why this measurement is considered the 'Holy Grail' for railway track maintenance and safety.

1.2.1 Current methods

Currently, the industry standard method of determining LS in rail is the Verse system from Vortok.

This requires the closure of the track while a 60m length of rail is unpinned (disconnected) from the ties/sleepers. A team of track engineers then use the Verse device to pull this unpinned length of rail vertically. The displacement achieved using a known force can be referred to empirical tables to determine the current LS and, as a result, the current Neutral Rail Temperature.

This is costly in both time and resource and is incompatible with current industry trends to automate rail condition monitoring.

1.2.2 Remote/automated monitoring

Rail stakeholders all over the world are transitioning towards automated and remote systems for collecting, processing and integrating rail measurement data into their maintenance operations [31] [32].

Companies such as HS2 Ltd. are developing a 'predict and prevent' approach to rail maintenance, with the planned implementation of thousands of remote monitoring locations to avoid unnecessary site visits from maintenance teams [33], thereby reducing cost, increasing safety and decreasing network downtime.

The development of a reliable ultrasonic system for measurement of rail stress would enable these essential measurements to be integrated into the data that will be provided to the planned £275m [34] Network Integrated Control Centre, enabling fast and accurate diagnosis of problem areas within the network without ever needing to visit track-side.

1.3 Aims & Objectives

1.3.1 Aims

The project aim was developed both in response to the identified need and through discussion with our funding partners NR and FRA, both major stakeholders in national rail infrastructure management and sources of expert advice on the requirements of the industry and the current method of infrastructure management.

Aim: Develop a system that can be attached to an in-service rail and return measurements of stress, and by inference establish the NRT accurate to ±5 °C or better.

The relationship of stress to NRT can be extracted by relating stress and strain along the longitudinal stress axis and utilising the relationship between strain and thermal expansion as follows.

If ϵ_1 denotes the thermally induced strain along the longitudinal axis, with τ_1 the corresponding axial stress and E the Young's Modulus of the material:

$$\epsilon_1 = \frac{\tau_1}{E} \tag{1.1}$$

and, in the absence of physical constraints, strain and change in temperature are linked via the thermal expansion coefficient α_L:

$$\epsilon_1 = \alpha_L \cdot \Delta T \tag{1.2}$$

When constrained, the rail will experience the resulting internal longitudinal stress. Using empirical values of $\alpha_L = 1.15 \times 10^{-5}$ for standard rail grade NR/L2/TRK/3011 [35] and $E = 207\,\text{GPa}$ we arrive at:

$$\Delta T = \frac{\epsilon_1}{\alpha_L} = \frac{\tau_1}{E} = \tau_1 \cdot 4.2 \times 10^{-7} \tag{1.3}$$

As such, a range of ±5 °C equates to a target accuracy in stress measurement of ±11.9 MPa.

1.3.2 Objectives

Project objectives:

- To respond to industry needs for a new device for measuring and monitoring rail LS
- To assess the current state-of-the-art, and from this analysis identify the most appropriate potential technologies for development

- To identify a novel technology or a novel application of a technology to this specific area of interest
- To advance the chosen technology as far as possible within the bounds set by the funders of the research

1.4 Thesis overview

The work completed fell into four main themes:

1. Selection of the most appropriate technology
2. Advancing the state of the art (where possible) within the selected technology
3. Developing a technique for the successful application of this technology to a real-world scenario
4. Design, prototyping and iteration of hardware and test platforms for the application of the developed technique

Themes 2 through 4, though initially undertaken consecutively became increasingly concurrent as the work progressed, with experimental results, improvements to technique and test platform (re)design all feeding back into one another.

1.4.1 Chapter overview

This thesis is divided into the following chapters, brief descriptions of which are given below.

1. Introduction

   A brief overview of the thesis, background, market scoping and impact assessment, detail of the problem to be solved and finally the thesis aims and objectives

2. Literature review

   A review of longitudinal stress management approaches to date, identification of potentially successful technologies and selection of the most appropriate technology

3. Ultrasonic theory

   An overview of the theory underpinning the selected measurement technologies and a description of the novel models that promise to overcome past disadvantages

4. Design development

   Details of the development process undertaken to design and manufacture 8 bespoke testing platforms and 8 novel sensor assemblies for conducting ultrasonic stress measurements.

5. Sensitivity analysis

   Numerical and experimental analysis of the theoretical sensitivity to variance in experimental parameters

6. Birefringence testing

   Details of the birefringence tests conducted, with brief summaries where applicable to show intersection with design development

7. Angled wedge testing

   Details of the angled wedge tests conducted, with brief summaries where applicable to show intersection with design development

8. Results

   Final results and discussion from birefringence and angled wedge testing

9. Conclusions

   Overall conclusions

10. Transfer to track

    Details of the problems, pitfalls and potential solutions to transferring the measurement technique to real-world track and suggestions for future work

1.4.2 Collaboration

This work was conducted in an externally funded research context. The author asserts that this thesis results from his own work, however, gratefully acknowledges the input from colleagues during the course of the project. A detailed account is provided in the first paragraphs of the relevant chapters.

Chapter 2

Literature review

This chapter summarises the literature review methodology then moves on to detail the sources of rail Longitudinal Stress (LS) and the complexity of the system, outlines and evaluates the previous technologies and methodologies used to manage rail LS, and develops the evidence basis for proceeding with ultrasonic LS measurement.

2.1 Search strategy

The key aims of this review were to:

- Determine the current incidence and trends in rail buckling events
- Identify the measurements of interest in rail condition monitoring
- Extract the current state of the art in longitudinal stress measurements in rail
- Identify previously unsuccessful longitudinal stress measurement approaches and understand their failure modes
- Determine, and justify the selection of, the most appropriate technology to pursue for a novel longitudinal stress measurement technique

This literature review was conducted using an adapted PICO methodology, details of which can be found in Appendix A. This evidence was supplemented by a locally curated library of papers found and maintained by the rail tribology researchers at the University of Sheffield.

The primary and secondary questions used in the evidence review were:

Primary: What is the best technology for measuring longitudinal rail stress?

Secondary 1: What is the history of past attempts with this technology?

Secondary 2: How does failure to manage longitudinal stress impact the railway industry?

The keyword tables and final search queries are detailed in Appendix A. Final numbers of relevant search results are detailed in Table 2.1.

Table 2.1: Results from academic database searches.

Database	Search returns	Duplicates	Relevant papers	Papers included
Scopus	493	5	27	5
STAR*	1003	6	24	12
Google Scholar	400	2	26	4
Tribology library	N/A	N/A	N/A	51

*Sheffield University internal library system

2.1.1 The 'Holy Grail' of rail maintenance measurements

A key factor underpinning the safe operation of all railway networks is an accurate and up to date knowledge of the track condition.

"The management of rail stress to prevent track buckles is one of the highest track risks on the network. CWR suffer(s) from a lack of stress and ballast. Despite understanding the controls necessary to maintain and manage a safe and reliable railway, we continue to suffer from track buckles each year. Systems for capturing and informing of rail stress aren't integrated and are out of date. These deficiencies can lead to train delays and impact on customers. Additionally, the ability to measure rail stress non-destructively, is still difficult. The only approved method for measuring rail stress, the VERSE testing equipment, has several limitations." [31]

When installing or repairing track, it is essential that the rail is tensioned correctly in relation to the ambient temperature. The aim of this operation is to set a NRT that minimises the risks of buckling (Figure 2.1) occurring on hot days and pull apart incidents in cold weather.

Figure 2.1: A typical track bucking failure. This failure mode can result from improperly managed longitudinal stress in a section of CWR. Image credit: Mandal-Lees [30]

Management of NRT is an issue for CWR as the rail is welded together in single sections several kilometres in length, and lacks the traditional fish-plated joints that accommodate the rail expansion and contraction due temperature changes.

Track failures contribute a significant cost to the running of rail networks, resulting in downtime, delays, accidents and increased maintenance costs. In the US, from 1997 to 2002, there were 38 derailments annually on average due to track buckling, with the cost in 2002 alone of $17 million [36]. In the UK, 137 buckling accidents were reported in the summer of 2003, which cost about £2.5 million [37], and two day heatwave in 2015 caused damage to railroads that cost the economy an estimated £12 million [30].

Due to the operational and theoretical difficulties in managing rail longitudinal stress, the myriad uncertainties and high cost of monitoring and maintaining a rail road in the correct longitudinal stress range, a fast, accurate, non-destructive and non-disruptive measurement of the NRT has been described by stakeholders on both sides of the Atlantic (FRA & NR) as the 'Holy Grail' of desirable rail condition monitoring measurements.

2.1.2 Rail longitudinal stress

Longitudinal stress is the stress experienced by the rail due to forces acting along its length. Rail is installed at a pre-determined level of stress that corresponds to a calculated NRT. This is selected for each location based on known variation in environmental conditions and set during the rails' installation. NR have indicated that the temperature used in the UK is usually 27 °C. On installation, and where the ambient temperature is below 27 °C – as is usually the case in the UK, the rail is extended by mechanical means prior to welding into the track. The extension (and thereby the amount of tension induced) is calculated so that the finished section will, when exposed to temperatures equal to the NRT, experience zero longitudinal stress. The thermally induced stress in the longitudinal direction can be expressed as:

$$\sigma = -\alpha \Delta T E \tag{2.1}$$

where α is the rail's coefficient of linear expansion, E represents the Elastic modulus of the rail steel, and the temperature difference relative to the NRT is expressed as ΔT [38].

2.1.2.1 Measurement & system complexity

Rail buckling is an issue of system stability, and in most locations, most of the time, the track exists in a stable state. The stability of the system is affected by a large number of variables such as the condition of the ballast, the condition of rail, ties and fasteners, and the presence of fixed spans and crossings embedded in or supported by other materials, such as concrete. The system as a whole is a complex set of nested inter-dependencies which makes the isolation of the impact of any one parameter incredibly difficult.

When a section of CWR is installed, a welding team will pre-tension the rail to achieve the nominal NRT. Rail traffic braking and accelerating can cause both instantaneous and permanent changes to the local longitudinal stress. Additional sources of change come from the movement of the entire track and ballast from continuous passage of railway vehicles and both daily and seasonal temperature variations. The presence of older sections of track that have not been recently/ever tested to determine their NRT introduce their own uncertainties into the system.

Instability can be reached by exceeding the restraining forces, often due to a confluence of different factors that include longitudinal thermal stresses, sometimes combined with the dynamic loading of a passing railroad vehicle. At the point of instability, very little is needed to push the system into a buckled state.

The incidence of pull-aparts is also dependent on correct management of NRT, however the fracture of rails in periods of extreme cold depends less on the overall track stability but on the condition of the rail and the presence of flaws and cracks where a failure might initiate.

He & Ling [39] found that traditional temperature-induced stress models do not agree with their modelled stresses when considering the effect of the fastenings:

"...no definitive answers have been given to the problem of calculating, under operating conditions, the frictional resistance generated by fastenings and the location in a rail of the maximum temperature-induced stress" [39].

Additionally, the rail surface temperature varies with micro-climate influences (such as the presence of shade trees, embankments and other features), local weather (wind, rain, air temperature) and can vary across the rail cross-section as much as 6°C, with the magnitude of the variation being dependant on proximity of the measurement location to a sleeper. Additionally, the modelled values for rail temperature also depend on the relative mass of the constituent parts of the rail (head, web, foot) [40].

The thermal stress within a rail at a given temperature is dependent on the current NRT of the rail, but buckling behaviour itself is not solely dependant on the thermal stresses, it is impacted by dynamic loads in lateral, vertical and longitudinal planes, as well as track and wheel defects. Samavedam et al. have also shown that track stability is strongly dependent on the track's lateral stiffness, the spacing of ties and the maintenance and consolidation of track ballast [41]. The permissible maximum stress value for used or worn rail can also be 26% lower than that for new rail [40].

A lack of data on key influencing factors also limits the applicability of modelling approaches and acts as a barrier to extracting clean or uncomplicated data from on-track measurements. In their 2022 review of NRT and it's variation, Skarova et al. highlight the combined effect of several factors, including differential rail temperature, acceleration and braking forces from rail traffic and fundamental track support and rail fastener stiffness can result in the redistribution of NRT along the track in response to cycling by temperature of traffic. They also note that permanent track settlements create deviation from the installed NRT and that a better understanding of all these factors is essential in developing resilience of the rail infrastructure to the impacts of climate change [42].

Currently, it is unlikely that the extent of track movement (the localised result of braking and accelerating rail traffic) is known and the accuracy of re-stressing activities after rail brakes or defect removal is uncertain. The cumulative effect of these uncertainties increases the risk of track buckling events. The currently available options for establishing the NRT of a section of railway are intrusive or destructive e.g. verse testing or cutting the rail, thereby releasing the stress, and measuring the change in length.

In short, NRT prediction is not currently reliable due to the complexity of the physical system, and so far, all previous efforts at using non-destructive or track closure-free measurements have failed to find a practical application [43].

2.1.3 Longitudinal stress management approaches

This section introduces and critically analyses a number of existing rail stress measurement methods using both destructive and non-destructive techniques. An excellent overview of methodologies [44] is reproduced below (Table 2.2), clearly identifying the limitations and considerations for each. Several principal methods have been assessed in more detail in subsequent subsections.

2.1.3.1 Rail cutting

One technique for measuring and monitoring of longitudinal rail stress involves releasing a length of rail from its clips. A series of punch marks are made on either side of the cutting location at an interval of roughly 100mm. A sliding caliper is used to measure the distance between punch marks L_f. Once cut, the new distance L_e between punch marks will change relative to the stress in the rail at the time of cutting. If the extension, calculated using the equation:

$$e = L_e - L_f \tag{2.2}$$

is positive, the rail is in tension and the rail temperature T_R is lower than the NRT or T_N. If e is negative, the rail is in compression and the rail temperature is higher than the NRT. Applying Hooke's thermoelastic law allows us to relate the extension to the difference in rail temperature:

$$T_R - T_N = \frac{e}{\alpha \cdot L}(T_R - T_N) = \frac{e}{\alpha \cdot L} \tag{2.3}$$

This method is both relatively simple and accurate, however it's destructive nature requires time consuming and costly track closures, maintenance crews and machinery.

Table 2.2: Existing technologies for NRT measurements (reproduced from [44]).

Method	Basic Principles	Shortcomings	References
Rail Cutting	Cut rail to release thermal deformations for direct measurement of rail deformations	Time consuming Destructive Disruptive to train operations	Arts[45] and Johnson[46]
Rail Lifting	Impose vertical force to unclipped rail until reaching a pre-determined distance. Vertical stiffness correlated to axial force to estimate NRT	Time consuming Semi-destructive Disruptive to train operations Rail must be in tension	Johnson [46] Kjell and Johnson [47] and Weaver and Damljanovic [48]
Hole-drilling	Material removal from a hole drilled into the rail web along the rail neutral axis relieves the stress that can be computed utilizing deformation measurement techniques	Semi-destructive Disruptive to train operations Sensitive to hole sources of error Sensitive to surface strain Potential plastic deformations caused by drilling procedure	Johnson [46] and Zhu and Lanza di Scalea [49]
Deformation measurements	Uses strain gage or extensometer data to measure rail thermal elongation to compute stress*	Contacting Instrumentation installation Relies on changing dimension Needs stress-free reference measurement	Arts [45] and Johnson [46]
Ultrasonic waves	Changes in ultrasonic wave characteristics (e.g. speed, polarization, non-linearity of guided waves) propagating in the medium are correlated to the stress state in rail	Contacting Needs stress-free reference measurement Sensitive to material structure/defects Sensitive to rail surface quality Potentially high instrumentation demands	Rizzo and Nasrollahi [50] Johnson [46] Alers and Manzanares [51] Szelazek [52] Hurlebaus [53] and Nucera et al. [54]
X-ray	Distance between two atomic planes in a crystal is measured and related to material stresses. Change in interplanar spacing is indicative of axial stress development	Measures a small surface volume Needs stress-free reference measurement Distance data of the atomic planes Requires clean rail surface High instrumentation demands	Johnson [46] Kjell and Johnson [47] and Hauk [55]
Magnetic	Electromagnetic and acoustic response signals (Barkhausen noise) produce a magnetic field. The permeability in the magnet field is correlated to the longitudinal stress	Time-consuming calibration Reference material measurement Eliminate local surface perturbations High instrumentation demands Sensitive to microstructure condition	U.S.A. Patent No. 5,655,120, 1991,18 U.S.A. Patent No. 5,992,241, 199919 and Wegner [56]
Vibro-elastics	Exciting the rail to obtain vibration mode characteristics that change with the axial force	High instrumentation demands High instrumentation accuracy Needs stress-free reference measurement Advanced FE calculations	Kjell and Johnson [47] and Weaver and Damljanovic [48]
Piezoelectric	The piezoelectric excites the rail to obtain an EMI response signal from the rail that indicates deformation	Contacting Instrumentation installation High instrumentation demands Exists in experimental stages	Phillips et al. [57] and Zhu and Lanza di Scalea [58]

*Note: In fixed CWR longitudinal stress can only be inferred by strain measured in non-constrained axes

2.1.3.2 Strain gauges

The installation of strain gauges can be used to monitor the stress within a rail. This, however, requires either the knowledge of the strain values at the time the gauges are mounted (generally by performing a cut and stress operation immediately prior), or gauges must be installed prior to the rail being installed and remain in position continuously. These methods are not considered cost-effective for whole-network management of NRT but are useful for permanent installations in targeted problem areas [59]. Additional considerations are the longevity of strain gauge installations, in terms of number of stress cycles, durability of adhesive bond between the gauges and the rail and the detrimental effect of weatherproofing on the aforementioned cycle count [60]. Liu et al. present a potential new device (Figure 2.2) which combines a full-bridge strain gauge within an enclosure that addresses some of the environmental concerns. However the measurement is indirect, requires a correction equation for different seasonal conditions and is susceptible to non-uniform rail temperatures [38].

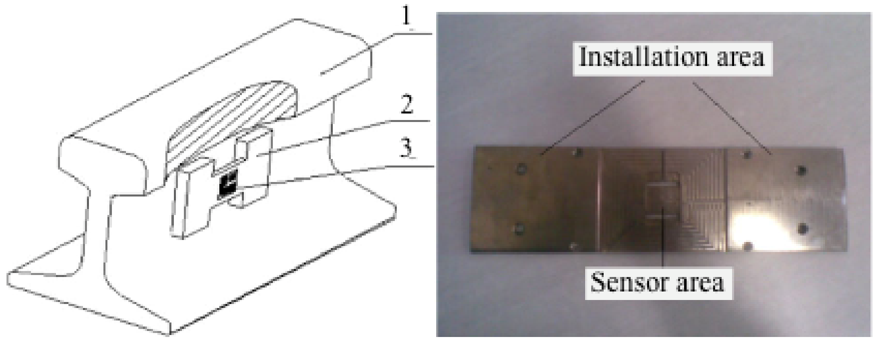

Figure 2.2: A novel device for measuring rail longitudinal stress using strain gauges [38]

2.1.3.3 Rail creep

Measurement of rail creep is considered a useful proxy measurement for NRT in some areas. Rail creep and strain gauge measurements have been shown to correlate well, giving a "a general indication of the track's longitudinal stress condition" [59] but this method does not offer access to numerical values.

2.1.3.4 Rail-wheel vibration analysis

Numerical models have been developed linking the low-frequency modes within the time-domain features of wheel-rail vibration responses to NRT [61]. While the authors establish numerical relationships of these frequency responses with track defects and vehicle speed, this review has not found subsequent prototypes developed using this system.

2.1.3.5 Rail natural frequency - mechanical method

Luo et al. [62] demonstrate a natural frequency analysis method, both numerically and in a controlled experiment, that "indicates the inherent relationship between the vibration characteristics of the CWR track structure and the rail temperature force". This method is not proven to extract the longitudinal stress. It also required that the rail be released from it's fasteners to calibrate for the zero stress state and the models are sensitive to the system variables (such as sleeper distance, rail wear & track type/profile). The quantification of these effects is unknown.

2.1.3.6 Hole drilling

Another method of stress analysis with strain gauges is shown in Figure 2.3. Strain gauges are arranged at 3 orientations around a single point. Changes in strain distribution as a hole is drilled give, with the appropriate correction factors, accurate knowledge of the state of the surface stress in the rail at that precise location [63].

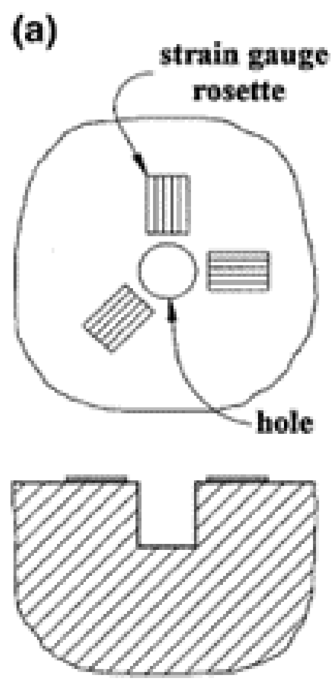

Figure 2.3: Conventional hole-drilling method with the strain gauge rosette [63]

While the use of strain gauges in examination of residual stresses are decades old, this method returns accurate deflection values related to the total stress local to the drilled hole. It is not possible to separate the residual surface stress from this measurement or to extrapolate accurately from the specific location to the entire depth of the specimen or entire length of a rail section. Additional considerations are a high time and cost per measurement, and a sensitivity to the eccentricity of the drilled hole. Šarga and Trebuňa [64] found potential application for two separate methods of using digital imaging to examine the changing stresses in the area surrounding the hole drilling technique, but in both cases the equipment is deemed more suitable to a laboratory environment and quantitative data is not reported.

2.1.4 Magnetic methods

An established principle, finding much use as an on-line flaw and fault detection method, Barkhausen noise analysis has found widespread use in the automotive, aerospace and metallurgical manufacturing industries [65]. A series of discontinuous changes or jumps appear in the response signals during the magnetization process of a ferromagnetic material. These discontinuities can be detected by electromagnetic or acoustic transducers. One layout is presented in Figure 2.4.

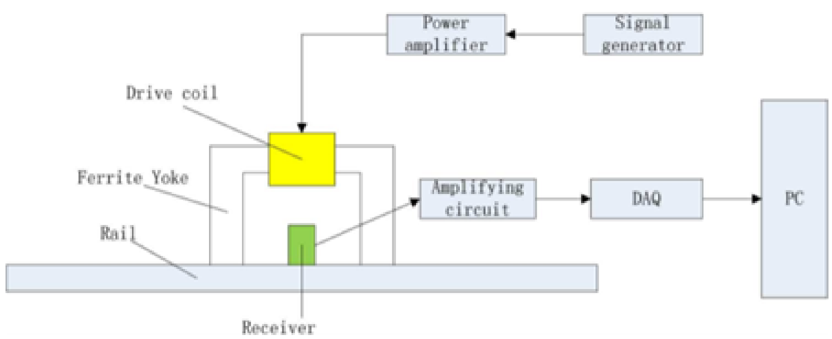

Figure 2.4: Magnetic measurement method [65]

The measurement depth limit for Magnetic Barkhausen Emission poses a potential issue and is variously quoted to be from 1mm [66] to between 50 and 200μm [67]. Maximum measurement depths of between 4 and 8mm are given for Magneto-Acoustic Emissions techniques, though there is debate surrounding the validity of the assumptions made in determining this theoretical depth. An investigation by Shu et al. [68] using a Metal Magnetic Memory-Magnetic Barkhausen Noise (MMM-MBN) system returned field tested results of NRT accurate to 4.78%. No subsequent mentions of this specific approach and more recent implementations have been found in this review. Temperature dependence of the measurement sensitivity has also been thought to be a limiting factor, though Ding et al. [69] have recently used the relationship between longitudinal and transverse RMS signals to improve their measurements. The Barkhausen noise method requires lengthy calibration, is significantly influenced by microstructure and requires measurements as two different temperatures [46].

2.1.4.1 Rail vibration

The D'stressen device, developed in Aotearoa (New Zealand) comprises a vibrating bar clamped onto the rail head and instrumented with accelerometers to capture it's vibration amplitude as it is excited at various frequencies. This device has been extensively evaluated at TTCI but required accurate calibration of the maximum amplitude found only at zero stress. Additionally, the linearity of the amplitude-stress response is equally dependent on capturing sufficient data at a single location and is not transferable between locations [70].

2.1.4.2 Rail lifting (VERSE)

The Vortok's VERSE device (Figure 2.5) is currently the state-of-the-art for measuring LS in rail, and can return NRT measurements to accurate approximately ±3.5℃. As such, it remains the benchmark against which any future measurement system will be judged.

The measurement requires a temporary track closure and a maintenance crew alongside engineers to operate the device. It is necessary to un-clip a 30m length of rail and apply a series of vertical loads to the free rail. By measuring the vertical deflections, a value for longitudinal stress in that section of rail can be calculated. Measurements are provided on a handheld computer. As NRT is reliant on the rails' stress state, a combination of empirical data and correction factors can be used to determine NRT.

Figure 2.5: VERSE rail stress measurement device performing measurements on track [71]

The VERSE method can only be used in cold weather when the track is certain to be in tension. Should a 30m length of rail be unclipped near or above the current NRT, the track could either immediately buckle would extend as stress is released and be impossible to return to the restraining clips without cutting and welding. This is a significant disadvantage as it restricts the management of NRT to the colder months of the year, while the main buckling incidences are seen throughout the summer months.

2.1.4.3 Ultrasound

Using techniques and technologies more familiar in the field of NDT, ultrasonic Time of Flight (ToF) measurements can be taken in high time based resolutions. Utilising the known relationships between the stress state of a host material and the difference in the SoS of ultrasonic waves travelling through that material polarised both in the direction of, and perpendicular to, the longitudinal stress, values for stress can be obtained directly from a non-destructive analysis. An installed ultrasonic device is shown in Figure 2.6.

Figure 2.6: An ultrasonic measurement device installed on in-service rail

Some ultrasonic measurements have the benefits of being a true full-depth measurement, in that the acoustic signals travel through the entire depth of the specimen, and are not only a measurement of the surface stresses.

The established maturity of the technology in the NDT arena means that the measurement hardware technology is already well developed and can be re-purposed to this novel area of measurement. As such, ultrasonic measurement solutions have strong potential to be fast, portable, low cost and usable by non-expert technicians.

The accuracy of these methods is somewhat dependent on accurate calibration and knowledge of the host materials' ultrasonic properties or reference measurements [72]. Johnson notes that ultrasonic birefringence methods rely on accurate knowledge of fewer material constants than those using only longitudinal waves, but that the directional dependency of the SoS of these waves can also be affected by micro-structure, plastic deformation, material texture and temperature [46].

2.1.4.4 Rayleigh waves

Yet another ultrasonic method uses Rayleigh waves produced by a wedge transducer mounted on the rail and their change in polarisation detected by a Laser Doppler Vibrometer (LDV). While the Rayleigh wave polarisation changed predictably with stress, the measurement was compromised by surface conditions such as rust and pitting [73]. Surface preparation was a key factor in achieving good signal quality for Djayaputra, as well as considerations of the focal distance and angle of the LDV [74].

2.1.4.5 Ultrasonic backscatter

A method was investigated by the University of Nebraska-Lincoln, using a derived relationship between the scattering by grains within a poly-crystalline material and applied stress (including the inherent relationship between grain size and scatter) to attempt to extract the longitudinal stress on in-service rail. Results showed that grain scattering of ultrasonic signals was susceptible to applied stresses, but was also dependent on each different transducer configuration. Laboratory results on tensile specimens in an ultrasonic scanning tank were inconclusive. In the field, using single point sensors, experimental variability was too high to make reliable measurements [75].

2.1.5 Previous ultrasonic analyses

Three categories listed in Table 2.2 [44]: ultrasonic waves, vibro-elastics and piezoelectric methods, rely on nearly identical sensors and digitsation. This subsection documents in more detail several previous attempts to develop a measurement of NRT using these methods to understand in more detail their current limitations.

2.1.5.1 DB-Method

A track-mounted method using propagation times for shear waves both along the top and side of the rail head [76]. No further information is readily available in published or grey literature, indicating that the method has not been developed further.

2.1.5.2 NIST & RIPL

Two methods for portable and vehicle mounted ultrasonic stress measurement solutions are mentioned in Johnson [46] but their respective web addresses are no longer active and no papers are referenced.

2.1.5.3 Natural frequency, standing & guided waves

Using impacts to generate a number of different wave forms has been investigated by Kjell & Johnson [47] & Dersch [77]. Guided bending waves were shown by experiment to successfully determine NRT in a short section of test track, however, accuracy depended on a large number of variables, both experimental and modelled, and required very high accuracy data on materials and rail profiles.

Dersch's initial investigation determined that the frequencies used were not suitable for returning values of NRT, the modelling indicated that higher frequencies should exhibit the required sensitivity. The authors state that laboratory testing for this type of vibrational analysis is not representative of real-world conditions and further development in this vein will require large scale data collection and neural-network machine learning in order to arrive at a usable model and technique.

A 2013 investigation by Aikawa et al. validated a resonant frequency model with on track measurements[78], showing a high degree of linearity between the change in resonant frequency and measured longitudinal stress levels below -180kN.

Developed by a team from the University of California San Diego, the Rail-NT device uses the effect of thermal stresses on a double harmonic wave propagating in the material [79]. Reliable measurements of NRT have been made both in the lab and in a controlled full-size test bed, however, interactions with multiple stakeholders in the USA have indicated that this method has not borne fruit, having failed to make the transition from controlled experiments to in-service track trials. It is believed that the elimination of additional signals/wave modes generated by a number of real-life on-track conditions posed an insurmountable challenge.

Xiangyu Dian et al. demonstrated the long-term reliability of several permanently installed LS monitoring station using guided waves. It is unclear whether the installation was undertaken on existing track on installed with the track its self, and the measurement error ranges between 3.6% and 41%, with higher errors tending to occurs at the lower stress ranges [80].

2.1.5.4 Electromechanical impedance

Directly bonding Lead zirconate titanate (PZT) transducer elements to a steel bar (approximating a rail) and using an Electromechanical Impedance (EI) analysis has shown correlation with frequency shift of resonance peaks with applied stress [58]. Access to values of absolute stress values using this approach face "non trivial" difficulties, such as access to accurate values for all the ultrasonic constants for both the host material and the PZT material itself. This technology may be more suited to detecting stress changes or continuous monitoring.

2.1.5.5 Wave velocity matching

Kang et al. propose a wave velocity matching-based neutral temperature estimation [81]. The method proposes to separate the capture of temperature-dependent and stress-dependent data to avoid the existing challenges associated with temperature induced wave and material property variations. The method has been validated using finite element analysis, but would require measurements to be conducted in both fixed and partially fixed (one end free) rail states, indicating that this would not be feasible in compression. Additionally, the finite element models do not include the full rail profile.

2.1.5.6 LCR

Vangi presents a method for determining NRT using sub-surface longitudinal waves (known as Longitudinal critically refracted (LCR)). Due to the influences of uneven temperature distribution within the rail, the influence of material properties and low repeatability the meothod is more suited to long-term installations with daily readings used to give estimations of the NRT [82].

2.1.5.7 EMAT

A number of investigations have been launched using Electro-magnetic Acoustic Transmission (EMAT) systems to generate and receive ultrasonic signals through rail sections. Hirao et al. report on two different methods of determining stress values from the birefringence effect, which gave promising linear responses to stress [83].

2.1.6 A change in the state-of-the-art

Johnson [46] provides an overview of the then state-of-the-art in ultrasonic measurements. At the time it was felt that ultrasonic solutions could not provide a sufficiently accurate determination of the longitudinal stress for the following reasons:

- Inaccuracy in measurement of ToF
- Inaccuracy in measurement of the zero-stress calibration
- Inaccuracy of the measured elastic constants
- Inaccuracies due to plastic deformations on the measured surfaces
- Wave scatter caused by surface plastic deformations

In the intervening years, signal processing technology and data acquisition systems have advanced significantly, and the Mechanical Engineering department at the University of Sheffield has been at the forefront both of using these new technologies as they have appeared and of developing in-house software and hardware solutions. The accurate measurement of ToF, previously considered to be an insurmountable source of error, is now significantly improved.

Prior work conducted by the author and Dr Yue Yang at the University of Sheffield [84] has shown that the ultrasonic constants can be measured to a significantly higher degree of accuracy than has been shown in previous literature [85]. It may even be possible to generate a reference library of these constants for different rail types, profiles, manufacturers and year of manufacture.

Restriction of analysis to the rail web also prevents inaccuracy, signal degradation and wave scatter due to plastic deformations.

Knopf et al. [44] also present the following shortcoming for ultrasonic measurement of NRT:

- Contacting
- Needs stress-free reference measurement

- Sensitive to material structure/ defects
- Sensitive to rail surface quality
- Potentially high instrumentation demands

For each of these valid issues there now exist realistic solutions. Stakeholders' interest in this 'Holy Grail' supersede the high instrumentation demands - to paraphrase our industry sponsors FRA & NR: "if you can build it, we'll buy it!".

Our discussions with our industry stakeholders have resulted in a measurement specification that includes surface preparation and measurement of the rail web. In a UK context, it is no longer permitted to access in-service track without a track closure. These most commonly occur when a section of rail is set to undergo maintenance. This affords any measurement team a number of hours to potentially prepare the surface of the rail for accurate measurement. It is also the considered opinion of our sponsors at the FRA that a non-trivial amount of track preparation is acceptable if it generates a suitably accurate measurement. This preparation will eliminate the surface quality considerations

New numerical models have been developed that identify a 'universal relation' between the longitudinal stress in a weakly non-isotropic solid such as rail steel based on the measurement of guided plane waves travelling at specific angles through the host material [86]. This universal relation does not rely on any measurement or prior knowledge of any of the second or third order ultrasonic material constants and could provide, for the first time, access to a reference-free measurement.

Pursuit of the angled wave method will not prevent parallel investigation into advancing the birefringnece method. A combination of both methods can be evaluated experimentally to advance our understanding of the measurement and its possible limitations as the state-of-the-art is pushed forwards.

Chapter 3

Ultrasonic theory

This chapter begins from basic ultrasonic theory, developing an understanding of different wave types, explains the interactions between ultrasonic waves and bulk stresses in the host material. It then follows to detail the proposed mathematical models for a novel angled wedge measurement that has potential to deliver a calibration free rail LS measurement and briefly details the decision on which signal processing method will be used to extract the ToF.

3.1 Introduction to ultrasonics

3.1.1 Ultrasonic wave types

There are a number of different wave types in common use for Non Destructive Testing (NDT) and other ultrasonic analyses. These are commonly divided into 3 broad categories:

Surface waves: These waves are generated using wedges or combs attached to the host material surface. There are many types of surface wave and they propagate along or close to the surface of the host material.

Guided waves: These waves have radiating wave-fronts and are guided 'actively' by using angled wedges to direct the wave or 'passively' by interactions with the geometry of the host material.

Bulk waves: These have a linear wave-front and are simplified to a constant 2D pressure wave moving though a host material.

This investigation used bulk waves. The polarization of a bulk wave is defined by the direction of particle motion relative to the direction of propagation. Waves where particle motion is parallel to the propagation direction are known as longitudinal waves, an illustration of which can be seen in Figure 3.1.

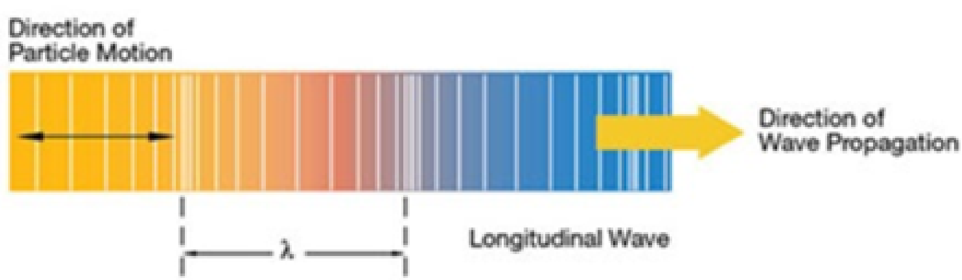

Figure 3.1: An illustration of the propagation of the energy of a shear bulk wave through a host material [87]

Waves where particle motion is orthogonal to the propagation direction are known as shear (transverse) waves, an illustration of which can be seen in Figure 3.2.

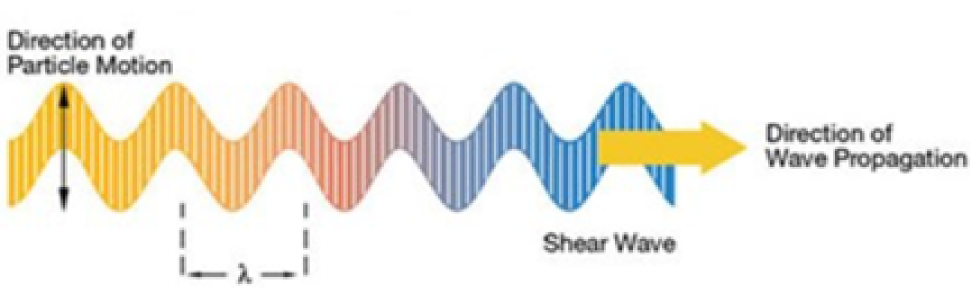

Figure 3.2: An illustration of the propagation of the energy of a shear bulk wave through a host material [87]

3.1.2 Ultrasonic terminology

Time of Flight

The ToF for an ultrasonic signal is the time it takes for a signal to be emitted from the transducer, travel through the host material and be received back at a transducer. Depending on the test being conducted, the signal may be received at the emitting transducer (after being reflected off the specimen materials' inner surface) or another transducer at a different location on the specimen.

The acousto-elastic effect

The relationship between ultrasonic wave speed and stress in a solid is defined as the Acousto-Elastic Constant (AEC). The speed of sound within a material is affected by the direction and magnitude of an applied stress. Figure 3.3 illustrates this stress-induced anisotropic behaviour and provides the fundamental principle of ultrasonic stress measurement. The subscripts relate to the direction of the principal strain axis, 1 denoting in-line with the strain, 2 and 3 are the mutually orthogonal directions.

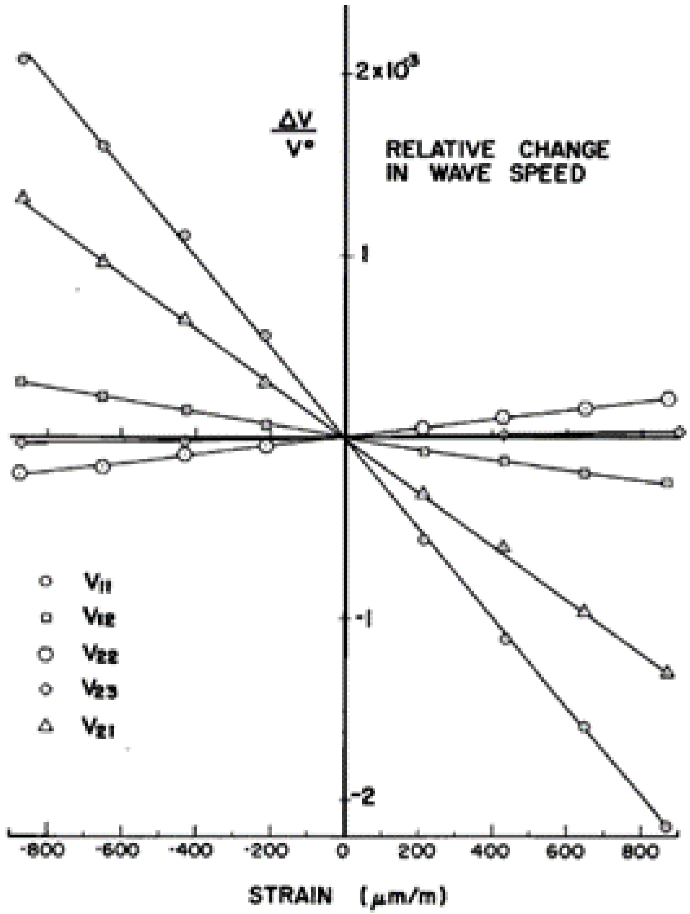

Figure 3.3: The change in ultrasonic wave speed vs strain for waves polarised and propagating in different directions through a uni-axially stressed test specimen [85]

3.1.3 Material microstructure considerations

An extensive characterization of both legacy and modern rails found that the microstructural variation was very small, with consistent Pearlitic microstructures. Egle & Bray concluded that 'acoustoelastic constants as well as third-order constants may be relatively independent of the specific composition and heat treatment as in the case for the second-order constants' [85]. The variance of both shear and longitudinal wave velocities within Pearlitic steels has been found to be very low [88] with the variance of the SoS between fine and coarse Pearlitic structures less than 0.5%.

To minimize boundary effects from interlamellar spacing and Pearlitic colony size on acoustic transmission and impedance, a wavelength at least 5 times, and ideally 10 times, larger than that of the average grain size is desired. Using a colony size of 6.5μm [89] and an with interlamellar spacing width found to be as low as 100 nm [90], thus suitable analysis can be conducted with ultrasonic frequencies between 1 and 20MHz. Figure 3.4 [91] shows the micro-structure of R260 rail steel, the alternating bands of cementite (silver/white) and ferrite (dark grey) within the pearlite colonies are evident, as is the grain boundary between the individual colonies themselves.

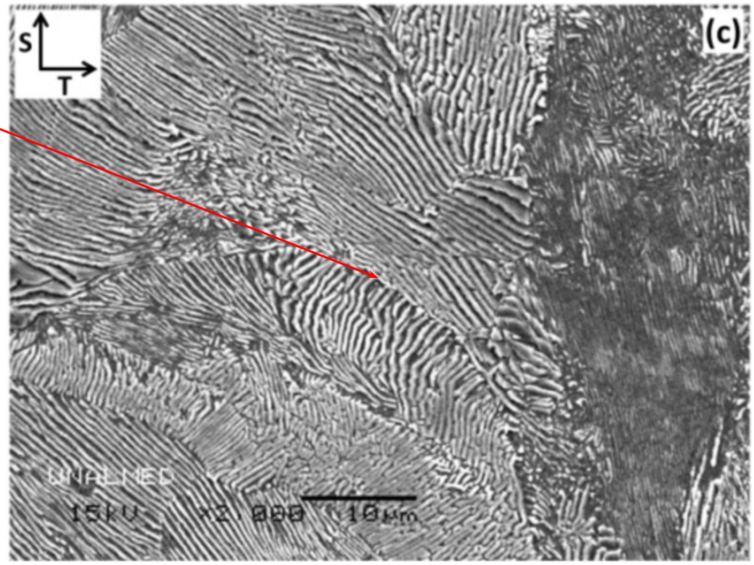

Figure 3.4: A photograph of the alternating cementite (silver/white) and ferrite (dark grey) bands within the pearlitic colonies in the micro-structure of R260 rail steel [91]

An important consideration may be that the AEC has been found to be affected by the ferrite content within Pearlitic steel, the trends and relations are shown in Figure 3.5.

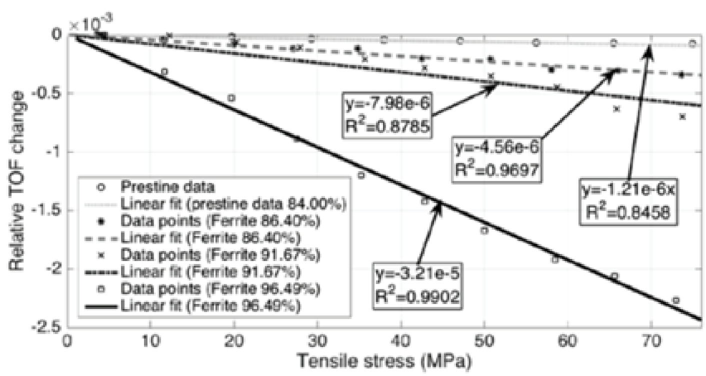

Figure 3.5: Relative Time-of-flight change with stress for different ferrite phase contents [92]

Discussions with industry contacts at NR, who have an extensive and detailed knowledge of the UK rail production methods, have indicated that while there will have historically been more significant variation in steel production methods, and thus variation in the resulting materials' microstructures, the last 20 years have seen much greater standardization. A high confidence is expressed that not only is it considered unlikely that significant microstructural variations like those shown above will be found in modern rail, but also that a method that will work for rail steel in this modern form will be more than sufficient in providing a valuable tool to aid in the maintenance of rail Neutral Rail Temperature (NRT). It must be noted, however, that with more attention paid to the consistency of the steel quality in the head and foot (as the running and supporting sections of the rail) during manufacture, it is in the web that 'inclusions' and impurities which may impact the measurements are more likely to be found.

3.2 Extracting stress values from ultrasonic signals

The most well known model for accessing the value of stress field using ultrasonic signals is ultrasonic Birefringence. A novel mathematical model is also presented that uses combined angled waves. A schematic diagram for both is shown in Figure 3.6.

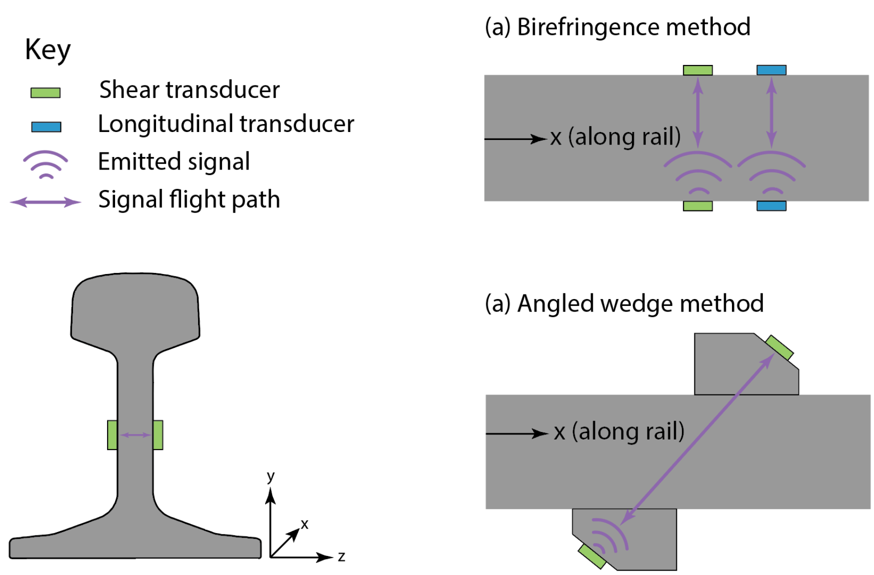

Figure 3.6: Schematic diagram of transducer arrangement for (a) birefringence and (b) angled wedge measurement

3.2.1 Birefringence

If two ultrasonic shear waves (sound waves that vibrate perpendicularly to their direction of travel) are polarized in mutually orthogonal directions and both travel along the same path within a material experiencing an applied stress, the ToF of each wave will be affected by a different amount. This effect is due to the stress-induced anisotropy [93]. Thus the ToF of a signal travelling parallel to the stress will increase, while a signal travelling perpendicular the stress direction will decrease [94]. While the density change in the material caused by the strain has a small effect on the ToF, the change in Speed of Sound (SoS) due to the effective change in the materials' elastic constant is more significant, and this in turn indicates a non-linearity in the relationship between ToF and strain when examining a material within its elastic range.

The acoustic birefringence effect has been proved sufficiently accurate to successfully characterize bulk stress and to determine the texture and texture related properties of rolled parts [95] during manufacture. In seeking to identify the magnitude of an unknown applied stress, knowledge of the material properties, including the material-specific third order elastic constants, the AEC and a measurement of the ratio between these two perpendicular wave speeds gives access to the stress value. The AECs are found to vary between the web and the head of the rail, but not between samples from different manufacturers [76].

A wave travelling through a medium has both a direction of propagation (the direction of travel) and a direction of polarisation (the axis of vibration). The widely accepted notation for differentiating between waves with different directions and polarisations is to use a double sub-script, the first number indicating the direction of propagation, the second the axis of vibration. For example: A shear wave, one that vibrates orthogonally to its direction of motion, may propagate in direction x_2 but vibrate in the x_1 direction. As such, the notation for that wave's speed (c) will be c_{21} The birefringence effect states that the difference between shear wave speed (c) in the stressed plane c_{21} and in an unstressed plane c_{23} is proportional to the stress, see equation 3.1, where ρ is the mass density and α depends on the rail's material properties. To use this technique only requires bulk waves that travel directly across the web, as shown in Figure 2.

$$\rho(c_{21}^2 - c_{23}^2) = \alpha\sigma_1 \tag{3.1}$$

Using the birefringence theory, and assuming the solid to be weakly non-linear and isotropic, we can predict how the different wave speeds change when increasing the stress.

By reducing an unknown material (that is isotropic at rest) to a simpler determination of 5 acoustoelastic constants, and by experimentally determining these constants, it becomes possible measure the stress using birefringence and many other techniques, including surface waves. To use birefringence, we need only 5 constants to completely characterise the material and know how it responds to stress. Those constants are: λ, μ; the Lamé parameters, and

λ_1, μ_1, and η_1; the third order Murnaghan constants [96]. Assuming that in a uni-axial stress case, e.g. longitudinal stress, the material is stressed along x_1 but no stress exists along x_2 and x_3. Let c_{ij} be the wave speed of a wave travelling in the x_i direction and polarised in x_j direction. This notation allows us to define the speed of a pressure (longitudinal) wave travelling through the thickness of the material (in this case the web of the rail) by c_{22}, and two orthogonally polarised shear wave speeds travelling the same path as c_{23} and c_{21} respectively. Building on the theory [96] we can derive the following equations [86]:

$$\rho c_{22}^2 = \lambda + 2\mu + (\lambda_1 + 2 \cdot \mu_1)_1 \tag{3.2}$$

$$\rho c_{23}^2 = \mu + \mu_1 \tau_1 \tag{3.3}$$

$$\rho c_{21}^2 = \mu + (\eta_1 + 2 \cdot \mu_1)\frac{\tau_1}{2} \tag{3.4}$$

where τ_1 is the stress along x_1, and ρ is the mass density (when the solid is unstressed), which in the bulk of a material is very stable over time. By measuring the wave speeds for different levels of stress 1, then we can use the intercept and slope of the above equations to determine the constants are λ, μ, λ_1, μ_1, and η_1. Any piece of homogeneous hard solid material that does not have significant texture anisotropy can be fully characterised by using these five constants. The three constants λ_1, μ_1, and η_1 are specific to this analysis, non-dimensional, and are equivalent to and can be translated to the Murnaghan constants.

In order to validate the method, the values of these constants, calculated from the ultrasonic measurements, can be directly compared with the values of the same constants derived directly from stress and strain measurements.

3.2.2 The continued value of birefringence

The birefringence principle and it's sensitivity to longitudinal stress in structural steels is long proven, yet is has never been developed into a successful measurement of rail LS. Working with a full understanding of past failures and current challenges, it is still worthwhile to pursue a birefringence-based solution due to the relative simplicity of the measurement. There are many potential solutions for the uncertainties in material constants and ToF accuracy, and running parallel investigations with the angled wedge method (detailed in the following sub-section) will allow direct comparison and potential hybridisation of the methods.

3.2.3 A novel method - angled waves

There also exists a fundamental relationship between the stress and shear wave speeds moving both in line with and orthogonal to the direction of applied stress which is valid for any material [86]. The advantage of this principle is that it gives, in theory, a direct measure of the stress and does not depend on material properties.

$$\begin{aligned} A &= \frac{\pi r^2}{2} \\ &= \frac{1}{2}\pi r^2 \end{aligned} \tag{3.5}$$

Governing equation:

$$\rho \frac{\partial^2 u_j}{\partial t^2} = A_{0ijkl} \frac{\partial^2 u_l}{\partial x_k \partial x_i} \tag{3.6}$$

where:
i,j,k,l are coordinate indices, u : displacement term, x : positional axis, $\frac{\partial^2 u_j}{\partial t^2}$: acceleration term for displaced particles, $\frac{\partial^2 u_l}{\partial x_k \partial x_k x_i x_i}$: the change in displacement of the wave, A_{0ijkl} : constants/instantaneous elastic moduli.

Assuming no edge effects (waves are propagating far from the edges of the specimen), waves only effect the material in their direct path, bulk wave modes do not change, that there is no motion in z direction and that the wave is propagating in the θ direction we can substitute the wave equation into the governing equation [97] we get:

$$u = (U_1, U_2, 0)e^{(ik(x_1 \cos\theta + x_2 \sin\theta - vt))} = \begin{bmatrix} U_1 e^{ik(x_1 \cos\theta + x_2 \sin\theta - vt)} \\ U_2 e^{ik(x_1 \cos\theta + x_2 \sin\theta - vt)} \end{bmatrix} \tag{3.7}$$

where:
U_1 is the amplitude component in the x_1 plane, U_2 is the amplitude component in the x_2 plane, k is the wavenumber $k = \frac{2\pi}{\lambda}$ and v is the speed of sound.

Differentiating 3.7 to arrive at $\frac{\partial^2 u_j}{\partial t^2}$:

$$\begin{aligned} \frac{\partial u_j}{\partial t} &= \begin{bmatrix} -ikvU_1 e^{ik(x_1 \cos\theta + x_2 \sin\theta - vt)} \\ -ikvU_2 e^{ik(x_1 \cos\theta + x_2 \sin\theta - vt)} \end{bmatrix} = -ikvu_j e^{ik(x_1 \cos\theta + x_2 \sin\theta - vt)} \\ \frac{\partial^2 u_j}{\partial t^2} &= -k^2 v^2 u_j e^{ik(x_1 \cos\theta + x_2 sin\theta - vt)} \end{aligned} \tag{3.8}$$

Differentiating 3.8 to arrive at $\frac{\partial^2 u_l}{\partial x_k \partial x_i}$ requires the following first differential

$$\frac{\partial u_l}{\partial x_1} = -ik \; \cos\theta \; u_1 e^{ik(x_1 \cos\theta + x_2 sin\theta - vt)} \tag{3.9}$$

$$\frac{\partial u_l}{\partial x_2} = -ik\ \sin\theta\, u_1 e^{ik(x_1\cos\theta + x_2\sin\theta - vt)} \tag{3.10}$$

and second differential steps:

$$\frac{\partial^2 u_l}{\partial x_1 \partial x_1} = -u_l k^2\ \cos^2\theta\, e^{ik(x_1\cos\theta + x_2\sin\theta - vt)} \tag{3.11}$$

$$\frac{\partial^2 u_l}{\partial x_2 \partial x_1} = -u_l k^2\ \cos\theta\ \sin\theta e^{ik(x_1\cos\theta + x_2 sin\theta - vt)} \tag{3.12}$$

$$\frac{\partial^2 u_l}{\partial x_2 \partial x_1} = -u_l k^2\ \sin\theta\ \cos\theta e^{ik(x_1 cos\theta + x_2 sin\theta - vt)} \tag{3.13}$$

$$\frac{\partial^2 u_l}{\partial x_2 \partial x_2} = -u_l k^2\ \sin^2\theta\, u_1 e^{ik(x_1\cos\theta + x_2 sin\theta - vt)} \tag{3.14}$$

Combining 3.9 and 3.10 where $\eta_i = \begin{bmatrix}\cos\theta \\ \sin\theta\end{bmatrix}$ allows the following identity to be resolved:

$$\frac{\partial u_l}{\partial x_i} = -ik\ \eta_i\, u_1 e^{ik(x_1\cos\theta + x_2\sin\theta - vt)} \tag{3.15}$$

and the combination of 3.12, 3.13 & 3.14 where $k_i = k\begin{bmatrix}\cos\theta \\ \sin\theta\end{bmatrix}$ and $k_k = k\begin{bmatrix}\cos\theta \\ \sin\theta\end{bmatrix}$ resolves:

$$\frac{\partial^2 u_l}{\partial x_k \partial x_i} = -u_l k_i k_k\ e^{ik(x_1\cos\theta + x_2\sin\theta - vt)} \tag{3.16}$$

Substitution of 3.15 and 3.16 into 3.6 gives:

$$\begin{aligned}
0 &= \rho\frac{\partial^2 u_j}{\partial t^2} - A_{0ijkl}\frac{\partial^2 u_l}{\partial x_k \partial x_i} \\
0 &= -\rho k^2 v^2 u_j e^{ik(x_1\cos\theta + x_2\sin\theta - vt)} + A_{0ijkl} u_l k_i k_k e^{ik(x_1 cos\theta + x_2 sin\theta - vt)} \qquad (3.17) \\
0 &= -\rho k^2 v^2 u_j + A_{0ijkl} u_l k_i k_k \\
0 &= -\rho v^2 u_j + A_{0ijkl} u_l \frac{k_i k_k}{k^2}
\end{aligned}$$

and where $\delta_{ij} = 1$ when $i = j$, expression in the form $[M]\begin{bmatrix} U_1 \\ U_2 \end{bmatrix} = 0$ gives:

$$\left[A_{0ijkl}\frac{k_i k_k}{k^2} - \delta_{ij}\rho v^2\right] U_l = 0$$

$$M = \left[A_{0ijkl}\frac{k_i k_k}{k^2} - \delta_{ij}\rho v^2\right] \tag{3.18}$$

$$M = \begin{bmatrix} A_{01111}\cos^2\theta + A_{02121}\sin^2\theta - \rho v^2 & (A_{01122} + A_{01221})\cos\theta\sin\theta \\ (A_{01122} + A_{01221})\cos\theta sin\theta & A_{01212}\cos^2\theta + A_{02222}\sin^2\theta - \rho v^2 \end{bmatrix}$$

We can express M to obtain its determinant with $M = \begin{bmatrix} a + v^2 & b \\ c & d + v^2 \end{bmatrix}$ so that $det(M) = (a + v^2)(d + v^2) - cb = 0$, which gives the following:

$$\rho v^2 = \mu + \left(b + \frac{d}{2}\right)(\sigma_1\sigma_2) + \sigma_1\cos^2\theta + \sigma_2\sin^2\theta \tag{3.19}$$

By substituting both $\theta = \theta_1$ and $\theta = \theta_2$ into two instances of 3.19 gives:

$$\rho v^2 = \mu + \left(b + \frac{d}{2}\right)(\sigma_1\sigma_2) + \sigma_1\cos^2\theta_1 + \sigma_2\sin^2\theta_1 \tag{3.20}$$

and

$$\rho v^2 = \mu + \left(b + \frac{d}{2}\right)(\sigma_1\sigma_2) + \sigma_1\cos^2\theta_2 + \sigma_2\sin^2\theta_2 \tag{3.21}$$

and in 3.21 instance, substituting $\theta_2 = \frac{\pi}{2} - \theta_1$ and $\theta_1 = 0$ we arrive at:

$$\rho v^2 = \mu + \left(b + \frac{d}{2}\right)(\sigma_1\sigma_2) + \sigma_1\cos^2\left(\frac{\pi}{2} - \theta_1\right) + \sigma_2\sin^2\left(\frac{\pi}{2} - \theta_1\right) \tag{3.22}$$

Subtraction of 3.20 from 3.21 gives:

$$\begin{aligned} \rho(v_1^2 - v_2^2) &= \sigma_1\cos^2\theta_1 + \sigma_2\sin^2\theta_1 - \sigma_1\cos^2\left(\frac{\pi}{2} - \theta_1\right) - \sigma_2 sin^2\left(\frac{\pi}{2} - \theta_1\right) \\ \rho(v_1^2 - v_2^2) &= \sigma_1\cos^2\theta_1 + \sigma_2\sin^2\theta_1 - \sigma_1\cos\left(\frac{\pi}{2} - \theta_1\right)\cos\left(\frac{\pi}{2} - \theta_1\right)\sin^2\left(\frac{\pi}{2} - \theta_1\right) \end{aligned} \tag{3.23}$$

Using the trigonometric relations $\cos\left(\frac{\pi}{2} - \theta\right) = \sin\theta$ and $\sin\left(\frac{\pi}{2} - \theta_1\right) = \cos\theta$, we get:

$$\rho(v_1^2 - v_2^2) = \sigma_1(\cos^2\theta_1 - \sin^2\theta_1) + \sigma_2(\sin^2\theta_1 - \cos^2\theta_1) \tag{3.24}$$

which allows further simplification using $\cos 2\theta = \cos^2\theta - \sin^2\theta$, yielding:

$$\rho(v_1^2 - v_2^2) = (\sigma_1 - \sigma_2)\cos 2\theta_1 \tag{3.25}$$

For the case of a longitudinally stressed rail, it holds that the stress in the x_2 direction is significantly smaller than the longitudinal stress of interest and can be eliminated. Rearranging for the longitudinal stress σ_1 gives us a universal stress relation linking the longitudinal stress to the c=difference between two differently angled shear waves polarised in the vertical plane:

$$\sigma_1 = \frac{\rho(c_1^2 - c_2^2)}{\cos 2\theta_1} \tag{3.26}$$

3.3 Relating stress accuracy to temperature

Advancing the scientific state-of-the-art requires not only the use of a novel identity in the field of stress measurement, but the linking of that identity to the parameters that influence stress. It is also necessary to understand the vernacular of the rail industry, and the perspective of the stakeholders in presenting information. As such, it is important to be able to translate the accuracy of the test platform results into a temperature scale for rail industry stakeholders. The term NRT derives from a wayside engineering perspective. It relates to the temperature at which a section of constrained rail would experience zero thermally induced longitudinal stress.

In an unconstrained state, we can allow ϵ_1 to denote the strain caused by an applied longitudinal stress, i.e.:

$$\epsilon_1 = \frac{(L_1 - L_0)}{L_0} \tag{3.27}$$

where L_0 is the rail length at zero stress and L_1 is the current length. Using τ_1 to represent the longitudinal stress and E the young's modulus of the rail material (207 GPa), then:

$$\epsilon_1 = \frac{\tau_1}{E} = \tau_1 \cdot 4.83 \times 10^{-12} \tag{3.28}$$

When a rail is constrained, there is no potential for expansion in the longitudinal direction. Using the thermal expansion coefficient α_L and a change in temperature ΔT in Celsius in the following form:

$$\epsilon_1 = \alpha_L \cdot \Delta T \tag{3.29}$$

we can determine the internal longitudinally-aligned stress experienced by the constrained rail, and by using an empirical value for α_L for a standard grade of rail track (NR/L2/TRK/3011) [35], and combining equations 3.28 and 3.29 we arrive at the following expression:

$$\Delta T = \frac{\epsilon_1}{\alpha_L} = \frac{\tau_1 \cdot 4.83 \times 10^{-12}}{\alpha_L} = \tau_1 \cdot 4.2 \times 10^{-7} \tag{3.30}$$

Each 1 MPa of stress equates to a temperature change of 0.42 °C or more usefully in this context, a measurement accuracy of 1 MPa would equate to a NRT accuracy of 0.42 °C.

3.3.1 Data processing methodologies

This sub-section briefly describes the types of data processing used to extract results, including ultrasonic ToF.

3.3.1.1 Linear regression fit

A common manner of applying a best fit line to a linear plot is a regression fit. For data processing the results from some early birefringence experiments, a linear regression fit was used to calculate intercept. This gave a simple calibration for what was to become termed 'zero-offset' - the feature of the results where the ultrasonically calculated stress at zero applied stress was not, in fact, zero.

3.3.1.2 Zero crossing

One method of calculating the time of flight of an ultrasonic signal is the 'zero-crossing' method. This relies on correctly applying a window to a time-based ultrasonic signal (A-scan), setting a threshold value as a trigger and using an algorithm to calculate the exact ToF that the signal next crosses the zero-amplitude line (often through interpolation between the closest two values of ToF as a signal is extremely unlikely to have a data point at that zero-amplitude position. The accuracy of this interpolation depends somewhat on the speed of the data capture system: the faster the rate of sampling the smaller the gap between data points and the more accurate the interpolation.

The primary limitation of the zero crossing method is susceptibility to noise or changes in the shape of the ultrasonic signal between reflections. Noise can significantly interfere with the accurate identification of the zero-crossing location, and changes in the signal shape create challenges in maintaining a consistent identification of the same peak within the signal.

3.3.1.3 Cross correlation

A more robust method of extracting the ToF is a cross-correlation algorithm. This extracts a windowed reference signal and moves the reference along the original signal, one time-step at a time. At each location the algorithm calculates how well correlated the two portions of signal are. A perfect correlation will occur at the reference signal itself, a high correlation should occur at each subsequent reflection.

This method can also be susceptible to changes in signal shape but is much less susceptible to signal noise.

3.3.1.4 Summary

Two models are proposed for ultrasonic measurement of the magnitude of the longitudinal stress in rail, birefringence and angled wave. Both use polarised shear waves travelling through the rail web.

It is possible to relate the ToF difference between differently polarised waves to the stress and temperature of the rail. This required several data processing methods, and that the frequency of the ultrasonic waves are suitable to prevent problematic interactions with the material properties.

Chapter 4

Design development

This chapter details the development of the measurement and test specification, beginning with a definition of the proposed measurement approach. It then continues to detail the iterative evolution of the designs for both the test platforms (defined as: the hardware designed and used for attaching and orienting the sensor assemblies onto the test specimen) and sensor assemblies (defined as: the housings and ultrasonic transducers contained within that send and receive ultrasonic signals).

8 bespoke test platforms and 8 novel sensor assemblies were developed with differing applications and measurement capabilities.

The design processes undertaken and justification for the decisions made is given for each test platform and sensor assembly, alongside photographs of the completed examples and rendered images of CAD models.

4.1 Measurement approach

Given that the University of Sheffield does not have a laboratory rig capable of testing large full cross-section rail samples, it was necessary to develop a test methodology that used test samples extracted from sections of rail.

It has already been discussed that the measurement would be undertaken through the rail web, a relatively thin and roughly parallel section of the rail (Figure 4.1).

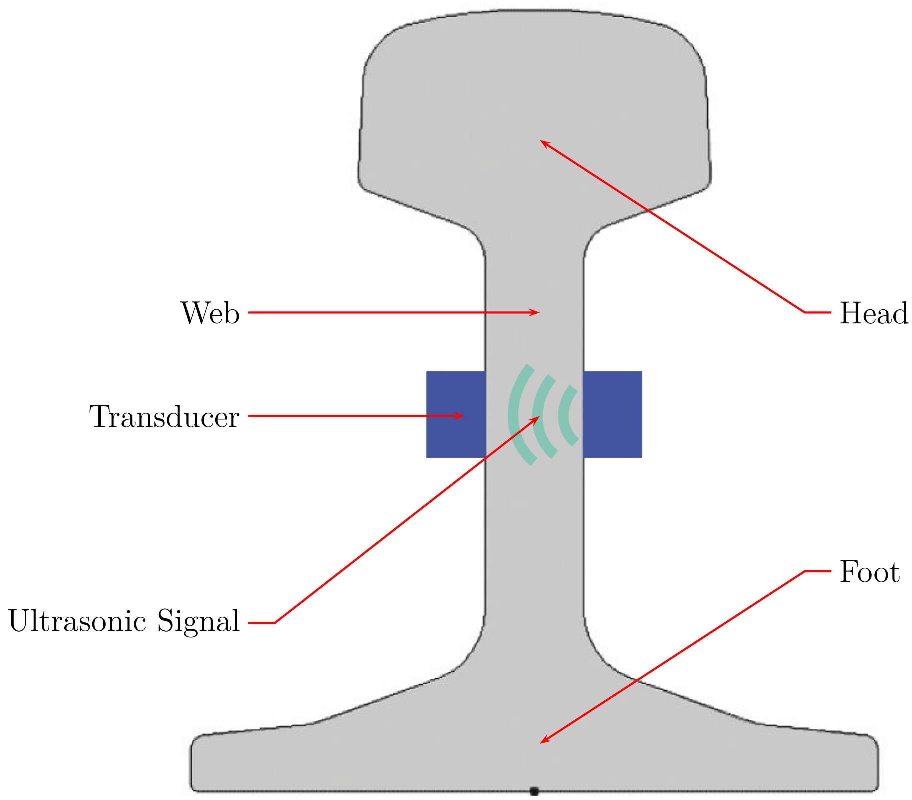

Figure 4.1: A diagram showing the path of an ultrasonic signal generated by a transducer attached to the web of a rail

Figure 4.2 shows a CAD model of the tensile specimen cut from the rail web.

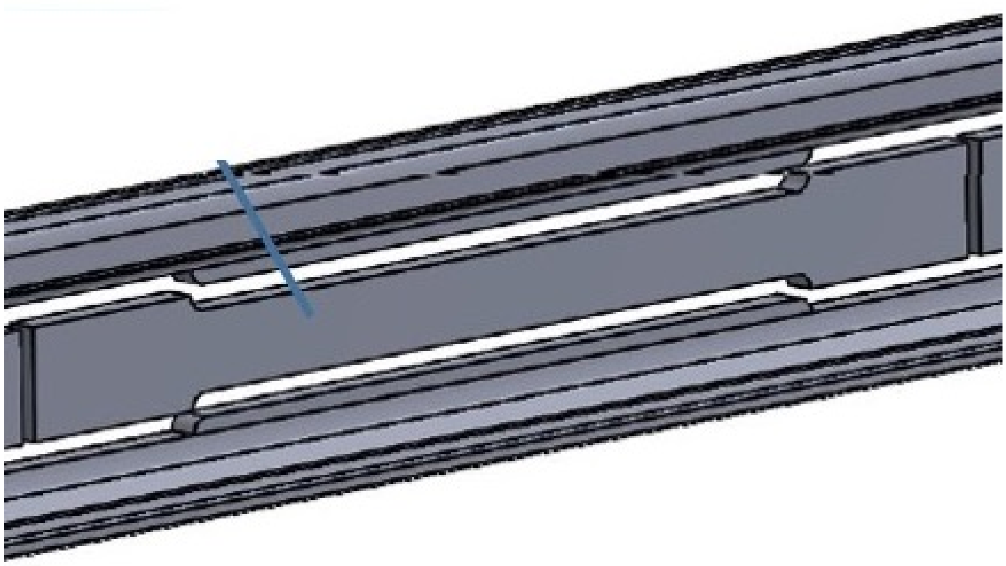

Figure 4.2: CAD image showing the tensile testing specimen cut from the rail web

Initial specimens were cut from the rail web using water-jet cutting, however the accuracy of the machining was not good. EDM was found to be much more accurate and used for all subsequent specimens.

Figure 4.3 shows a CAD model of the initial tensile test specimen in its vertical testing orientation with the first iteration of angled wedge sensors (yellow) and birefringence sensors (green) arranged on the parallel front and back faces.

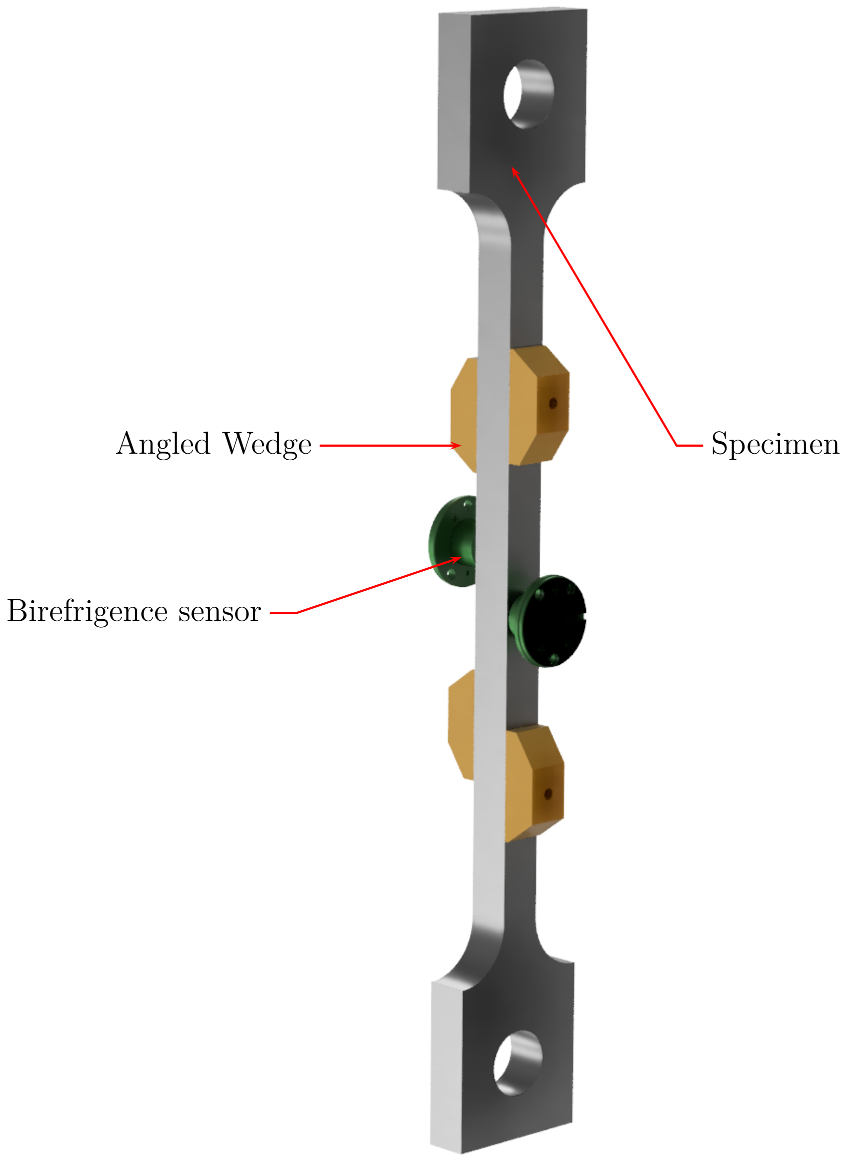

Figure 4.3: A CAD model showing a tensile test specimen in its vertical orientation with angled wedge sensors (yellow) and birefringence sensors (green)

4.2 Establishing design priorities

In addition to the need for tight control of the specimen dimensions and parameters, the error analysis (which assesses the predicted and experimentally determined sensitivity of the measurement to variations in experimental parameters and is detailed in Chapter 5) has established that correct flight path measurement and sensor alignment is essential for accurate stress measurement.

For the birefringence method, the orientation of the sensors relative to the applied stress direction and the perpendicularity of the positioning of the sensors on either side of the web are the important considerations for the design analysis; the flight path is purely the thickness of the specimen itself.

The angled wedge method, however, is additionally susceptible to variations in the relative sensor positioning on both sides of the specimen, in terms of rotation, parallelism, vertical and horizontal alignment.

The test platform design has been therefore focused on tightly controlling the position and orientation of the sensors both within the assemblies and also controlling the location of those assemblies relative to the test specimen.

The work completed in the design phases has taken an iterative approach, for two primary reasons:

Contractual obligations:
During the course of this research there have been numerous stage gates and deliverable deadlines throughout the project timelines for both NR and FRA. All work completed was required to be directed towards the time dependant and overall goals of two parallel projects with sometimes differing focuses.

De-risking the development process:
In order to de-risk the investment cost, in both time and finance, of developing novel test platforms and sensor assemblies, I needed to establish the validity of the measurement approach with least irrecoverable investment at each stage, learning from the outcomes and improving the test platform and experimental procedure with each iteration.

This has resulted in a number of iterations of both sensor assemblies and test platforms for both birefringence and angled wedge methods, detailed in this chapter.

4.3 Measurement specification

I undertook a combination of research and stakeholder engagement to develop the initial specification for the measurement of longitudinal rail stress.

4.3.1 Stakeholder engagement

I conducted a number of informal interviews with potential stakeholders interested in the development of a reliable system to determine the thermally induced stress state of rail. These included representatives from the FRA, NR the United States Department of Transportation Volpe Centre (Volpe) and the The National Railroad Passenger Corporation (AMTRAK). The outcome of this process, along with the research completed under subheadings 4.3.1.2 & 4.3.1.3, was the identification of the most important headings and a desired specification under each. These are detailed in Table 4.1.

Table 4.1: Design criteria for measurement of longitudinal stress in rail using ultrasound, with a detailed specification for each criteria

Design criteria	Detail
User Profile	The device should be operable by a highly trained operator with skill and experience in conducting stress measurements using ultrasound
Durability Criteria	The device should be sufficiently durable to operate in an on-track environment, though should not be environmentally sealed nor conform to any specific regulations (at this stage)
Environmental Conditions	The device should be able to operate in temperatures between $-10\,°\mathrm{C}$ to $40\,°\mathrm{C}$. The device will not be required to operate during active precipitation
Measurement Time	The device will ideally return immediate fast measurements, but could require an overnight installation
Range of longitudinal stresses	The device will be able to measure longitudinal stresses in rails, both compressive and tensile, up to $250\,\mathrm{MPa}$
NRT accuracy	A value of NRT will be returned to an accuracy of $\pm 5\,°\mathrm{C}$
Data Storage & management	On-board data processing not required
Rail materials	The device will return accurate measurements on fully pearlitic rail
Rail profiles	The device will be able to return measurements on the most used rail profiles in the North American and UK rail networks. Namely 136RE, 141RE and 56E1
Resistance to to other in-track waves	The device will be able to differentiate and ignore dynamic bending stresses caused by railway vehicles moving along the track
Rail Preparation	Rail surface preparation will be required to mount the device
Calibration Requirements	Software will require prior calibration, device will ideally operate without calibration

4.3.1.1 Design objectives

The design objectives (listed below) were also jointly developed in discussion with the stakeholders during initial project scoping discussions. It was essential that the work completed was aligned with the desires of the stakeholders as well as the real-world application, environment and user groups that would most benefit from this development.

- The methodology must be proven in the laboratory before track trials are undertaken
- The device must be portable
- The device should take quick measurements (minutes, not hours)
- The device should be operable by an expert technician with specific ultrasonic stress measurement experience
- The measurement protocol can include significant pre-testing preparation of the surface of the rail
- The measurement system should be sufficiently physically robust to conduct on-site measurements but the work should focus on developing a rigorous scientific and technical solution as a priority over other requirements, such as weatherproofing and long-term durability
- The final device should attach to an in-service rail without disturbing the track or it's connection to the supporting structures

4.3.1.2 Rail steel: materials & microstructure

The ultrasonic wave velocity in steel can be significantly affected by the microstructure. It was therefore important to characterize the material and microstructural properties of the rail steels that were within scope. In order to achieve the necessary combination of hardness and failure resistance, Austenitic steel is subjected to a number of tightly controlled heat-treatment processes. Many specialized steels have been developed for use in rail steel. While Martensitic and Bainitic steels have been used in certain 'niche' areas, the metallurgy encountered in nearly all standard grades of rail is Pearlitic [98]. Indeed, a fully Pearlitic microstructure in the rail head is demanded by AREMA when setting the standard for production of all rail steel produced for the US networks. Pearlitic steel does not contain any major alloying and is also considered to be an isotropic material on a global scale, due to the small size and random orientation of the pearlite colonies [98]. An extensive characterization of both legacy and modern (including head-hardened) rails found that the microstructural variation was very small, with consistent Pearlitic microstructures, and that hardness is correlated with the fineness of the interlamellar spacing between the layers of ferrite and cementite within the pearlite colonies that make up its microstructure [99]. Additionally, in conversations with representatives from Transportation Technology Centre Inc. (TTCI) I was informed that:

> "As far as microstructure goes, currently all rails we have tested are 100% Pearlitic and I have not seen any recent interest from rail manufacturers in trying other microstructures in rail steels" - Ananyo Banerjee, Principal Investigator - TTCI

It is important to note that these findings are principally concerned with the rail head. In standard grades there are no subsequent head hardening processes. As such, the working assumption was that the same Pearlitic structure found in the rail head will also be found throughout the rail and specifically in the web. A large scale investigation would be required to fully validate this assumption involving random sampling and photo-micrography of rail web samples from both legacy and current rails of different profiles from multiple manufacturers.

4.3.1.3 Effects of steel microstructure on acoustoelasticity

The effects of microstructure on the acoustic properties of steels is a field of active worldwide research in the fields of NDT and material characterization. It seems, however, that these fields have not yet developed a significant body of research specifically about rail steels. The current primary goal for those investigating microstructure for material characterization seems to be to determine an unknown microstructure from the application and processing of ultrasonic signals. The main parameter of interest in these analyses is signal attenuation due to the scattering of the waves by the grain boundaries as they pass through the host material [100]. In this study, the only consideration was the possible variance of ultrasonic Speed of Sound (SoS) due to differences in microstructure across and between test samples, not the absolute magnitude of the signal response. Investigations of the effects of different steel microstructures on both longitudinal and transverse (shear) wave velocities in AISI 4140 and AISI 5140 steels have found that, although there is a significant difference between SoS in Martensitic, Bainitic and Pearlitic structures, the variance of the SoS between fine and coarse Pearlitic structures was less than 0.5% [88]. A further, large scale, rail-specific investigation would be required involving ultrasonic SoS testing of a number of random samples from many different rail profiles and from multiple manufacturers to fully characterize the expected SoS variation within the rail web.

4.4 Transducer selection

To determine the most appropriate transducer frequency I conducted a theoretical analysis. To minimize boundary effects from interlamellar spacing and Pearlitic colony size (an analogue in Pearlitic steels for grain size) on acoustic transmission and impedance, a wavelength at least 5 times, and ideally 10 times, larger than that of the average grain size is desired. A baseline value for colony size for fully Pearlitic rail steel of 6.5µm [89] was considered as representative of the materials under consideration. Interlamellar spacing within the Pearlitic near-eutectoid rail steels manufactured with modern cooling techniques is found to be as low as 100 nm [90]. The relationship between longitudinal and shear wave velocities within most common steel microstructures has been found to remain constant, between 1.83 and 1.84. Additionally, the variance of both shear and longitudinal wave velocities within Pearlitic steels has been found to be very low even between grades, 0.43% and 0.34% for shear and longitudinal respectively [88]. Table 4.2 shows a number of shear and longitudinal wave frequencies alongside their corresponding wavelengths in rail steel, calculated using a mean value between those velocities reported for ANSI4140 and ANSI5140: shear at 3247.5 $\mathrm{ms^{-1}}$ and longitudinal at 5945 $\mathrm{ms^{-1}}$ [88].

Table 4.2: Shear and Longitudinal wavelengths for different frequencies of ultrasonic wave propagating through rail steel and their ratios to the Pearlitic colony size

Frequency (MHz)	Longitudinal Wavelength λ_l (μm)	λ_l:Colony Size Ratio	Shear Wavelength λ_s (μm)	λ_s:Colony Size Ratio
1	5945	914.6	3247.5	499.6
2	2972.5	457.3	1623.75	249.8
5	1189	182.9	649.5	99.9
10	594.5	91.5	324.75	50.0
20	297.25	45.7	162.375	25.0

Table 4.2 shows that all frequencies meet the specified requirements. With no theoretical restrictions the choice to proceed with transducers of 2 and 5MHz was primarily a practical one: the transducer thickness is greater the lower the frequency. The extremely brittle transducer material is therefore stronger and more resilient to damage during handling, instrumentation and use. 1MHz transducers are too thick too cut accurately by hand and have even proven too thick for processing by laser cutting contractors.

4.5 Input from sensitivity analysis

The results of the sensitivity analysis (Chapter 5) point to the need for extremely tight control of the positioning of the sensor assemblies, both in relation to one another (angled wedge method) and in relation to the rail web (both methods).

Each iteration of the test platforms and sensor assemblies began with the intention to maximise the alignment while minimising the initial investment in design complexity, especially in the earliest stages where the technical challenge of receiving high quality angled measurements over multiple angles had not been proven.

4.6 Design development overview

During the course of this work, 8 new test platforms and 8 bespoke and novel sensor assemblies were designed, built and iterated.

The physical design development has taken place with two parallel strands:

1. the 'Test Platform' is defined as the assembly of components that attaches the sensor assemblies to the test specimen.
2. the 'Sensor Assembly' is the small removable assembly, a number of which fit into each test platform, and contains the ultrasonic transducers.

Both test platforms and sensor assemblies have been improved through an iterative process, with some sensor assemblies designed to work with multiple test platforms. Additionally, there were two different measurement technologies (Birefringence and Angled Wedge) under investigation that required different sensor assemblies.

Each iteration responded to the changing demands of the project, experimental results dictating direction and areas in need of improvement, while a focus was kept on rapid prototyping, thereby retaining agility, minimising iterative development costs and and de-risking investment at each stage.

The author developed the design briefs at each stage, seeking feedback from collaborators in conversation. With the following exceptions, the author has been responsible for the design, drawing, modification, manufacturing oversight and assembly of each iteration of test platform:

Test platform 1:
Initial design brainstorming completed collectively between the project team.

Test platform 2:
Collaboratively designed with Dr Henry Brunskill.

With the following exceptions, the author has been responsible for the design, drawing, modification and manufacturing oversight and some instrumentation of each iteration of sensor assembly:

Sensor assembly 1:
Initial design brainstorming completed collectively between the project team.

Sensor assembly 2:
First prototype angled wedge was manufactured and instrumented by Dr Henry Brunskill and Dr Giorgios Tyreas.

Sensor assemblies 3 - 6:
Sensor assembly instrumentation (attaching transducers and cables) was primarily completed by Dr Yue Yang and the author and with occasional support from Dr Gary Nicholas and Dr Will Gray.

Figure 4.4 shows the different stages of design development, with the evolution of the test platforms in the middle, flanked by the parallel evolution of the birefringence and angled wedge sensor assembly developments. The chart shows which sensor assemblies were compatible with each sensor platform and references the thesis section in which the results captured with that set-up are discussed. A summary of the material, manufacturing process and transducer elements within each assembly is also given.

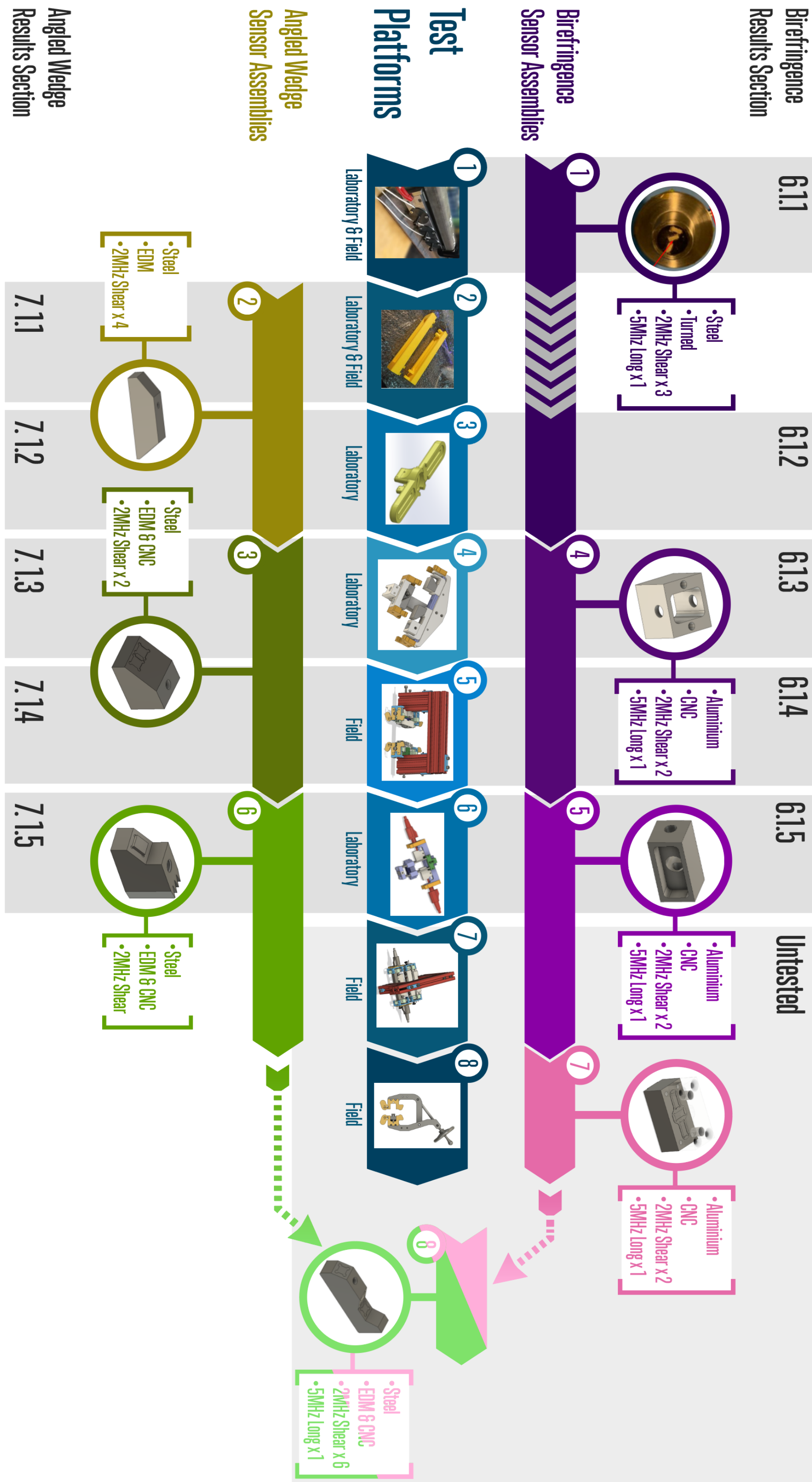

Figure 4.4: This flow chart shows the different stages of design development, with the evolution of the test platforms and sensor assemblies.

The term ‘sensor assembly’ refers to the sub-assembly of ultrasonic transducers within a housing that are aligned and clamped onto the specimen within the test platform.

These two development processes were conducted in parallel and are discussed in different sub-sections of this thesis.

The following sub-section deals with the evolution of the test platforms. The development of the birefringence sensor assemblies is discussed in section 4.8 and the Angled Wedge sensor assemblies in section 4.9.

4.7 Test platform development

The term ‘test platform’ is used to refer to the overall assembly of components that comprise the clamping and alignment mechanism attaching the ultrasonic sensors to the test specimen.

Figure 4.5 summarises the process of design feedback and decision making throughout the project, as well as giving brief outlines of the impacts that these design changes have had on the experimental results. It can be seen that design changes have improved the accuracy and zero-offset steadily throughout the project.

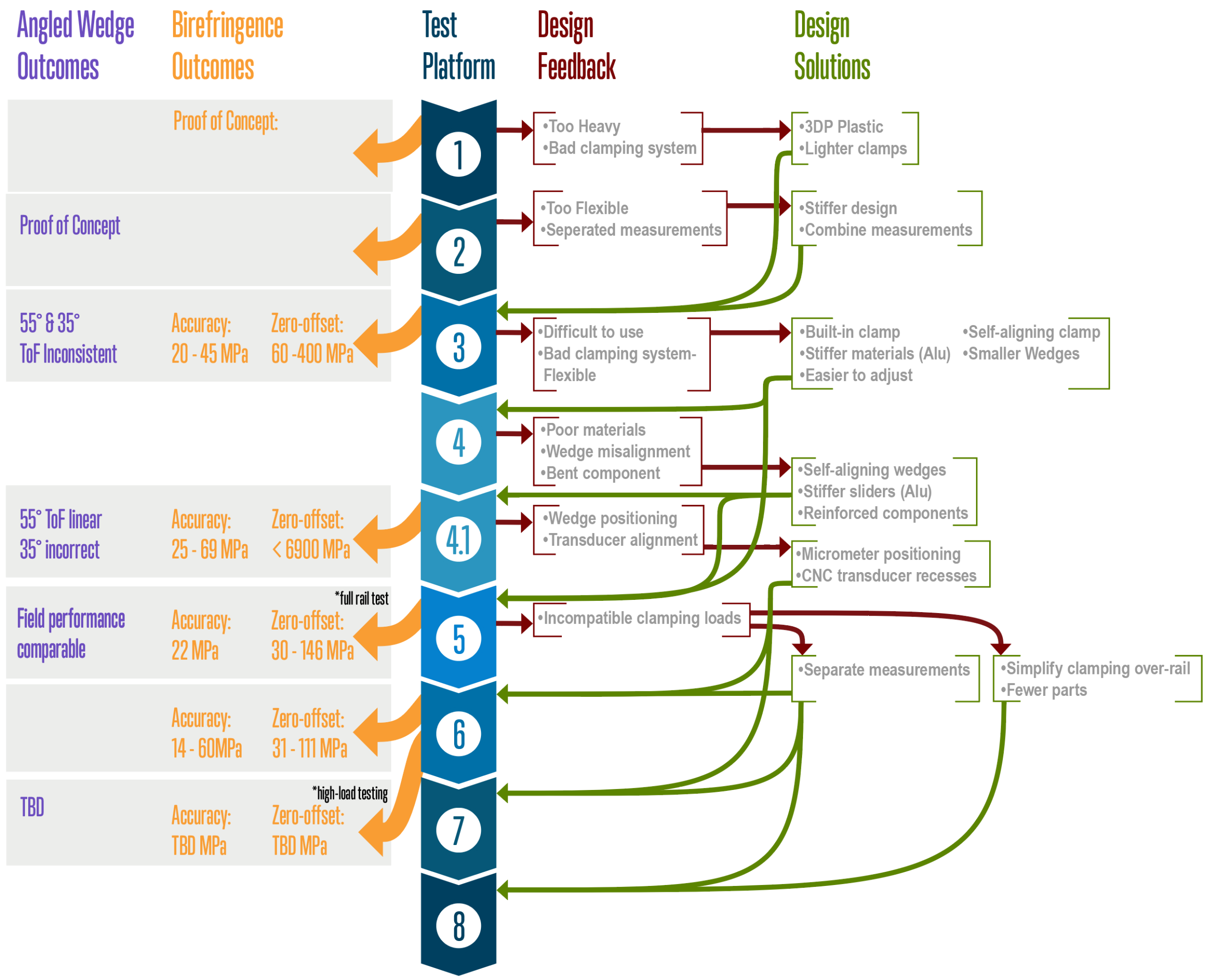

Figure 4.5: This flow chart summarises the design decision justifications and test outcomes throughout the design development process.

4.7.1 Test platform 1

4.7.1.1 Design specification

From the outset, with unproven technology and a significant technical task to develop a measurement solution, I was aware that there would be a number of iterations of the design concept. I decided that the first attempts should be quick and easy to manufacture, investing as little as possible into the initial proof of concept. I therefore selected turning and hole drilling as the two cheapest and fastest manufacturing processes.

Initially, I decided to have 3 separate housings within the test platform to give robust assessments of repeatability and variability. The device was also intended for use in field testing, and therefore had to be robust enough for the demanding rail wayside environment. I chose

EN24T steel as a dimensionally stable, easily machined, readily available and durable material with a similar chemical composition to the R260 rail steel that was the focus of the investigation.

The sensor bar was machined from a single piece of EN24T. Springs were used to pre-load the sensor assemblies when located into the sensor bar with retaining caps holding them both in place. Hex-drive bolts were used to apply load to each sensor housing individually. The test platform was attached to the rail by means of a G-clamp at either end (Figure 4.6).

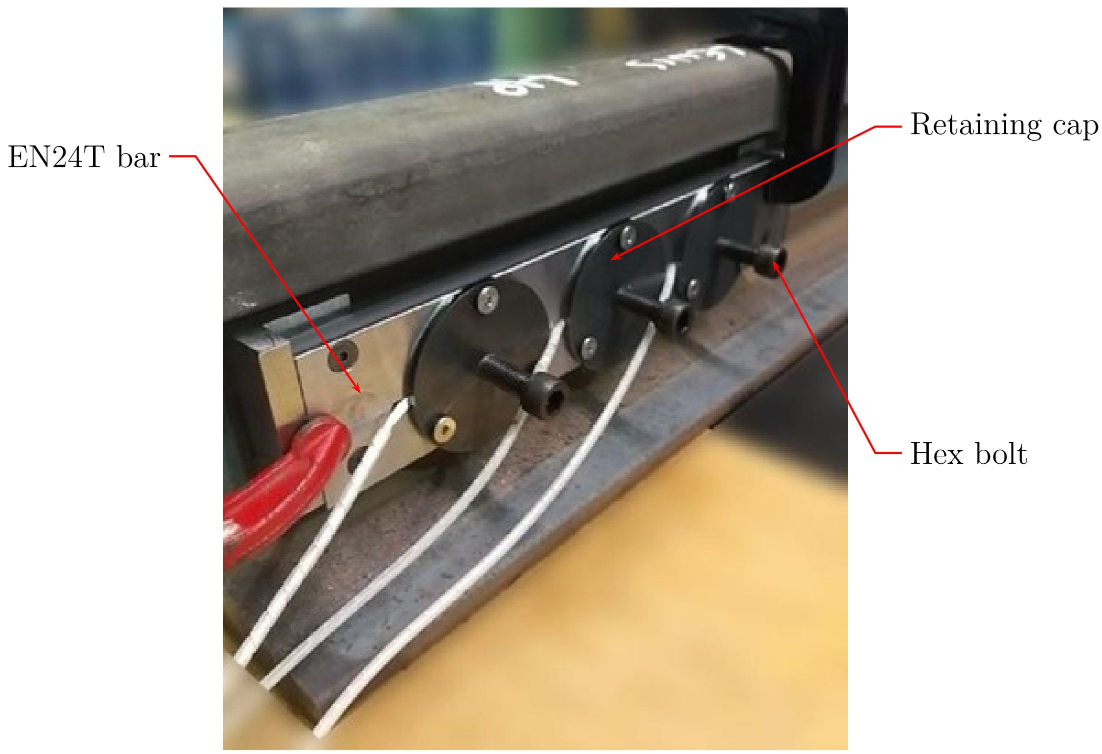

Figure 4.6: Image of the first test platform - machined from a sold section of EN24T and incorporating three birefringence sensor assemblies

The first use of this design was a field test, for which the team, system and process were not sufficiently prepared or advanced. The design proved to be robust, capturing clear signals throughout the testing in bad weather. The results showed responsiveness to applied stress and acted as an initial proof of concept but without confidence in the maximum values of applied stress, or the accuracy of the strain gauges (Figure 4.7).

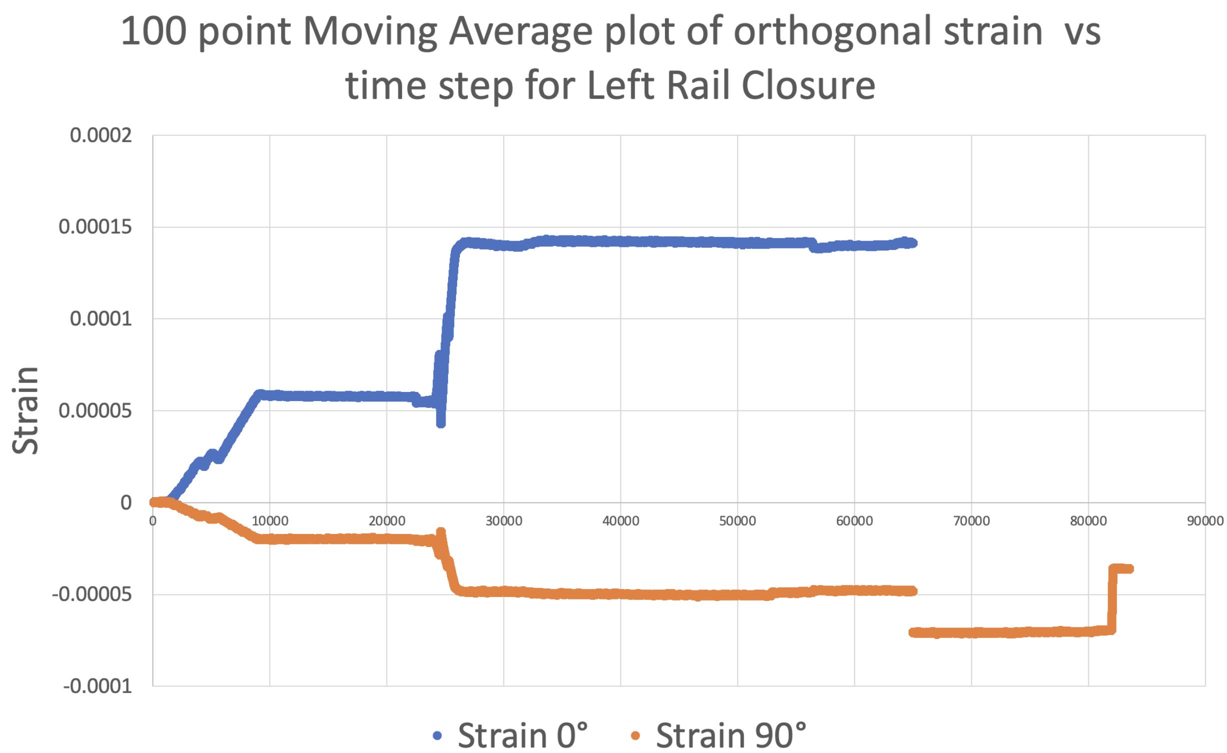

Figure 4.7: A screenshot of strain gauge results from first field testing, showing a discontinuity in the orthogonal strain and a failure in aligned strain gauge during the weld operation

The figure shows a large discontinuity in strain readings for the orthogonally aligned strain gauge during the welding operation and a failure of the axially aligned gauge. Without an accurate baseline the data was not of sufficient quality to draw any reliable results.

In the laboratory, initial testing showed large deviations from expected values of ultrasonic time of flight (Figure 4.8).

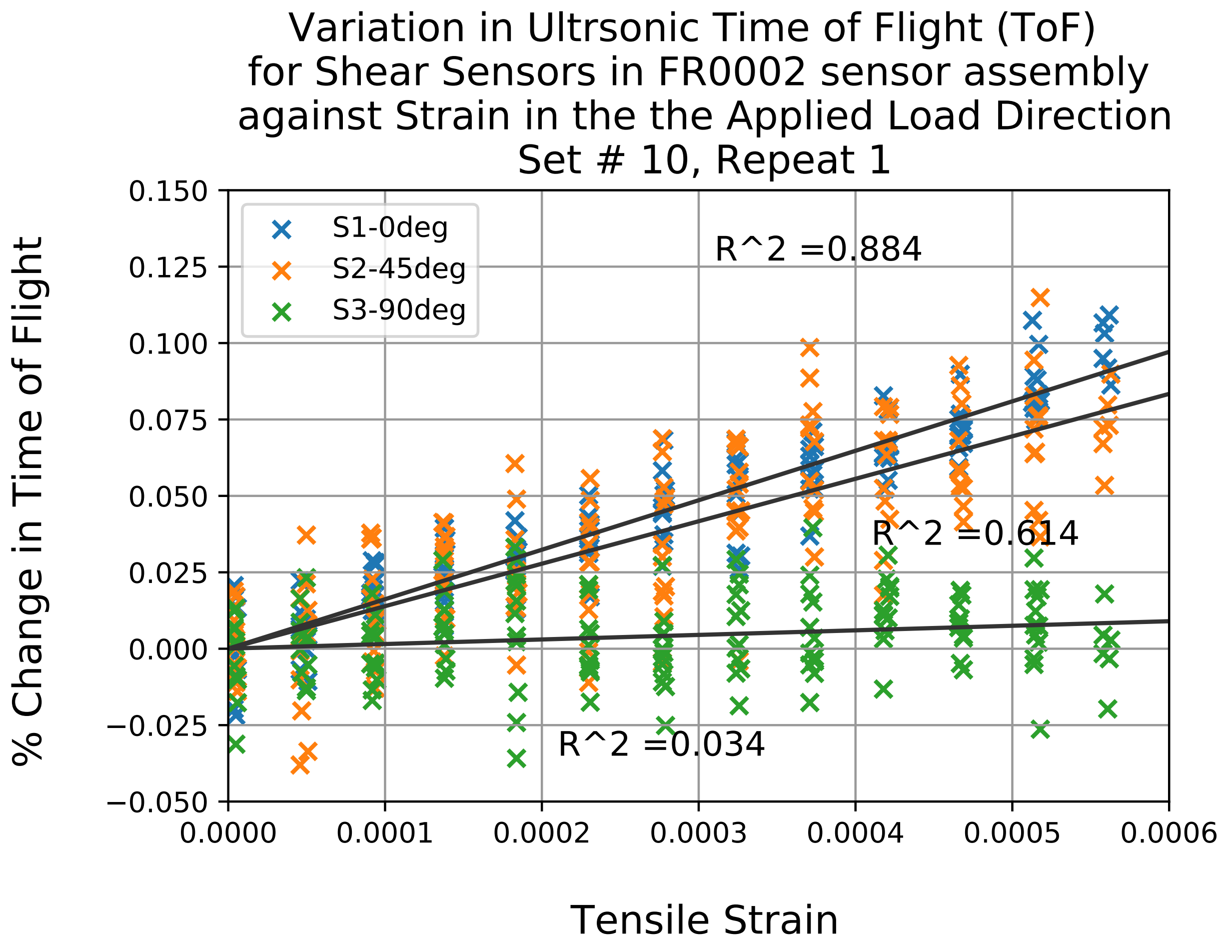

Figure 4.8: A screenshot of ultrasonic ToF vs. Strain results from laboratory testing, showing high scatter and low R^2 values for all three transducers

The large spread of results and the corresponding low values for R^2 did not allow for accurate conclusions.

I suspected that the sensor bar, having been designed for full-rail measurements and resilience in the notoriously abusive environment of the rail wayside, was too heavy for the small tensile specimen cross-section. Additionally, the combination of using large G-clamps to attach the bar to the specimen, along with the application of clamping force in three locations behind the sensor assemblies induced multi-point bending in addition to the desired tensile forces.

This was verified in person by watching the live readings of the strain gauges change in an eccentric manner while tightening and releasing the clamps. These changes to the experimental baseline invalidated the captured test results.

4.7.1.2 Design brief forward

The user experience and test results resulted in the following design critiques, needing to be overcome in the next iteration:

- Sensor bar too heavy
- Clamps too heavy and too much clamping force needed

4.7.2 Test platform 2

The core tenet of quick and cheap was again the fundamental basis of the first angled wedge test platform. I designed and commissioned a pair of 3D printed holders to secure the angled wedge sensors to both sides of the rail web. Channels were incorporated to allow the distance between the angled wedges facing each other across the rail web to be adjusted and fixed in place (Figure 4.9). These holders were connected with a pair of Off the Shelf (OTS) quick clamps for use in the field.

Figure 4.9: Image of the first angled wedge sensor holders

This test platform was used in field testing and conducted the first angled wedge measurements taken through the web of a rail at different levels of longitudinal stress. Due to the long experimental duration, the ultrasonic signals were observed in real-time but not captured at this initial stage. It was possible to see a definite change in ToF as the location of the peaks of the reflection signals changed in response to changes in applied stress. The design was a successful proof of concept for sending and receiving polarised angled shear waves with a longitudinal component through the web of a rail.

4.7.2.1 Design brief forward

The user experience and test results resulted in the following feedback, needing to be overcome in the next iteration:

- To speed up laboratory testing, there was a requirement for simultaneous Birefringence and Angled Wedge measurements
- More compact form factor required to minimise specimen bending/twisting

4.7.3 Test platform 3

Responding to the identified shortcomings of the previous test platforms:

- Sensor bar too heavy
- Clamps too heavy and too much force needed
- Need for simultaneous Birefringence and Angled Wedge measurements
- More compact form factor required,

I began a series of fast-prototype iterations using 3D printed components.

For the angled method, shear waves needed to be transmitted through the stress field at different angles, with controlled polarisations relative to the applied stress. Having established that angled measurements were possible, I improved the initial prototype designs by re-designing both the sensors and the clamping assembly with three primary aims: to incorporate both angled wedge and birefringence measurement capability at the same time, to create a lightweight lab testing platform that would not cause bending of the specimen, use the existing sensor assemblies to save on time and development costs, perform quicker and cheaper initial validations of the novel angled measurement. Incorporating both angled wedges and birefringence measurements into the same test platform also reduced testing time.

Using 3D printing enabled fast prototype generation and iteration with minimal investment, and allowed me to confirm, by comparing strain gauge values on opposite sides of the test specimen, the suspicion that the larger steel sensor bar was responsible for inducing bending in the test specimen and undermining the accuracy of the results. OTS metal quick clamps replaced the flexible, plastic ones previously used, to hold the test platform to the specimen and to apply load behind each sensor.

Figure 4.10 shows a CAD model of the first 3D printed sensor carrier component.

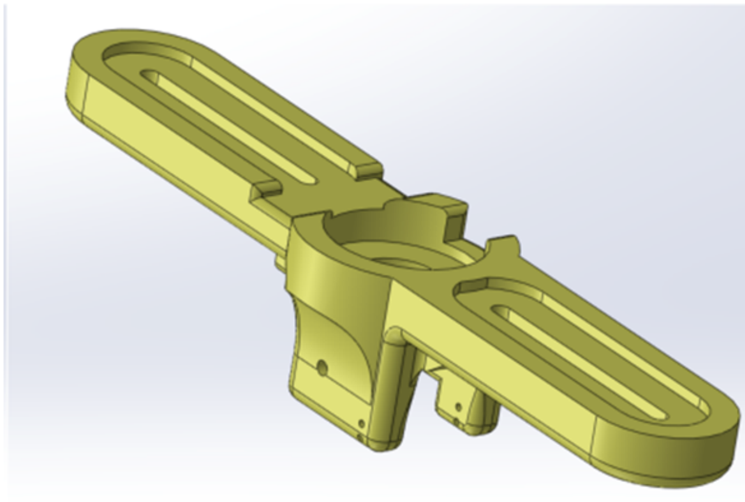

Figure 4.10: Image of the third test platform, showing a 3D printed carrier for both angled wedge and birefringence sensor assemblies

Figure 4.11 shows a CAD render of a pair of interlocked carriers (red) and the sensor assemblies arranged (wedges in yellow, birefringence in green) on a test specimen. Figure 4.12 shows this assembly in the lab during a tensile test, and Figure 4.13 shows the same assembly used on full rail in compression, with metal quick clamps used to provide the sensor clamping force onto the test specimen.

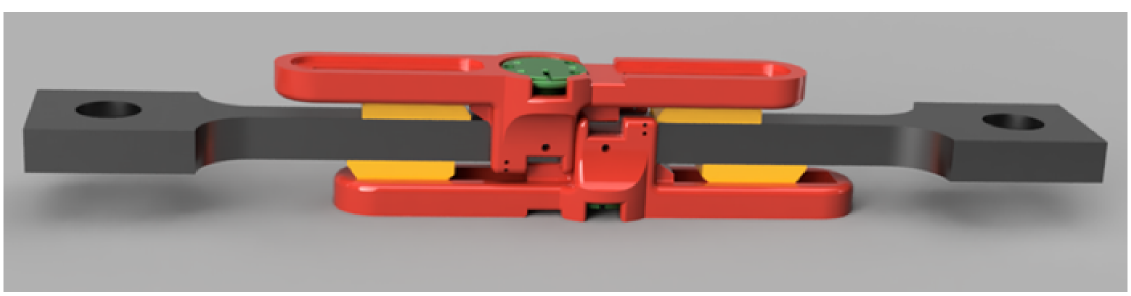

Figure 4.11: A CAD render of the third test platform, showing a pair of 3D printed carriers (red), angled wedge sensor assemblies (yellow) and birefringence sensor assemblies (green) arranged on a test specimen (grey)

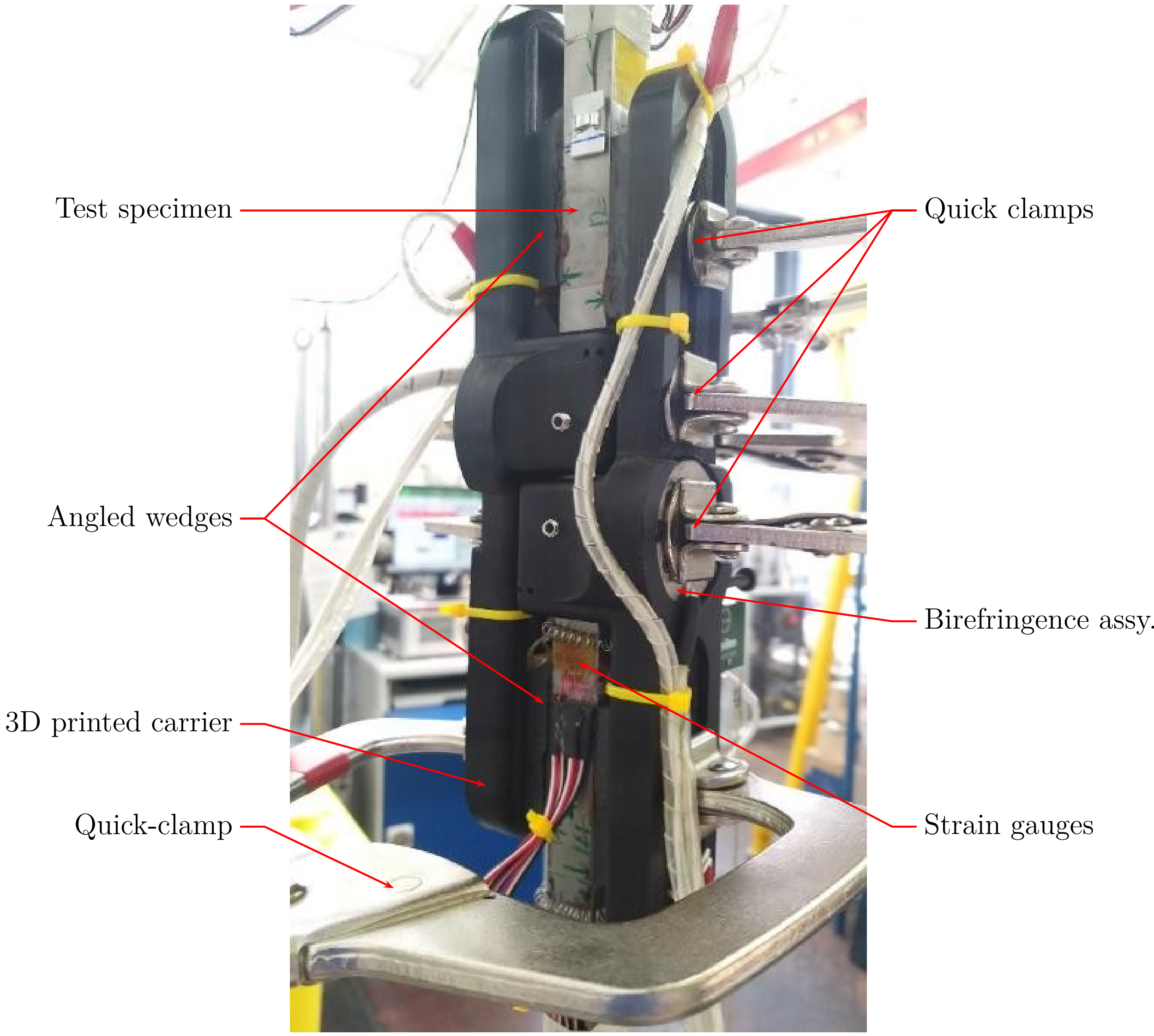

Figure 4.12: Image of the third test platform being used for tensile testing in a laboratory environment, showing the test specimen, 3D printed sensor carrier, quick clamps, and strain gauges

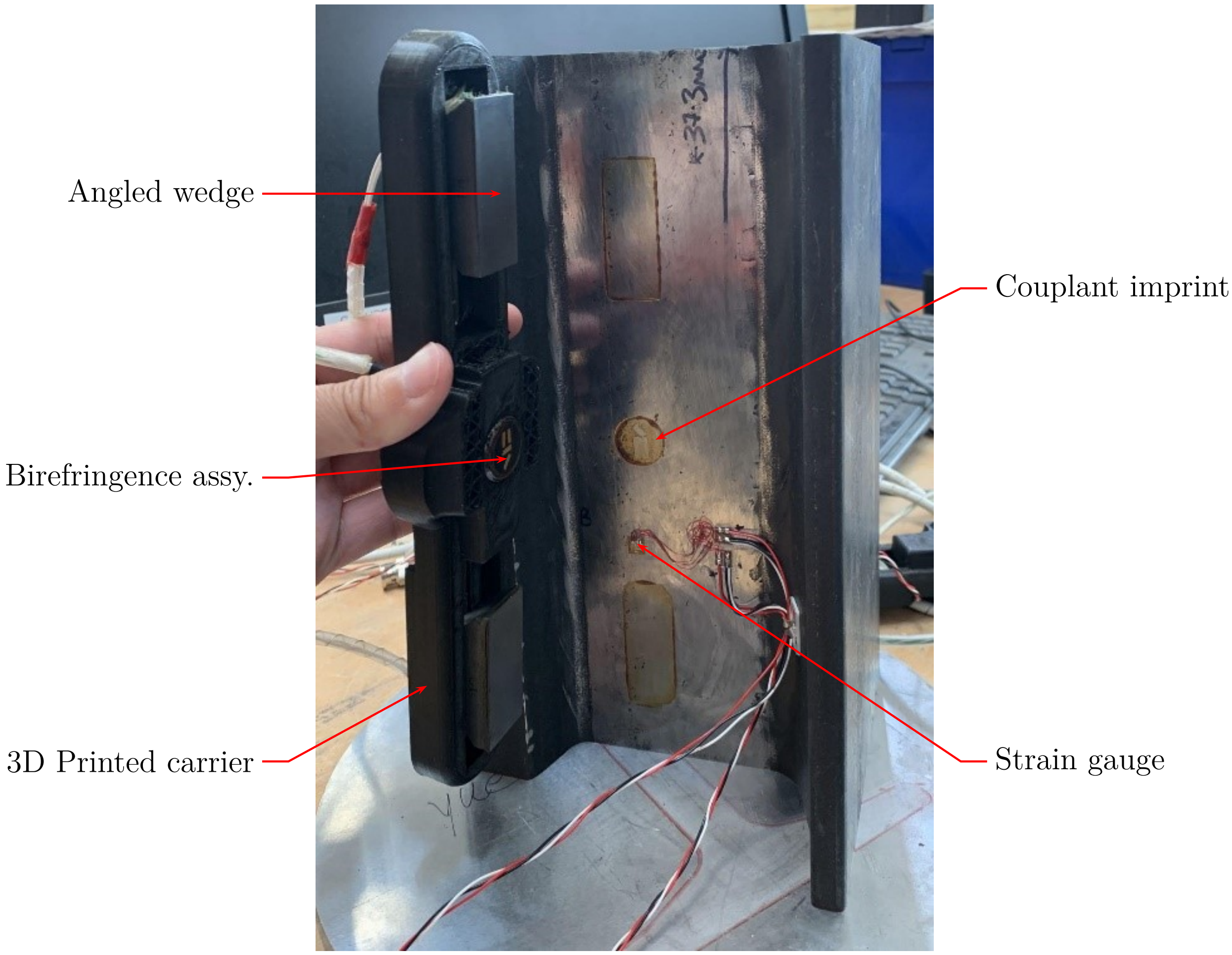

Figure 4.13: Image of the third test platform, being applied to a full rail sample for compression testing - showing the 3D printer carrier, angled wedges, birefringence assembly, strain gauge and imprint of couplant on the rail web

4.7.3.1 Test platform 3 Design analysis

The sensor platform update achieved the identified design goals by combining both methods into one device and reducing the distortion of the specimen due to the clamping loads and device weight. Test platform 3 was able to return Lamé parameters, the foundational constants for birefringence, with a higher confidence than empirical values (Table 4.3).

Table 4.3: Table of calculated Lamé parameters from ultrasonic ToF data using test platform 3 in comparison to converted empirical values [85].

	Lamé values (GPa)	
	λ	μ
Rail steel (empirical)	$112 \pm 2.3\%$	$80.8 \pm 2.3\%$
Test Platform 3 results	$109 \pm 0.3\%$	$79.6 \pm 0.3\%$

However, the ToF values for orthogonally polarised shear transducers were not equal at zero-stress (Figure 4.14).

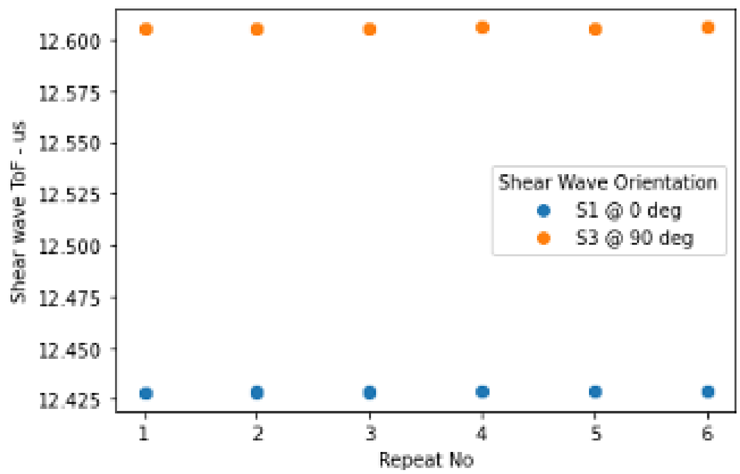

Figure 4.14: ToF for shear waves with different polarisations at zero applied stress, broken down by experimental repeat number, test platform 3

Table 4.4 shows the error performance of the test platform 3 design for birefringence measurements.

Table 4.4: Test platform 3 error performance

Measurement	Specimen	Error (uncorrected)	Error (corrected)
Birefringence - Tensile	EN24T	40MPa	20MPa
Birefringence - Compression	R260 full rail		45MPa

The angled-wedge signals were sufficiently strong to capture a single clear reflection for each of the transducers, and there was a clear movement of the reflection peaks with increasing applied stress, but there as insufficient consistency of these reflections throughout the experiments to effectively process the data. In addition, the calculated values for speed of sound were more than 40% out from the values returned from the birefringence transducers. These issues were likely caused by poor instrumentation of the angled wedge transducers alongside a number of design drawbacks identified during the hands-on testing:

- Heavy clamps with an offset Centre of Gravity (CoG) created inconsistent clamping of the sensors to the specimen
- The 3D printed components were flexible, leading to low angled-wedge sensor positioning accuracy
- Signal quality was inconsistent in response to the inconsistency of clamping loads, requiring re-adjustment during experiments
- Alignment of birefringence sensors to the specimen surface was not sufficiently consistent

These findings allowed me to reassess the design criteria and develop the following specification for the next stage of development.

Design requirements:

- Integrate the sensor clamping force into the design – no requirement for additional clamps
- Allow simple adjustment of the wedge sensor position
- Allow simultaneous angled wedge and birefringence measurements
- Self-align to the test specimen – preventing misalignment of the sensors
- Reduce required sensor clamping loads – prevent distortion of specimen or test platform
- Improve alignment of birefringence sensors to the specimen surface

The transducers on the angled wedges were also re-instrumented.

4.7.4 Test platform 4

Having proven that capturing multiple reflections from angled wedges was possible I began an in-depth re-design using traditional engineering materials, based on the outcomes from the test platform 3 design analysis.

I redesigned the assembly from the ground up, using 6061 aluminium for high-strength components due to its good strength-to-weight ratio and ease of machining. The components were manufactured using CNC machining for accuracy and ability to create more complex geometry. I designed the intersections between each component to self-align to improve measurement accuracy. Components with lower strength requirements were made from engineering polymers to reduce weight.

A single-sided arm with threaded end was used to retain an M10 bolt, used to push one angled wedge carrier towards the opposing sensors and clamp them to the test specimen, while the relative position of the sensors was controlled using captive bolts attached to polymer sliders.

I also combined both angled wedge and birefringence housings into the same assembly to allow testing to be performed simultaneously.

I designed an improved birefringence sensor housing, simplifying elements of the manufacturing process, aiming for improved repeatability in transducer positioning and using a flat-faced square profile to enable better perpendicular alignment to the test specimen (Figure 4.15).

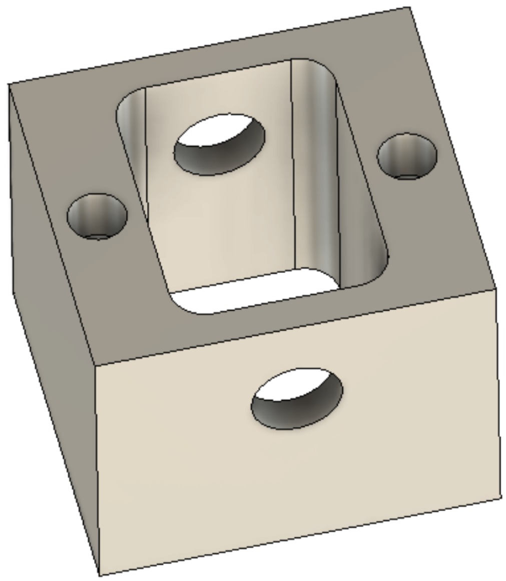

Figure 4.15: A CAD representation of the aluminium housing for the birefringence sensor assembly 4 showing through holes for cable ejection and potting and blind threaded holes for attachment to the test platform

I also reduced the surface area of the angled wedges and changed the sensor alignments within the clamp to allow a consistent and more even distribution of clamping pressure across all sensor assemblies (Figure 4.16).

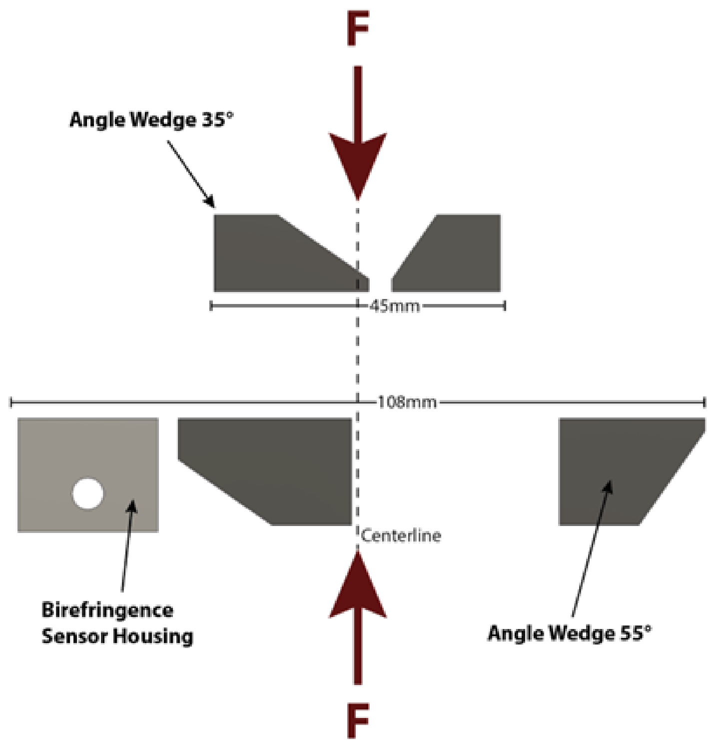

Figure 4.16: Schematic diagram of the sensor locations within lab test platform 4

A CAD render of the test platform is shown in Figure 4.17 and an image of the test platform being used for tensile testing is shown in Figure 4.18.

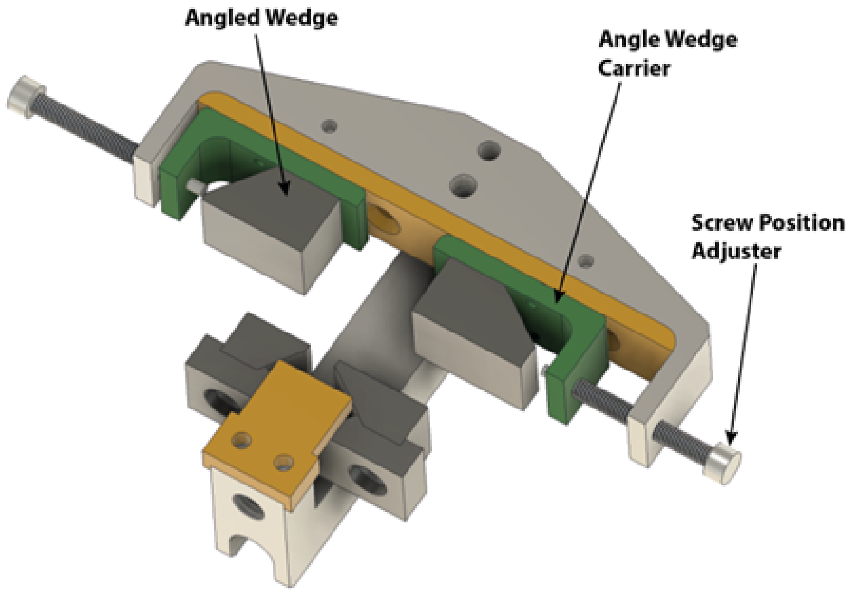

Figure 4.17: A CAD render of the fourth test platform, showing CNC manufactured aluminium clamp components, angled wedges and polymer components (green & yellow)

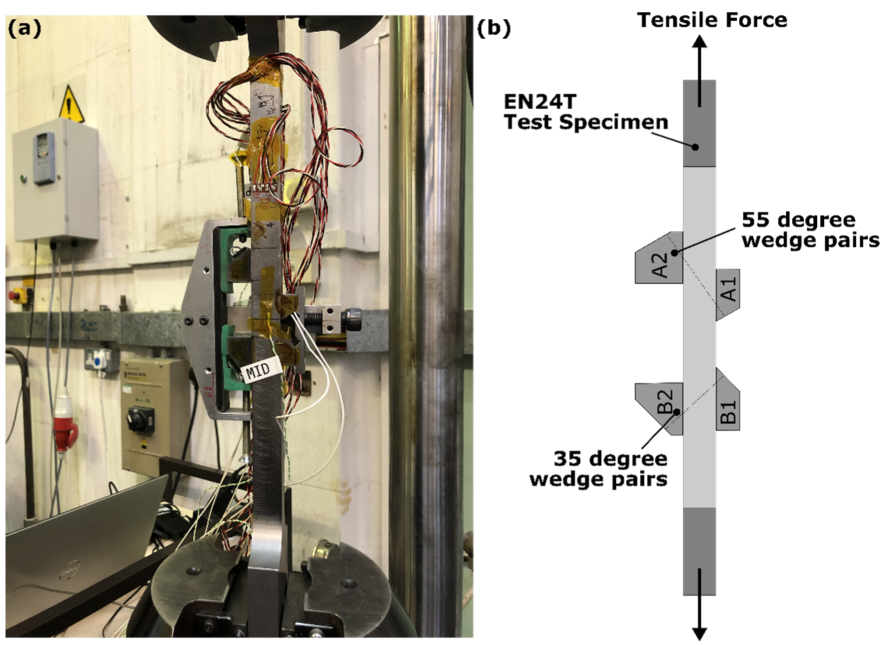

Figure 4.18: Image of the fourth test platform taking measurements on a specimen undergoing tensile testing. [Image credit: Gary Nicholas]

The signals achieved from the angled-wedge sensors are shown in Figure 4.19.

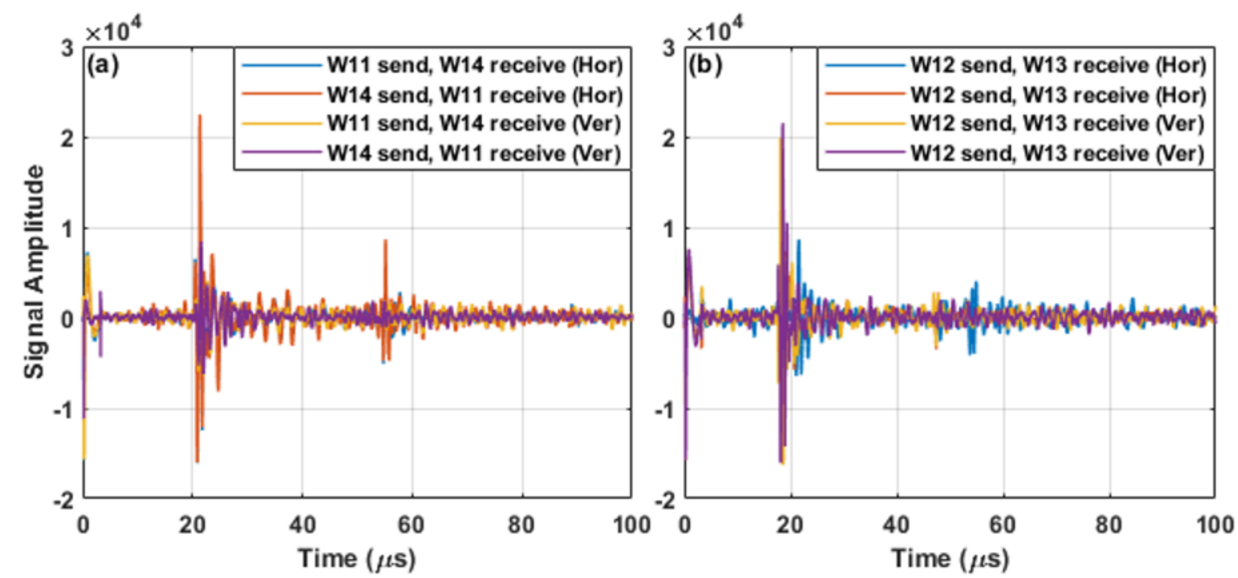

Figure 4.19: A-scans for the first-look at the signal performance of test platform 4. [Image credit: Gary Nicholas]

There is a clear first reflection with a lower amplitude second reflection for both 55- and 35-degree signals. The SoS measurements for the initial testing on test platform 4 are shown in Figure 4.20.

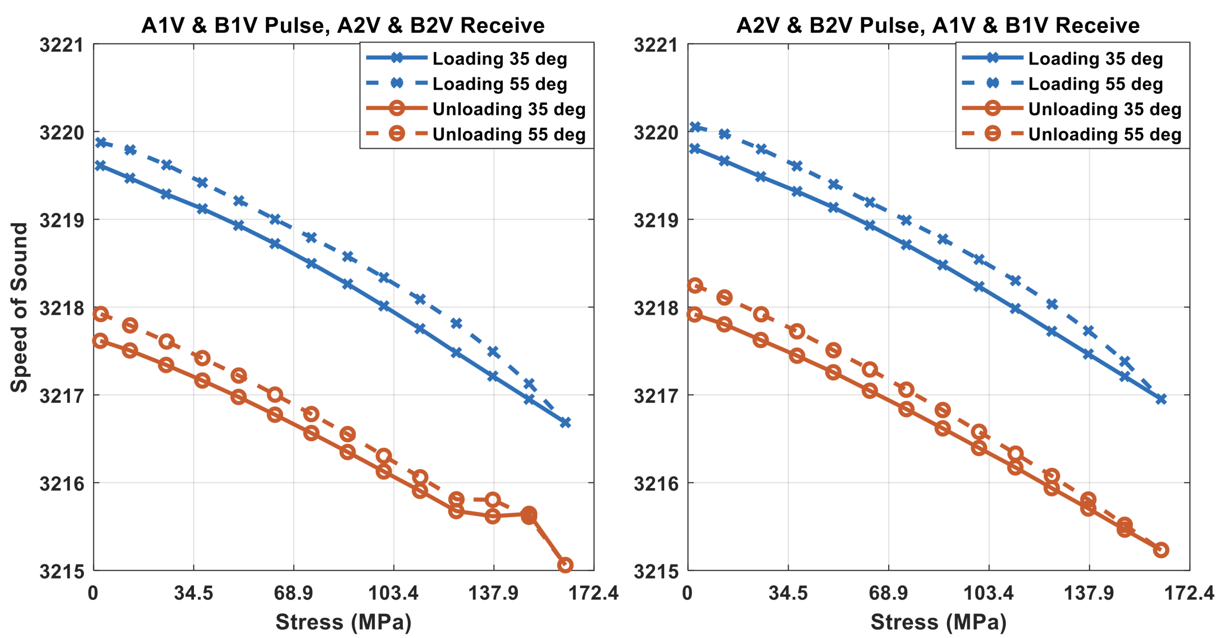

Figure 4.20: Speed of sound measurements for (a) 55° and (b) 35° wedge sensor - test platform 4. [Image credit: Gary Nicholas]

There is a clear trend, as expected, of decreasing SoS with increasing applied stress, however, the results exhibited a $-200ms^{-1}$ disparity in SoS between the 55-degree data (at the expected $3200ms{-}01$) and the 35-degree data (Figure 4.21).

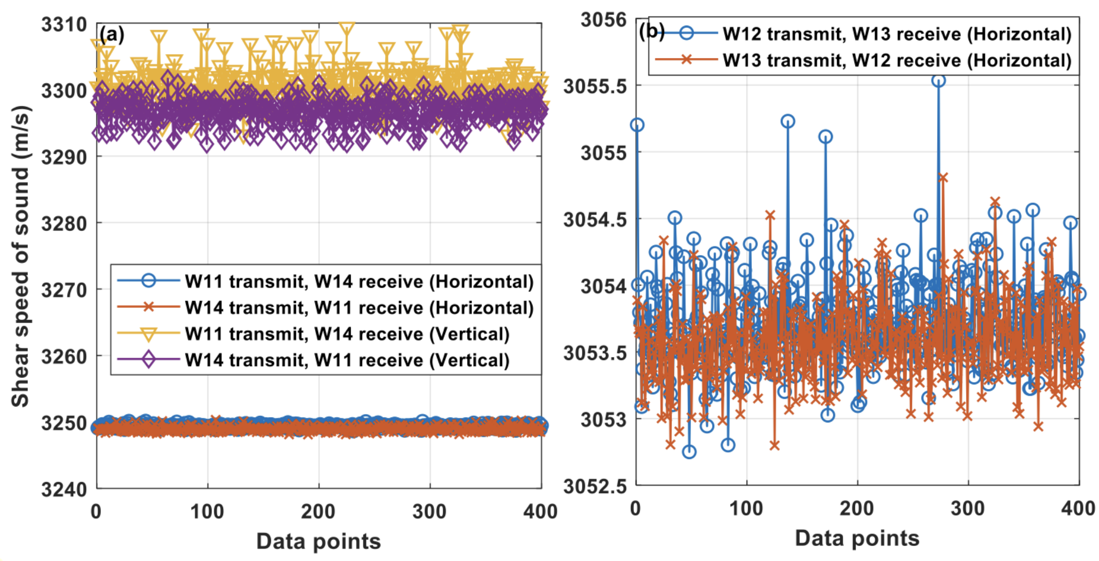

Figure 4.21: Left: Plot of ultrasonic SoS from 35-degree signals (yellow & purple) and 55-degree data (red and blue) Right: A close-up plot of the variance of the 55-degree SoS data

s

In addition, it was clear from the user experience that there were some shortcomings in the design of some of the new test platform components.

The polymer components designed to hold the wedges in place aligned them correctly in the first instance, however, due to supply of poor quality material they were not stiff enough to prevent undesired movement or variance in the wedge position during clamping and while stressing the specimen. Additionally, the wedges were not fully retained and were, at times, challenging to align and could move from their nominal positions as torque was applied to the sensor clamping bolt. I decided to suspend testing immediately to resolve the design issues.

4.7.5 Test platform 4 - improved

My solution to the aforementioned design shortcomings is shown in Figure 4.22.

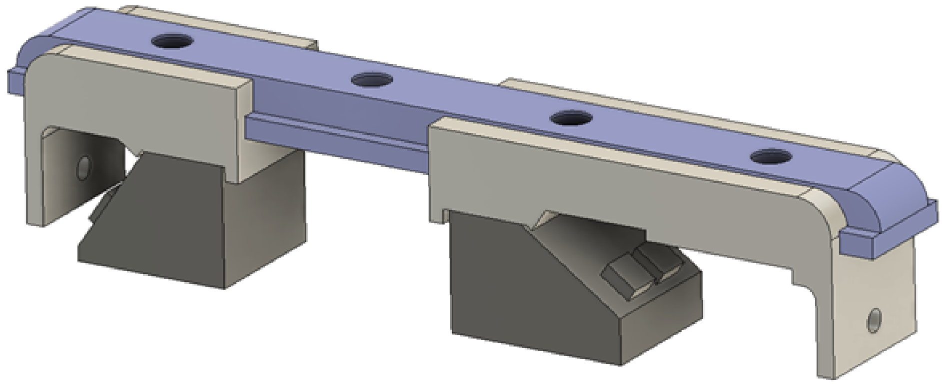

Figure 4.22: Detail image of fourth test platform components, showing aluminium sliders (light grey) and t-slot modification (blue)

I re-designed the sliders, and had them made from from aluminum and add a t-slot slide, creating more elegant and effective alignment and retention of the wedges within the assembly.

Having to move within the constraints of an industry-funded project meant that a fast prototyping and iteration design process was needed to provide results at regular intervals. This meant that the desired accuracy for positioning the wedge sensors relative to one another was not achievable in this first re-design.

The initial iteration of this test platform required the operator to use a set of digital calipers to measure to distance from the leading edge of one wedge to the trailing edge of another across the width of the specimen. The solution was to manufacture an aluminum jig with accurately machined steps and an identical thickness to the test specimen. This allowed exact positioning of both pairs of wedges relative to one another, guaranteeing a consistent and accurate calculation of flight path (Figure 4.23) as long as the thickness of the test specimen was also accurate.

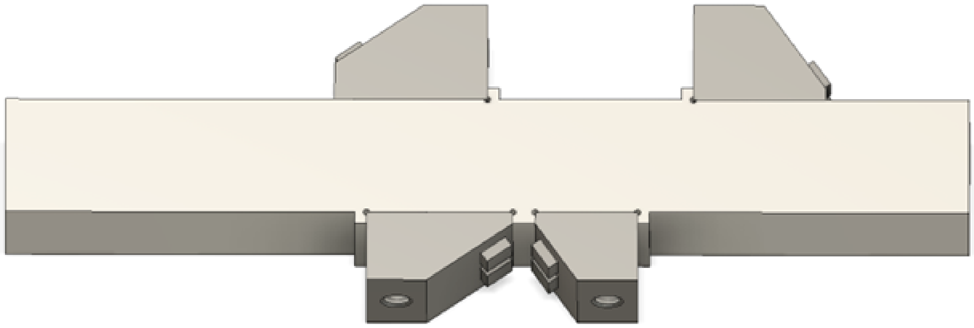

Figure 4.23: Image of the aluminium positioning jig aligning the angled wedges into the geometric ideal location

Additional calibration of the signal ToF was needed to account for the travel time of the ultrasonic signals though the (relatively) unstressed wedges either side of the stressed rail specimen. This required the design of a pair of calibration jigs to clamp the wedges in situ and measure the ToF directly. These calibration clamps are shown in Figure 4.24.

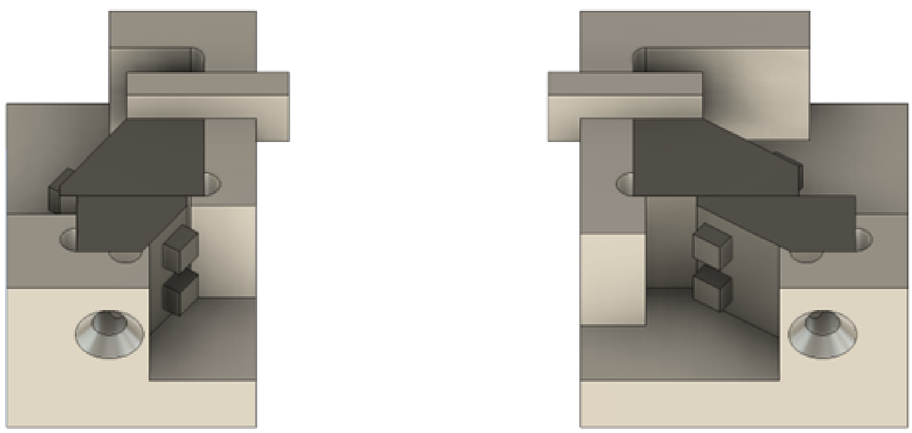

Figure 4.24: CAD representation of the ultrasonic ToF calibration jigs

Due to the relatively large size of the angled wedges, it was necessary to apply a high sensor clamping force using the M10 bolt. This caused the bending initially of the sensor carrier, which was re-manufactured in thicker EN24T steel (Figure 4.25) with additional features to prevent misalignment. A later failure was the aluminium arm that formed the back of the clamp. Also a casualty of the high loads, once this failure was identified the test platform needed a further iteration.

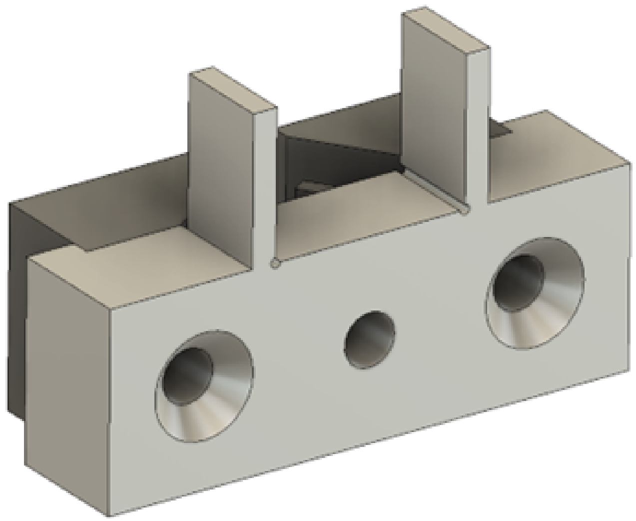

Figure 4.25: Detail view CAD render of the redesigned wedge sensor carrier

The final improvement at this stage was the addition of 3D printed guides (yellow) to align the test platform to the test specimen. These guides prevented rotation of the test platform as the clamping screw was tightened (Figure 4.26).

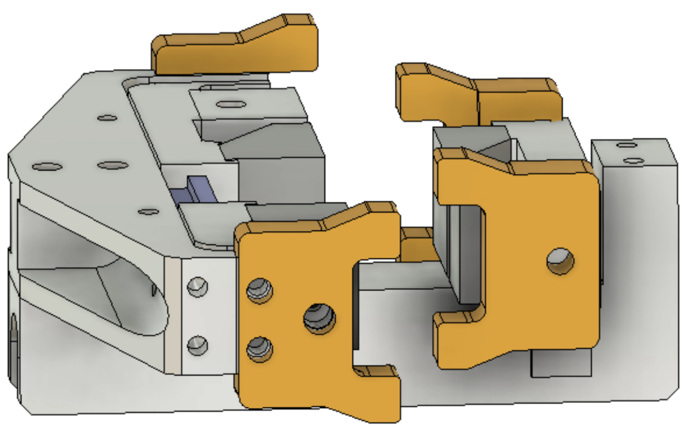

Figure 4.26: A detail view of the laboratory test platform showing the specimen alignment guides (yellow) giving rotational stability to the test platform

The final laboratory test platform, incorporating the above improvements is shown in full in Figure 4.27.

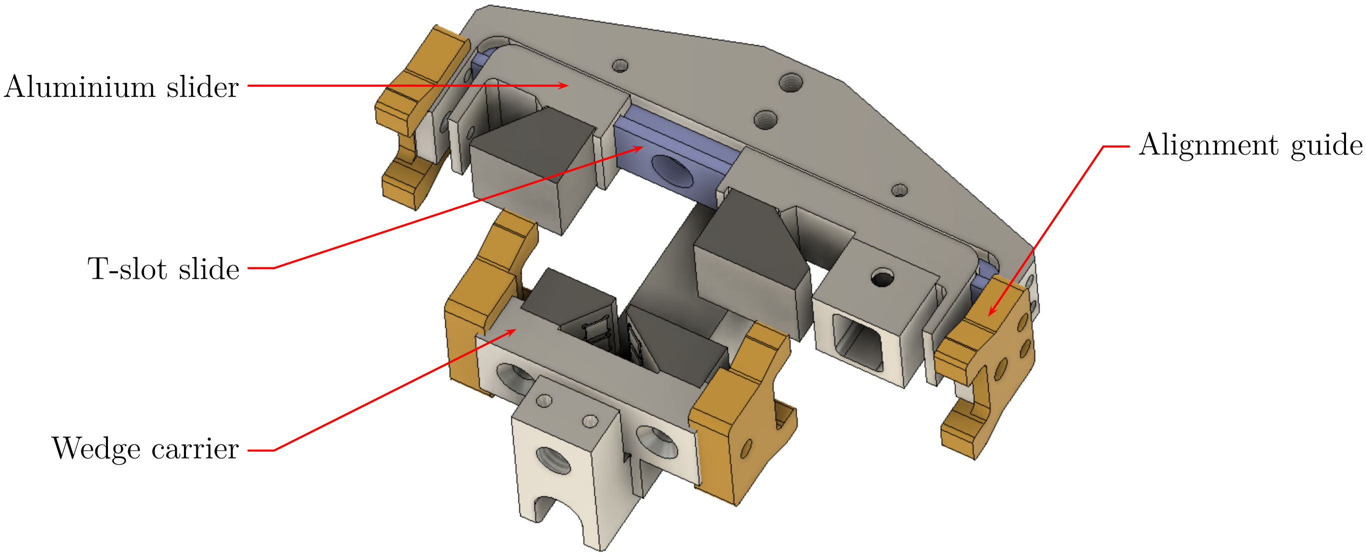

Figure 4.27: A full view of test platform 4 incorporating all improvements

The re-design improved the test platform rigidity and allowed more precise location of the angled wedge sensors relative to one another. Multiple reflections were achieved from both angled-wedge sensor assemblies (Figure 4.28).

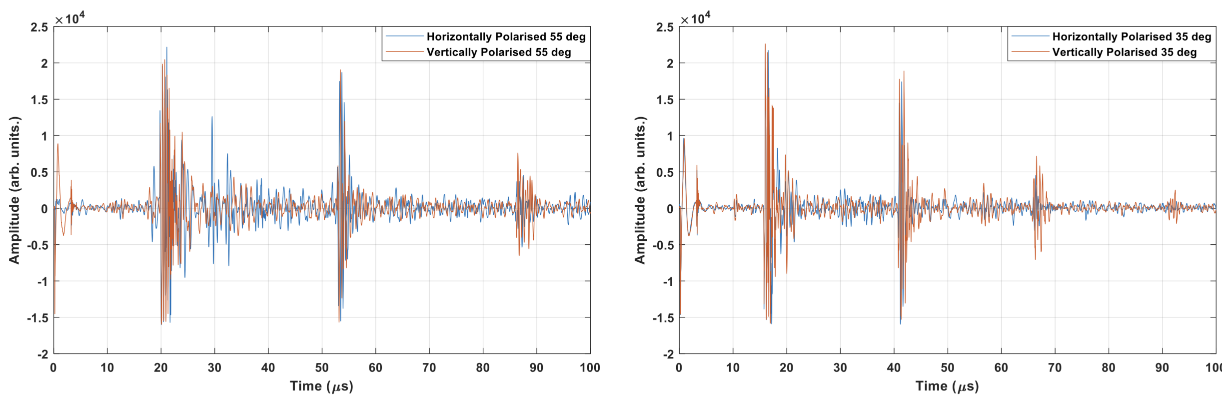

Figure 4.28: Image of the fourth test platform taking measurements on a specimen undergoing tensile testing. [Image credit: Gary Nicholas]

While the initial design for test platform 4 improved the signal quality and allowed access to multiple reflections, thereby improving the rigour of the ToF extraction by using multiple peaks, the 35-degree SoS was consistently low, pointing to an underlying issue with the instrumentation of the transducers themselves.

The birefringence sensor assemblies also experienced significant degradation in performance over the duration of the testing. This led to a loss of signal clarity. In an attempt to compensate, higher and higher clamping loads were applied to the test platform. This led to the bending of the arm that formed the back of the test platform clamp. The implications of this were significant for the reliability of the results. This bending jeopardised the parallelism of the measurements, and therefore the correct calculation of flight-path length, and as a result, reduced the confidence in the calculations for ultrasonic SoS for both methods.

4.7.6 Test platform 5

Having developed lightweight test platforms for use in laboratory experiments, a new system was needed for full-rail testing that allowed accurate positioning of both sets of wedges on opposite sides of the web of a rail, constraining each sensor in both absolute and relative positions to both the rail and the other sensors in 6 degrees of freedom.

The design requirements were:

- Suitable for both birefringence and angled wedge measurements
- Use the existing shortened angled wedge and square aluminium birefringence sensors
- Accurate relative positioning of angled wedges along either side of the longitudinal axis of the rail web
- Accurate vertical positioning relative of all sensors at the centre or minimum thickness position (the location at which the web surfaces are most parallel) on the web
- Incorporate a load cell to regulate sensor clamping force
- Each component, and the test platform as a whole, be resistant to deformation under clamping loads
- The design should be cost effective and quick to manufacture - consideration that there would be a need for further iterations of this design
- The device needed to be operable in winter conditions by trained operatives in cold weather clothes
- The device should not need to operate in conditions of precipitation
- The device should be compatible with the existing adjustable slide components from test platform 4

To meet these needs, I specified large cross-section OTS aluminium extrusion to form the back of the clamp, with large diameter high-tensile steel bolts and bespoke key-nuts to create strength and accurate longitudinal self-alignment of the sensor sub-assemblies (Figure 4.29).

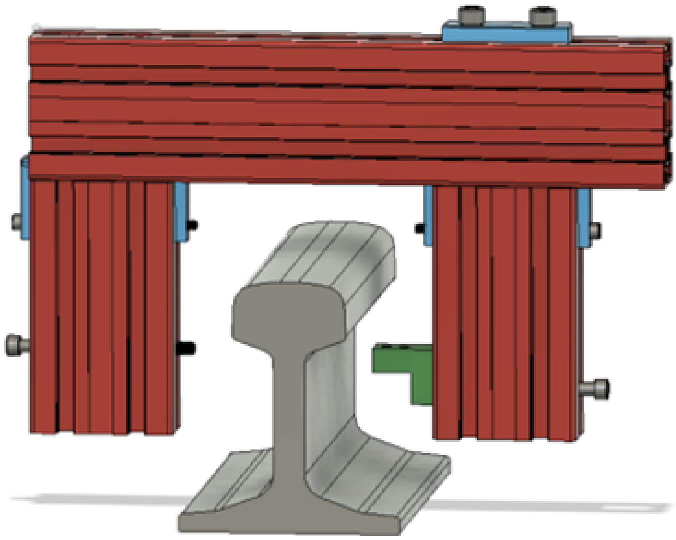

Figure 4.29: A CAD render of the over-rail v1.0 clamp body, composed of a number of sections of aluminium extrusion (red), assembled with steel bolts and aligned with bespoke aluminium key-nuts (blue)

4.7.7 Sensor alignment

The sensor-holding assemblies were aligned on both sides of the web using alignment sub-assemblies, each spring loaded and running on a pair of hardened stainless steel linear bearing shafts to aid installation (Figure 4.30). Their vertical position relative to the rail was constrained by laser-cut guides matching the contours of the specific rail profile, and self-alignment with the larger test platform was achieved by using machined recesses for component location (Figure 4.31). The rail-specific alignment guides I designed to be easily swapped with gloved fingers by incorporating knurled knobs for securing the guides, while the exact positioning was triangulated by a pair in-situ steel dowels (Figure 4.32).

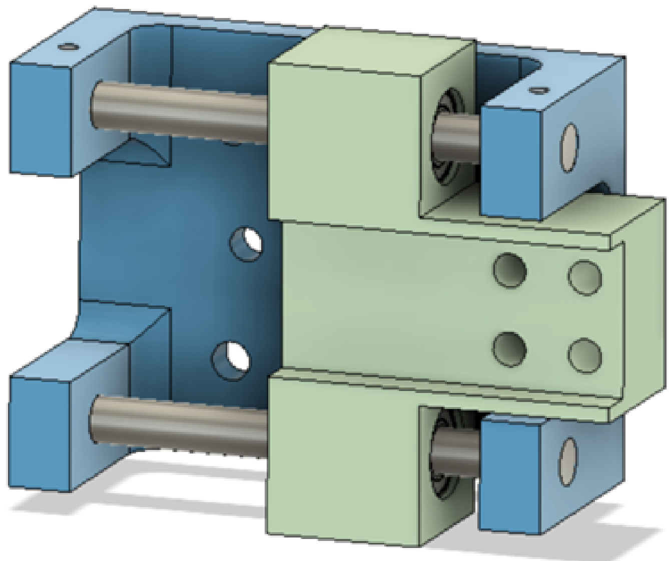

Figure 4.30: A CAD render of the over-rail v1.0 alignment guides, including linear bearing shafts, rail profile guide plates and attachment and alignment components for connecting to the over-rail v1.0 clamp

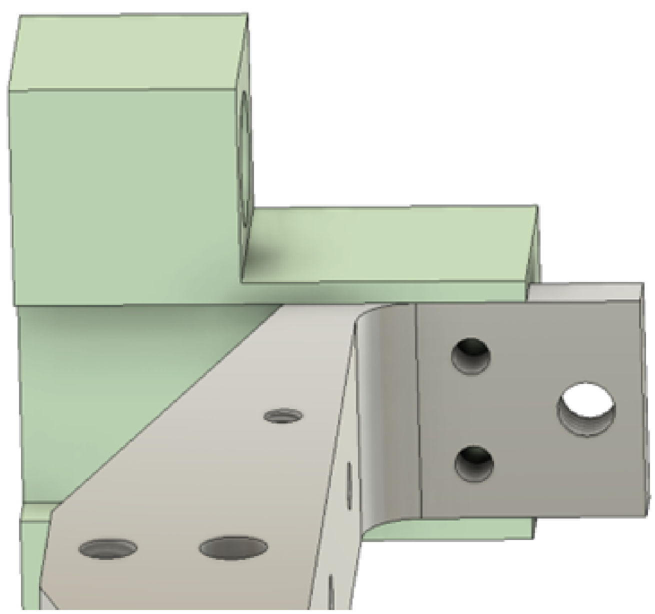

Figure 4.31: A CAD render of the over-rail v1.0 alignment guides, detailing the machined recess interface between components resulting in exact self-alignment

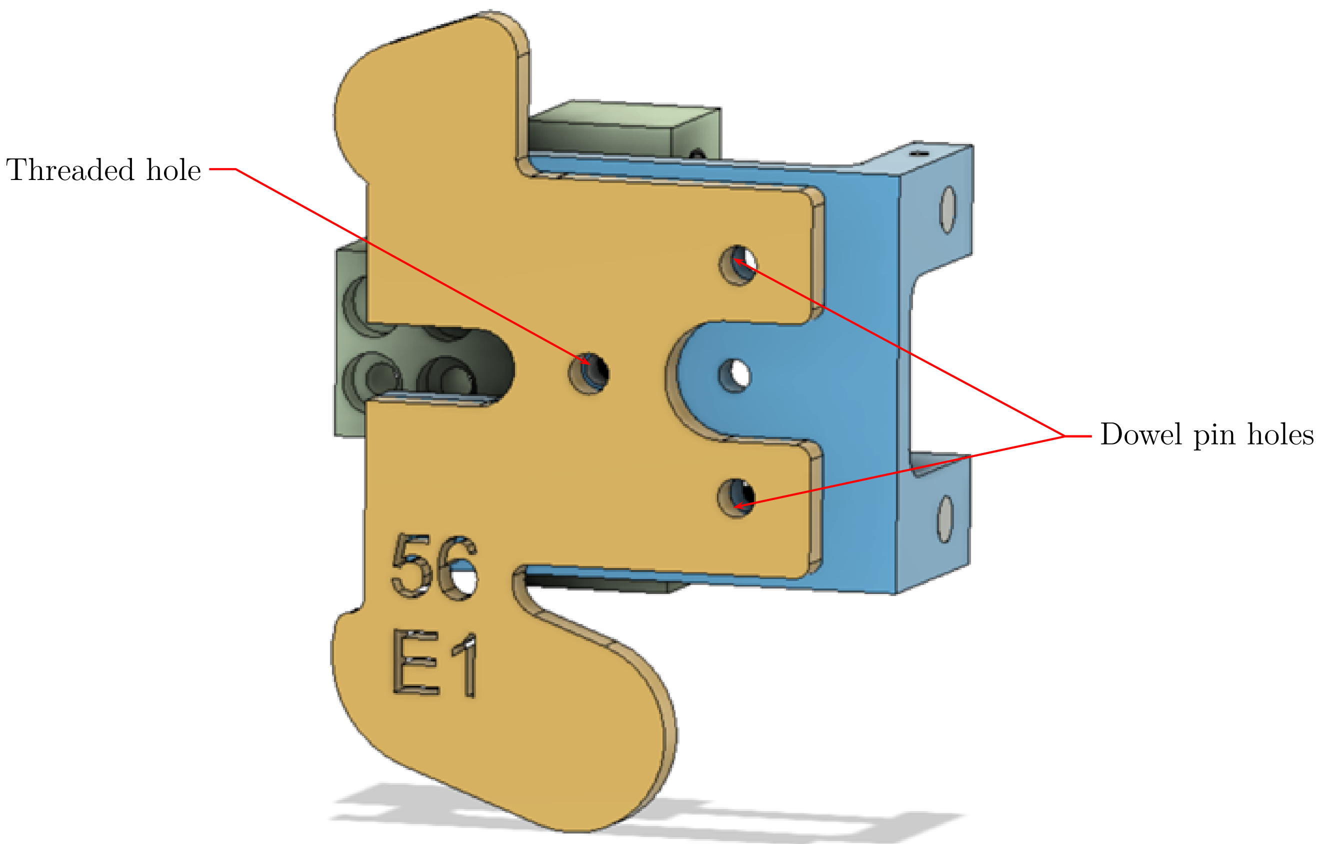

Figure 4.32: A CAD render of the over-rail v1.0 alignment guides, rail profile guide (yellow) and threaded and dowel pin holes for positioning

The 'load slide block' self aligned to the keyway slots in the extrusion and attached using a high-tensile steel bolt (Figure 4.33). These features ensured the load was delivered exactly perpendicularly to the face of the rail web in all planes and was correctly aligned with the sensor locations.

Figure 4.33: A CAD render of the over-rail v1.0 fixed sensor sub-assembly, showing the self-aligning aluminium component in relation to the aluminium extrusion of the clamp

4.7.8 Load application

The application of force was by means of a captive M12 cap-head bolt driving an aluminum piston against the load cell (Figure 4.34), which I incorporated into the moving section of the moving sensor bar to remove the reliance on the torque applied to the sensor clamping bolt as a proxy for sensor clamping load. This was recessed into the load side sensor bar, which was itself aligned on two 10mm stainless steel linear bearing shafts, sliding along them on two high quality and accuracy linear ball bearings. The transfer alignment of the force application was maintained by an accurately machined 'Load Slide Block' which holds the two 10mm bearing shafts perfectly parallel and aligned in the x-z plane.

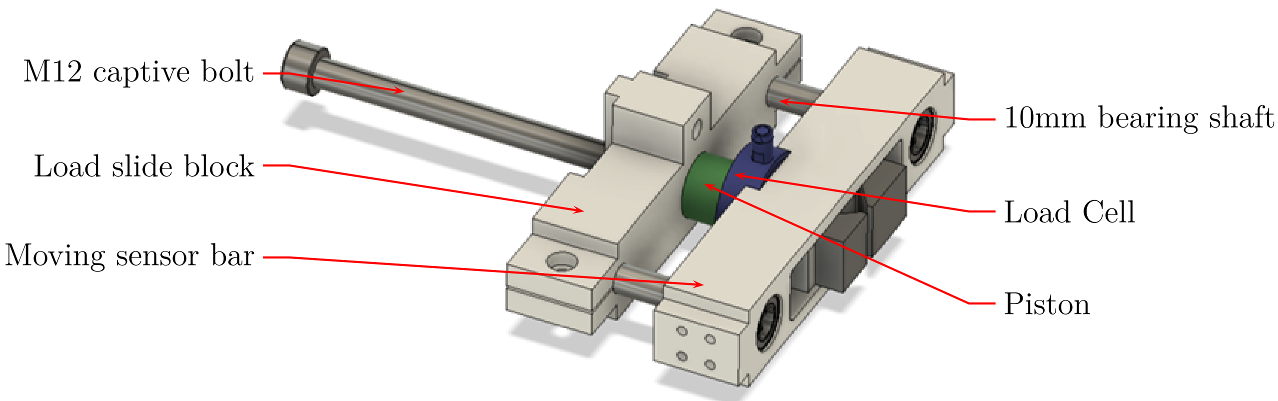

Figure 4.34: A CAD render of the over-rail v1.0 moving sensor sub-assembly, showing the self-aligning aluminium component, steel linear bearing rails, load cell and loading piston & bolt

The opposing sensor sub-assembly contained the adjustable slide positioning system taken directly from test platform 4, with rail alignment sub-assemblies attached on either end (Figure 4.35).

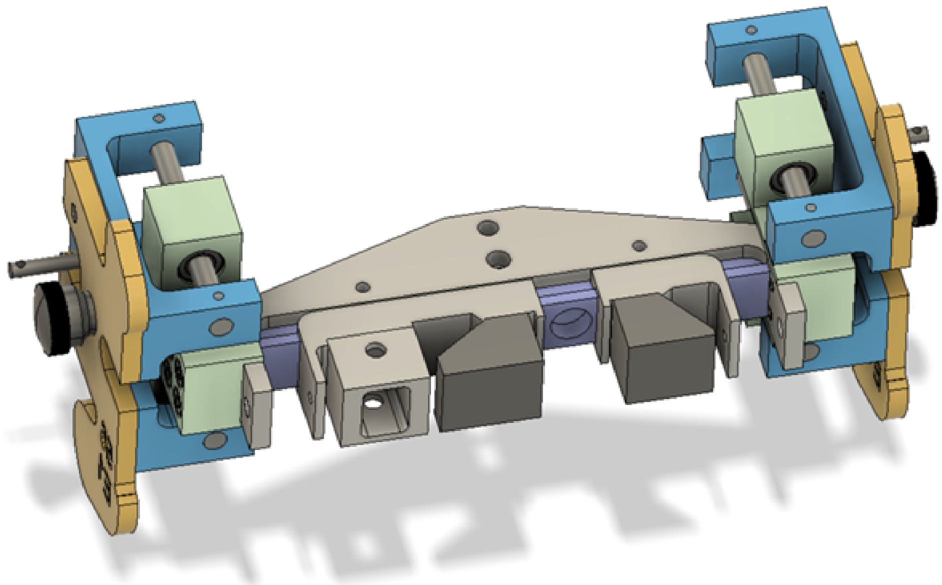

Figure 4.35: A CAD render of the adjustable slide sub-assembly taken from test platform 4, assembled with a pair of rail-alignment sub-assemblies

4.7.9 Future demands

As the initial investigations focused on parallel web rail (56E1), it remained possible to use the 20mm wide sensor format used in the laboratory. However, as work progressed towards investigating other non-parallel profiles these 20mm wider sensor assemblies would not have allowed correct contact between the web and the sensor face, especially for the angled wedge method.

I designed the load-side sensor holder with multiple rebates and bolt patterns to allow for narrower sensors to be used and at several different locations (Figure 4.36).

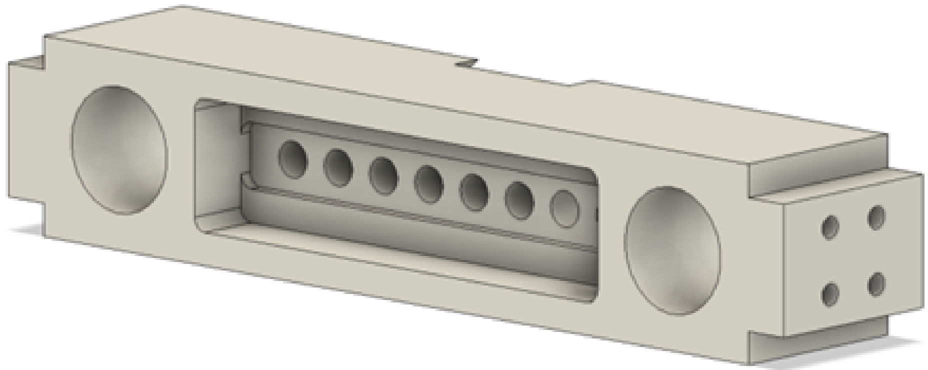

Figure 4.36: A detailed CAD representation of load-side sensor bar, featuring multiple fixing holes and narrower recess for future sensor designs

4.7.10 Design performance

The resulting test platform was successful in achieving the design goals (Figure 4.37) and taking measurements from full-rail undergoing compression testing (Figure 4.38).

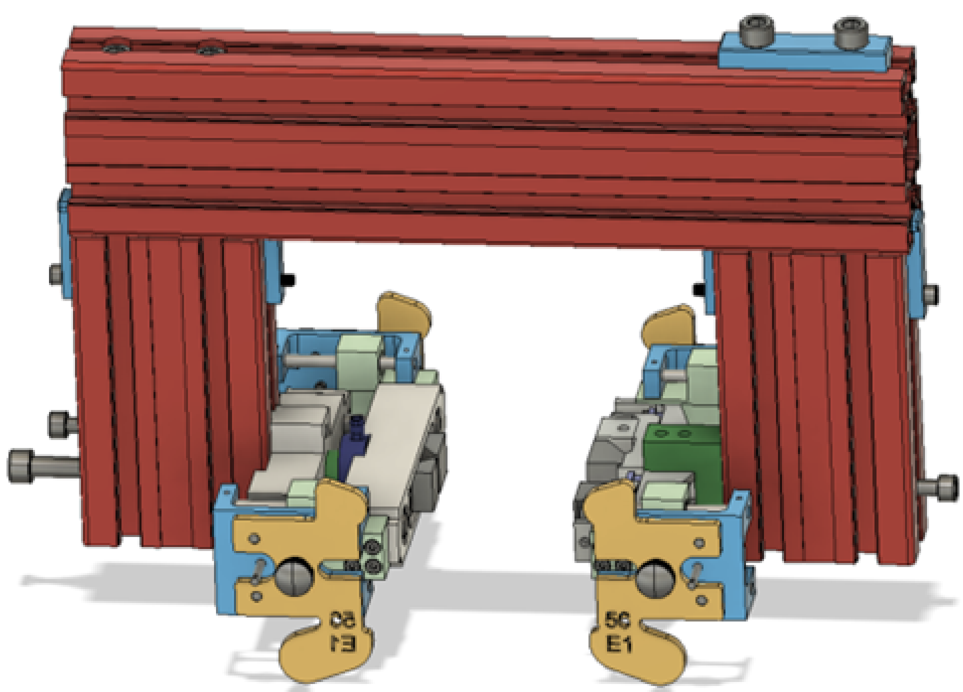

Figure 4.37: A CAD render of the fully assembled over-rail v1.0 test platform.

Figure 4.38: An image of the fully assembled over-rail v1.0 test platform attached to a rail undergoing compression testing

Experimentally, the results were comparable with those obtained in the laboratory, however that also included the continued presence of a significant ‘zero offset’ (a difference in SoS between orthogonally polarised shear waves at zero stress) in both birefringence and angled wedge measurements. In addition, the zero-offset was unpredictable in both direction and magnitude.

The offset was thought to be a result of insufficient alignment accuracy of the transducer assemblies with the rail surface as well as the variable interaction between the sensor faces, the couplant and the surface of the rail.

The quality of the signals from the birefringence further sensors deteriorated over time. I suspected that the high sensor clamping forces needed to achieve strong signals from the angled wedges, being much higher than that required for the birefringence measurements, was damaging the exposed ultrasonic transducers on the latter and that subsequent designs should aim to separate these measurements.

4.7.11 Test platform 6

Responding to both the bending under load of test platform 4, and the low confidence in relative positioning of the angled wedges on either side of both the specimen and the rail web in test platforms 4 and 5, I conducted a full re-design of the lab testing platform. Test platforms 6, 7 & 8 were designed concurrently to allow each design to benefit from any improvements, ensure compatibility with the same sensor assemblies and to manufacture the least possible number of components.

It was also at this stage that I re-instrumented the angled-wedge sensor assemblies, which successfully eliminated the low 35-degree SoS values.

The design criteria were:

- Retain and ensure cross-compatibility with as many components from the existing over-rail v1.0 as possible
- Incorporate micrometer adjustment of the wedge sensor positions
- Compatible with new sensor assembly designs 5 & 6
- Robust alignment to the specimen axis of loading
- Eliminate potential for bending and out-of-axis clamping loads applied to the sensor assemblies
- Incorporate a load cell
- Compatible with wider (50mm x 20mm) test specimens

I designed the new adjustment component, incorporating micrometer heads, to finely tune the location of the angled wedges. This component was made to be compatible with the existing over-rail test platform, operate interchangeably with angled wedge and birefringence measurements and make use of the new sensor assembly designs. New components for the fixed sensors included recesses for different sensor formats, a load cell and for linear bearings to align with the 4 hardened steel linear shafts that replaces the single-sided clamp in the previous iteration. This ensured correct alignment of the sensors (Figure 4.39).

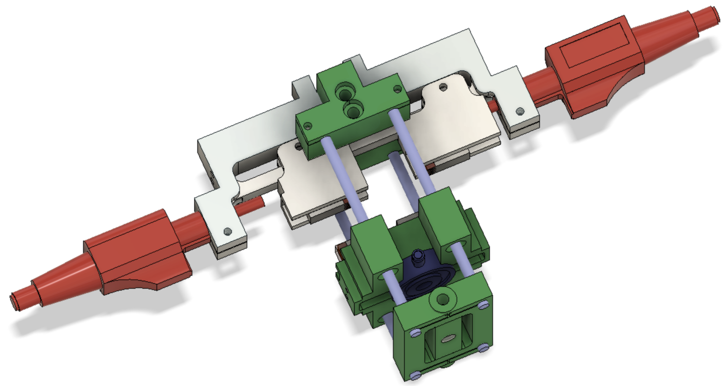

Figure 4.39: A CAD render of the sixth test platform, showing linear alignment shafts (light blue), micrometer adjustment (red), load cell (blue) and clamping components (green)

I designed 3D printed alignment guides to centre the test platform onto the specimen (Figure 4.40) and a new set of sliders to accommodate the new sensor assemblies (Figure 4.41).

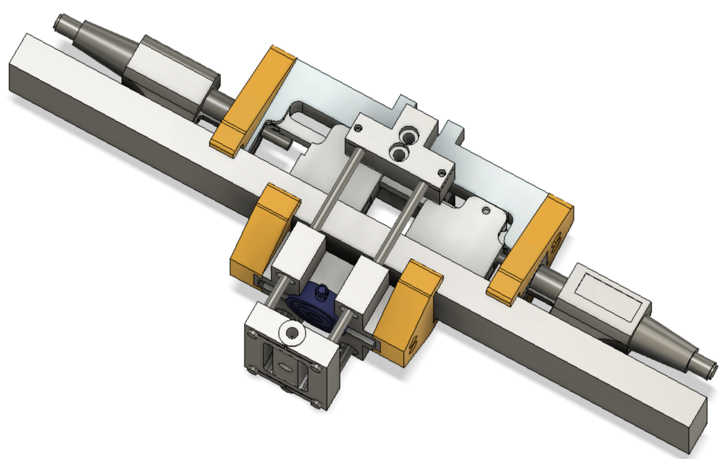

Figure 4.40: A detail view of the guides (yellow) for aligning test platform 6 with the test specimen

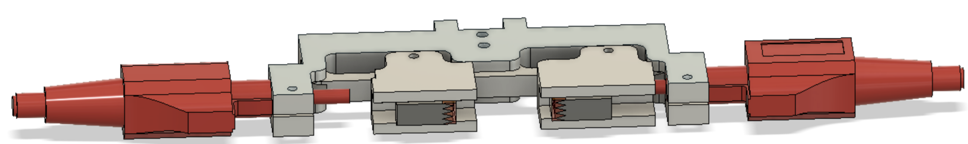

Figure 4.41: A detail view of test platform 6 showing sliders for attaching and positioning angled wedges

Figure 4.42 shows a photograph of the final manufactured design for test platform 6.

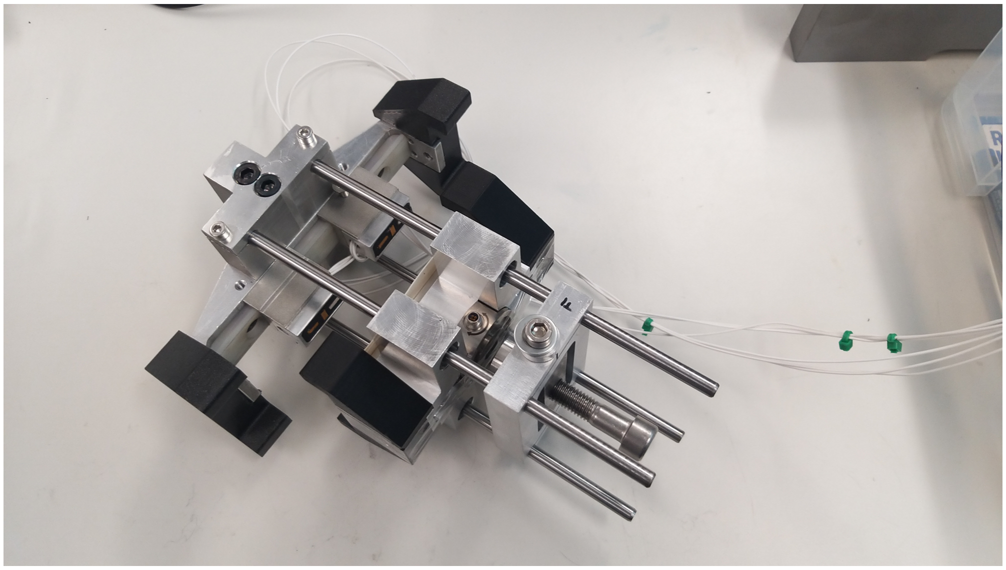

Figure 4.42: A photograph of the final manufactured design for test platform 6

4.7.12 Test platform 7

Bringing on board updates developed for the lab-testing platform, the main goal of test platform 7 was to incorporate the micrometer adjustment into the over-rail system, as shown in Figure 4.43.

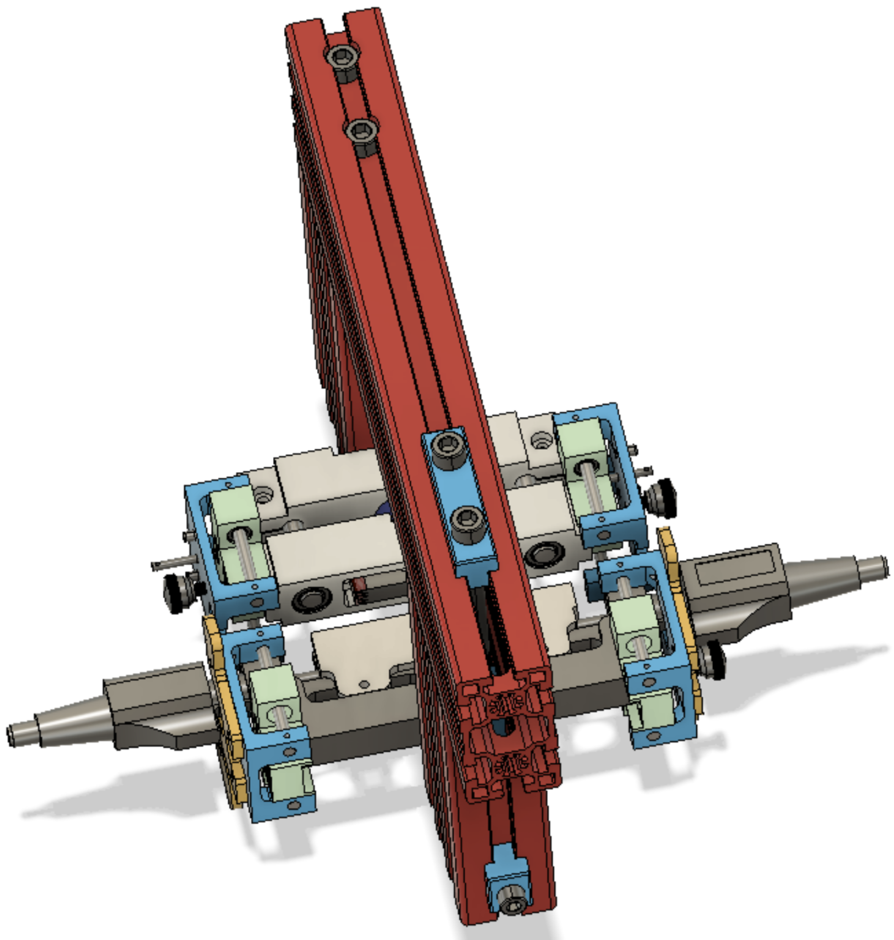

Figure 4.43: An image of test platform 7, showing addition of micrometer adjustment bar to the existing over-rail test platform

4.7.13 Test platform 8

Learning from the results of the previous over-rail tests, we had identified the need to separate the angled wedge and birefringence measurement systems. I designed an entirely new system to explore a different method of clamping and alignment, use fewer moving parts, simplify the manufacture and assembly process and reduce manufacturing costs. Design criteria were:

- Ensure exact alignment of sensor assemblies with the centre-axis of the rail web
- Be lightweight, simple to use and quick to apply/remove from a rail profile
- Ensure exact alignment of sensor assemblies to the longitudinal axis of the rail
- Fit two birefringence sensor assemblies (design 5)
- Minimise cnc machining requirements
- Contain fewer moving parts

The design consisted of a laser-cut stainless steel frame and rail alignment guides, aluminium CNC sensor holder and load application components with simple drilled aluminium spacers. The clamping of the device onto the rail was achieved using OTS threaded bar and hand wheel running on a thrust bearing (Figures 4.44 & 4.45).

Figure 4.44: An CAD side-view render of test platform 8, showing steel frame, CNC machined load and sensor holder components with hand wheel clamping system

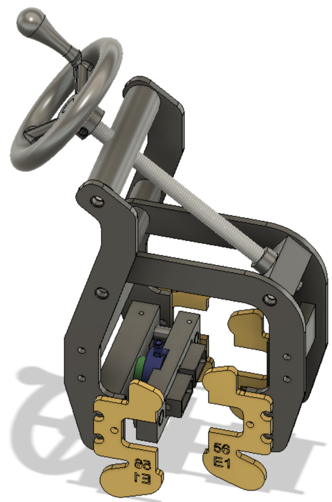

Figure 4.45: An CAD render of test platform 8, showing details of the load cell (blue), sensor alignment rods and sensor housing assembly, as well as the wheel, screw and bearing components used to clamp the test platform to the rail

Figures 4.46 and 4.47 show the finished design attached to a section of rail in the laboratory.

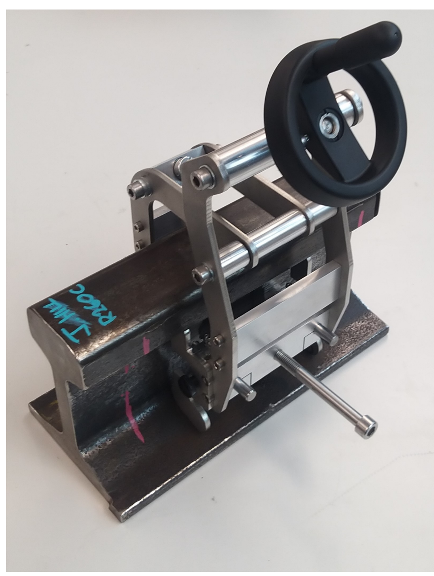

Figure 4.46: A photograph of test platform 8 attached to a section of 56E1 rail in the laboratory

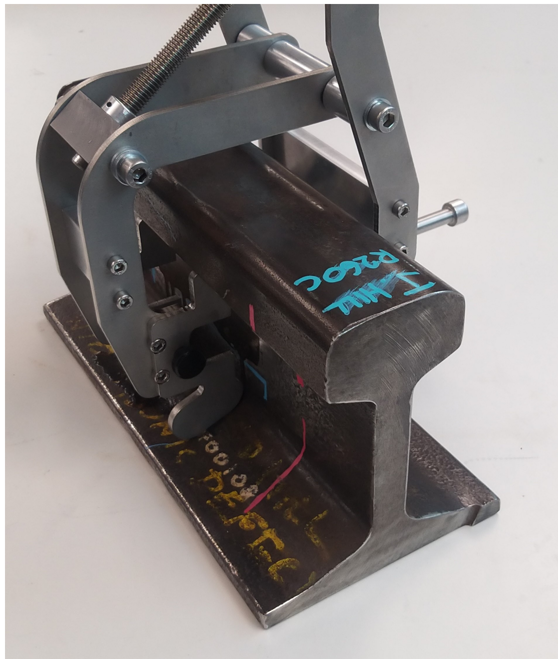

Figure 4.47: A photograph of the reverse side of test platform 8 attached to a section of 56E1 rail in the laboratory

Unfortunately, due to time constraints, this test assembly was never used for tensile or compressive testing.

4.8 Birefringence sensor assembly development

4.8.1 Sensor assembly 1

I assessed the signal response from a number of different frequencies and element sizes. From those that demonstrated a clear signal response, I used the criteria developed in section 3.1.3 to determine an acceptable frequency of 2 to 10 MHz. The end-use application to US rail profile with a curved web required the use of small sensors to fit within the curvature. It was determined that 3 x 5 mm was the largest size that would permit good contact. We included the minimum number of ultrasonic transducers to achieve the birefringence measurement (2 x orthogonally polarised shear and 1 x longitudinal) within a circular housing turned from EN24T bar stock (Figure 4.48).

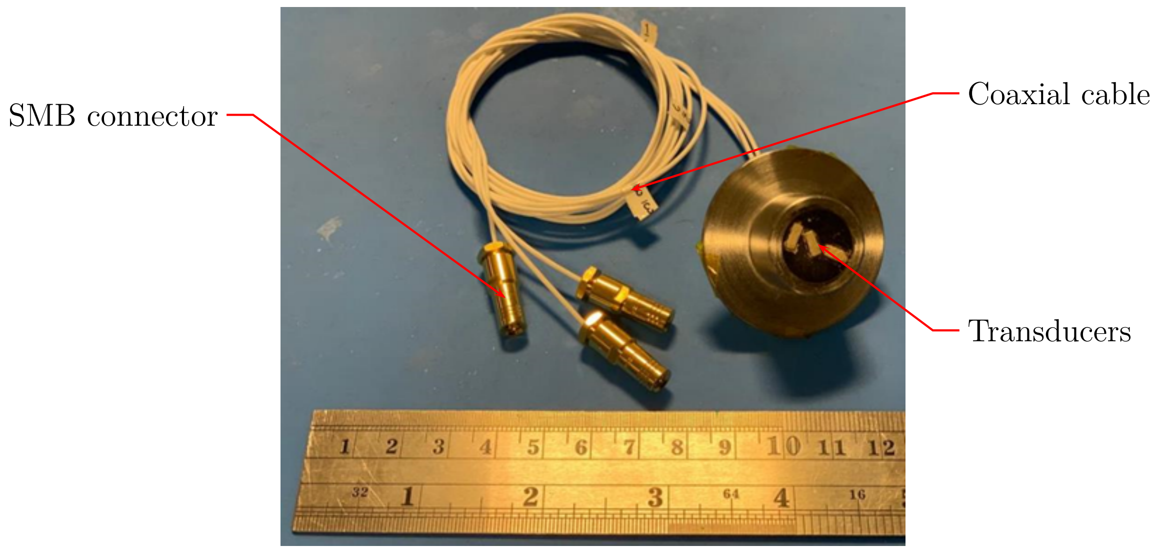

Figure 4.48: Image of the first turned EN24T birefringence sensor assemblies, showing three piezoelectric transducer elements and the coaxial cables with SMB connectors - ruler for scale

4.8.2 Sensor assembly 4

The turned birefringence housings were no longer suitable for the new design. I designed new sensor housings, CNC manufactured in Aluminum for stiffness and low weight (Figure 4.49).

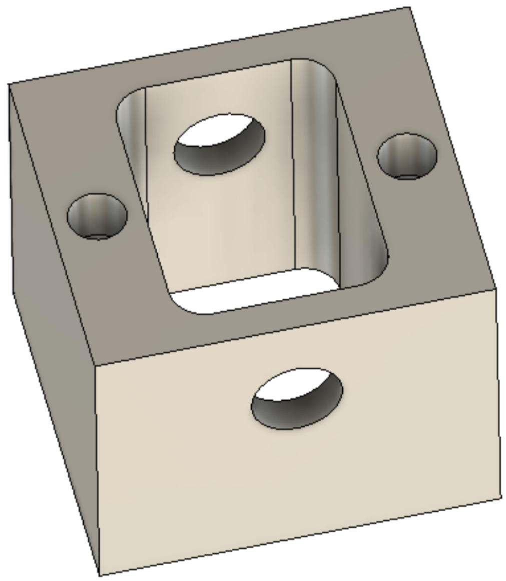

Figure 4.49: Image of the CNC machined aluminium housing for the fourth (birefringence) sensor assembly

4.8.3 Sensor assembly 5

In response to the signal shown by the previous birefringence sensor assemblies, I re-designed the housing to fit the following criteria:

- Smaller form factor
- Solid rear face to support potting resin - stiffen the sensor face and prevent degradation
- Larger holes for cable exit

The design is shown in Figure 4.50.

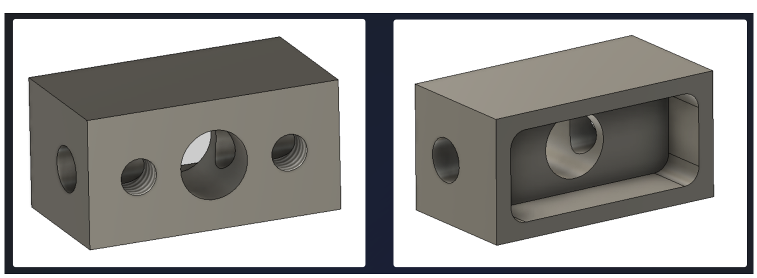

Figure 4.50: A CAD render of sensor assembly 5 showing CNC machined features including enlarged cable exits, narrower body profile and reinforced rear face

I also developed a new assembly template and instrumentation procedure, using a CNC machined plate to ensure total control of the position of the transducers within the assembly. This eliminated any possibility of misalignment of the shear waves relative to the axis of applied longitudinal stress (Figure 4.51).

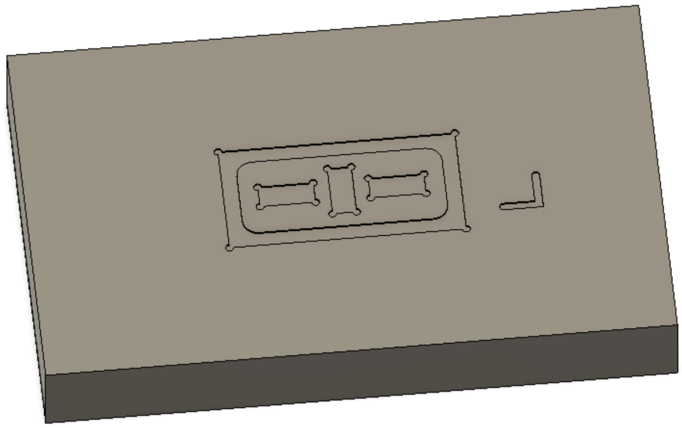

Figure 4.51: An image of the CNC machined instrumentation block for sensor assembly 5 showing recesses for sensor and housing location

While these assemblies gave increased confidence in the alignment of the transducer elements relative to the direction of applied stress, the results did not show a significant improvement.

The exposed transducers also became increasingly damaged with repeated use. This at times led to difficulties in extracting the best signal wave forms. Though each set of data captured had a suitably good signal quality, this led me to conclude that a solid faced sensor assembly would perhaps be beneficial for the measurement in the field.

4.8.4 Sensor assembly 7

Following the degradation of the exposed transducer in a relatively high impact environment, I designed the 7th sensor assembly with a solid front face. The introduction of an intermediary face in a perpendicular ultrasonic system created a critical design factor: the thickness of the front face. A good connection to the test specimen would ensure a high proportion of signal transmission. However, there would inevitably be some unwanted reflections. It was important that the geometry allowed the expected arrival times for the signals of interest (those from the back face of the specimen) to fit into a gap between the periodic internal reflections. A thickness of 11mm allowed for a sufficient gap between the arrival time of the different signals, ensuring signal clarity could be achieved.

A CAD render of the sensor design, both back and front faces, are shown in Figure 4.52, with the internal details, including sensor alignment recesses and cable ejection channels are shown in Figure 4.53.

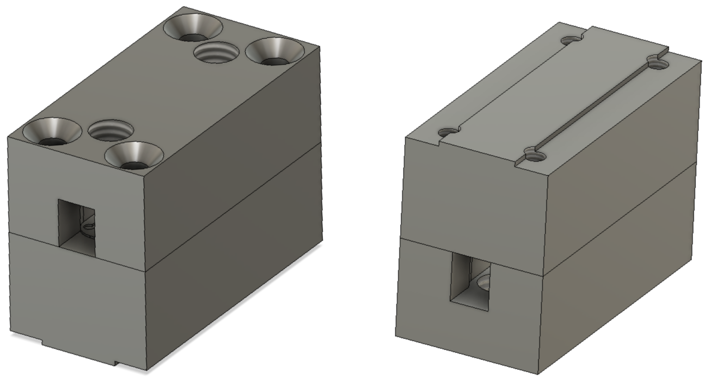

Figure 4.52: A CAD render of the CNC machined sensor assembly 7. Left: Top view showing attachment holes to test platform components, Right: Bottom view (sensor face) showing stepped face to reduce required clamping force

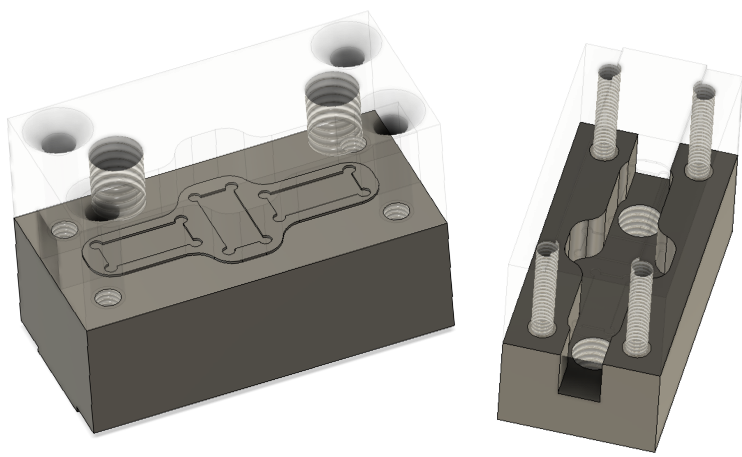

Figure 4.53: A CAD render of the CNC machined sensor assembly 7. Left: showing transducer location features, Right: showing clearance recess in top housing to allow space for transducers, potting and cabling

There was not enough time to finish the instrumentation of these sensor assemblies and conduct trials. The larger issues surrounding the accuracy and reliability of both birefringence and angled wedge measurements were a much higher priority than pursuing potentially marginal gains or solutions to in-track issues while the system as a while was not performing sufficiently well to exit laboratory trials.

4.9 Angled wedge sensor assembly development

4.9.1 Sensor assembly 2

4 angled wedges were cut from EN24T using EDM and instrumented with a pair of 2MHz orthogonally polarised shear transducers (Figure 4.54). These were the first sensor assemblies to conduct successful captures of multiple guided angled waves through the rail web.

Figure 4.54: Image of the first angled wedge sensor, with two orthogonally polarised shear transducers installed on an EN24T angled wedge

4.9.2 Sensor assembly 3

In order to save weight and space for the next iteration of the sensor platform, the angled wedges were shortened (Figure 4.55). These wedges were used for multiple iterations of the test platform. Signal quality was sufficient but sometimes challenging to achieve consistent third reflections, needed in this case as the OpMux DAQ system triggering remains undefined and inexact in the time domain, rendering first reflection calculations impossible. These designs were re-manufactured and instrumented a number of times, due to cable and transducer failures over the project duration. With inconsistent results in early testing stages, I had low confidence in the exact alignment of the transducers themselves relative to the sensor face as the instrumentation method was challenging and had no manner of preventing rotation or slippage of the transducers as they were being bonded.

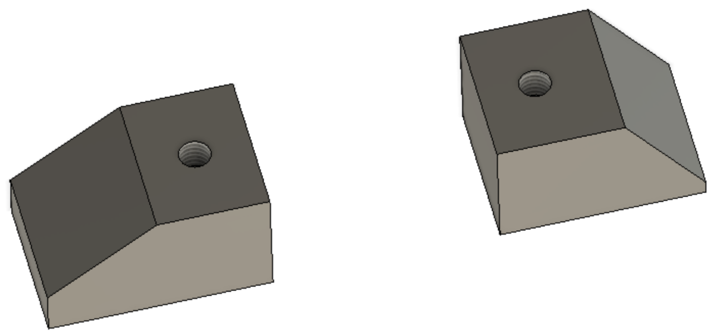

Figure 4.55: Image of the third sensor assembly, with wedges shortened from earlier iterations

4.9.3 Sensor assembly 6

Previous testing resulted in the high clamping forces used to secure the sensors to the specimen bending components. Additional design issues became evident from a user-experience perspective. As I conducted the experiments, I learned from hands-on experience that it was challenging to keep the different sensor assemblies perfectly aligned. This therefore needed addressing in the subsequent iterations of the design. Furthermore, I was looking ahead towards the final use case, where the angled wedges would have to fit to the curved web surface of the US rail profiles of interest. These considerations required me to redesign the angled wedge sensor assemblies. This assembly had to:

- Have a reduced contact area to reduce required clamping force
- Reduce the width of the wedges to minimise the required surface preparation of curved rail webs
- Incorporate features from commercial ultrasonic probes to reduce signal noise
- Fit within sliders that were compatible with test platform 6
- Ensure perfect alignment of the shear transducer element

The outcomes were wedges with saw-toothed rear profiles, a CNC machined recess for aligning the transducer, 10mm body width and using a single 5mm x 5mm shear sensor (Figure 4.56). The design achieved all the required goals. Signal clarity was improved, as was confidence in overall alignment, however, with smaller sensor faces the alignment across the web was more critical. Very small misalignment could cause signals to drop to zero. The accuracy of manufacture was also an issue. When initially assembled the assembles found not to be exactly square to the specimen surface. Shims were used to correct for this, without which there were no viable signals.

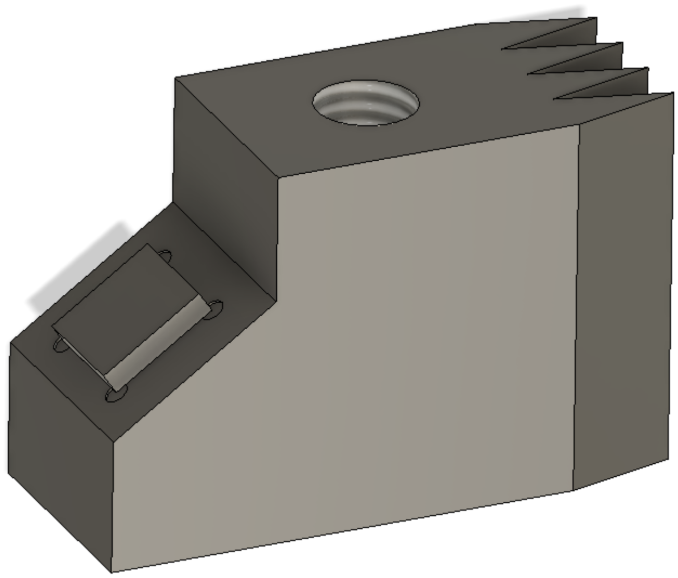

Figure 4.56: A CAD render of the EDM and CNC machined wedge for sensor assembly 6, showing recess for sensor alignment and saw-tooth rear profile

4.9.4 Sensor assembly 8

The final iteration of the angled wedge sensors was conceived for two reasons:

- To equalise the contact pressure across all wedge sensors
- To allow a 'hybrid' measurement, using a 90° perpendicular shear sensor alongside the angles wedges

Using FE modelling to analyse the load distribution and eccentricity across the contacting faces the sensor angles, footprints and alignments were redesigned to reduce variance in sensor contact pressure with the rail web. Figure 4.57 shows the individual sensor assemblies for the 55°, 35° and hybrid assembly, while figure 4.58 shows the assemblies in their nominally perfect positions constrained by the positioning jig.

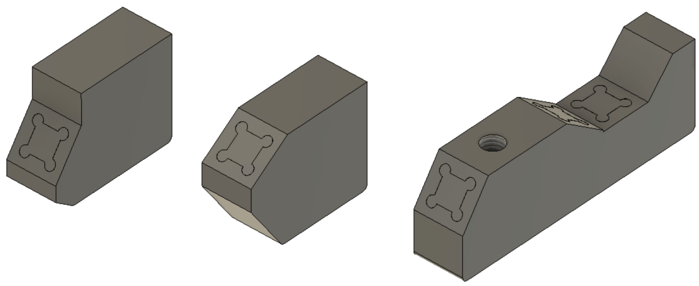

Figure 4.57: A CAD render of the EDM and CNC machined hybrid measurement sensor assembly 7 showing machined recesses for transducer location and alignment. Left: 55 degree angled wedge, Centre: 35 degree angled wedge, Right: Hybrid wedge, combined 35, 55 and 90 degree transducer arrangement

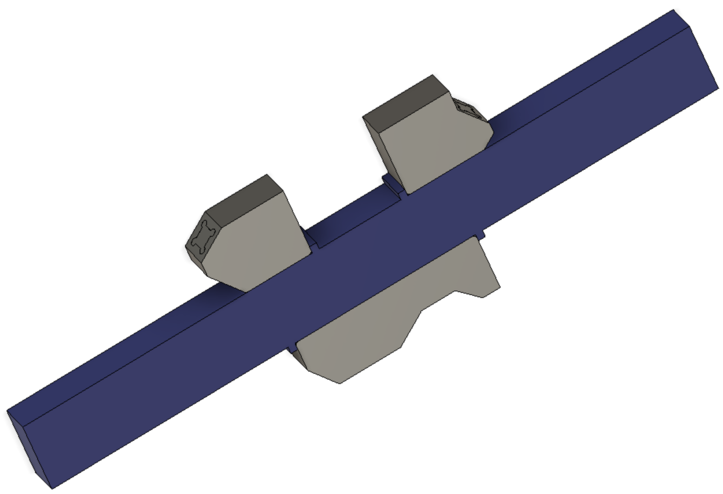

Figure 4.58: A CAD render of the EDM and CNC machined hybrid measurement sensor assembly 7 and the position jig for accurate setting of nominal flight path distances between wedges

The previous angled wedge sensor platform and sensor assemblies had a large variance in eccentricity of each sensor from the central loading axis, resulting in unequal clamping pressure between each of the sensor assemblies and the rail web. This design reduced that inequality for each of the 4 angled sensors to ±0.8MPa (Max. 6.1MPa, min. 4.5MPa), with the 90° wave-path experiencing a clamping pressure of 2MPa (Figure 4.59). It is important to note that the absolute values quoted here are a very rough approximation and change readily with the mesh properties. Their relative magnitudes, however, is the important feature and this remains consistent.

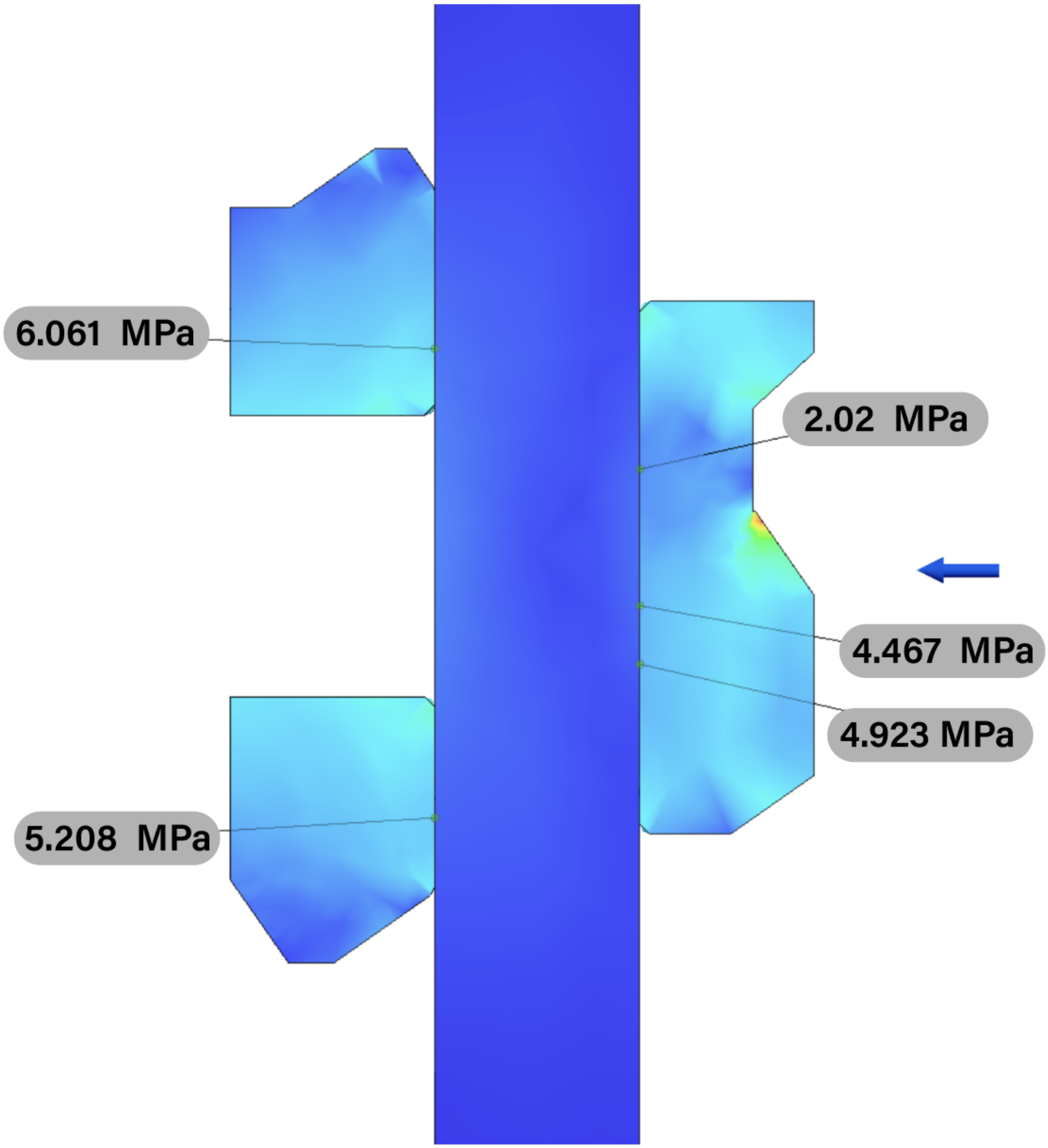

Figure 4.59: A basic FE model of the sensor assembly 8 hybrid sensors clamped to a rail web specimen, showing the range of sensor clamping pressures across the sensor assemblies at the locations of the individual wave paths

Chapter 5

Sensitivity analysis

This chapter describes the methodology and outcomes of the theoretical analysis of the sensitivity of the ultrasonic LS measurement. Dr. Art Gower undertook the fundamental mathematical analyses. The author, alongside colleague Dr. Gary Nicholas, determined the scope & specification for the analysis and was responsible for the interpretation within this thesis and the integration of the results in the design and experimental development processes to make best use of the findings.

Potential variations in the properties and dimensions of the specimen, the alignment and position of the ultrasonic sensors and the implications of encountering these variations without accounting for them within the models or calculations of results have been investigated.

A summary of the calculated error percentages from all sources is presented.

5.1 Establishing theoretical errors

In order to establish the focii for the design of the test platforms it was important to quantify the potential errors from both mathematical models, the birefringence and angled wedge methods, which are detailed in chapter 3.

A number of factors relating to the geometry and physical dimensions of the test specimen could result in an unaccounted for difference in the ultrasonic flight path, and therefore an unaccounted difference in ToF, causing error in the calculation of the ultrasonic SoS through the material.

Summaries and theoretical quantification of the considered factors are detailed below. Full mathematical models for the sensitivity analyses can be found in Appendix B.

5.1.1 Specimen surface finish

The potential impacts of surface finish are twofold:

Contact stiffness: Variation in the specimen's surface profile could result in variation in the stiffness of the asperity contact between the sensor and specimen. A change in contact stiffness could affect the transmission of ultrasonic waves and perhaps the speed of sound through the interface.

It is not possible to conduct a robust investigation of the intricacies of impact of asperity contact on transmission of acoustic waves within the bounds of this thesis. It is assumed, however, that with a consistent surface preparation regime, the impact will be consistent across all experiments. The contact area between the ultrasonic sensor and the specimen is many orders of magnitude larger than the asperity size in all planes. As such, it is assumed that any impact from slight variation in positioning of the sensor between repeated tests would be averaged out over the entire contact area.

It is also assumed that is unlikely that any variance in sensor position below 1-2mm would result in local changes to the specimen AECs.

Pitting and other surface defects: Undulations, pits from corrosion and variance in web thickness due to the relatively loose dimensional tolerances in rail manufacturing processes could all impact the flight path of the ultrasonic signals. The presence of these features in the surface of the rail specimens must be eliminated or accounted for when calculating flight path (and, as a result, ToF) to avoid errors in stress measurement.

In the laboratory, it is a simple task to prepare the tensile specimens by grinding both surfaces back to bare metal. The grinding operation will have an equivalent finish to that of 400 grit wet and dry sandpaper, leaving a surface finish of Ra 0.23 µm [101]. Achieving this level of accuracy will be much more challenging on samples of full rail and yet again in the field.

5.1.2 Flight path through unstressed wedges

The angled wedge measurement necessarily involves a portion of the signal flight path travelling through the unstressed material of the wedges themselves, as well as the stressed test specimen. The AECs and density of this material will be different o that of the test specimen. The potential impact was investigated mathematically and the potential errors were not small. To account for this, the wedge sensor assembly was calibrated using a jig, measuring the flight path only through the wedges, allowing the elimination of this error from subsequent calculations.

5.1.3 Density variation

Data on the density of specific rail steel metallurgical compositions is not readily available, however, analysis of the overall variance of Medium to High Carbon steels gives a range of $7.65\,\mathrm{gcm}^{-3}$ to $7.75\,\mathrm{gcm}^{-3}$[102].

From Equation 3.26, the stress prediction error is directly proportional to the variation in density: 1.3%.

5.1.4 Non-parallel surfaces

A lack of parallelism between font and rear faces of the test specimen will introduce errors when calculating accurate ultrasonic flight paths.

In the laboratory the parallel grinding of the specimens will all but eliminate this issue. In the field the parallelism (or lack thereof) could be measured using a number of topographic methods, from laser topography to manual measurement of a reference grid across the measurement site. However, without exact alignment of a measurement system, it would prove very challenging to establish the location of the normal plane and thus the relative angle of any section of the rail relative to another. It is likely of more benefit to develop a rigorous surface preparation regime, the effectiveness and repeatability of which can be experimentally proven on short rail samples. All told, a conservative estimate of error in this preparation regime in the field could reach $\pm 2°$.

5.1.5 Specimen thickness

Should the surface preparation and parallelism be tightly controlled, direct measurement of the specimen thickness is still required. The accuracy to which this can be measured is limited by the measuring tools available. For a laboratory specimen it is possible to use a micrometer to achieve values accurate to $\pm 0.003mm$.

For a full rail measurement in the field it will be necessary to purchase a custom designed caliper. Even so, it is likely that the accuracy limit will be in the region of $\pm 0.03mm$.

5.1.6 Data acquisition system time resolution

The sample rate of the digitiser in the Data Acquisition (DAQ) system will create approximation errors when converting from the analog to the digital domain. These errors are linked to the size of the discreet time-step between individual samples (data points), determined by the the maximum capturing speed (sample rate).

Should a particular feature of an ultrasonic signal arrive at the receiving transducer in the gap between two sampling points, there will be an inaccuracy linked to the time difference between that moment and the subsequent capture point. This potential error can be reduced by increasing the sample rate at which the DAQ operates. This, however, is limited by the hardware and software capabilities of the system as a whole.

The current OpMux and Picoscope system operates with a maximum resolution that is necessarily split across both the vertical axis (how fine the system registers the amplitude of the signal in volts) and in the time domain (how long between sample captures). These analyses are only concerned with ToF measurement (and not amplitude change as is common in many tribological ultrasonic applications). As such it is legitimate to trade-off some vertical resolution in favour of a finer time-domain resolution.

The maximum sample rate of the current system that can be achieved using while maintaining sufficient vertical resolution to allow accurate data processing of the ToF is 250 MHz.

A plot of the error relationship with applied stress for different sampling rates is shown in Figure 5.1.

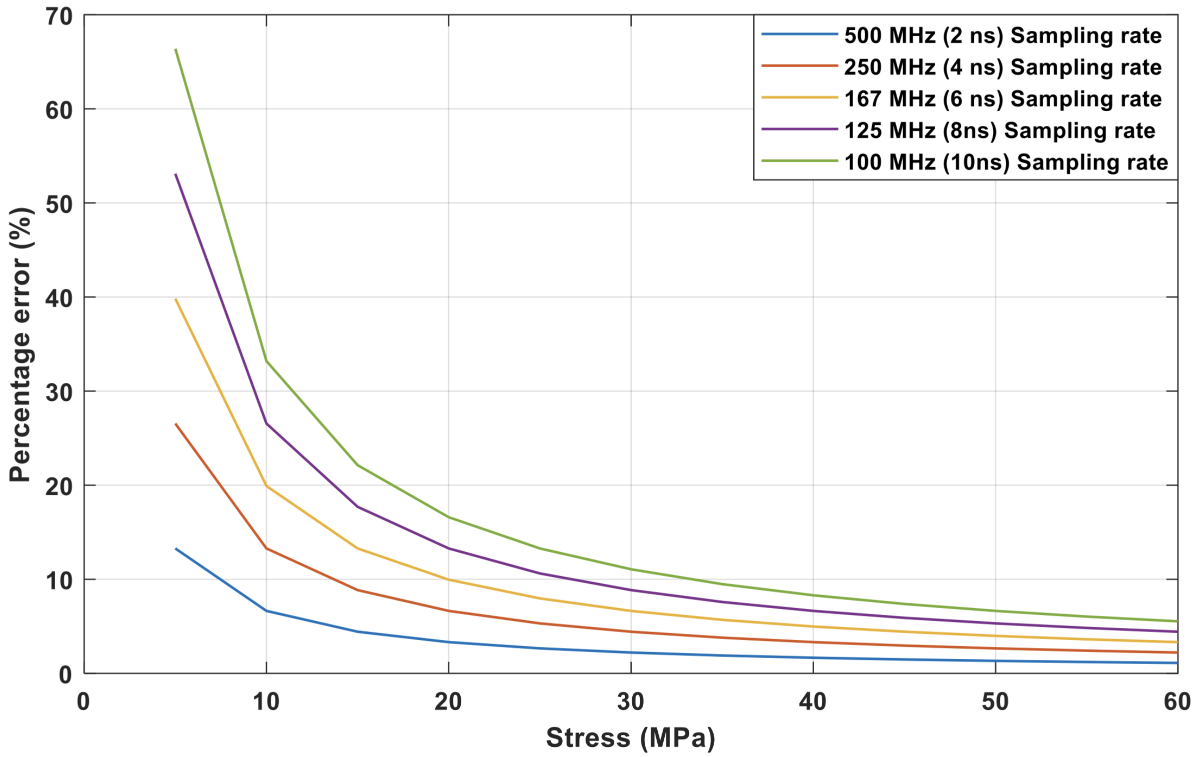

Figure 5.1: Chart showing the percentage error in stress measurement from sampling inaccuracy against applied stress for different sampling rates

5.1.7 Sensor orientation

Aligning the sensor assemblies accurately to the axis of applied stress is a fundamental experimental requirement. Error in alignment will introduce error in measurements. This error was investigated numerically with a summary of results included in Table 5.1.

5.1.8 Wedge manufacturing tolerance

All manufacturing processes have their inherent dimensional tolerances. For the angled wedge method the accuracy of the machined angles will influence the error inherent within the sensor platform. Modern wire erosion processes can operate to angular tolerances as small as $\pm 0.01°$. Figure 5.2 shows the relationship between measurement error and variation in wedge angle. Using a conservative manufacturing error value of $0.1°$ we return an error value of 1%.

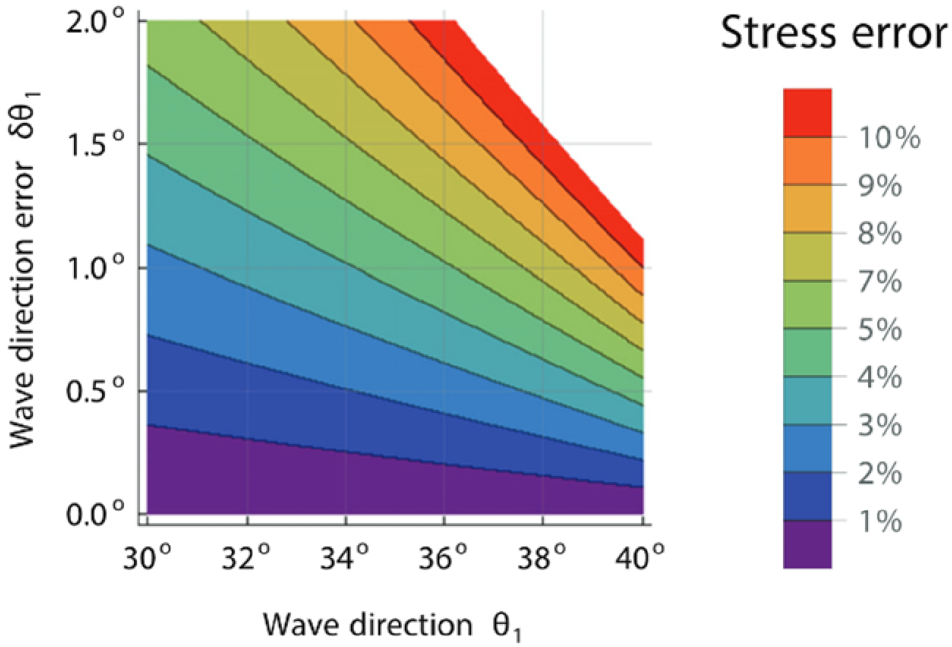

Figure 5.2: Chart showing the percentage error in stress measurement vs the angular tolerance of a 35° angled wedge. [Image credit: Art Gower] [86]

5.1.9 Modelling of stress-dependant error

A numerical simulation was run using the universal stress relation (equation 3.26) to predict the errors in the angled wedge measurement model. The universal stress relation is an asymptotic approximation, in that it disregards the second and third order terms of the general velocity-stress relation (as they are very small).

The left-hand plot in Figure 5.3 shows the predicted error from the approximation against the stress from the exact ultrasonic wave speed. The error expresses as a function of the absolute magnitude of the stress, as shown in the right hand plot of Figure 5.3.

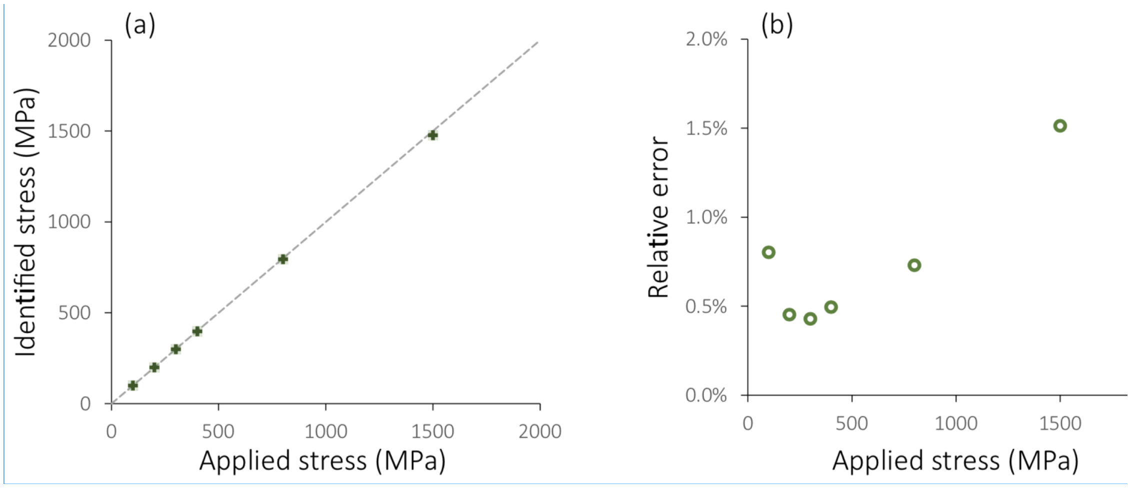

Figure 5.3: Plot (a) of the modelled accuracy of the angled wave method, and (b) the modelled error of the angled waves method for different values of applied longitudinal stress [Image credit: Art Gower]

The model is shown to predict excellent measurement accuracy and a variable error, which finds its lowest value at 350MPa applied stress. With the measurement requiring a stress accuracy of 11.9 MPa and the measurement range between 0 and 250 MPa it can be seen that the relative error from the mathematical model would be above 0.45%, with the maximum potentially increasing exponentially as the measurement absolute value decreases towards zero applied stress.

This error relation is inherent to the angled wedge method using the universal stress relation and cannot be minimised through any experimental means.

5.2 Summary of potential errors

Using numerical models, the impact of uncontrolled and unaccounted-for variations were calculated. A summary is shown in Table 5.1.

Table 5.1: Modelled error values for each type of specimen variance

Variation Type	Best Achievable Accuracy/ Tolerance	Max.Error (%)	
		Birefringence	Angled Wedge
Surface finish	$\pm$ 0.2 µm	4.6	17.5
Density variation	$\pm$ 0.1 kgcm^{-3}	1.3	1.3
Non-parallel surfaces	$\pm$ 2°	1500.0	30 000.0
Specimen Thickness	$\pm$ 0.03mm	0.4	513.9
Time resolution	250MHz	2.0	4.4
Wedge tolerance	$\pm$ 0.1°		1.0
Stress-dependant error	$\pm$11.9 MPa		2.0

It is worth noting that the errors from surface roughness, non-parallel surfaces and web thickness can really be consolidated into one practical issue: the requirement for effective surface preparation and accurate dimensioning of the measurement site on the rail. A simple summing of these potential errors would lead to overestimation of the risks and likely errors in this measurement in the real world.

Quantification (where possible and practical) of these errors by experimental analysis established how conservative, or otherwise, these numerical analyses were. Discussion of the results and comparison with modelled values can be found in chapters 7 and 8.

5.3 Experimental validation of sensitivity analysis

This section describes the experiments conducted to experimentally validate and qualify, where practical and possible, some of the findings of the theoretical sensitivity analysis.

It was not feasible to conduct thorough and in-depth investigations into many of the theoretical elements of the sensitivity analysis. Time and budget constraints were paramount, and with so many inter-dependent factors, isolating a single element within the test design to a sufficiently high confidence level needed a prohibitive investment in time and testing costs.

Gary Nicholas undertook the experimentation and data processing, the analysis presented here is my own.

Experimental investigations included:

- Specimen surface texture
- Sensor assembly clamping force

- Specimen web thickness
- Couplant application

5.3.1 Surface texture

One from a pair of identical tensile specimens, manufactured from EN24T, was sandblasted to create a rougher surface texture than that of it's polished counterpart.

To isolate the surface texture effects a constant sensor clamping force was used. A total of 3 repeat measurements were taken at each of 3 separate locations along the specimen with two different sensor assemblies simultaneously.

The difference in SoS between sensor assemblies was negligible in all cases. The averaged SoS values for sensor assembly 1 at each location on both specimens are tabulated below (table 5.2).

Table 5.2: Modelled error values for each type of specimen variance

Specimen	Longitudinal ms^{-1}	Shear $0°$ (ms^{-1})	Shear $90°$ (ms^{-1})	σ_{offset} (MPa)
EN24T (Polished)	5920±0.1	3237±0.4	3236±0.2	-31.4±143%
EN24T (Roughened)	5924±0.1	3245±0.3	3245±0.3	-127±32%
Difference	+4	+8	+6	+95.6

While the surfaces of both tensile specimens appeared visibly different, and the sand-blasted specimen felt textured while the polished specimen did not, subsequent Alicona testing of the specimen surfaces, conducted by Dr Will Gray, revealed that there was no statistical difference in the surface roughness of the two specimens. Perhaps the treatment selected was not appropriate to developing a rougher surface texture. Observed differences in the SoS are unlikely due to the impact of surface preparation in this case. It does not follow that surface preparation does not impact the accuracy of the measurement, merely that the study conducted does was insufficiently well designed to draw conclusions.

The consistent direction of the differences in both SoS and zero-offset stress could be explained by changes in residual stress due to the surface preparation process, though this is also uncertain and would require more in-depth investigation.

5.3.2 Clamping force

In an attempt to understand the effect of varying clamping force on the accuracy of the birefringence sensors, three sets of data were captured from each of three locations on both R260 tensile specimens. The clamping force was increased from 50N to 1000N at an interval of 200N.

Figure 5.4 shows the variation of the difference between the squares of the orthogonally polarised shear waves as they pass through the unstressed specimen. There are clear outliers in the data below 500N, which disappear for all data captured above that threshold.

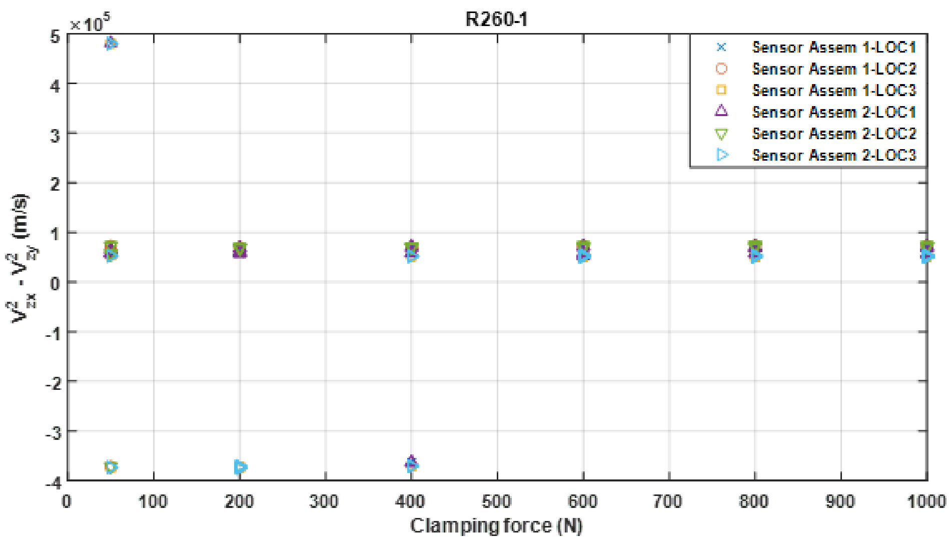

Figure 5.4: Variation in orthogonally polarised sound speed with clamping force for R260-1 rail steel. [Image credit: Gary Nicholas]

Excluding the outlier data, a variance of approximately $\pm 40MPa$ in the 'zero-offset' is consistent, thought the range could be said to stabilise above 400N (Figure 5.5). though this is perhaps of uncertain statistical validity due to the small sample size.

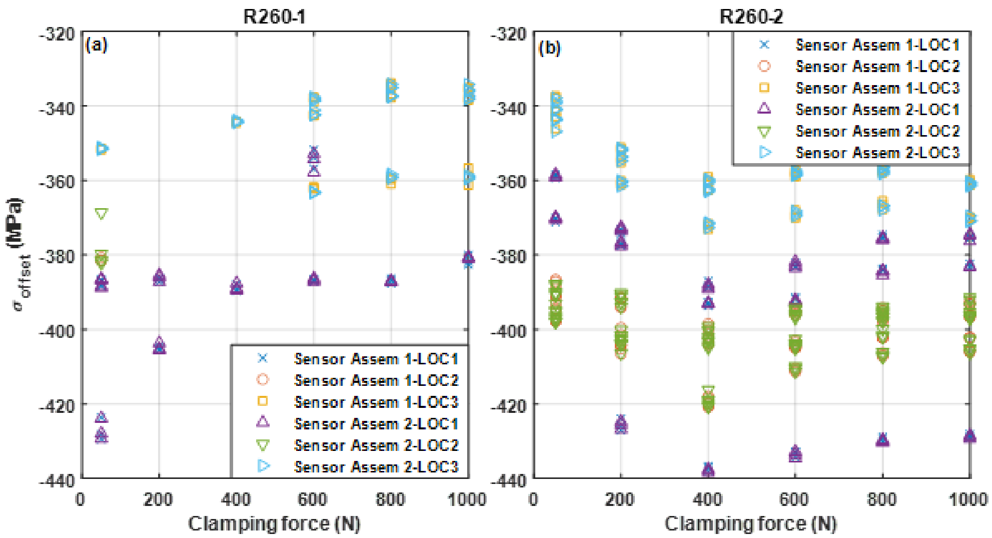

Figure 5.5: Variation in zero-offset with clamping force for both R260 rail steel specimens, excluding outlier data. [Image credit: Gary Nicholas]

It is worth noting that the 40MPa variance corresponds to the $\pm 1ms^{-}1$ difference in ultrasonic SoS, which in turn corresponds to the $\pm 2ns$ time step limit of the DAQ system. This is perhaps an indication that the limits of the data acquisition system are responsible for the scatter. Increasing the clamping force above 500N does not seem to produce any further improvement.

5.3.3 Couplant application

I do not think it hyperbolic to assert that a number of PhD theses could be completed investigating the effect of coupling bond material and thickness on the ultrasonic SoS through a specimen, as measured with removable sensors. However, noting the constraints mentioned earlier, a simple investigation was conducted with the existing sensor platform, varying the volume of couplant applied to the sensor assembly faces. The sensor assembly clamping force was fixed at 500N and the weight of the applied couplant was varied between 0.1 and 0.5 per sensor. Figure 5.6 shows a consistent value for the difference between the square of orthogonally polarised shear waves, with one outlying data point at 0.2g of couplant applied.

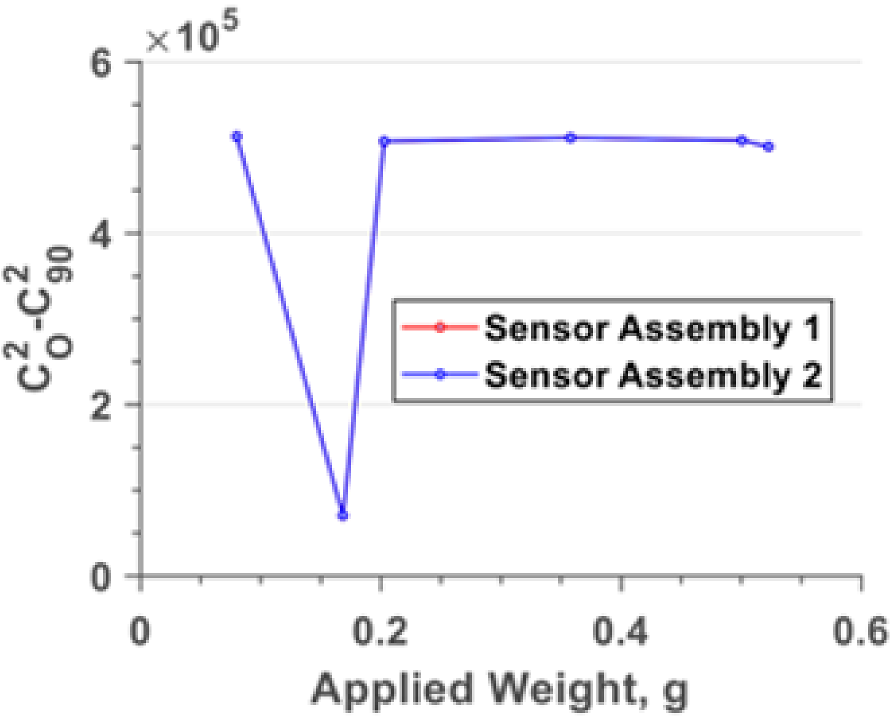

Figure 5.6: Variation in the orthogonally polarised shear SoS with varying amount of applied couplant. [Image credit: Gary Nicholas]

The function of the couplant is to fill the voids between asperities, allowing a continuous transmission of ultrasonic signals across the entire contact area. As such, the required volume is very small. It is, in fact, noticeable each time new couplant is applied, the system takes some time to settle and display the highest signal amplitudes. Additional couplant is consistently squeezed out from the interface by the application of the sensor clamping force and there is therefore little to no impact of variation in the amount of couplant applied within the range investigated.

5.4 Conclusions

Theoretical investigations revealed that both birefringence and angled wedge methods had very large error susceptibility from misalignment or miscalculation of ultrasonic signal path length. The predicted errors for the angled wedge method were orders of magnitude higher than for the birefringence method.

Some of the the experimental investigations did not produce clear results. Attempts to measure the impact of surface texture were inconclusive. Clamping forces above 500N have been shown to produce a stable value for variance in the 'zero-offset'. The use of a calibrated longitudinal sensor reduced the error in web thickness measurement to a maximum of 0.013mm and no discernible impact was seen from varying the amount of couplant used.

5.5 Error mitigation

For the potential sources of error that could not be eliminated or proven inconsequential, even where experimental validations were not successful in determining the impact of an experimental variable, good physical and experimental design was used to minimise and mitigate the impacts.

5.5.1 Surface finish and parallelism

From the theoretical analysis, surface preparation using a 400 grit abrasive (a finish of 0.2 microns) would introduce and error of 4.6% and 17.5% respectively for the birefringence and angled wedge measurements.

In laboratory conditions for the tensile testing specimens this potential error was reduced significantly by polishing the parallel surfaces of each specimen. For the full-rail compression test it was necessary to hand polish the surface using 400 grit paper. In an on-track scenario it is impossible to reproduce the flatness and parallelism of ground and polished surfaces used in the laboratory.

It remains a significant but not insurmountable design task to develop a sufficiently rigorous and reliable surface preparation process for the on-track measurements to account for the sensitivity to surface tilt. Another approach could be to map the surfaces of the rail to sufficient detail that any tilt can be measured, calculated and accounted for within the data processing.

5.6 Web thickness (measurement of)

Web thicknesses can easily be measured to an accuracy of $\pm 0.03mm$. This was done on each of the tensile specimens using a micrometer. For full-rail testing, a carpenters caliper was used with an error of $\pm 0.3mm$. To improve this accuracy value, a custom-made caliper would have to be manufactured, large enough to fit over the rail head yet have a narrow enough measurement range to account for the relatively small web thickness.

Again, accurate mapping and measurement of the flight paths, combined with the use of a calibrated longitudinal sensor for the birefringence measurement and the use of micrometers to accurately position the angled wedge sensors could eliminate this error.

5.6.1 Sensor alignment

The relative positioning of the sensor assemblies relative to the specimen and each other was entirely addressed through the sensor platform design process. It is impossible to entirely eliminate this error. Likewise, it is impractical and potentially impossible to quantify it within a design. The accuracy of a given part or assembly is also a function of the money spent on the machining and GD&T processes. For an investigation with a limited budget and at early TRL stages, it was not possible or practical to specify tighter tolerances across all components to achieve a more perfectly reliable mechanical control of the sensor positioning.

As the iterative design process progressed, I focused on applying the following principles to my design process with the aim of reducing the inaccuracies as far as practically possible.

- Using simple geometry and preferencing high-accuracy manufacturing processes
- Designing components to self-align rather than depending on accurate assembly
- Using accurate fixed jigs to position the angle wedge sensors
- Use guides to align the test platform to the primary stress axis

5.6.2 DAQ sample rate

An error that cannot be addressed using the OpMux DAQ system is the time resolution. Sampling at 250MHz results in a 2% and 4.4% error for birefringence and angled wedge measurements respectively.

Chapter 6

Time of Flight extraction methodology

This chapter describes in detail the issues with the original data processing software, the process undertaken in an attempt to optimise the ToF extraction code and improve the variance and reliability of the novel angled wedge measurement.

I undertook a detailed investigation into the ToF extraction software, visualising and assessing all the intermediate variables for inconsistencies and trends.

I implemented three separate methods for extracting ultrasonic ToF, and compared the results. The measured stress values and trends changed significantly depending on which method was used.

Also presented are the impacts of those changes, some conclusions on the effectiveness and limitations of the final algorithm, and considerations of the limitations of the DAQ system and the inherent trade-off challenge that this measurement presents for signal quality.

6.1 Original software - features and issues

The Matlab module for extracting ToF from a .tdms file (the native data file format in LabVIEW, the program used to control the DAQ) was provided by Dr Gary Nicholas. In it's first iteration, ToF values were determined by a peak-find algorithm, applied to a windowed section of the correlation values - the results of applying the cross-correlation analysis between the reference and second and third reflections.

By the time of conducting the high-stress testing, I had exhausted all the reasonable physical and experimental design improvements aimed at improving the reliability and repeatability of the measurement, yet the experimental results had not achieved the required repeatability or accuracy. In fact, the high-stress test results, processed with the existing software, showed features that had not been shown in the data for earlier experiments that were processed by Dr Gary Nicholas; large jumps in ToF values between load steps and outlier data that had not been evident earlier.

6.2 Initial results

When applying the v4 code, used to process the results shown in previous rounds of experimentation, to the high stress results, the outputs were dramatically inconsistent. Figure 6.1 shows a plot of 55-degree ToF vs 35-degree ToF (top left), plots of 35- and 55-degree ToF vs applied stress (top right & bottom left) and the measured vs applied stress (bottom right).

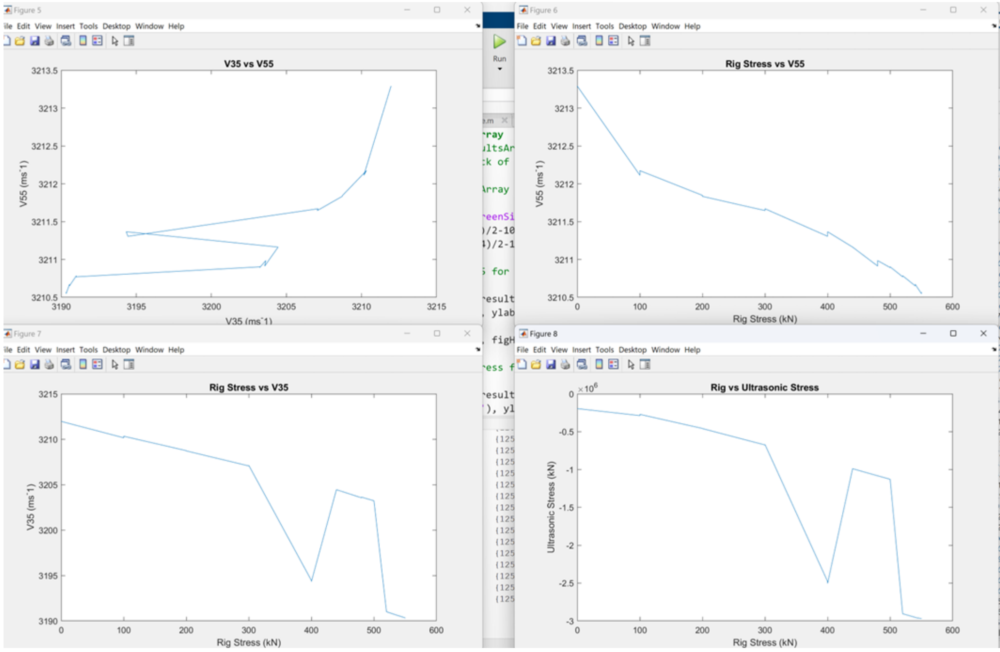

Figure 6.1: A screenshot of 4 charts showing the output from the v4 ToF processing code. Top left: 35-degree vs 55-degree ToF, Top Right/Bottom Left: Ultrasonic SoS for 55- and 35-degree angled wedge sensors vs applied tensile stress. Bottom right: predicted vs applied stress.

The expectation in each of the plots would be a linear relationship; this is clearly not the case. Large jumps in ToF are seen between different load steps, resulting in large jumps in calculated stress. The trend is also in the incorrect direction for a tensile test.

To debug the code, I began extracting each intermediate variable, restructuring the data processing and visualising each variable across the loading steps in an attempt to correct the issues.

6.3 Investigation and improvement

6.3.1 Interpolation

The supplied code (v4) used linear interpolation after data capture. On a nonlinear signal, however, linear interpolation does little to improve ToF analysis, it merely adds more data points to the straight lines between non-interpolated data. Using spline interpolation completes the curves at peaks and troughs that are otherwise eliminated by digitization, adding an approximation of the lost data points. The re-created peak achieves a closer approximation to the actual ToF than either of the nearest captured data points or any interpolated point between them. Figure 6.2 shows a peak from the ultrasonic signal before interpolation, and after linear and spline interpolation, showing the recreation of the peak location eliminated by digitisation.

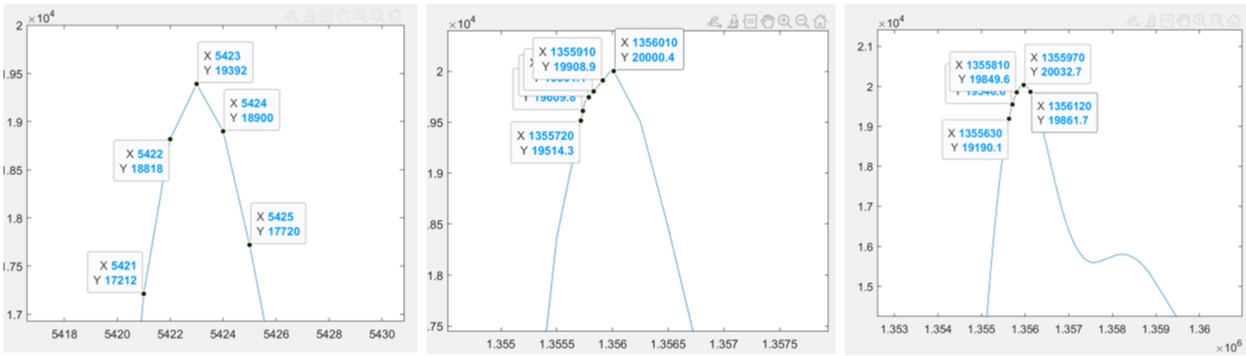

Figure 6.2: A zoomed-in peak from the ultrasonic signal before interpolation (left), after linear interpolation (middle) and after spline interpolation (right)

6.3.2 Signal change

An ideal signal for most accurate cross correlation results would be one in which the reference and target signals had near-identical wave-forms. This is not the case with the signals from the angled wedge sensors. A comparison of reference and second reflection (target) signals is shown in 6.3

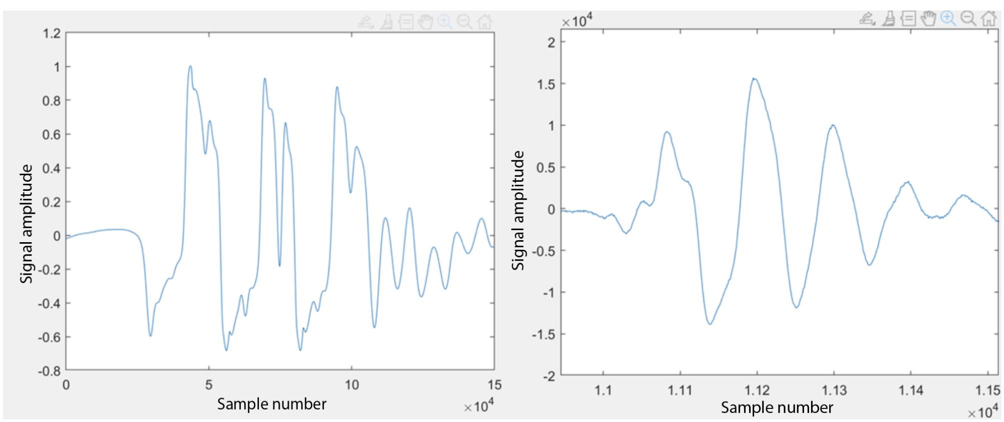

Figure 6.3: A screenshot of the digital oscilloscope outputs, comparing the shape of the wave-forms of reference signals for 55-degree sensor (LHS) and 35-degree sensor (RHS), captured at 500MHz

This quality of an ultrasonic waveform is a function of how well executed the process of sensor assembly instrumentation is carried out, combined with the complexity of the wave path and any interference modes. The angled wedge sensors have complex geometry, that could account for the difference in signal shape, and this difference will certainly be negatively affecting the accuracy of the cross-correlation results. Numerous instrumentations have been completed on the angled wedge sensors, and these signals represent the best from a batch of attempts. I believe that improvements in manufacturing processes could certainly yield better results but these have not been feasible in the lab.

6.3.3 Cross-correlation performance evaluation

I created plotting modules for each variable to visually inspect the changes throughout the load cycle. Figure 6.4 shows the evolution of the raw reference signals for an increasing load-ramp test from 0 to 540kN. The green and red colour maps show waves traveling in opposite directions through the specimen.

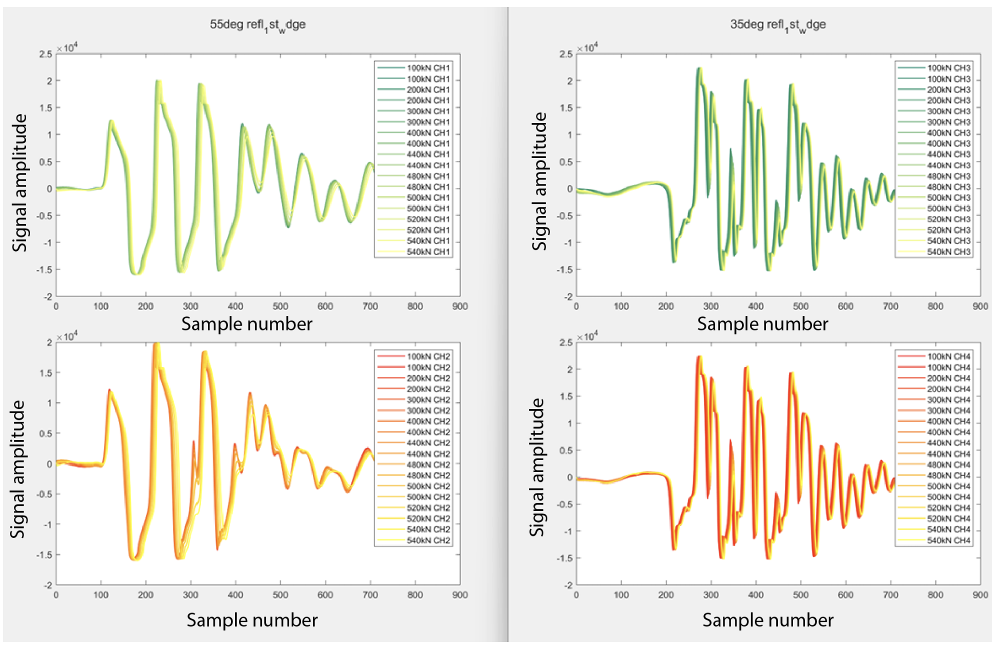

Figure 6.4: Evolution of reference signal a-scans throughout loading ramp. Greens and Reds represent waves travelling in opposite directions through the specimen

Although the changes are too small to see accurately on the above plot, or to assess any inaccuracies in signal or data processing method, they acted as a first sense check. It is clear that there is progressive change from beginning to end of the load ramp. The signals also progress along the x (time) axis as load increases. The similar statement can be made for the plotting of the correlation values. Figure 6.5 shows the evolution of the correlation values window from the reference signals over the load cycle, separated by direction of travel through the specimen, CH1 and CH3, and CH2 and CH4 are pairs of identical directions, CH1 & 2 being 55-degree, and CH3 & 4 35-degree angles.

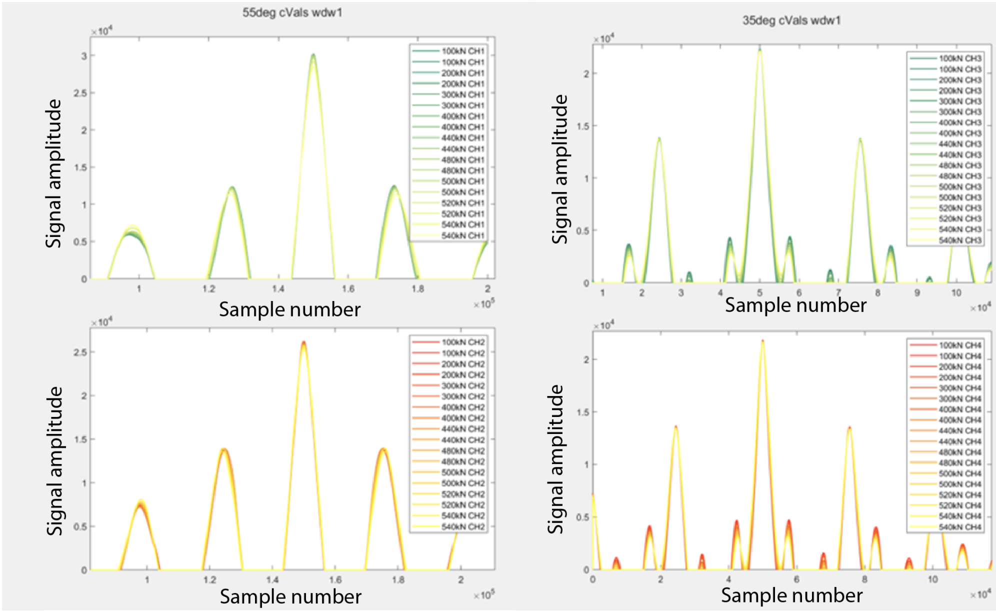

Figure 6.5: Evolution of reference signal correlation values throughout loading cycle. Greens and Reds represent waves travelling in opposite directions through the specimen

As expected, there is a clear, single, highest peak that does not travel along the x-axis as the applied load is changed. The form is similar between both directions for both angles, however the maximum amplitude of the 55-degree CH2 direction is lower than its counterpart.

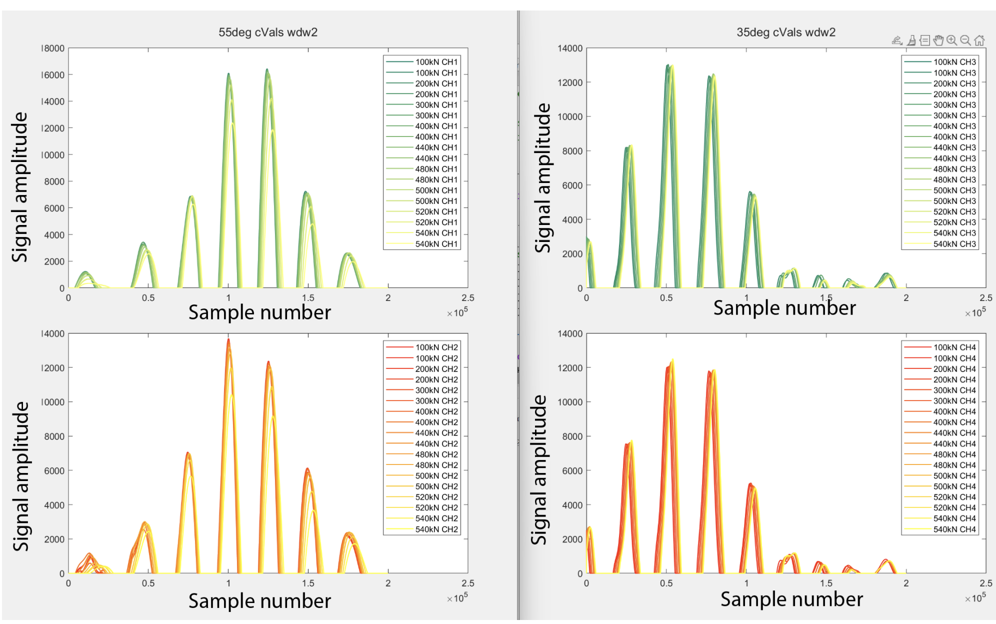

Figure 6.6: Evolution of second reflection signal correlation values throughout loading cycle. Greens and Reds represent waves travelling in opposite directions through the specimen

Figure 6.6 shows the evolution of the second reflection correlation values. In contrast to the reference signal, these plots show a pair of competing peaks at the center as well as the expected movement in time as the applied load is increased. It also shows that the window has not been set correctly as a portion of the signal used for cross-correlation is missing from the 35-degree plot. The relevant limits were updated in the software to correct this.

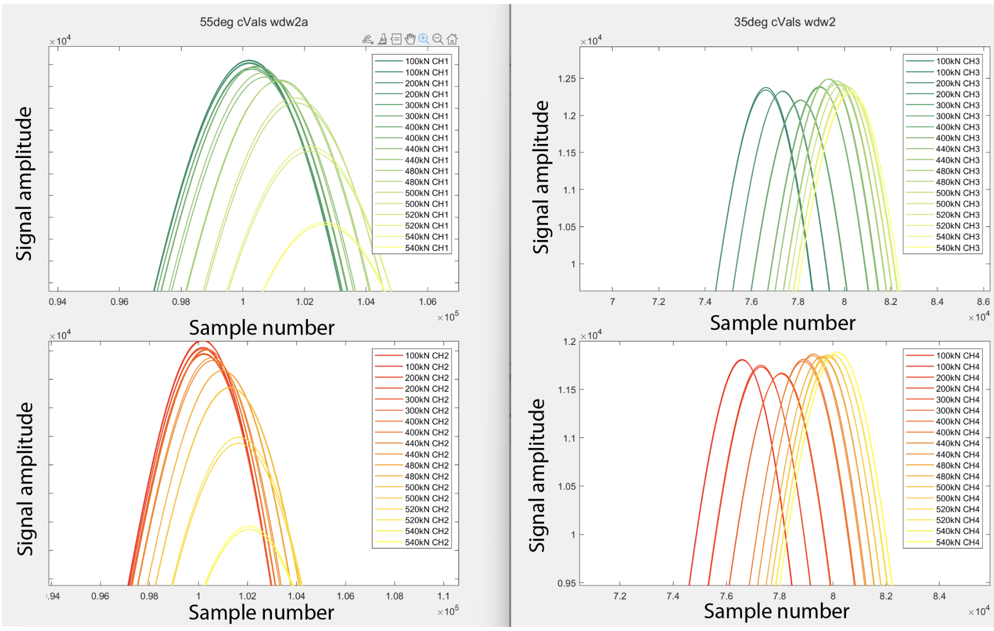

Figure 6.7: Zoomed-in view - Evolution of second reflection signal correlation values throughout loading cycle. Greens and Reds represent waves travelling in opposite directions through the specimen

Figure 6.7 shows a zoomed-in view of the first of the two highest peaks for all 4 plots shown in Figure 6.6. The movement in time is clearer to see here, but also clear is a marked drop in amplitude for 55-degree correlations as load increases. An additional concern highlighted is the fact that, for 55-degree signals, the highest peak is different for CH1 and CH2.

Changing the color representation to differentiate between loading and unloading cycles, and limiting the plot series to only the datasets immediately either side of the highest load step gave the plot shown in Figure 6.8.

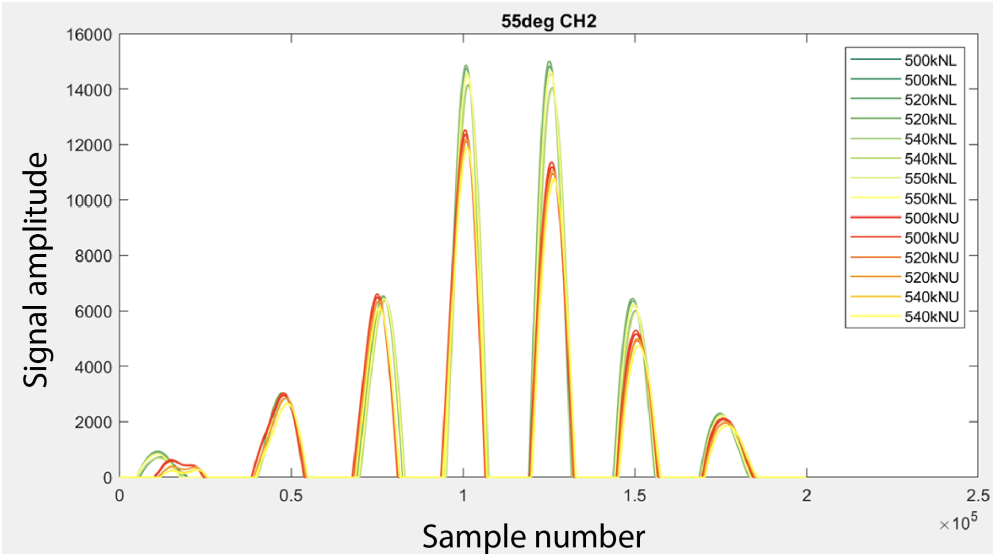

Figure 6.8: Evolution of second reflection signal correlation values throughout loading cycle. Greens and Reds represent waves travelling in opposite directions through the specimen

Figure 6.9 shows an enlarged view of the top of the highest peak for all 4 plots in the correlation values window shown in Figure 6.8. A distinct change in amplitude of the correlation as well as a change in the dominant correlation peak occurs between loading and unloading. This indicates that there is some change occurring in either the reference of second reflection waveform at this point in the experiment, moving the point of best correlation along the time domain axis, perhaps due to even very slight movement in the sensor clamping system when the rig changes loading direction.

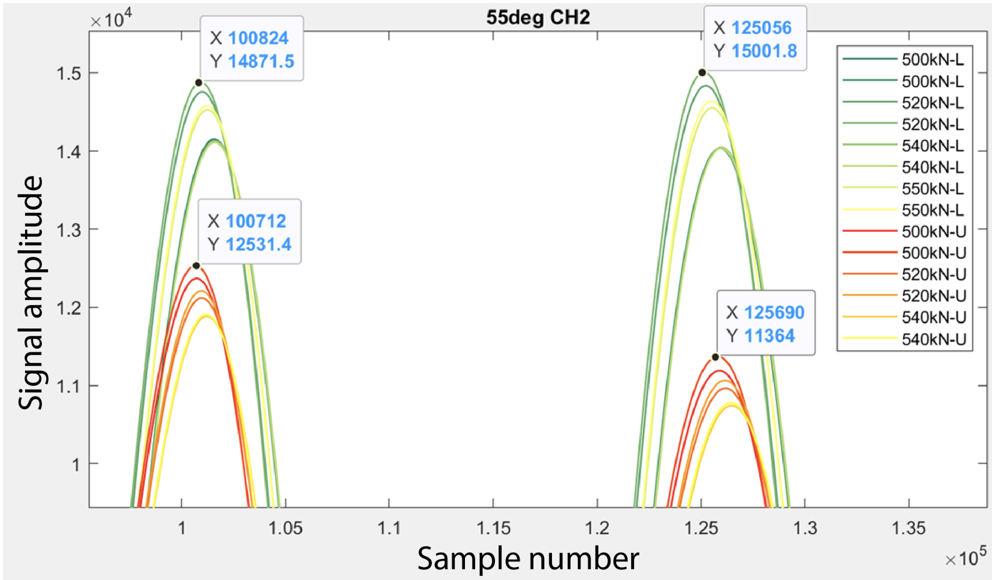

Figure 6.9: Close-up view: Evolution of second reflection signal correlation value peak throughout loading cycle. Loading cycle data shown in reds and unloading in greens

6.4 Initial improvements

The initial improvements to the processing code iterated the software version from V4 to V10.

To diagnose the problems with the software I inspected each line of code, extracting and plotting the intermediate variables for a small subset of data. This enabled me to visually inspect each step and identify errors. To compare each code adjustment and track the changes, I up-issued the software version. Useful/successful changes included:

- Change interpolation from linear to spline
- Correct the timestep values for selecting the correct window of the ultrasonic signal
- Remove a secondary windowing operation that over-constrained the algorithm, effectively pre-determining the ToF instead of reporting the actual value
- Interpolation and re-sampling after the windowing operation to reduce memory use and software cycle time

Some software versions did not help diagnose or improve the code. Software version 10 was the most reliable and was chosen as a comparative with the supplied version 4.

Figures 6.10 & 6.11 show the plots of ToF vs applied stress for one three sets of data processed with the original V4 and V10 software versions respectively.

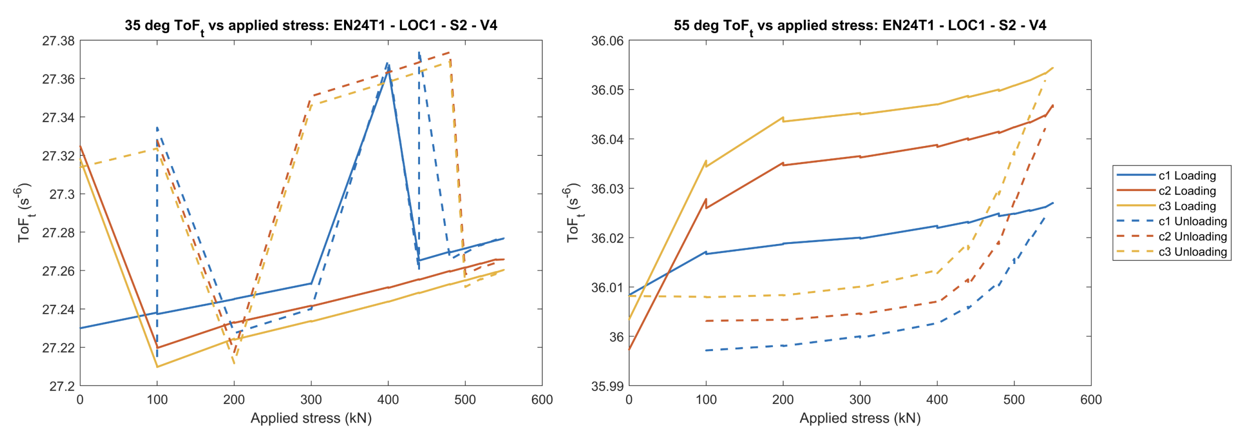

Figure 6.10: A plot of ToF vs applied stress for 3 loading cycles for 35-degree signals (Left) and 55-degree signals (Right) - software V4

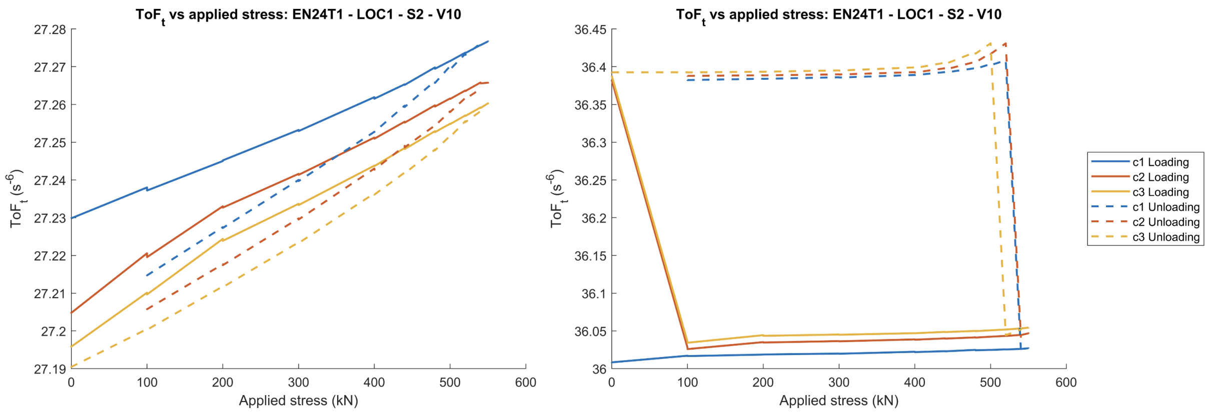

Figure 6.11: A plot of ToF vs applied stress calculated with a weighted average ToF extraction model, for 3 loading cycles for 35-degree signals (Left) and 55-degree signals (Right) - software V10

By tweaking the existing code, improving the windowing and peak detection, the large jumps in ToF between loading steps for the EN24T Location 1 data were eliminated, greatly improving the variance of the data. On changing the code to select the highest peak within the correlation value window, however, the jump in ToF for the 55-degree signals increased dramatically between loading and unloading ramps. This is due to a change in waveform, changing the dominant peak identified in Figure 6.9. Also evident is a precession away from the origin over subsequent loading cycles. This could result from the thinning of the couplant layer and the specimen is stretched and released, creating a small, but not negligible, movement relative to the sensor assemblies.

Figures 6.12 & 6.13 show the plots of predicted stress vs applied stress for three sets of data processed with the V4 and V10 software respectively.

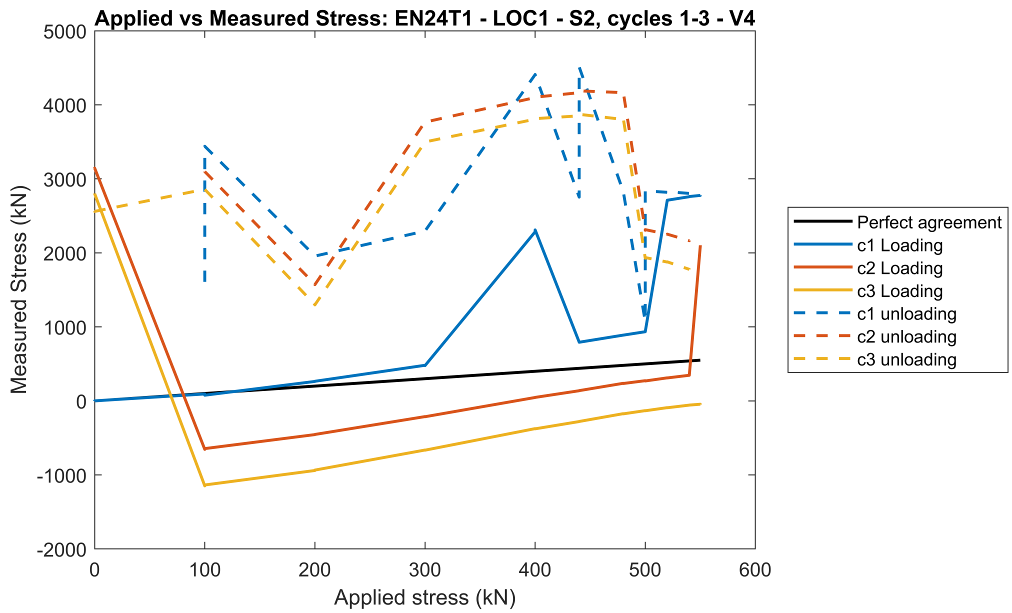

Figure 6.12: A plot of ultrasonically predicted stress vs applied stress for 3 loading cycles - software V4 - EN24T, Location 1, Set 2

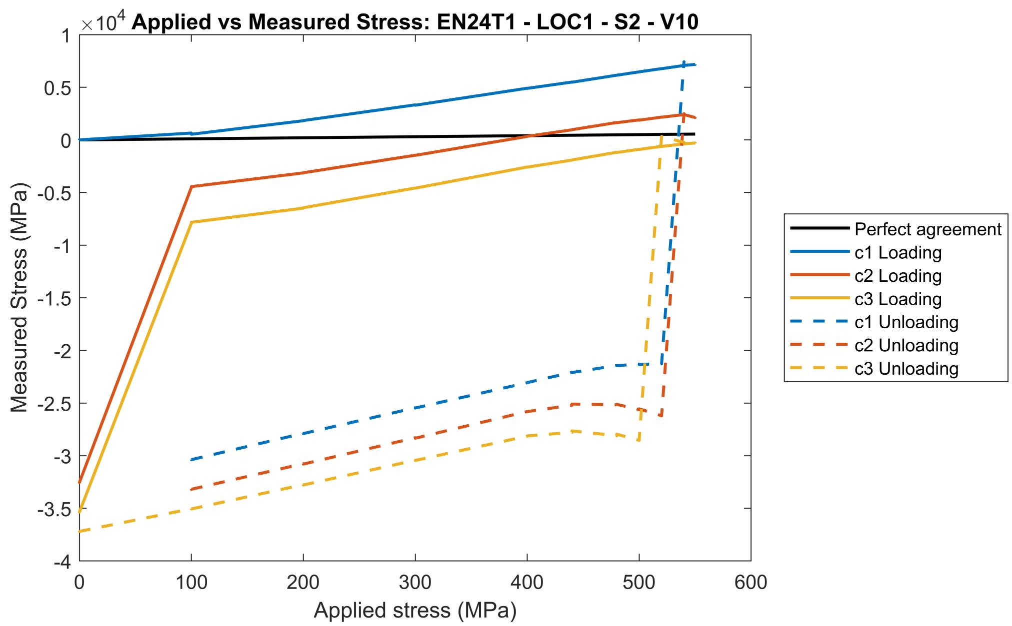

Figure 6.13: A plot of ToF vs applied stress calculated with a weighted average ToF extraction model, for 3 loading cycles - software V10

The identification and selection of the correct peaks has eliminated the sharp jumps in stress prediction between load steps, however, the precession away from the initial zero-point and the disparity between loading and unloading cycles remains. The results also exhibit a large jumps

6.5 Alternative ToF algorithms

The selection of the highest peak within the arrival time window of correlation values caused the algorithm to return highly variable stress predictions. These were, in no small part, due to changes in the waveform between loading and unloading steps - with changes in shape came changes in the position of the correlation value maxima.

Faced with such variance in the data sets, including unexpected variability in the locations in the time domain of the maximum correlation values, I investigated the impact of using two alternative methods for extracting the ToF.

In ultrasonic signal analysis, it is common custom and practice to use a Hilbert transform analyse ultrasonic signals as it allows a clear representation of both the instantaneous frequency and amplitude of a signal [103]. This transform provides a robust signal envelope with a single maximum which addresses the challenges of determining the peak signal energy from an original time-amplitude plot containing high-frequency oscillations within a small time window of interest.

With the location of the highest correlation peak fluctuating along the time axis, I also attempted a weighted average model. The weighted average had the potential to better approximate the arrival time of the wave energy by solving for the combined function of amplitude and time-step of the entire window of the signal rather than relying on a single data point from a location of highest amplitude.

6.5.1 Weighted average

Figure 6.14 plots the ToF extracted using the Hilbert Envelope against applied stress for 55- and 35-degree signals.

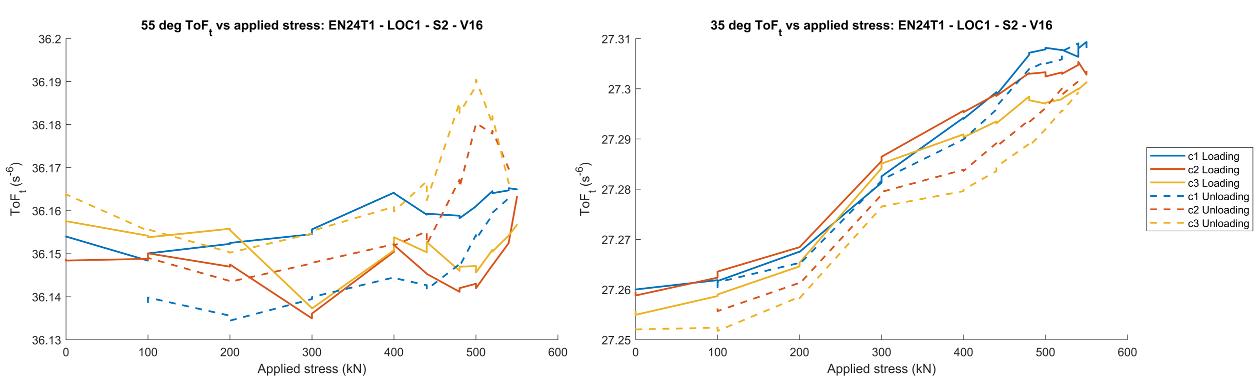

Figure 6.14: A plot of ToF vs applied stress calculated with a weighted average ToF extraction model, for 3 loading cycles for 55-degree signals (Left) and 35-degree signals (Right) - software V16

The variance increased relative to the peak-find approach, but the results show less precession from the start point over subsequent load cycles. Again, the 35-degree ToF data show better linearity and lower variance.

Figure 6.15 shows the subsequent measured stress against the applied stress for the same data.

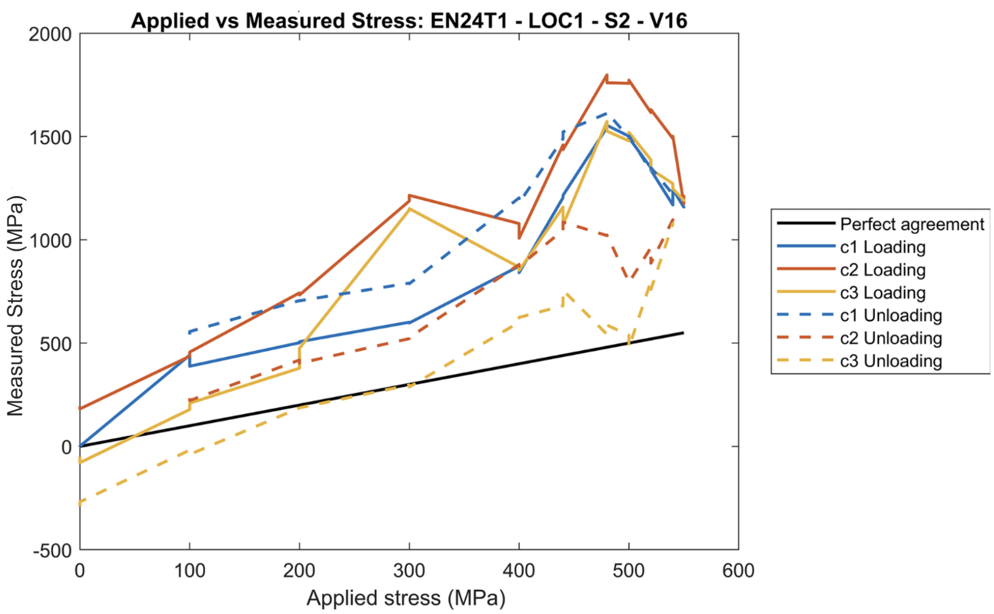

Figure 6.15: A plot of Measured vs applied stress calculated with a weighted average ToF extraction model, for 3 loading cycles - software V16

6.5.1.1 Envelope

Figure 6.16 shows the ToF values for 55- and 35-degree signals vs applied stress.

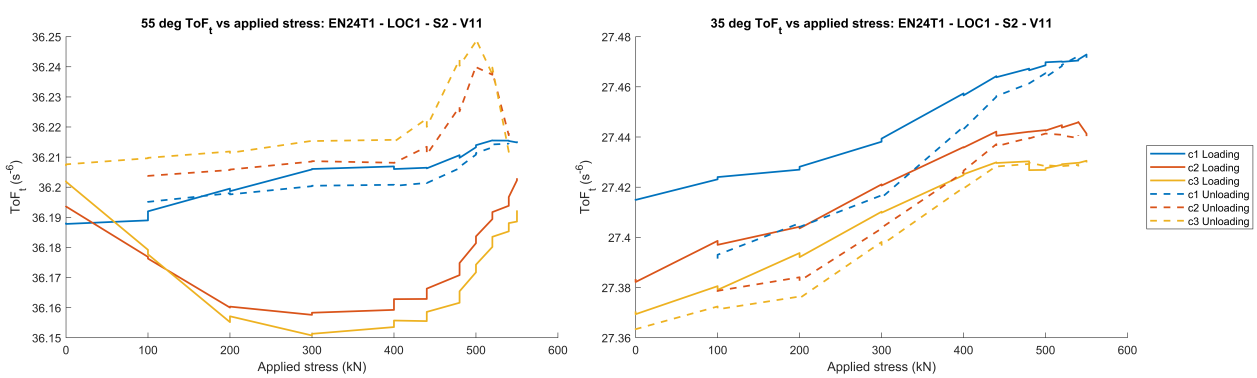

Figure 6.16: A plot of ToF vs applied stress calculated with an envelope ToF extraction model, for 3 loading cycles for 55-degree signals (Left) and 35-degree signals (Right) - software V16

The 35-degree signals show very similar behaviours to the peak-find methods used previously, with slightly higher variance and similar precession from initial values. The 55-degree data, however, differs dramatically, with the first loading cycle behaving somewhat as expected, but subsequent cycles delivering loading data that bears no relation to the first cycle. Unloading data, however, does somewhat map the expected trend, notwithstanding the large jumps at higher loads.

The stress prediction results for the envelope model are shown in Figure 6.17.

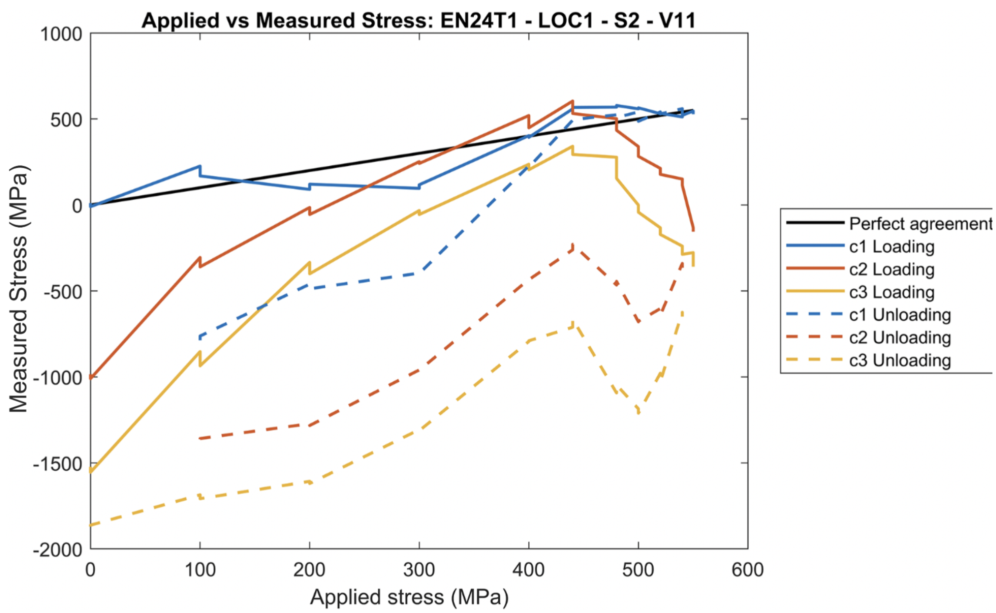

Figure 6.17: A plot of ToF vs applied stress calculated with an envelope ToF extraction model, for 3 loading cycles - software V16

The measured stress results for the envelope model are influenced by the deviations in the 55-degree ToF data. The first loading cycles follows the perfect agreement line relatively well. Subsequent loading cycles have significant deviations at low and high applied stress values.

6.5.1.2 Cross-correlation maxima

In the hope that the recurrent issues were resulting from errors in the data processing code, I plotted the amplitude and sample number for the correlation value maxima to visualise the locations of the maxima as selected by the algorithms.

Figures 6.18, 6.19 & 6.20 plot the increasing load-ramp data in the green colour map, with unloading data in reds. All three plots show a perfect correlation (as expected) for the 35 degree reference signal (top-right). A signal, cross-correlating itself with itself and within an identical pre-defined sample window, should correlate exactly in the centre of the window with no variation in the time domain. The 55-degree data (top left panels) show three distinct locations in the time domain for maximum correlation, varying apparently at random throughout the loading cycles.

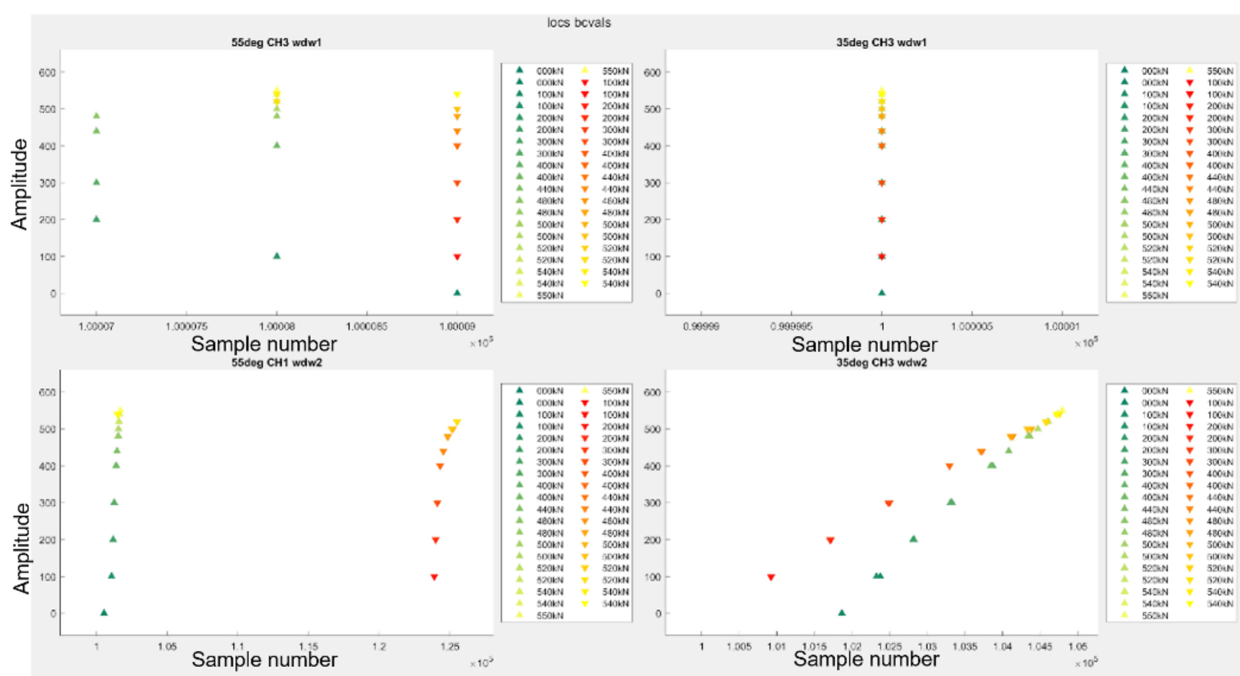

Figure 6.18: Plots of sample number vs. normalised amplitude of the points of maximum correlation for a single load-cycle, extracted using a peak-find ToF algorithm - software V10. Top Left: 55-degree reference signal, Top Right: 35-degree reference signal, Bottom Left: 55-degree reflection signal, Bottom Right: 35-degree reflection signal

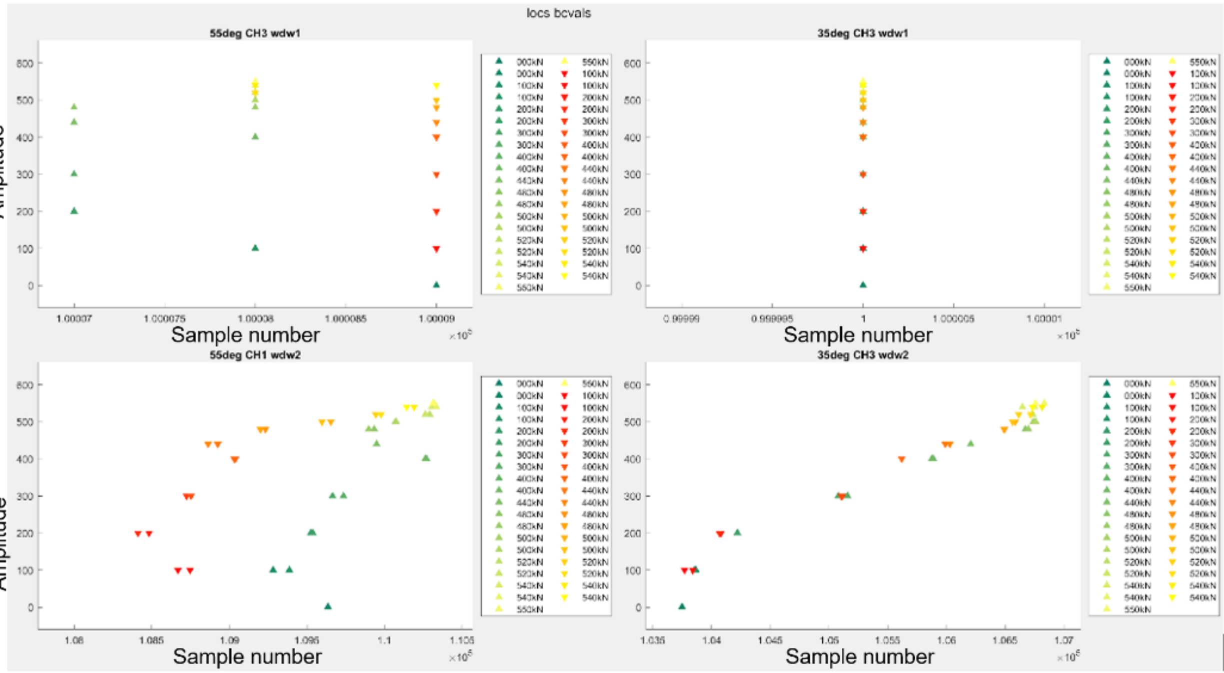

Figure 6.19: Plots of sample number vs. normalised amplitude of the points of maximum correlation for a single load-cycle, extracted using a Weighted Average ToF algorithm - software V16. Top Left: 55-degree reference signal, Top Right: 35-degree reference signal, Bottom Left: 55-degree reflection signal, Bottom Right: 35-degree reflection signal

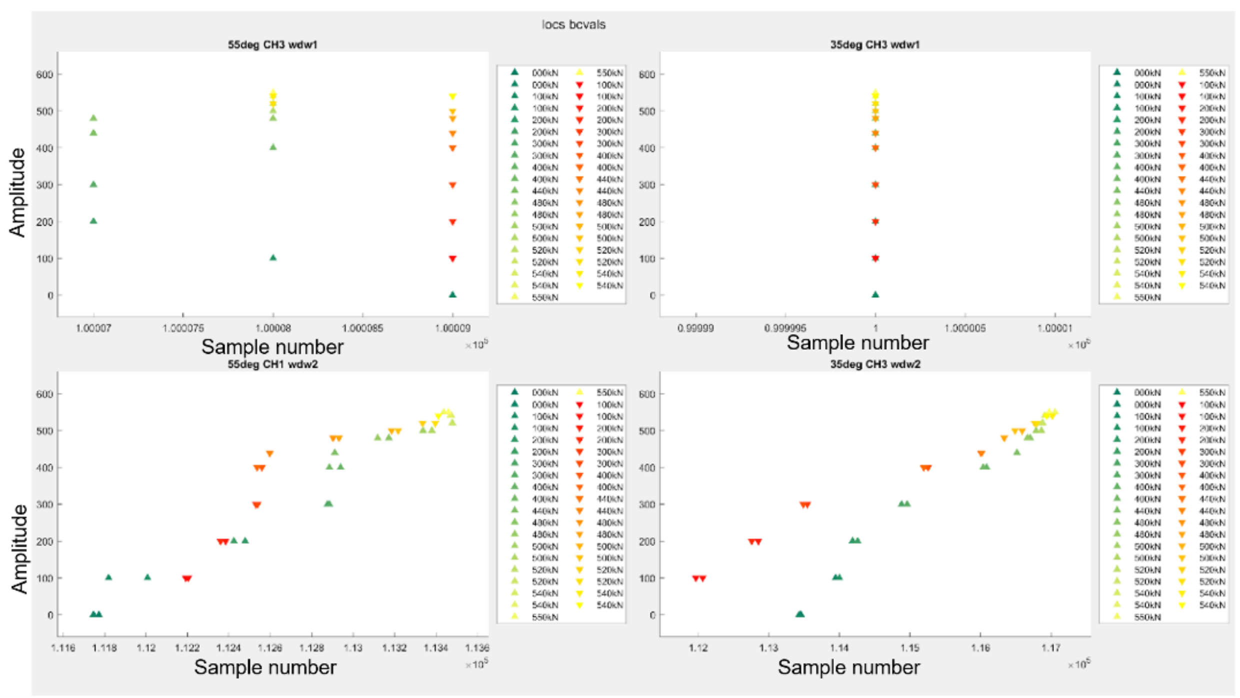

Figure 6.20: Plots of sample number vs. normalised amplitude of the points of maximum correlation for a single load-cycle, extracted using a Hilbert envelope ToF algorithm - software V11. Top Left: 55-degree reference signal, Top Right: 35-degree reference signal, Bottom Left: 55-degree reflection signal, Bottom Right: 35-degree reflection signal

The bottom-right panels from all three groups of plots show trends of varying linearity in the 35-degree second reflection correlation points (the expectation would be a perfectly linear relationship). Peak-find data (Figure 6.18) is most linear and has the least difference in slope between loading and unloading. The weighted average data (Figure 6.19) is less linear, but shows the best tracing between loading and unloading ramps. The envelope model (Figure 6.20) seems to fall in between the peak-find and weighted average in linearity, but a larger difference in loading and unloading ramps than the peak-find data.

The correlation maxima plots confirmed that while experimental issues wee likely at play in the divergence and hysteresis patterns in ToF values over multiple loading cycles, the issues with the variance of ToF measurements, particularly the 55-degree data, lay within the captured ultrasonic data itself.

6.5.2 The irony of 20-20 hindsight

It is common practice to improve accuracy in ultrasonic ToF measurements by using several peaks and taking a mean of the ToFs as this normally reduces random and DAQ resolution errors. I therefore prioritised using a higher voltage input to enable the capture of a second reflection. As the project continued, there was a slow degradation of signal quality from the angled wedge sensor assemblies. This also necessitated using the highest possible voltage. At this (very late) stage in the data analysis, however, it occurred that the clear, high-amplitude, but somewhat irregular wave-forms shown in the reference signals (Figure 6.21) could be the result of the non-linear clipping within the OpMUX multiplexer used to receive the ultrasonic signals.

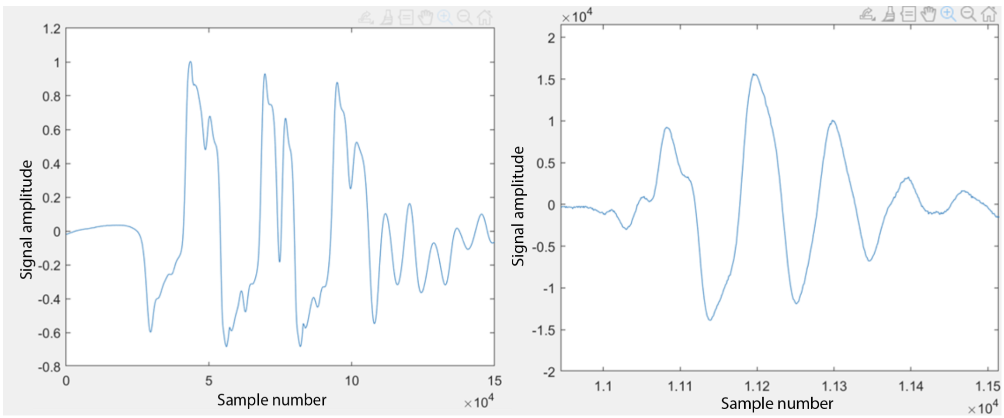

Figure 6.21: A screenshot of the digital oscilloscope outputs, comparing the shaope of the waver-forms of reference signals for 55-degree sensor (LHS) and 35-degree sensor (RHS)

This could also explain the non-linear decrease in amplitude between reference and second reflection, and the second and third reflections shown in Figure 6.22.

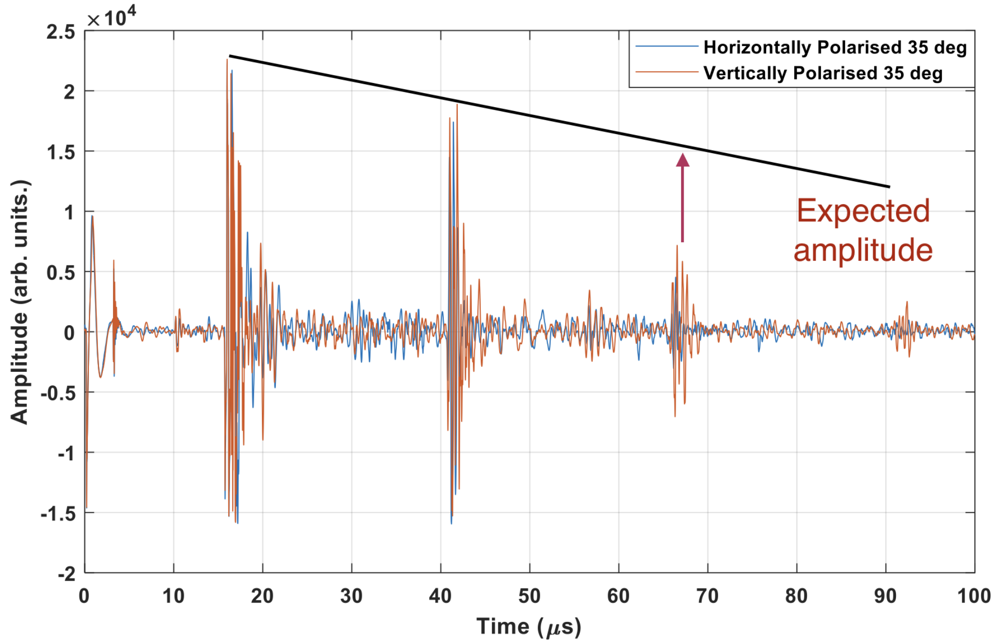

Figure 6.22: A screenshot of the digital oscilloscope output showing the non-linear amplitude drop in the ascan between first (reference), second and third reflections

Ironically, since the deterioration of the sensor assemblies rendered the SNR of the third reflection signals too low to confidently use (in some cases they disappeared altogether), the very step aimed at improving accuracy may have undermined it. If the signal were being clipped, particularly in a non-linear fashion, it would cause changes to the reference waveform, rendering the use of cross-correlation as a ToF extraction method invalid.

With the raw ultrasonic data as it currently stands, it may not even be possible to use a zero-crossing approach, as the combination of low SNR of the leading edge of the second and entire third reflections, the multiple peaks of similar amplitude in the reference (and some second reflections) and the change in dominant correlation peaks due to changing from loading to unloading would make it challenging to apply appropriate threshold values for a zero-crossing algorithm that would prove robust across an entire dataset.

6.5.3 Data acquisition system limitations

There are several features of the DAQ system that are potential limiting factors and causes of the variance and lack of repeatability of the measurement.

Sample rate: The confluence of a similar error magnitude to that implied by the daq time resolution.

Voltage overhead: The DAQ system could not handle high enough voltage to get multiple reflections without clipping - needs a bigger overhead.

Noise floor: The high signal noise floor makes use of smaller third reflection signals difficult.

6.5.4 Physical limitations

There are several physical limitations imposed by the technical design brief that contribute to the issues seen in the results, and therefore present data processing challenges.

Small sensor assembly size: Challenging to get multiple reflections.

Precession of ToF values: These changes are likely due to the thinning of the couplant, resulting from the slight relative motion of the specimen to the sensor assemblies while undergoing multiple loading cycles.

Changes in signal shape: Changes are evident in the signal shape as the experiment transitions from loading to unloading - not an issue in the field, but makes laboratory validation difficult.

Complex sensor geometry: Sensor assembly geometry is complex. This causes signal noise and makes it hard to extract the ToF from the third reflection.

6.5.5 Impact of ToF extraction algorithm selection

Notwithstanding the challenges above, the model used for identifying the ToF peak has a large effect on the predictions from the angled wedge measurement. Each of the methods uses the same model to extract the reference window correlation values for two reasons:

1. The zero or negligible variation (relative to the ToF of interest) in the reference correlation location across the different loading steps shown by the exiting algorithm indicates reliable identification of the reference signal in the time domain.

2. When the cross-correlation algorithm makes the comparison of an identical reference and target signal, the match is perfect and any additional processing is likely to reduce accuracy.

The differences are most evident in the extraction of the arrival time of the second reflection, here the choice of algorithm produces very different results from the same data.

The Peak-find model shows the least variance but also displays the largest jumps between loading and unloading. This, I suspect, is a result of imperfect signal generation and recognition. The DAQ sample rate would impact the 35- more than the 55- degree signals (due to the longer 55-degree flight time); this investigation has not shown conclusively that the sample acquisition rate is the primary failure mode for the angled wedge measurement.

The weighted average model shows significantly higher variance in ToF than the peak-find model, with the 55-degree varying significantly more than the 35-degree signals. The predicted stress plots share a very similar shape across the sets (EN24T), the unloading curves do not jump dramatically away from the loading curves, and predicted stress data oscillates on both sides of the perfect agreement line rather than deviating away in one direction.

Results from the envelope model show less variance that the weighted average for sets 2 and 3, though set 4 has huge jumps for ToF and predicted stress. The 55-degree ToF deviation from the expected linear trend seems repeatable for the second and third loading cycles on sets 2 and 3. Deviations are similar to the weighted average, oscillating both sides of the prefect agreement line for sets 2 and 3, though the results show very large decreases in predicted stress in later cycles and sets.

Chapter 7

Birefringence results

Results from multiple iterations of birefringence testing are summarised here, with an extended analysis for the most recent data set.

The birefringence results from test platform iterations 1, 3 & 4, along with sensor assemblies 1 & 4 have formed the basis for Dr Yue Yang's PhD thesis [84]. This author, having conducted most of the original data processing and the original analysis (for submission to our funding partners), and a significant portion of the testing and data capture for that work, includes a summary of this work as a backdrop to the work documented in this thesis. This author conducted a large proportion of the testing and data capture for all the subsequent work. While the data plotting was conducted by Dr Gary Nicholas, this author presents his own analysis and conclusion in this thesis.

Testing conducted on platforms 1 & 2 was conducted outside the time-frame of this thesis and were preliminary in nature. The results have therefore been excluded from this thesis.

7.1 Initial laboratory testing

This section describes the evolution of the initial laboratory testing phases, covering experiments conducted with both EN24T and R260 tensile specimens, across two different test platforms.

EN24T was selected as a readily available, high quality and consistent material with similar strength properties and sufficiently similar chemical composition to R260 rail material. Table 7.1 compares the chemical composition for both materials, Table 7.2 compares their material properties.

Table 7.1: A comparison of the chemical composition of test specimens

Material	Content of chemical elements, %									
	C	Si	Mn	S	P	Cr	Mo	Ni	Al	V
EN24T	0.36 - 0.44	0.10 - 0.35	0.45 - 0.70	0.04 max	0.035 max	1.00 - 1.40	0.20 - 0.35	1.30 - 1.70	-	-
R260	0.74	0.31	1.08	0.0018	0.013	0.04	-	-	0.03	0.04

Table 7.2: A comparison of the material properties of test specimens

Material	R_m	R_{pe}
EN24T	850 - 1000	680
R260	923	528

Figure 7.1 shows the dimensions of the test specimens used in this phase. A hydraulic Mayes loading rig was used to apply load to the specimens. On paper, the maximum loading capacity of the rig was 100kN, though the rig did not perform to its maximum capacity and was limited to 60kN. The maximum tensile stress applied to the specimens was 162.5MPa. The test specification is detailed in Table 7.3.

Table 7.3: Test summary for platform 3

Rig	Specimen(s)	Locations	Sets	Stress Range
Mayes 100kN	EN24T	1	1	0 – 162.5MPa

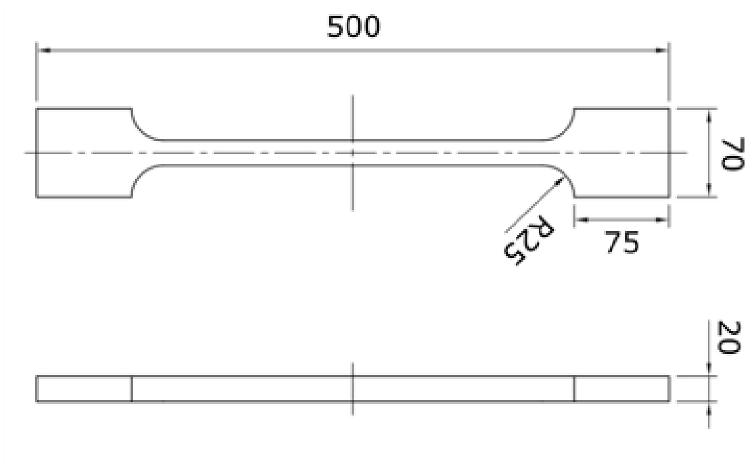

Figure 7.1: Dimensions of the initial tensile testing specimen

Both the results produced by, and the process of testing with, each test platform informed the improvements required and drive the design developments of the next.

7.1.1 Test platform 3 - prior work

Figure 7.2 shows the sensor platform set-up for this test.

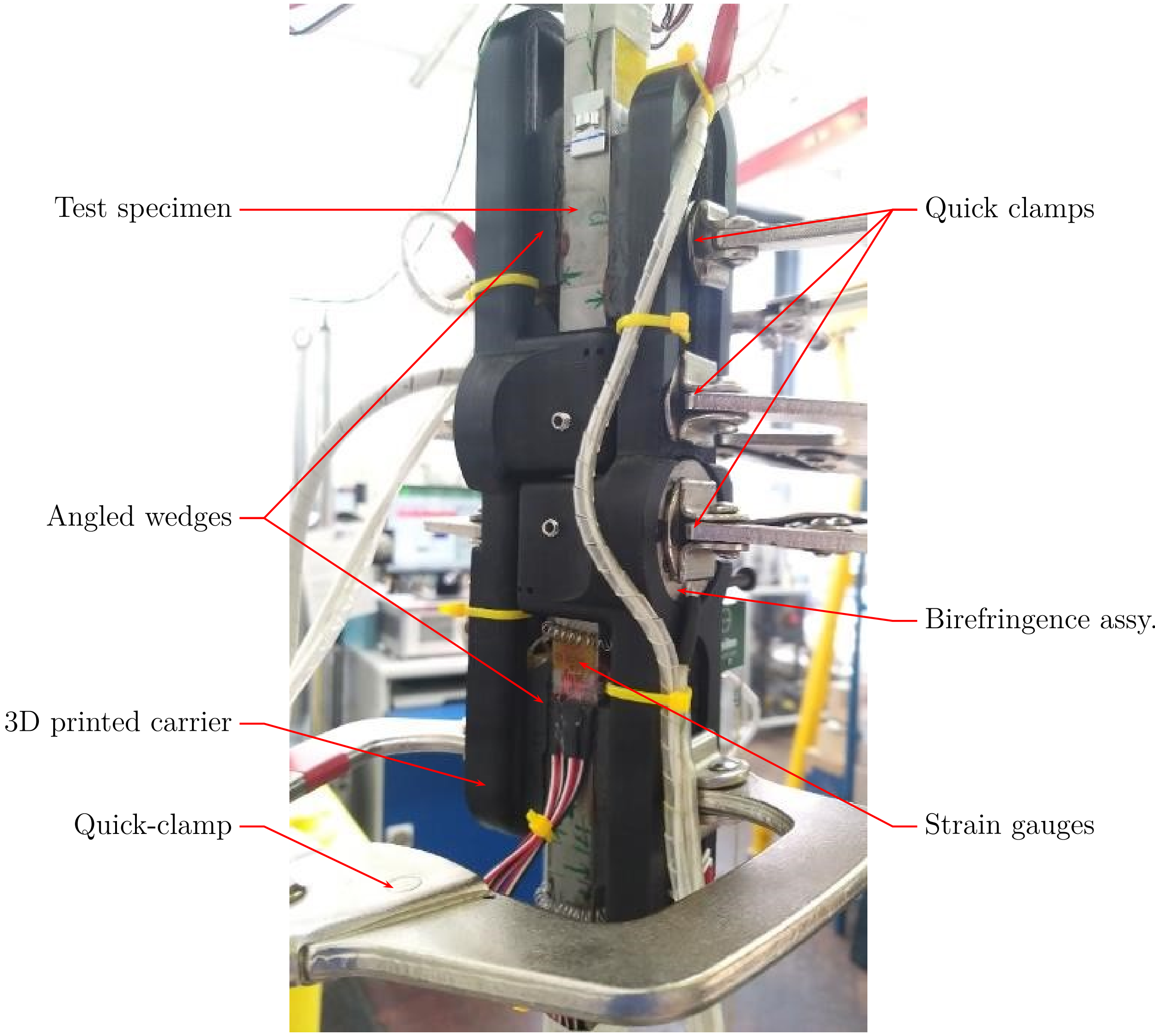

Figure 7.2: Image of the third test platform being used for tensile testing in a laboratory environment, showing the test specimen, 3D printed sensor carrier, quick clamps and strain gauges

Ultrasonic ToF measurements were calculated using a zero-crossing method described in subsection 3.3.1.2. Strain data was zeroed from the initial stress-free state. Stress was plotted against strain values (measured from bi-axial strain gauges installed in all 4 faces of the specimen), the incidence of the linear regression fit was used to correct the stress measurements. The ToF was plotted against the stress, and a regression fit incidence was used to correct for the zero-stress state (see subsection 3.3.1.1). The change in ToF from that initial measurement was calculated and plotted against the corrected measured strain over 6 experimental repeats. The ToF results are shown in Figure 7.3. The results show excellent repeatability.

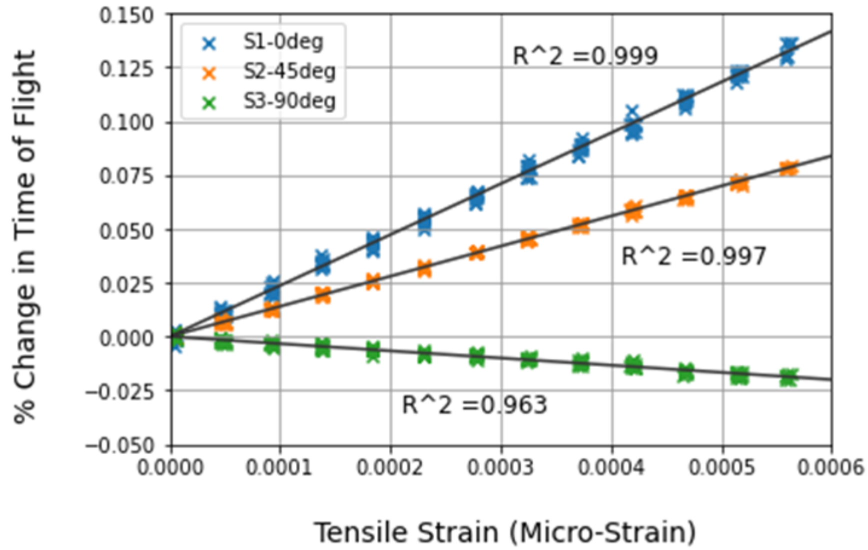

Figure 7.3: Percentage Change in ToF for shear waves polarized at different angles to the applied stress

Table 7.4 shows a comparison between the empirical values and measured values that were calculated from the birefringence experiments using test platform 3.

Table 7.4: Table of calculated Lamé parameters from ultrasonic ToF data using test platform 3 in comparison to converted empirical values [85].

	Lamé values (GPa)		Third-order elactic constants		
	λ	μ	λ_1	μ_1	η_1
Empirical	$112 \pm 2.3\%$	$80.8 \pm 2.3\%$	$0.537 \pm 45\%$	$-0.129 \pm 50\%$	$-2.45 \pm 2.5\%$
Platform 3	$109 \pm 0.3\%$	$79.6 \pm 0.3\%$	$0.776 \pm 24\%$	$0.297 \pm 8\%$	$-3.43 \pm 4\%$

The results show a much improved accuracy of the relevant material constants. However, the data showed a significant and variable 'zero-offset' (where the SoS for both orthogonally polarised shear waves were not identical at zero stress, as expected).

The variance in the offset was thought to be a function both of the experimental technique and manufacturing limitations, as well being believed to originate in some interaction with the material anisotropy. It was not thought that they originated from any errors within the modeling or scientific principles. With this small dataset, it was possible to manually extract the zero-offset at each stage and enter it into the data processing software between each set of results. This process somewhat mimics how a machine learning algorithm could be programmed to behave on a much larger dataset. This method improved the accuracy, determining the longitudinal stress accurate to 20MPa, equivalent to an NRT accuracy of

8.4°C in a tensile sample and 15.3°C in a section of full rail. The accuracy of the data without using this approach was much lower.

7.1.2 Test platform 4

Platform 4 was tested on the same tensile rig as platform 3. Table 7.5 shows the test details for the tensile test.

Table 7.5: Test summary for platform 4

Rig	Specimen(s)	Locations	Sets	Stress Range
Mayes 100kN	EN24T R260A R260B	2	3	0 – 162.5MPa

Figure 7.4 shows the dimensions of the tensile specimen.

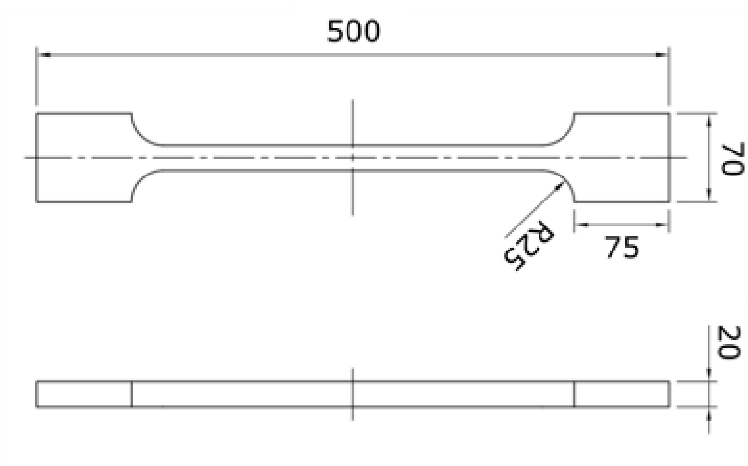

Figure 7.4: Dimensions of the initial tensile testing specimen

This section shows results from the entirely new improved version of test platform 4, seen in section 4.7.4.

Figures 7.5, 7.6 and 7.7 plot the ultrasonically calculated stress values against the applied tensile stress for all data sets for three tensile specimens, one manufactured from EN24T and two from R260 rail steel. The intercepts have been corrected for 'zero-offset' to best assess the performance of the measurement across the loading range. This would correspond to performing a zero-stress calibration measurement in a real-world scenario. Errors have been calculated and tabulated in Table 7.6.

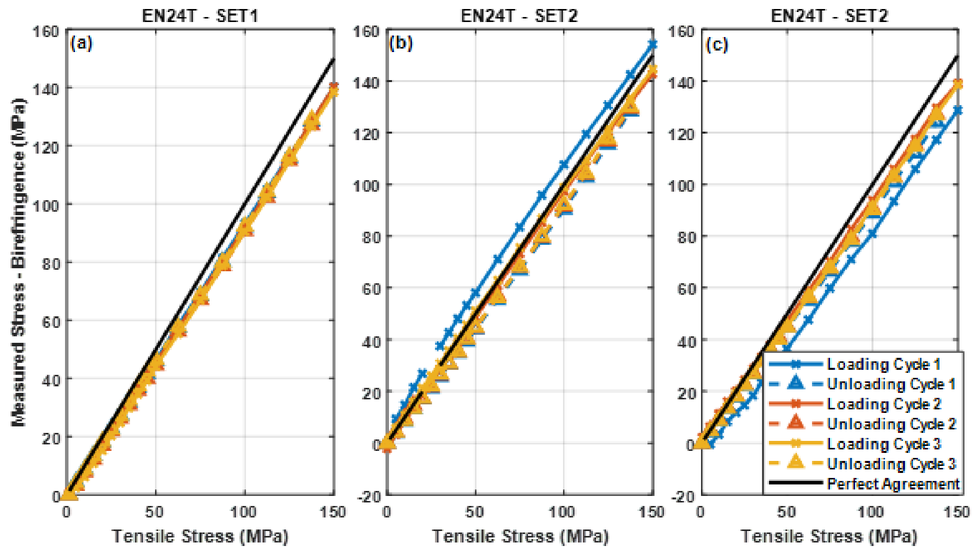

Figure 7.5: Plot of ultrasonically measured stress using birefringence vs applied rig stress, separated by set and loading/unloading cycle for measurements conducted on an EN24T specimen [Image credit: Gary Nicholas]

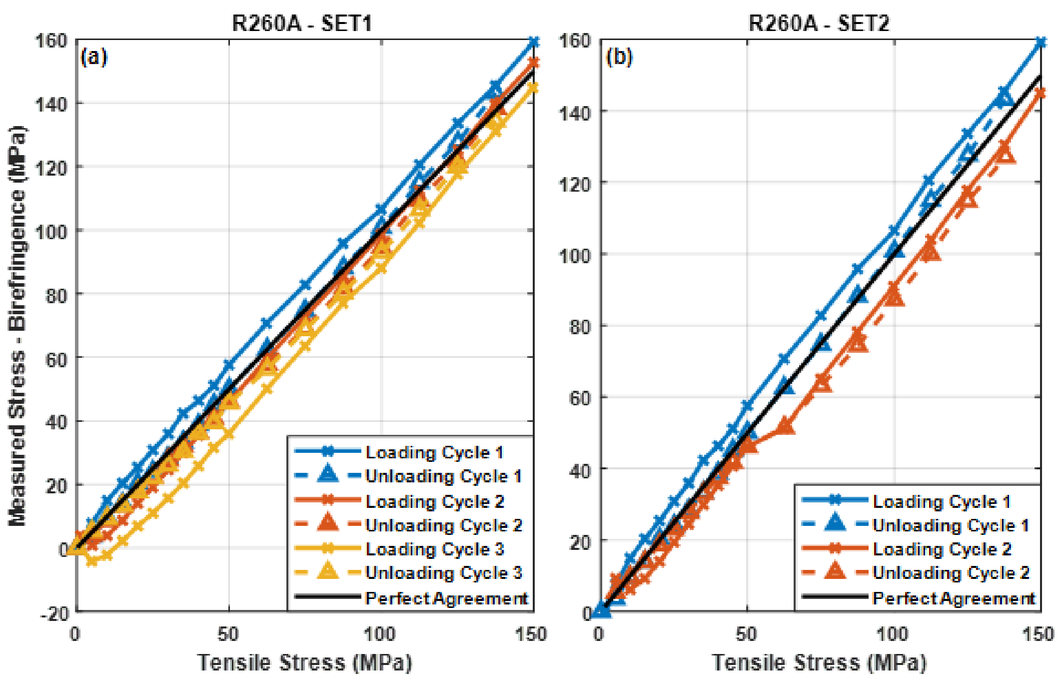

Figure 7.6: Plot of ultrasonically measured stress using birefringence vs applied rig stress, separated by set and loading/unloading cycle for measurements conducted on specimen R260A [Image credit: Gary Nicholas]

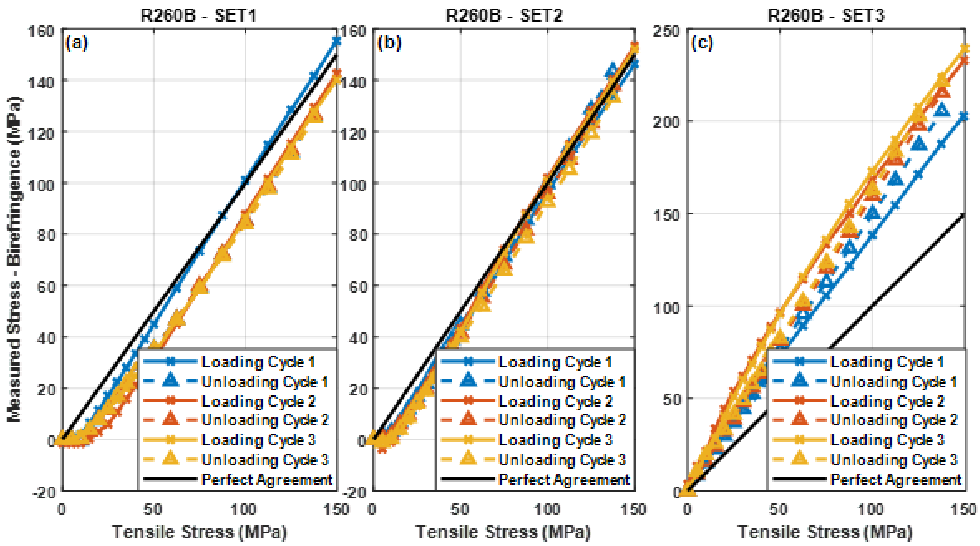

Figure 7.7: Plot of ultrasonically measured stress using birefringence vs applied rig stress, separated by set and loading/unloading cycle for measurements conducted on specimen R260B [Image credit: Gary Nicholas]

The gradients of the measured stress values are dependent on the values of the acoustoelastic constant (C_{brfg}). Many of the plots show a reasonable correlation with the line of perfect agreement, indicating a relatively consistent calculation of the acoustoelastic constant for the different materials.

It can be seen that the ultrasonically measured stress is highly non-linear in the lower stress ranges in Figure 7.7, and the third set shows a very large divergence from the applied tensile stress. This has not, however, led to an increased C_{brfg} error.

Table 7.6 shows the mean of the calculated errors for both the expected vs measured constant of birefringence and the that induced by the zero-offset for each test specimen from the tensile testing of test platform 4.

Table 7.6: Variation and errors for measured acoustoelastic constant and 'zero-offset' for birefringence testing of EN24T and R260 specimens

Specimen	C_{brfg}	σ_{offset} (MPa)	Error C_{brfg} (MPa)	Error σ_{offset} (MPa)	Cumulative max error (MPa)	Cumulative max error (°C)
EN42T	-1.146±7.78%	1524±165%	11.7	2506	2718	1058
R260-A	-1.197±36.8%	4141±0.42%	55.2	17.4	72.6	37.8
R260-B	-1.462±34.8%	91±774%	52.2	6897	6949	2919

These errors show that the zero-offset is by far the largest contributor to the overall error in stress measurement, and that the error from the relative velocities of the orthogonally polarised signals is consistent across both R260 rail specimens.

The acoustoelastic constant error is significantly lower in the data from the EN24T tests, though the error values are consistent across both R260 rail steel specimens. This is perhaps due the fact that EN24T is a tightly controlled steel grade that also undergoes an annealing treatment. It is likely that these manufacturing processes lead to a more reliable and isotropic grain structure. Additionally, variation in acoustoelastic constants for rail steel are thought to be heavily influenced by variation in the structure and the presence of 'inclusions' of manufacturing impurities in the rail web.

While the average values for C_{brfg} are somewhat close to each other, there is a greater difference between the two rail steel specimens than the EN24T and it's closest rail steel counterpart.

While specimen R260A has by far the highest zero-offset, the overall error is the lowest by an order of magnitude. Much greater experimental control is needed to attempt to eliminate the variance in the measurement.

7.2 Full rail testing

7.2.1 Test platform 5

To assess the potential of transferring the measurements on-track, it was important to conduct a test on a representative section of full rail. An 8m long track panel, consisting of two rails, of different ages and service lives, fixed to a set of concrete ties (sleepers) was delivered to the University. A TR75 hydraulic rail tensioning set (Figure 7.8), normally used for closing gaps in rails that are being welded together, was used to apply a compressive stress along each rail individually.

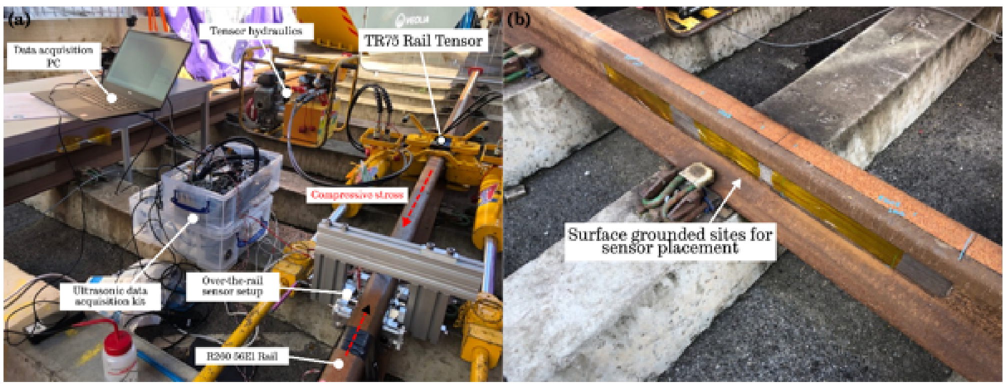

Figure 7.8: Left: The over-rail test platform 5 and DAQ system undergoing testing. Right: prepared locations for measurement on the web of rail [Image Image credit: Gary Nicholas]

A narrow belt sander was used to prepare the surface, removing rust and attempting to leave a flat and clean surface for the sensors. This was an imperfect solution as there was no way to leave the finished surface truly flat using hand tools.

The results in this section were returned from a sequence of compression tests on both rails, identified as specimens R260D and R260E. Compressive stresses from 0 to 89MPa were induced and the over-rail test platform 5 (section 4.7.6) was used for the first time.

Table 7.7 provides a summary of the test parameters.

Table 7.7: Test summary for platform 5

Rig	Specimen(s)	Locations	Sets	Stress Range
TR75	R260D R260E	2	3	0 – 89MPa

Figures 7.9 through 7.12 plot the C_{brfg} value for each data set, separated by loading cycle, for each of the two locations on both rails (R260D and R260E).

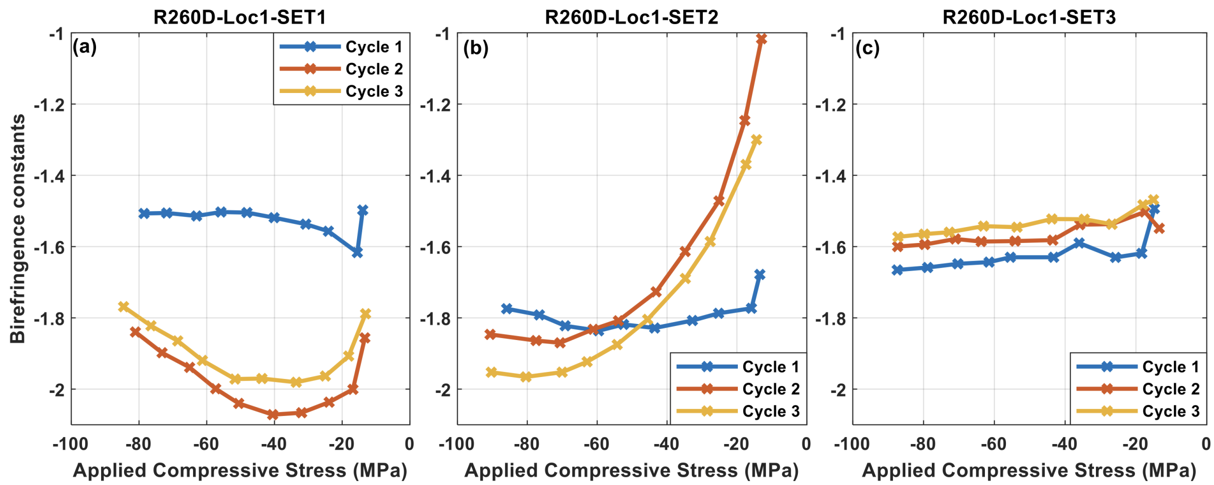

Figure 7.9: Calculated birefringence constant plotted against applied stress for rail R260D at location 1 [Image Image credit: Gary Nicholas]

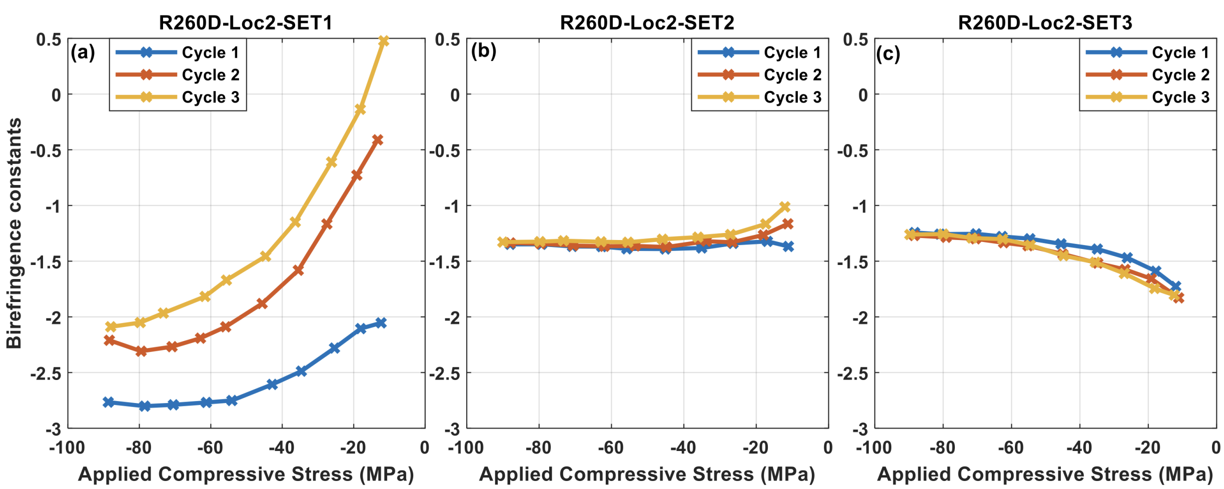

Figure 7.10: Calculated birefringence constant plotted against applied stress for rail R260D at location 2 [Image Image credit: Gary Nicholas]

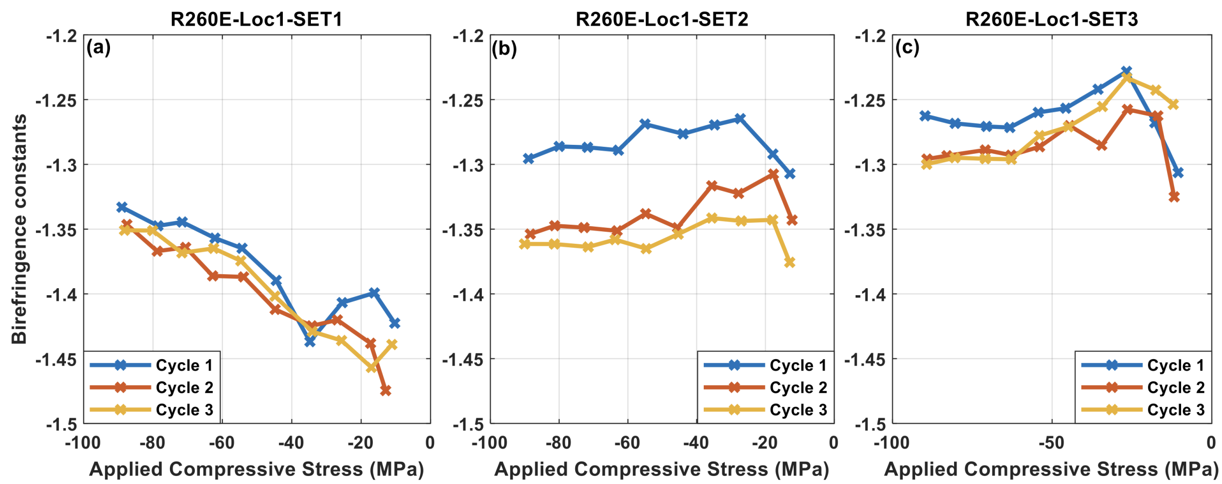

Figure 7.11: Calculated birefringence constant plotted against applied stress for rail R260E at location 1 [Image Image credit: Gary Nicholas]

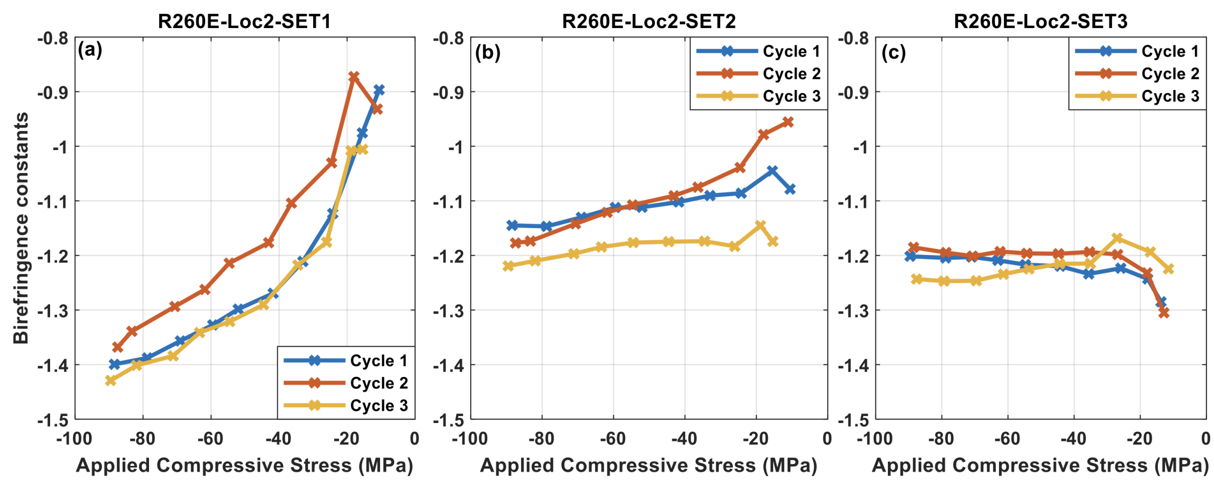

Figure 7.12: Calculated birefringence constant plotted against applied stress for rail R260E at location 2 [Image Image credit: Gary Nicholas]

While all data display sensitivity of the C_{brfg} value in response to changing applied stress, the expected linear trend is absent in all cases. There is some consistency in the C_{brfg} values at a single location, through the trend direction and scatter is variable between sets.

The variance in the range of C_{brfg} is similar for both rails, from $\Delta C_{brfg} \sim 3$ (R260D: location 1 - set2 & location 2 - set 1. R260E: location 2 - set 1) to $\Delta C_{brfg} \sim 0.1$ (R260D: location 1, set3 & R260E: location 2, set 3).

Figure 7.13 plots the zero-offset values for the three loading cycles in each of the data sets for both test locations on both rails. All plots show a lower variance of C_{brfg} between subsequent loading cycles in the same set and a much larger variance between sets. As each set is conducted at the same location, this variance cannot be a result of non-homogeneity or material constants. As the test platform is removed and re-applied between sets, I suspect that these changes could be due the ultrasonic couplant or very slight changes in alignment of components within the test platform assembly.

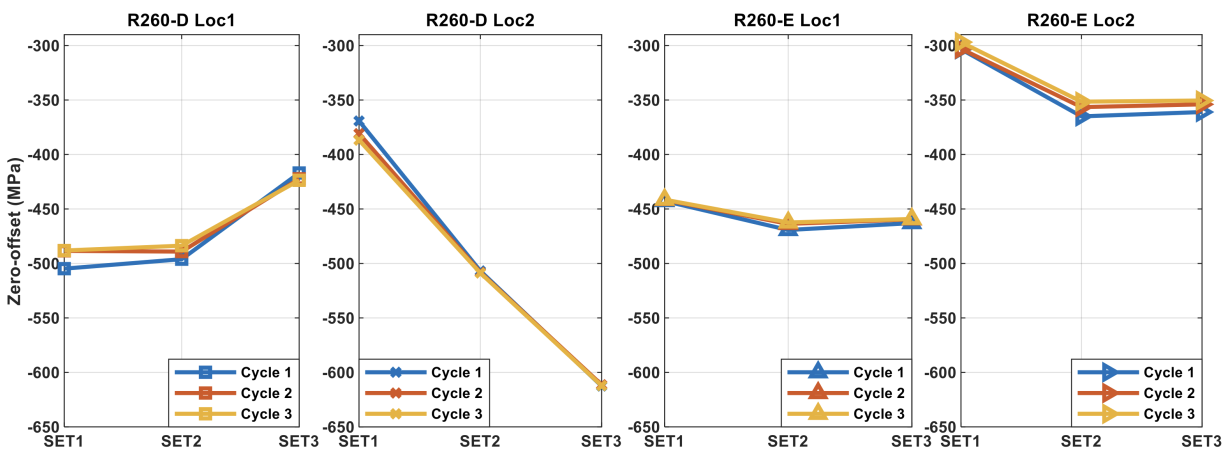

Figure 7.13: Zero-offset for each full rail specimen, separated by set, location and loading cycle number [Image Image credit: Gary Nicholas]

These zero offset values have a much higher consistency across different locations and rails than the previous laboratory testing data. This indicates that the test platform set-up is more reliably repeatable.

Table 7.8 gives the average values for C_{brfg}, zero-offset and their respective error percentages, and also tabulates the impact these errors have on the measurement of both stress and NRT.

Table 7.8: Variation and errors for measured acoustoelastic constant and 'zero-offset' for birefringence testing of two full rail R260 specimens and the effect of this variation on the error in stress measurement and NRT

Specimen	C_{brfg}	σ_{offset} (MPa)	Error C_{brfg} (MPa)	Error σ_{offset} (MPa)	Cumulative max error (MPa)	Cumulative NRT error (°C)
R260D-L1	-1.62±21.1%	-468±11%	18.8	51.2	70.0	29.0
R260D-L2	-1.34±36.8%	-500±26%	16.1	130.4	146.5	60.7
R260E-L1	-1.14±34.8%	-456±03%	15.8	14.5	30.3	12.5
R260E-L2	-0.98±34.8%	-388±12%	38.2	41.1	79.3	32.8

The over-rail test platform produces results that were comparable to, and in some cases more accurate than those obtained on machined and polished test specimens in the laboratory in a setting representative of a real-world, on-track measurement. The errors from test platform 5 were smaller and more consistent than those from the lab testing on test platform 4. The improved design and increased stiffness of the test platform is one likely contributor to this. It is difficult, however, when viewing the variance in trends and scatter, to feel confident in any conclusions from this data.

The average error from the ultrasonic determination of C_{brfg} was 22.2MPa (Range: 15.8 to 38.2MPa). The average zero-offset error was twice as large, 53.9MPa (Range: 14.5 to 130.4MPa).

More than $\frac{2}{3}$ of the total cumulative error in measurements conducted on rail R260D is due to the unpredictability of the zero-offset value. This reduces to $\frac{1}{2}$ for R260E.

This variation could result from metallurgical differences in the year of manufacture or from changes experienced by the rails in their service life. It could also be a result of a number of experimental considerations that have not yet been sufficiently well controlled, or from unknown dependencies that the data has yet to uncover with a discernible pattern.

Chapter 8

Angled wedge results

This section details the experimental stages in the development of the angled wedge measurement.

Test platform 4 underwent a preliminary validation (section 8.1), which led to a number of design improvements. The improved test platform was then used to capture a full set of test data, which is analysed in Section 8.3. The over-rail prototype device was also tested, analysis is presented in section 8.4. Final testing was conducted at high stress levels with a further iteration of the test platform (Section 8.6).

This author conducted the majority of the testing and data capture for the following testing. While data processing and plotting for sections 8.1 and 8.4 was conducted by Dr Gary Nicholas, this author conducted the data processing for the latter stages, and at all times presents their own data analyses and conclusions in this thesis.

8.1 Test platform 4 - Preliminary validation

The test platform was first checked on a test specimen at zero stress. The SoS results from this initial investigation are shown in Figure 8.1

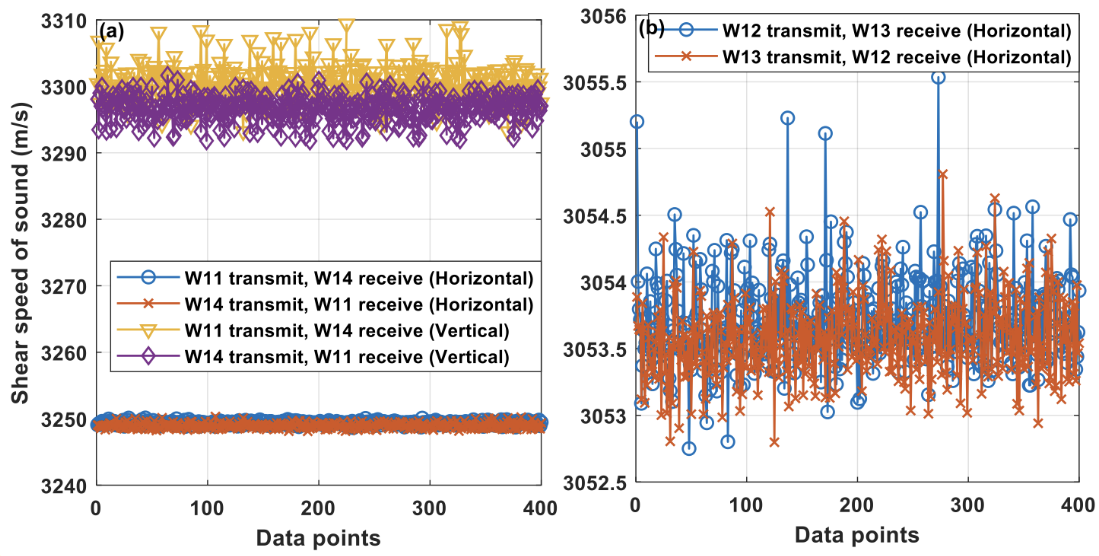

Figure 8.1: Shear SOS for test platform 4 preliminary wedge signal capture. LHS: Plots of both horizontal and vertically polarised waves vs. data point. RHS: Zoomed-in plot of horizontally polarised SOS values by data point

While there is a modest difference in SoS between the horizontally and vertically polarised transducers in the left-hand plot for the 55-degree data, this was not considered overly problematic as the horizontal polarisation was the measurement of interest. The primary concern was the near $-200ms^{-1}$ deviation of the 35-degree SoS from the expected values.

8.2 Test platform 4 - initial validation

While the testing program included data capture for both birefringence and angled-wedge methods, I decided to undertake an tensile test validation, notwithstanding the 35-degree angled wedge SoS issues. The testing setup for test platform 4, along with a schematic diagram showing sensor assembly locations relative to the test specimen, is shown in Figure 8.2.

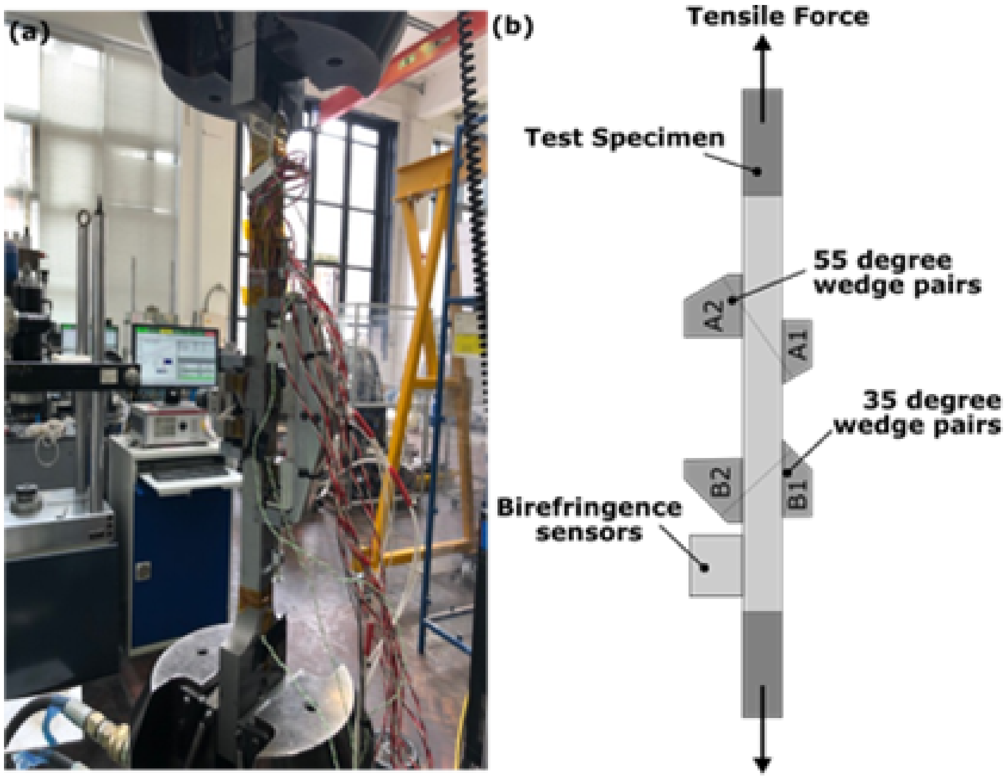

Figure 8.2: Photograph and schematic diagram for Test platform 4 with birefringence and angled wedge sensors

These initial tensile tests consisted of loading the test specimen at intervals between 0 and 162.5MPa, capturing data on both loading and unloading cycles. Table 8.1 shows the test details for the tensile test.

Table 8.1: Test summary for platform 4

Rig	Specimen(s)	Locations	Sets	Stress Range
Mayes 100kN	EN24T	1	1	0 – 162.5MPa

Figure 8.3 plots the strain measurements taken from all 4 faces of the test specimen. These values are linear and consistent with the theoretical values. The small degree of variance between strain readings on different faces could indicate either the possibility of slight bending of the test specimen (potential causes include incorrect alignment within the test rig or the specimen itself being slightly bent) or inconsistent instrumentation of the strain gauges, where the pressure applied to the specimen during the bonding of the gauges could create an offset from an accurate zero point.

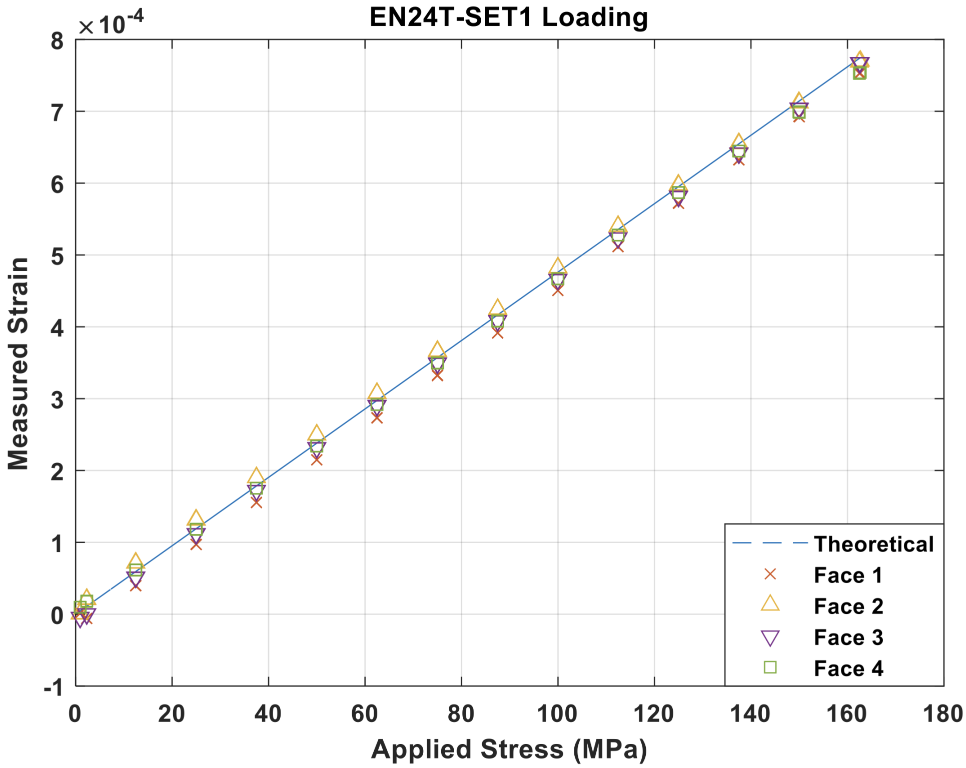

Figure 8.3: Strain gauge values for all 4 faces of the tensile specimen under load compared with an idealised theoretical value

Figures 8.4 and 8.5 show the wave-forms of the 55 degree and 35 angled wedge signals respectively. The signals show a clear set of 3 or more reflections from all sensors.

The first signal corresponds to the initial pulse, though due to issues with inconsistent triggering time, this signal is not useful for extracting the ToF. The next two peaks for all sensors in both polarisations are clear and have good signal to noise ratio. The third reflection, present only in the 35 degree angled wedge signals, has significantly lower signal to noise ratio, and therefore is likely to introduce error into the calculations of ToF.

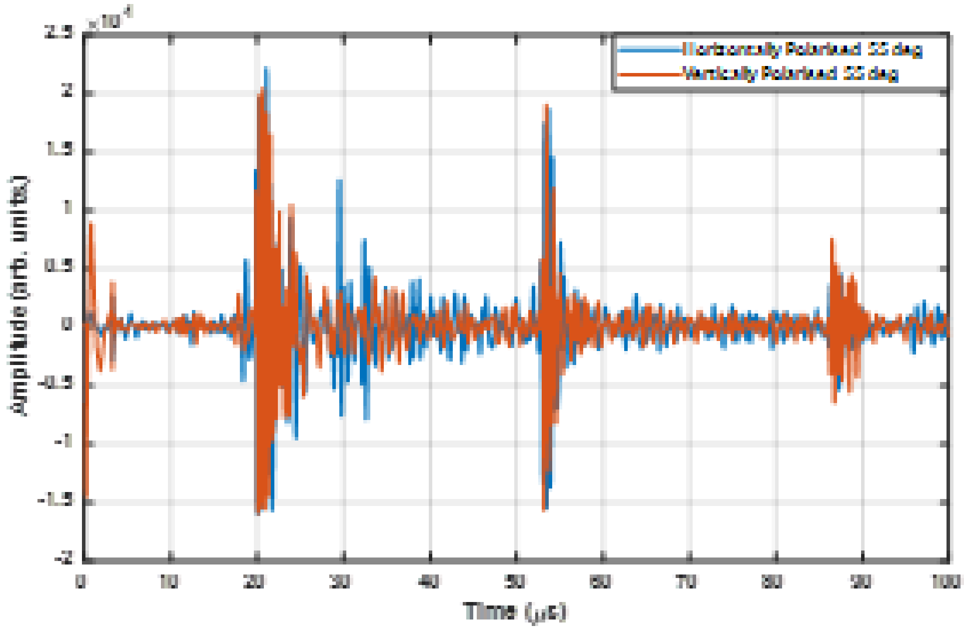

Figure 8.4: 55 degree angled wedge ultrasonic signal waveform [Image credit: Gary Nicholas]

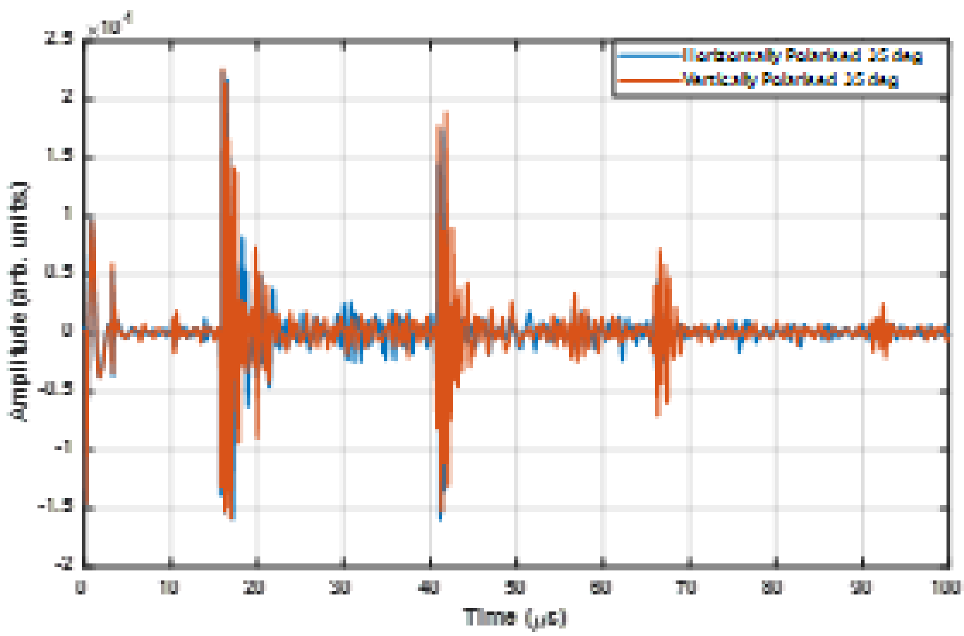

Figure 8.5: 35 degree angled wedge ultrasonic signal waveform [Image credit: Gary Nicholas]

Figure 8.6 plots the ultrasonic ToF for the vertically polarised (aligned with the applied axial stress) signals from 55 and 35 degree wedges against the applied stress for two loading cycles. The ToF increases with increasing stress as expected, though the results are not entirely linear. The variance between loading and unloading values are within 5ns, which is smaller than the 8ns time sampling error, that is a fundamental error floor for the DAQ system.

There is also a clear difference between the loading and unloading cycles. These tensile tests are at conducted at very low stress levels relative to the yield strength of the materials, therefore the patterns cannot relate to any plastic hysteresis. Slippage in the test rig grips or some work-hardening response to repeated loading cycles could be responsible.

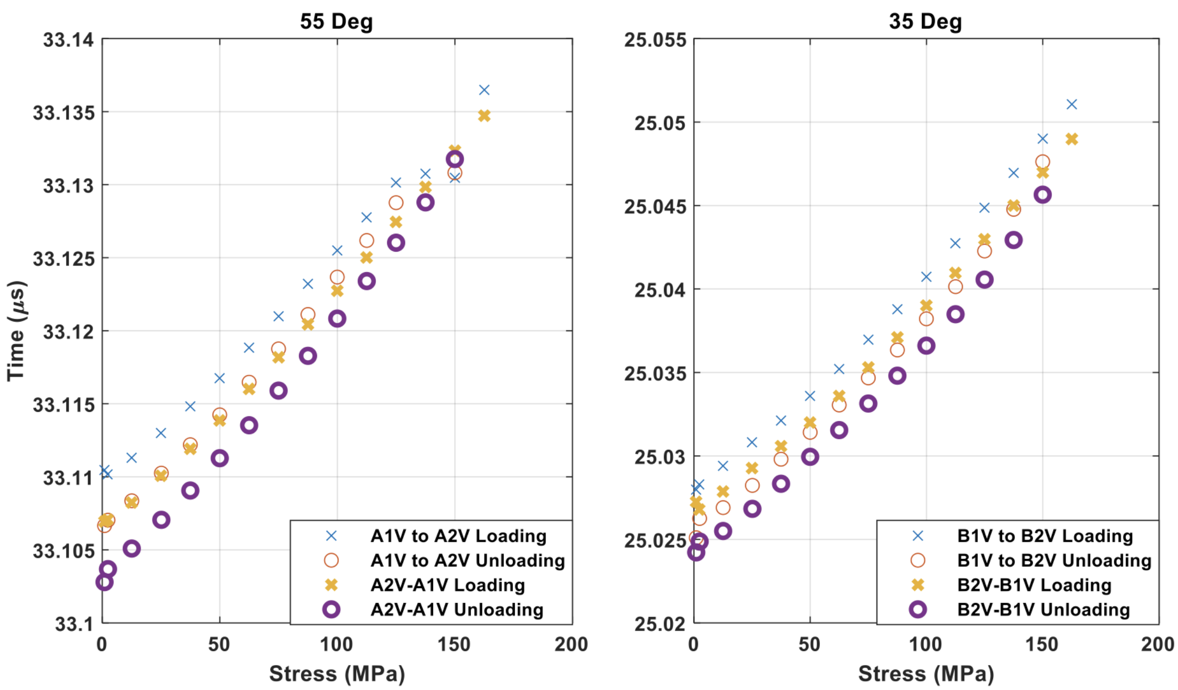

Figure 8.6: Variation in the ToF for both 55 and 35 degree wedge sensors, separated by pulsing direction and loading/unloading stress cycle [Image credit: Gary Nicholas]

On plotting the SoS from the above ToF values (Figure 8.7) we see that the data is not fully linear as would be expected, however, there is very little variance between pulsing direction. The ToF at zero-stress is lower at the end of the loading-unloading test than it was at the beginning. When accounting for the different flight paths, the zero-stress ToF values correspond to a $2ms^{-1}$ difference in SoS from 35 and 55 degree at zero-stress. These SoS values are consistent when pulsed in both directions across and specimen, and are consistent with expected values.

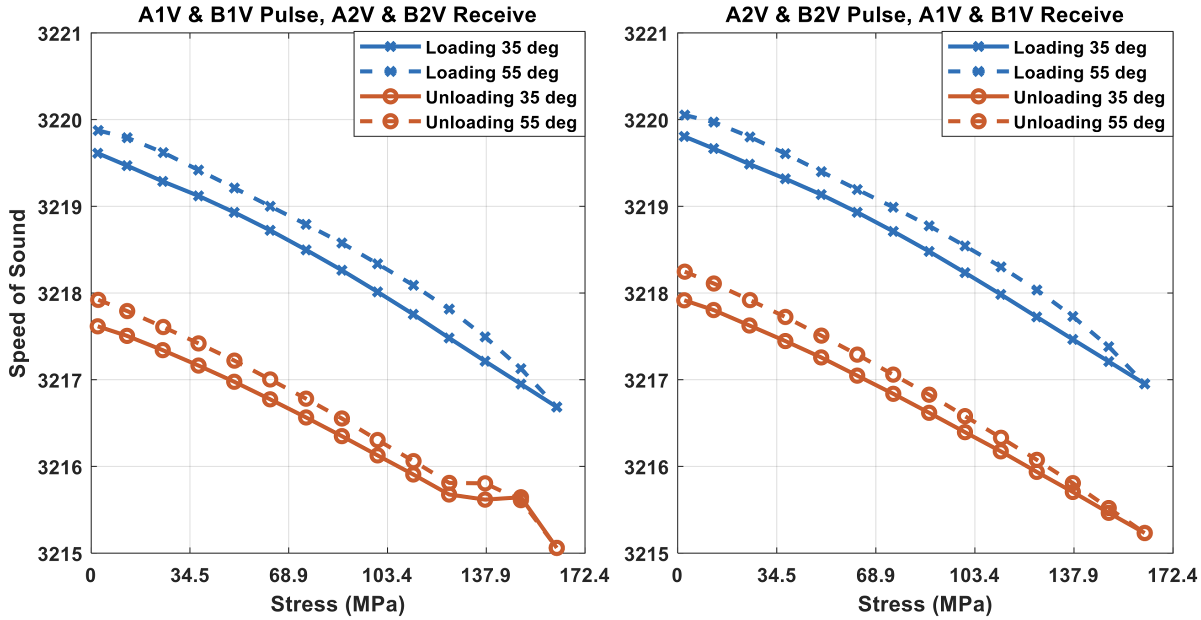

Figure 8.7: Angled wedge SoS plotted against changing stress (left) pulsing from wedge 1 and receiving on 2, (right) pulsing on 2 and receiving on 1, separated by wedge angle [Image credit: Gary Nicholas]

Figure 8.8 plots the ultrasonically measured stress vs the applied stress values, separated by set and loading/unloading cycle. The apparently small discontinuity in SoS between loading and unloading cycles results here in significant deviations in stress values between loading and unloading cycles. However, the principal features of this data set are the lack of linearity and significant deviation from the line of perfect agreement. While some of the sets show proximity to perfect agreement at lower stresses, this is not observed in all cases, and the deviation in all cases increases significantly at stress values over 40MPa.

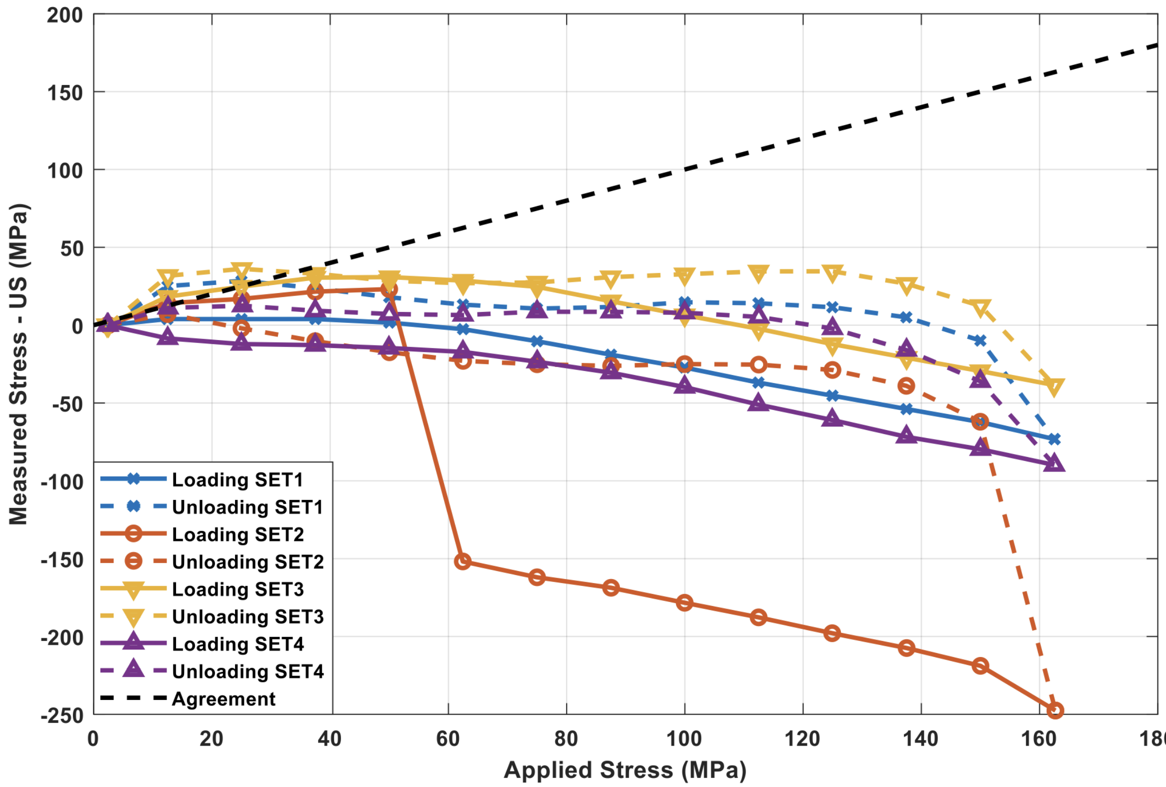

Figure 8.8: Stress for ultrasonic measurement vs applied rig stress separated by set and loading/unloading cycle [Image credit: Gary Nicholas]

The user experience of conducting these experiments exposed a number of inadequacies in the test platform design, as detailed in subsection 4.27. These design limitations, including insufficient control of the sensor assembly alignment relative to the clamping mechanism and the test specimen itself, are very likely contributors to the poor agreement. However, with a somewhat repeated pattern of poor agreement, there could be more factors at play such as the limited time sampling resolution.

There were also concerns that the individual transducers on the sensor assemblies could have become mis-oriented during the instrumentation process, which would change the interaction of the ultrasonic signals with the aligned stress field.

8.3 Test platform 4 - improved

A number of improvements were made to the test platform. This platform still used the same sensor assemblies as they could not be re-instrumented within the existing time constraints. Table 8.2 shows the test details for this tensile test.

Table 8.2: Test summary for the improved platform 4

Rig	Specimen(s)	Locations	Sets	Stress Range
Mayes 100kN	EN24T R260A R260B	1	3	0 – 150MPa

Figure 8.9 shows the dimensions of the tensile specimen.

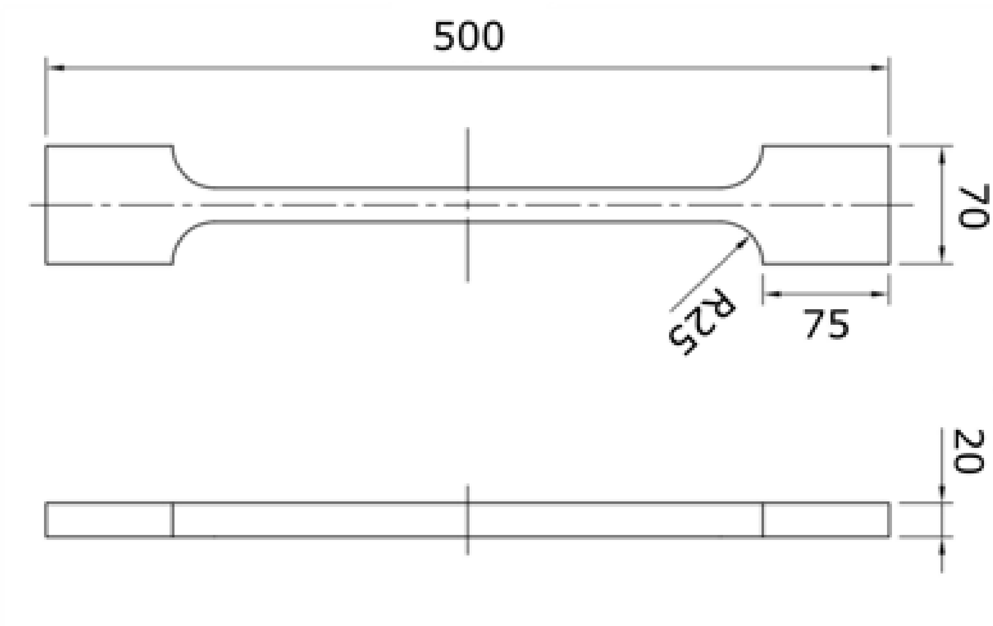

Figure 8.9: Dimensions of the tensile testing specimen

Following the updates test platform updates, clear signals were achieved from all transducers apart from the horizontal 35 degree transducer (Figure 8.10). This could indicate a significant issue with the alignment of the transducer itself within the sensor assembly.

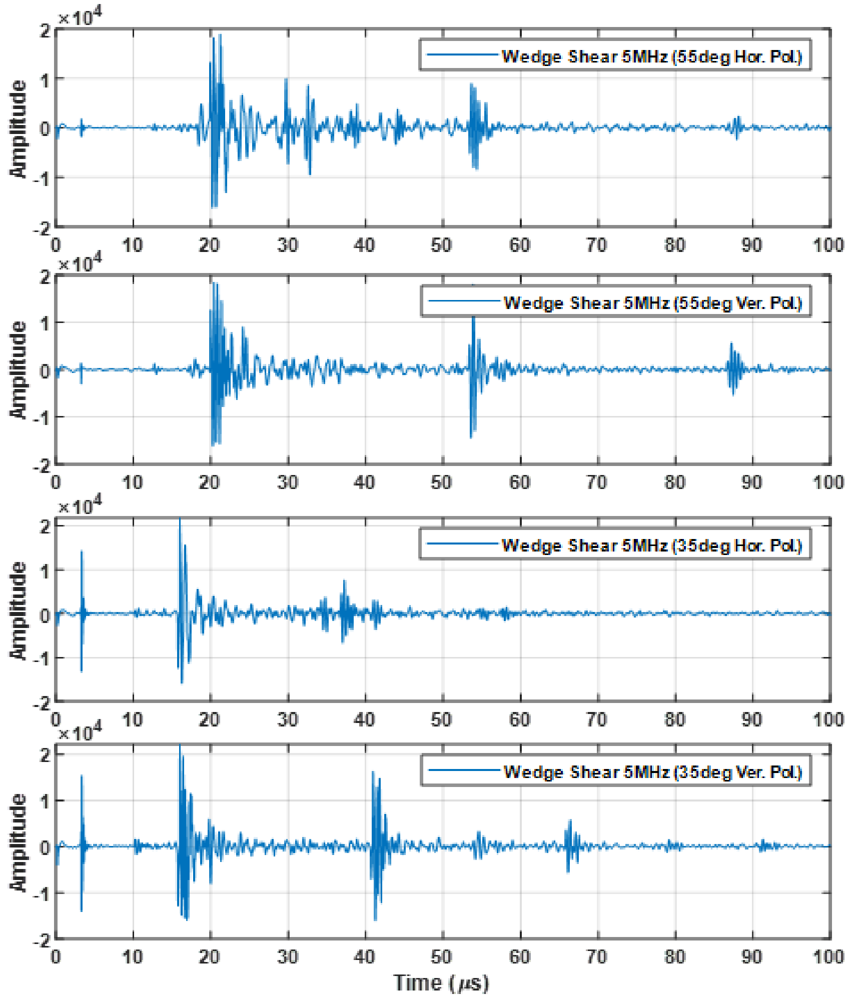

Figure 8.10: Clear A-scan signals from angled wedge transducers in the improved test platform 4 [Image credit: Gary Nicholas]

The ultrasonically measured stress vs applied tensile stress is plotted for three sets of tensile tests on the EN24T specimen, separated by loading and unloading cycles (Figure 8.11). These results have been corrected for zero-offset to allow direct comparison between sets.

The results are significantly improved from the preliminary investigation, with lower variance, more stable trends and smaller differences between loading and unloading phases.

While the general trends are clear between all sets, the data show low repeatability both between the loading/unloading ramp of each loading cycle, and between subsequent loading cycles within each set.

Set 3 shows the best agreement. All three loading cycles deviate from the perfect agreement immediately. The first loading cycle displays a shift back to agreement between 25 and

50MPa, where values begin to diverge dramatically, back into step with cycles 2 and 3.

The second and third loading phases show immediate deviation from perfect agreement, but the unloading phases return to agreement between 40 and 50MPa, where they then drop beneath the line of agreement before returning to zero. Sets 1 and 2 show a similar patterns, with loading deviating quickly (earlier than set 3) and returning to undershoot the perfect agreement (this time between 25 and 75 MPa). The variance in sets 1 and 2 is higher in absolute, and variance between sets is also higher (highest for set 1).

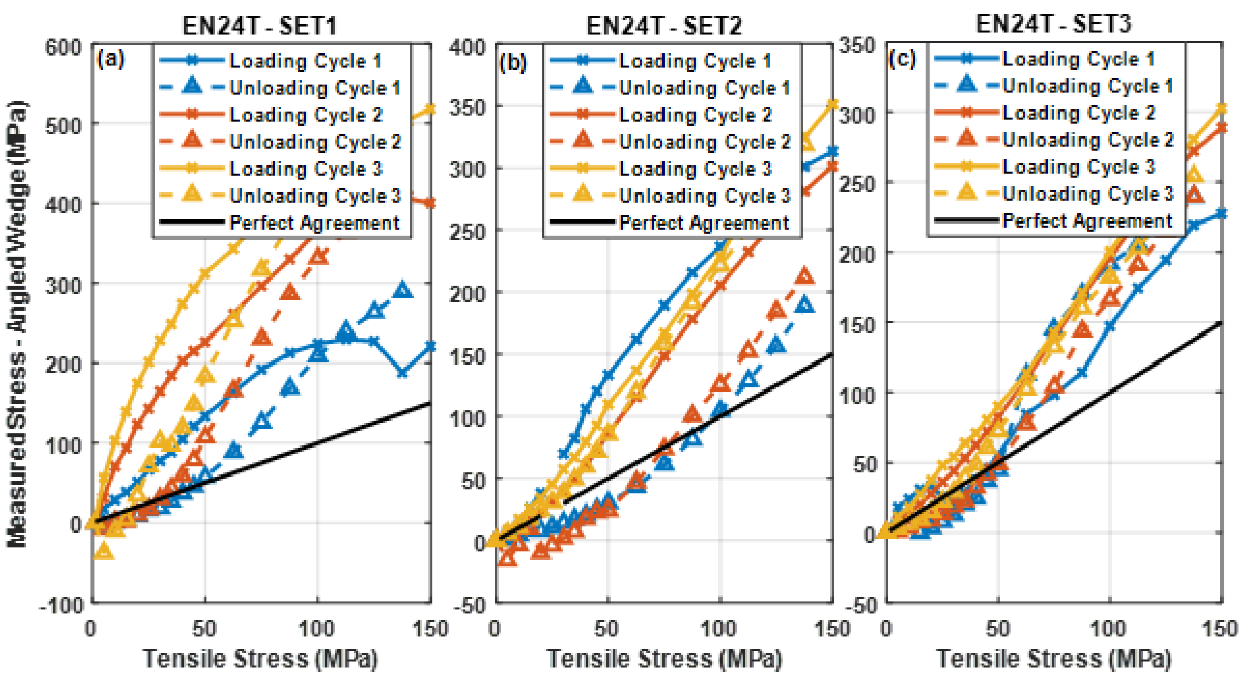

Figure 8.11: Plot of ultrasonically measured stress using the angled wedge method vs applied rig stress, separated by set and loading/unloading cycle for measurements conducted on specimen EN24T [Image credit: Gary Nicholas]

Figures 8.12 and 8.13 show the same plots of ultrasonically calculated vs applied stress for both R260 specimens. Set 2 on specimen R260B shows the most accurate results, with excellent agreement on loading cycles 1 and 3 up to 25MPa.

Maximum divergence is larger than for EN24T on all cycles, and especially interesting is the swift downward trend shown in the set 2 loading cycle. The unloading phases show the same return and undershoot of the perfect agreement in a similar pattern and magnitude to those from the EN24T results.

Results from R260A are so dramatically different that I suspect there were inadvertent errors in experimental set-up. While the first set of measurements on R260A (but none of the subsequent cycles) end up converging on the perfect agreement at maximum stress (following a very roundabout path), there is a clear disconnect between these data points and the max load of the unloading phase across all loading cycles and sets.

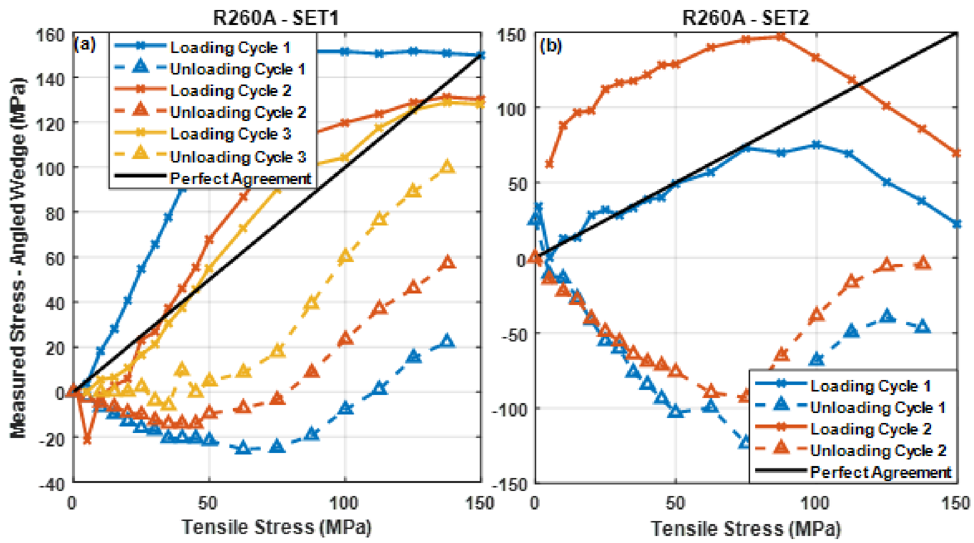

Figure 8.12: Plot of ultrasonically measured stress using the angled wedge method vs applied rig stress, separated by set and loading/unloading cycle for measurements conducted on specimen R260A [Image credit: Gary Nicholas]

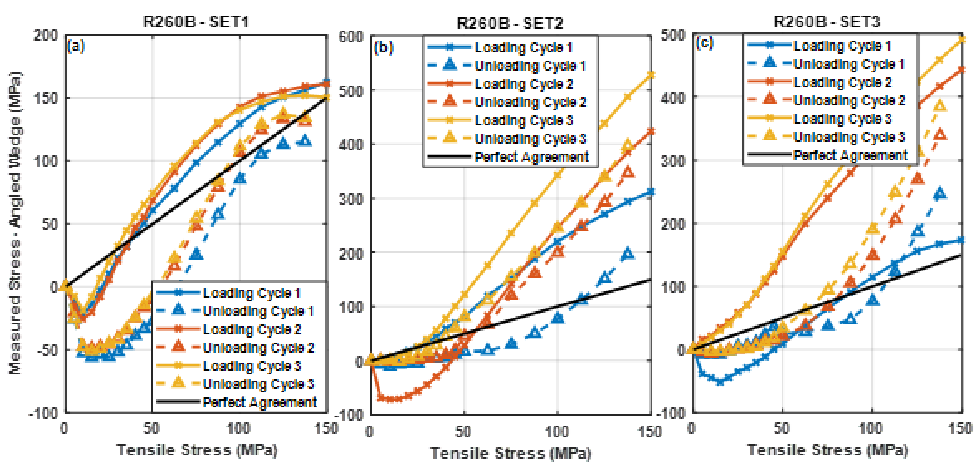

Figure 8.13: Plot of ultrasonically measured stress using the angled wedge method vs applied rig stress, separated by set and loading/unloading cycle for measurements conducted on specimen R260B [Image credit: Gary Nicholas]

The existing concerns regarding angles of the transducers within the 35 degree sensor assembly could explain at least part of the non-linear behaviour in the above results. A more reliable experimental set-up could also increase repeatability.

Though the data show poor trends compared the line of perfect agreement, the similar shape of the plots between loading and unloading cycles across the different sets are perhaps interesting. The deviations do not appear random, though I can find no concrete explanation for them within the current model and understanding of the physical system. There could be issues with friction between the sensor assemblies and the specimen as it extends during testing or flexion within the test platform assembly, causing the ultrasonic flight path to change and thereby introducing errors in a manner that is repetitive between repeats for each loading cycle.

It is again worth noting that the results have been corrected for zero-offset, which continues to be a significant issue, and the magnitude of the variance is still often greater than the maximum applied stress within these experiments.

8.4 Test platform 5 - over-rail

To assess the potential of transferring the measurements on-track, it was important to conduct a test on a representative section of full rail in an identical testing setup to that described in section 7.2.1 and shown in 8.14.

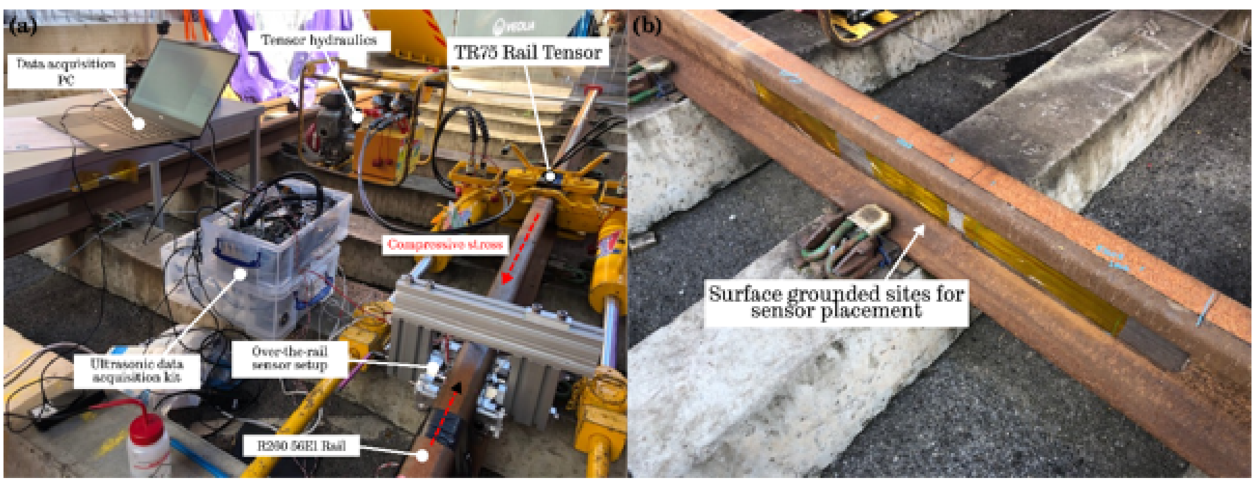

Figure 8.14: Left - A TR75 rail tensioner attached to the full-size track panel for ultrasonic testing. Right - Preparation of the rail surface [Image credit: Gary Nicholas]

A narrow belt sander was used to prepare the surface, removing rust and attempting to leave a flat and clean surface for the sensors. This was an imperfect solution as there was no way to leave the finished surface truly flat using hand tools.

The results in this section were returned from a sequence of compression tests on both rails, identified as specimens R260D and R260E. Compressive stresses from 0 to 89MPa were induced and the over-rail test platform 5 (section 4.7.6) was used for the first time.

Table 8.3 provides a summary of the test parameters.

Table 8.3: Test summary for platform 5

Rig	Specimen(s)	Locations	Sets	Stress Range
TR75	R260D R260E	2	3	0 – 89MPa

The signals from 35- and 55-degree angled wedge transducers are shown in Figure 8.15

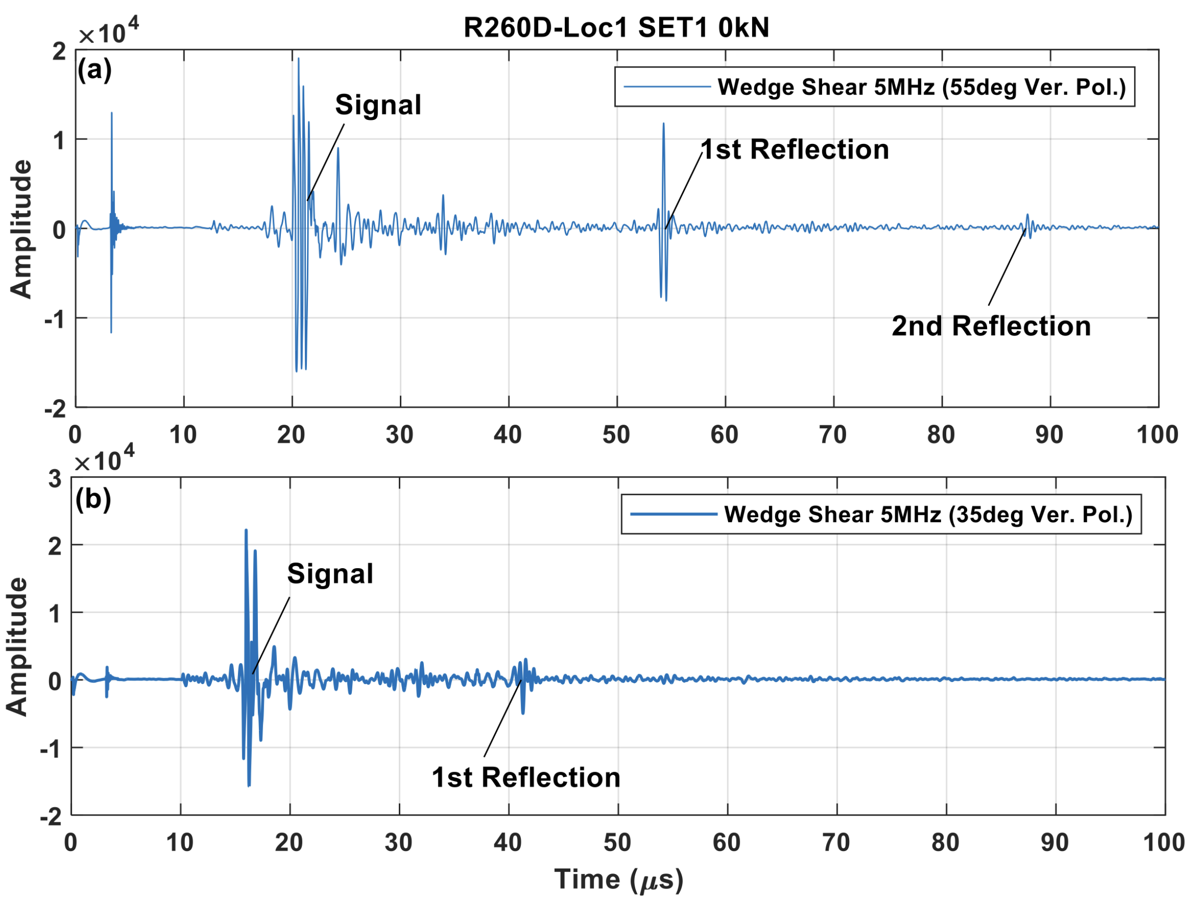

Figure 8.15: A-scans of 55- and 35-degree angled wedge signals from R260D location 1 [Image credit: Gary Nicholas]

There are fewer and smaller consecutive reflections in the signals taken from the full rail tests compared with those in Figure 8.10 taken from a flat-ground laboratory specimen. It was still possible, however, to process the data and extract the ultrasonic ToF.

Figures 8.16 and 8.17 show a representative selection of results for ToF vs applied stress for 55- and 35-degree angled wedge transducers across both locations on rail R260D.

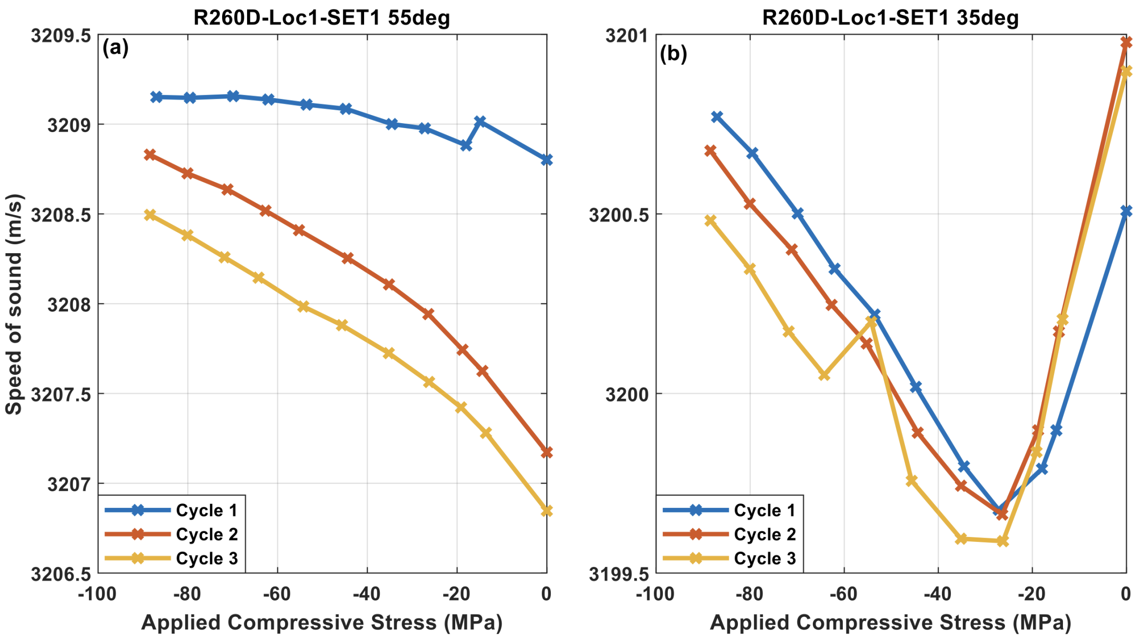

Figure 8.16: ToF vs Applied stress, separated by loading cycle for set 1 - platform 5 R260D Loc1 [Image credit: Gary Nicholas]

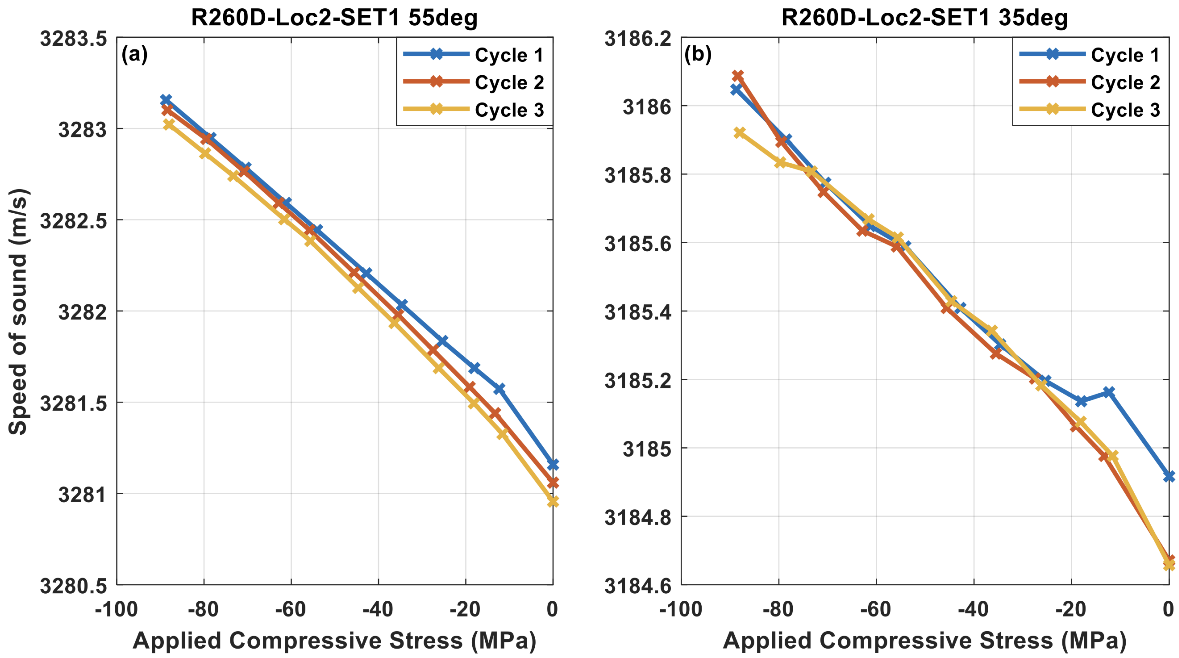

Figure 8.17: ToF vs Applied stress, separated by loading cycle for set 1 - platform 5 R260D Loc2 [Image credit: Gary Nicholas]

The figures show a marked difference in the magnitude and absolute values for SoS in both 55- and 35-degree signals for location 1. Values for location 2 are more consistent between loading cycles but the absolute values are different to those at location 1 and there is also a relatively consistent difference of $100ms^{-1}$ between the SoS values from the two different angles throughout the loading range.

Across both locations, the 35-degree SoS values show more non-linearity and are somewhat less reliable than the 55-degree values. This has been an unexpected outcome, as it would have been expected that the signals with the shorter flightpath (and therefore lower signal attenuation) and a less oblique angle of incidence to the side-face of the specimen would be more reliable. This is consistent with the patterns discussed in more detail in section 6.5.2.

Figure 8.18 shows the measured vs. predicted stress values for all three data sets taken at location 1.

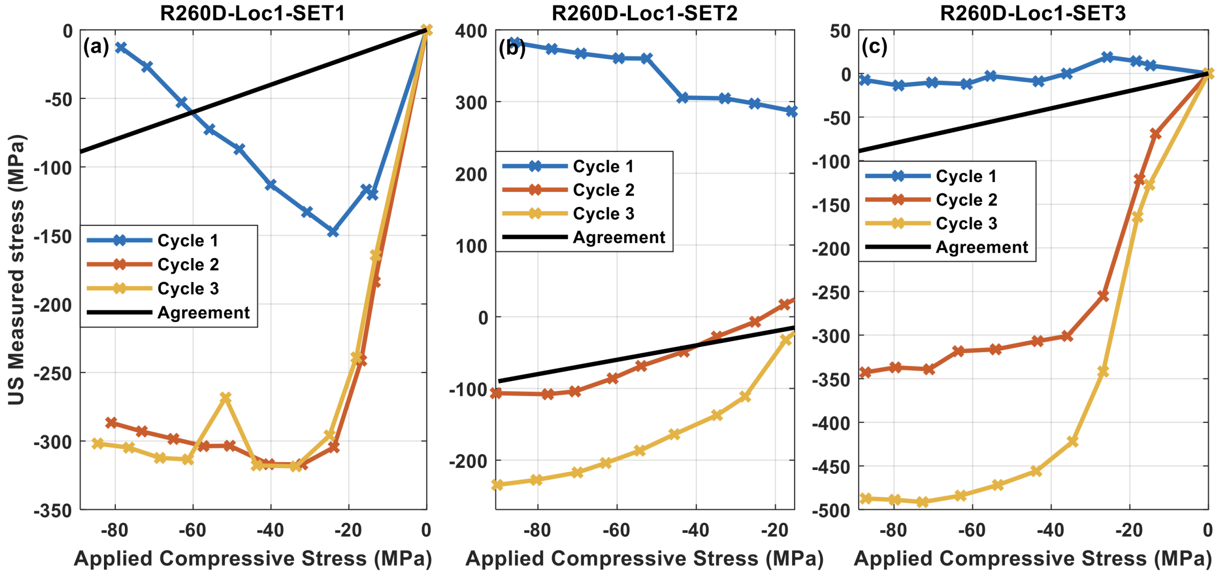

Figure 8.18: Measured vs applied stress, R260D, Sets 1-3, separated by loading cycle [Image credit: Gary Nicholas]

All three sets show very poor agreement, with some plots even showing an opposite trend. This is very likely due to the inconsistent SoS values, particularly evident in the 35-degree data in Figure 8.16. Using a hybrid approach, by combining the 55-degree angled wedge data with the 0-degree shear data from the birefringence method yielded the results shown in Figure 8.19.

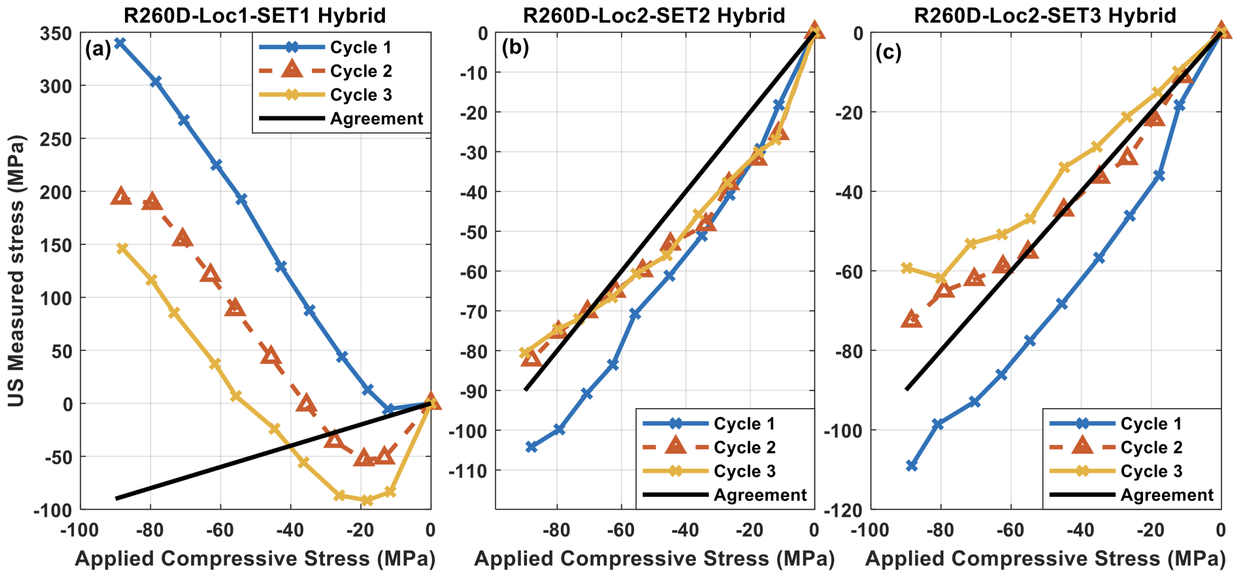

Figure 8.19: Hybrid model measured vs applied stress, R260D, Sets 1-3, separated by loading cycle [Image credit: Gary Nicholas]

This shows much better agreement for sets 2 and 3, though all results show significant variance and divergence from the line of agreement.

The angled wedge method returned results from full-scale rails that were comparable to those achieved in the laboratory from accurately ground and parallel tensile specimens. This indicates that the surface preparation and material constants, while being far from irrelevant, are not the primary failure mode for the technique.

The 35-degree data proved to be the least reliable across all experiments, pointing to the need to re-instrument the 35-degree sensor assemblies.

By eliminating the 35-degree signals and using a more reliable 0-degree birefringence data, the overall agreement for the dataset was improved, though it would not be rigorous to claim any quantitative conclusions from that improvement due to the high levels of inconsistency and repeatability.

8.5 Focusing on calibration-free measurement

The investigation so far had advanced both birefringence and angled wedge methods for measuring the stress state of rail. The birefringence method was providing more reliable results but both methods were suffering from significant zero-offset errors, and so far the methods had not been accurate enough to demonstrate reliable and repeatable sensitivity to variations in test parameters.

The angled wedge method was, however, the most novel and of higher scientific value. If it were successful, it could enable a calibration-free measurement; a step change in the science and practicalities of railway safety maintenance. I therefore made the decision to focus solely on the angled wedge method for the remainder of the investigation.

8.6 Test platform 6 - high stress testing

Previous tests identified two primary sources of error in the stress predictions from the angled wedge method:

- Measurement inaccuracy – The relatively small Signal-to-Noise-ratio (SNR) of the measured change in ToF relative to the experimental noise and digitization rate has been a significant contributor to measurement inaccuracy.
- Zero-offset – The fact that the measured stress has not equaled zero at zero applied stress creates a significant error in the angled wedge stress predictions

In this phase of testing, higher applied stress values (4x) were used as a proxy for a faster data acquisition rate. It was hoped that the increased stress-related deviations in ToF would increase the overall experimental SNR and thereby improve the accuracy of the stress predictions. It was an important factor that this approach would not improve the zero-offset error.

The high stress testing was conducted with test platform 6 clamped onto a test specimen in the ESH 1MN hydraulic rig in tensile test set-up (8.20).

Figure 8.20: Test platform 6 undergoing high-stress testing on the ESH 1MN rig. [Image credit: Will Gray]

Table 8.4 shows the test details for the tensile test.

Table 8.4: Test summary for platform 6 high stress testing

Rig	Specimen(s)	Locations	Sets	Stress Range
ESH 1MN	EN24T	1	4	0 – 540MPa

The dimensions of the tensile specimens were increased to reduce the impact of eccentric loading caused by the weight and clamping of the test platform on to the specimen. Figure 8.21 shows the dimensions of the updated tensile specimen.

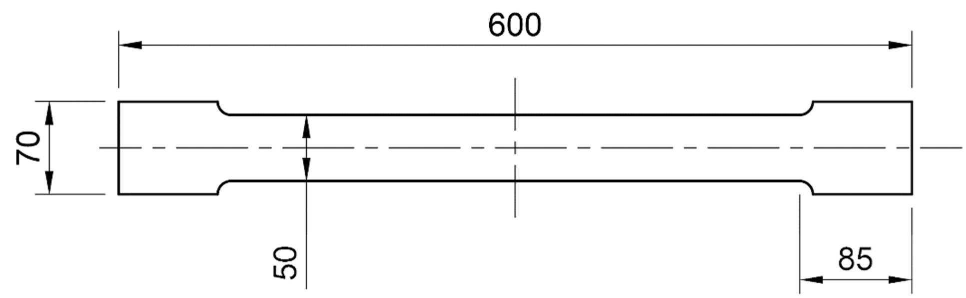

Figure 8.21: Dimensions of the updated tensile testing specimen

A CAD representation of test platform 6 is shown in 8.22, detailing the alignment components.

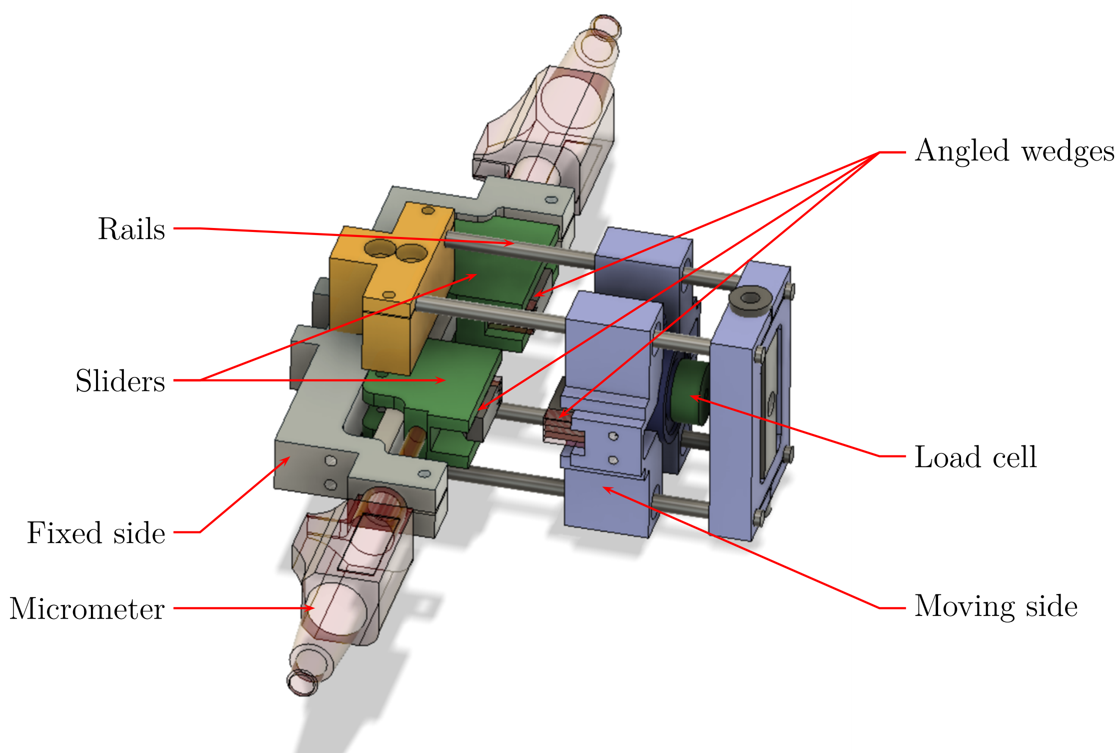

Figure 8.22: A CAD rendering of test platform 6 showing Micrometers, sensor assemblies and clamping system, composed of 4 parallel rails aligning fixed and moving sides of the clamp, and the load cell for accurate clamping loading

It was at this point in the investigation that the multiple data processing algorithms detailed in Section 6 were implemented.

Figures 8.23 through 8.25 show the extracted ToF for 55- and 35-degree angled wedge signals for three sets if data captured through the stressed tensile specimen.

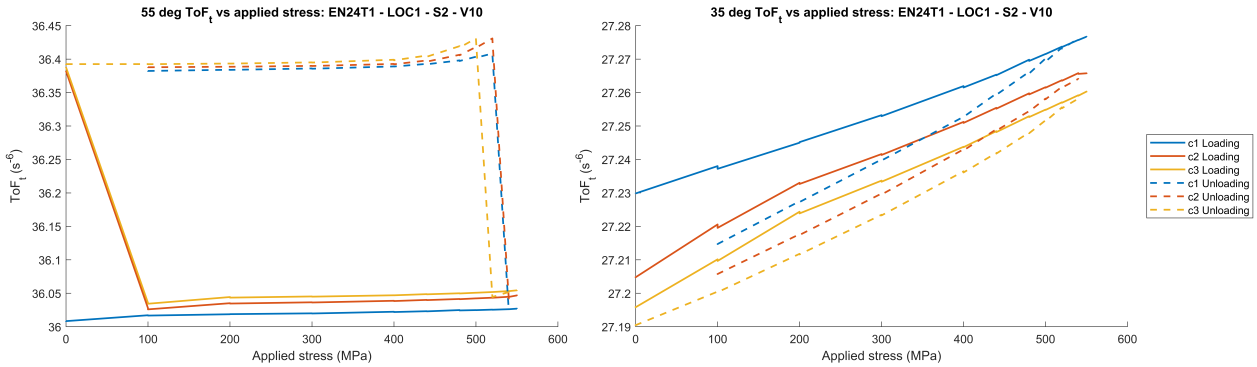

Figure 8.23: Applied stress vs ToF for 3 loading and unloading cycles for specimen EN24T1, location 1, Set 2 calculated using the peak-find ToF algorithm

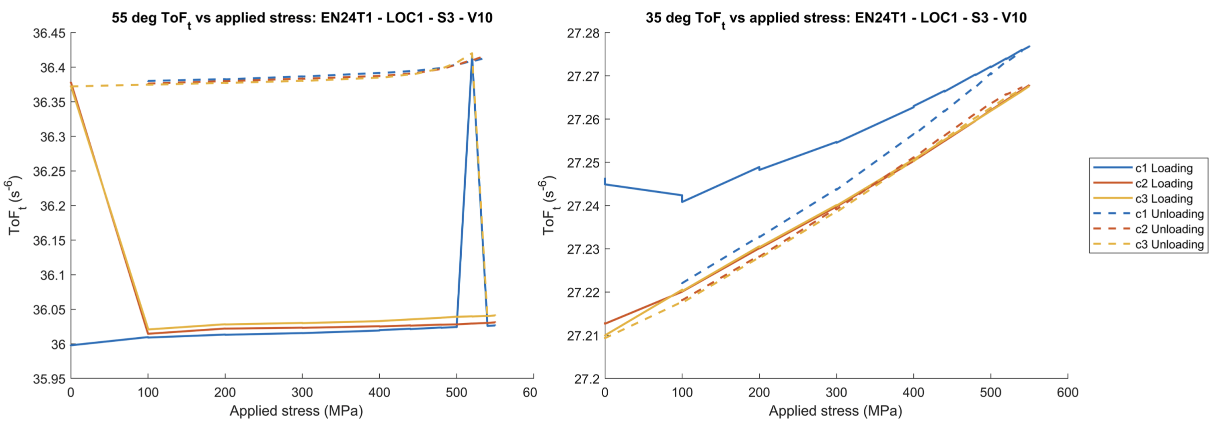

Figure 8.24: Applied stress vs ToF for 3 loading and unloading cycles for specimen EN24T1, location 1, Set 3 calculated using the peak-find ToF algorithm

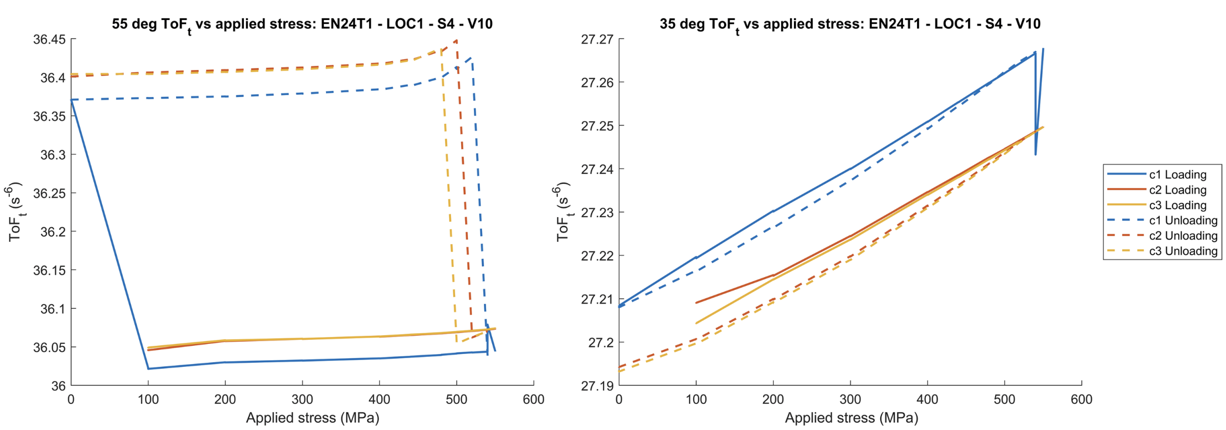

Figure 8.25: Applied stress vs ToF for 3 loading and unloading cycles for specimen EN24T1, location 1, Set 4 calculated using the peak-find ToF algorithm

All three sets show broadly the same pattern, with large jumps in ToF at the change in rig movement at peak load transitioning to the decreasing load ramp. This indicated that the 55-degree sensor assemblies are shifting by a very small amount relative to the surface of the specimen. There is also a precession away from the starting ToF from the first to the last loading cycle. This could indicate that there is a progressive thinning of the couplant thickness due to the oscillation of the specimen relative to the sensor assemblies.

The algorithm was fine-tuned to processes the first set of data, and there are several jumps in the ToF values that persist in the subsequent sets, most likely due to the sensitivity of the algorithm in selecting the correct reflection maxima peaks.

The absolute values for ToF are appear quite consistent across all three sets, though, as seen in the following plots, not consistent enough for the high sensitivity of the measurement.

The figures below show the applied stress plotted against the measured stress for the first set of data using the peak-find (8.26), weighted average (8.27) and envelope (8.28) methods.

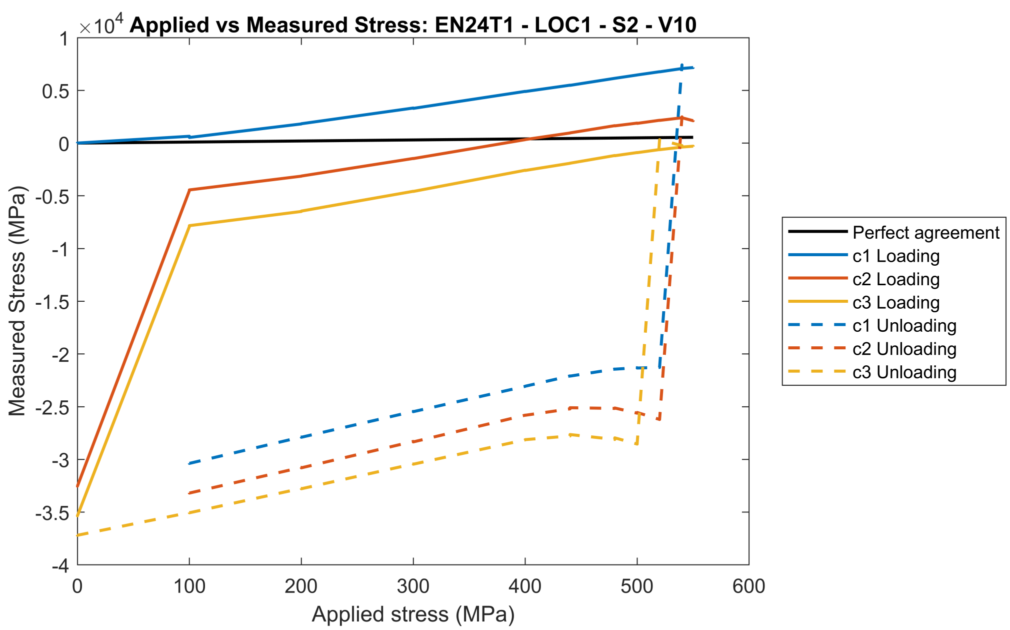

Figure 8.26: Applied stress vs measured stress for the 3 sets of loading and unloading data for specimen EN24T1, location 1, calculated using the peak-find ToF algorithm

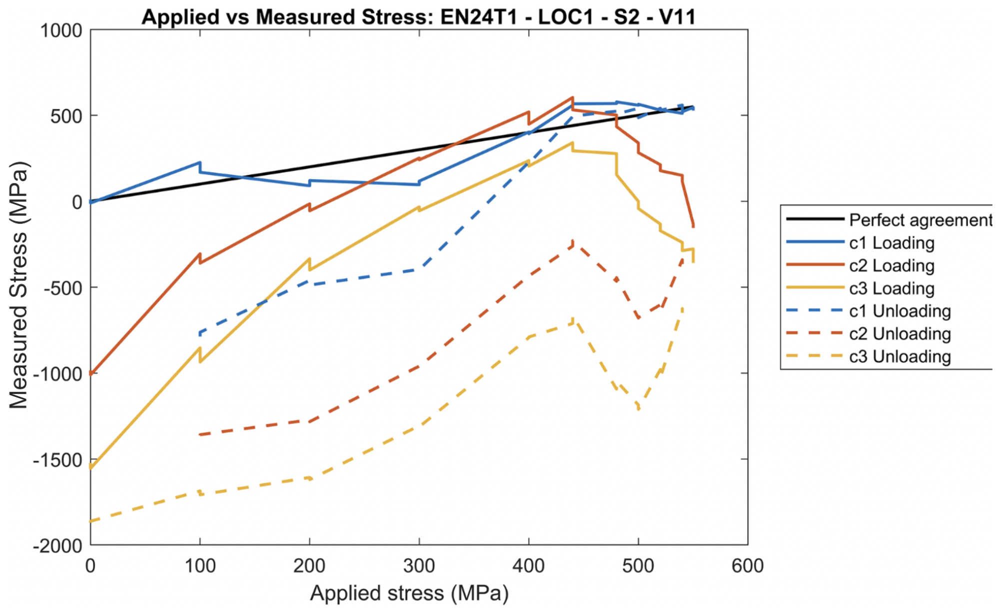

Figure 8.27: Applied stress vs measured stress for the 3 sets of loading and unloading data for specimen EN24T1, location 1, calculated using the weighted average ToF algorithm

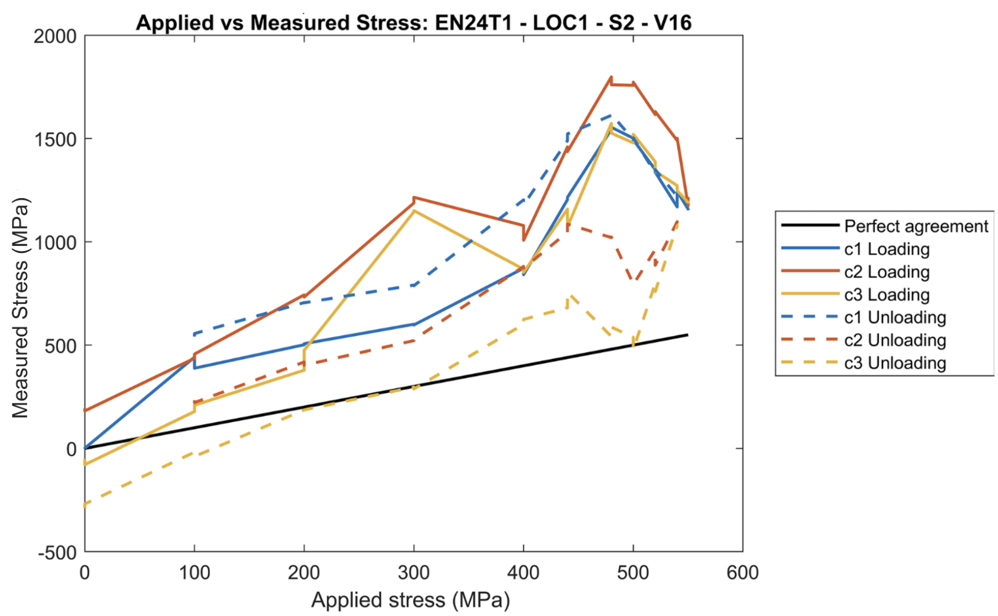

Figure 8.28: Applied stress vs measured stress for the 3 sets of loading and unloading data for specimen EN24T1, location 1, calculated using the envelope ToF algorithm

Figure 8.29 shows the three sets of measured vs. applied stress for the previous low-stress testing.

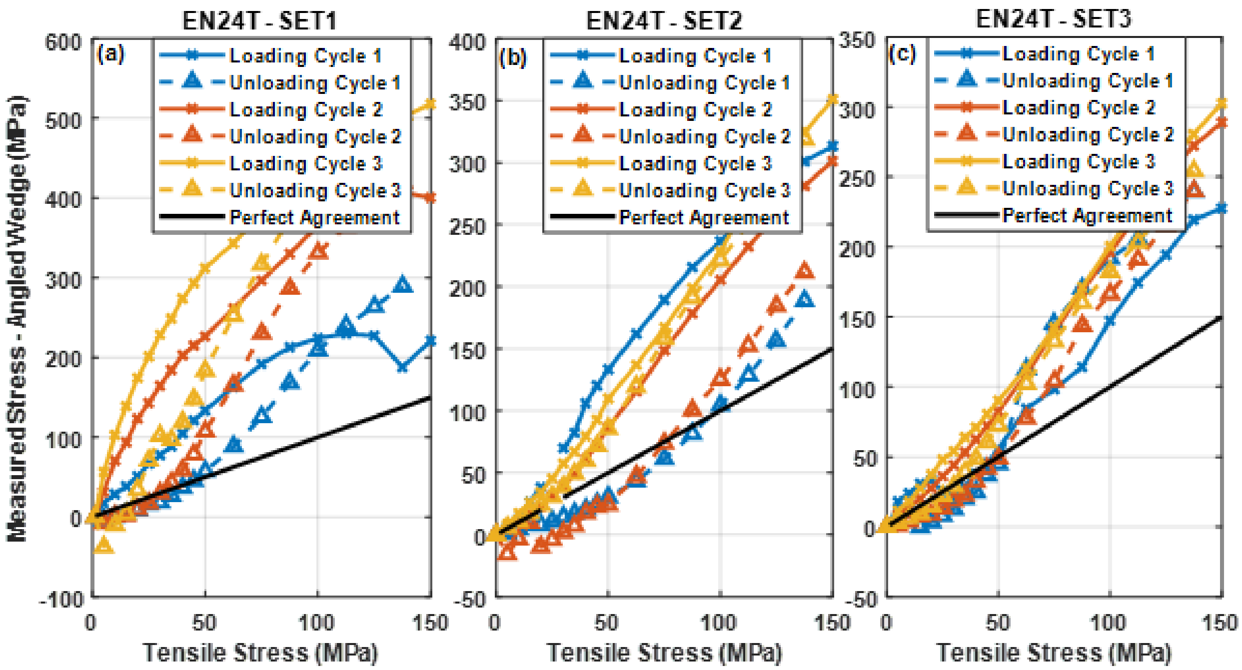

Figure 8.29: Plots of ultrasonically measured stress using the angled wedge method vs. applied rig stress for low stress testing, separated by set and loading/unloading cycle for measurements conducted on specimen EN24T [Image credit: Gary Nicholas]

Figures 8.30 through 8.32 show the measured vs. applied stress results for 3 sets of high stress data using the peak-find algorithm.

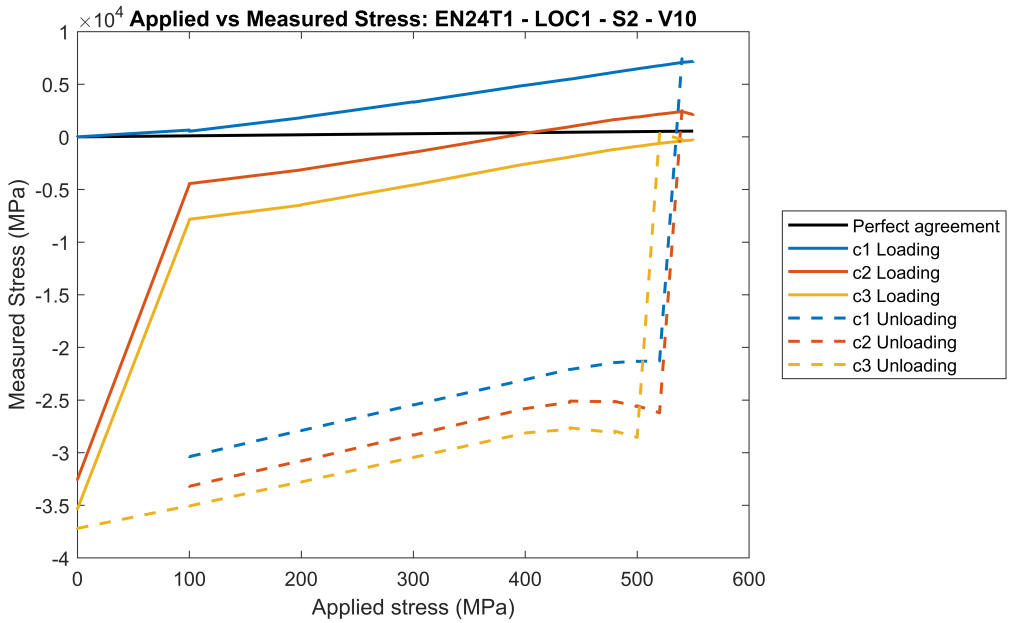

Figure 8.30: Plot of ultrasonically measured stress using the angled wedge method vs. applied rig stress for set 2, high stress testing, separated by loading/unloading cycle for measurements conducted on specimen EN24T

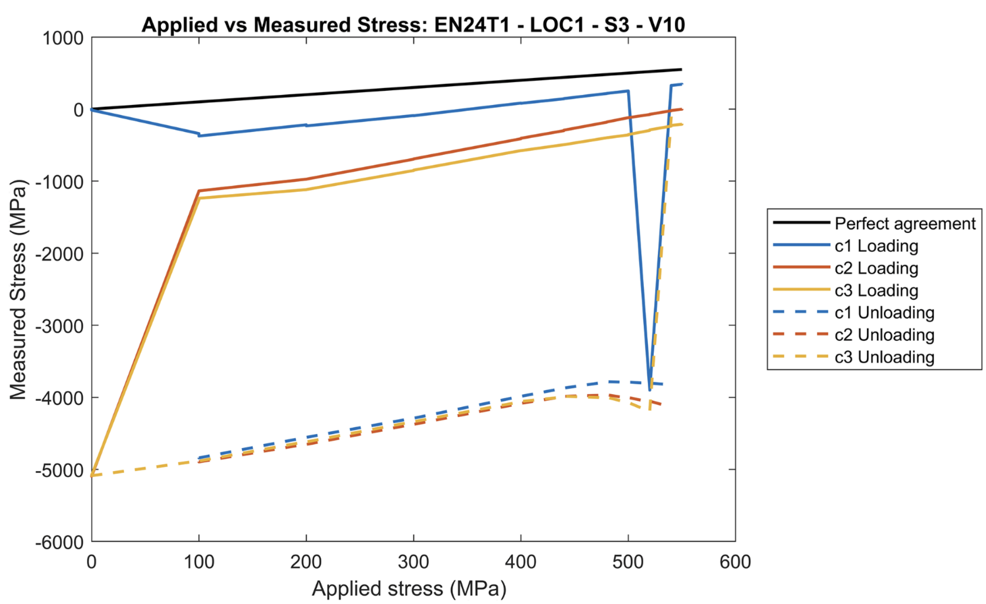

Figure 8.31: Plot of ultrasonically measured stress using the angled wedge method vs applied rig stress for set 3, high stress testing, separated by loading/unloading cycle for measurements conducted on specimen EN24T

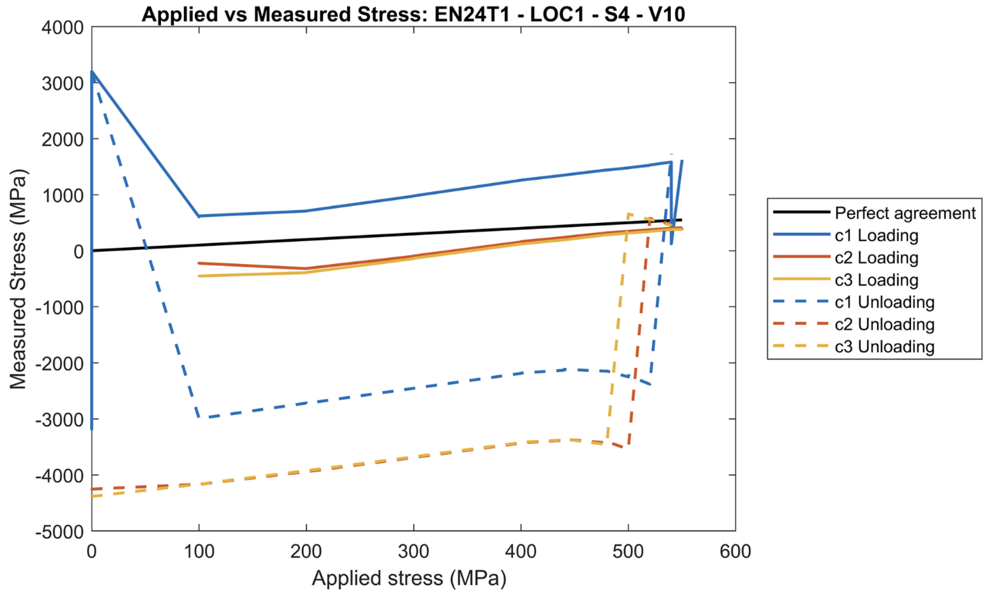

Figure 8.32: Plot of ultrasonically measured stress using the angled wedge method vs applied rig stress for set 4, high stress testing, separated by loading/unloading cycle for measurements conducted on specimen EN24T

Notwithstanding the obvious jumps resulting from the occasional incorrect peak selection within the data processing software, the 4x load range used in these high-stress tests has resulted in modestly improved accuracy. Contrasting results from the same data processing algorithm (peak find) from low- and high-stress testing we can see that the deviation from the perfect agreement line at maximum applied stress for EN24T (ranging from 500 – 1000 MPa) is proportionally less over the 540 MPa stress range than the 300 - 500 MPa deviation seen at 150 MPa applied stress in the previous round of testing. This is still, however, too high for a useful measurement technology.

8.7 Test platform 6 - high-speed DAQ testing

Previous tests identified two main sources of error in the stress predictions from the angled wedge method:

1. Measurement inaccuracy – The relatively small Signal-to-Noise-ratio (SNR) of the measured change in ToF relative to the experimental noise and digitisation rate has been a significant contributor to measurement inaccuracy.

2. Zero-offset – The fact that the measured stress has not equaled zero at zero applied stress creates a significant error in the angled wedge stress predictions. Once the high-stress testing had confirmed a positive outcome from increasing the SNR, I moved on to conducting a validation experiment using a High-Speed DAQ (HSDQ) system.

A modern HSDQ system was beyond the means of the project budget, however I was fortunate to have the help of a colleague, Dr Will Gray, to assemble a high speed system from some existing equipment.

The oscilloscope did not interface with any modern IT equipment, the only way to take high speed digitised signals from the device was to take a single wave-form saved on a floppy disk and transfer this manually each time. This had to be done for each of the individual wave-forms used in the averaging at each load step.

The restrictions on equipment access and vastly increased testing time necessitated a very short test matrix, so I conducted a short investigation as a proof of concept, using a single EN24T test specimen, with dimensions shown in Figure 8.33, to take a single set of data with 2 loading cycles.

Figure 8.33 shows the dimensions of the tensile specimen.

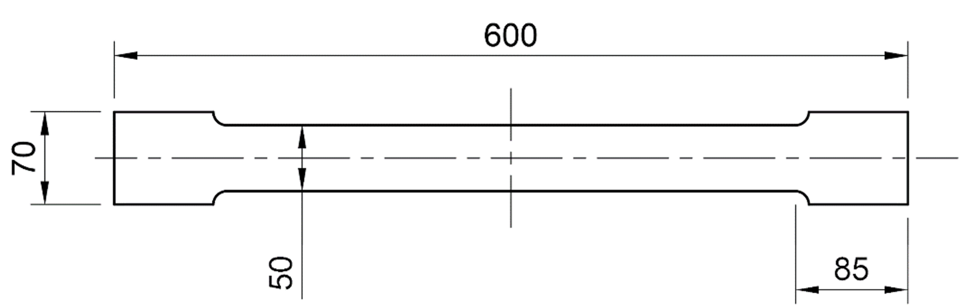

Figure 8.33: Dimensions of the tensile testing specimen

Table 8.5 shows the test details for the tensile test.

Table 8.5: Test summary for platform 6 high-speed DAQ test

Rig	Specimen(s)	Locations	Sets	Stress Range
Mayes 100kN	EN24T	1	3	0 – 55MPa

The correlation values are plotted for the reference and second reflection windows for both 35- and 55-degree signals, those for loading cycle 1 in Figure 8.34 and loading cycle 2 in Figure 8.35.

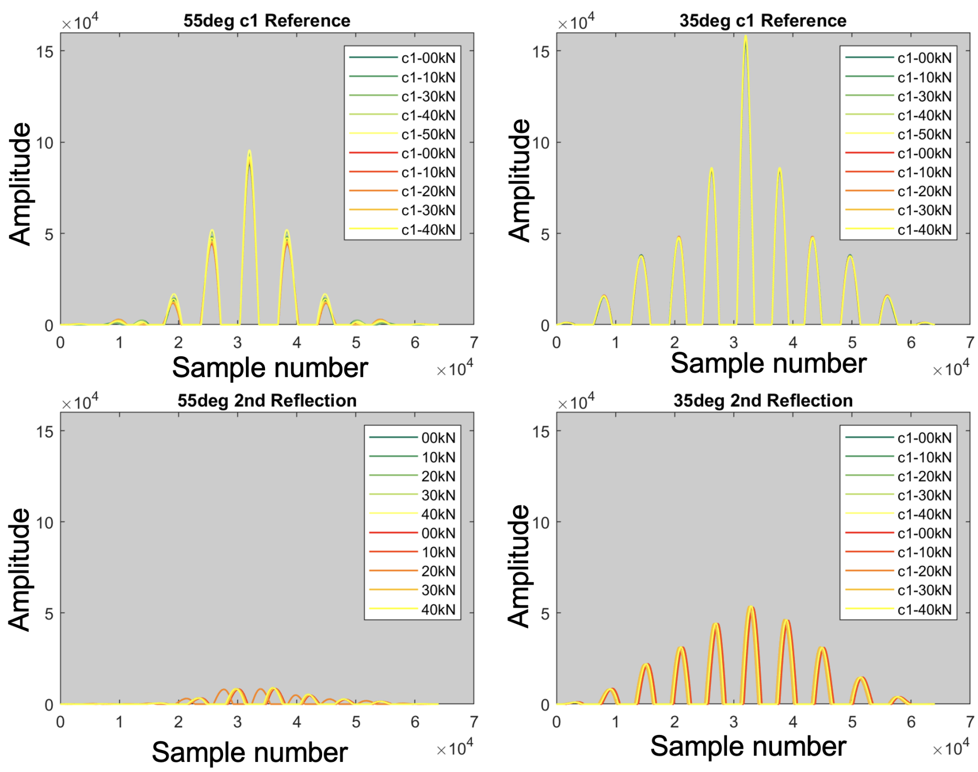

Figure 8.34: A screenshot of correlation value plots for each loading step for reference and second reflection signals, for both 35- and 55-degree signals – loading cycle 2

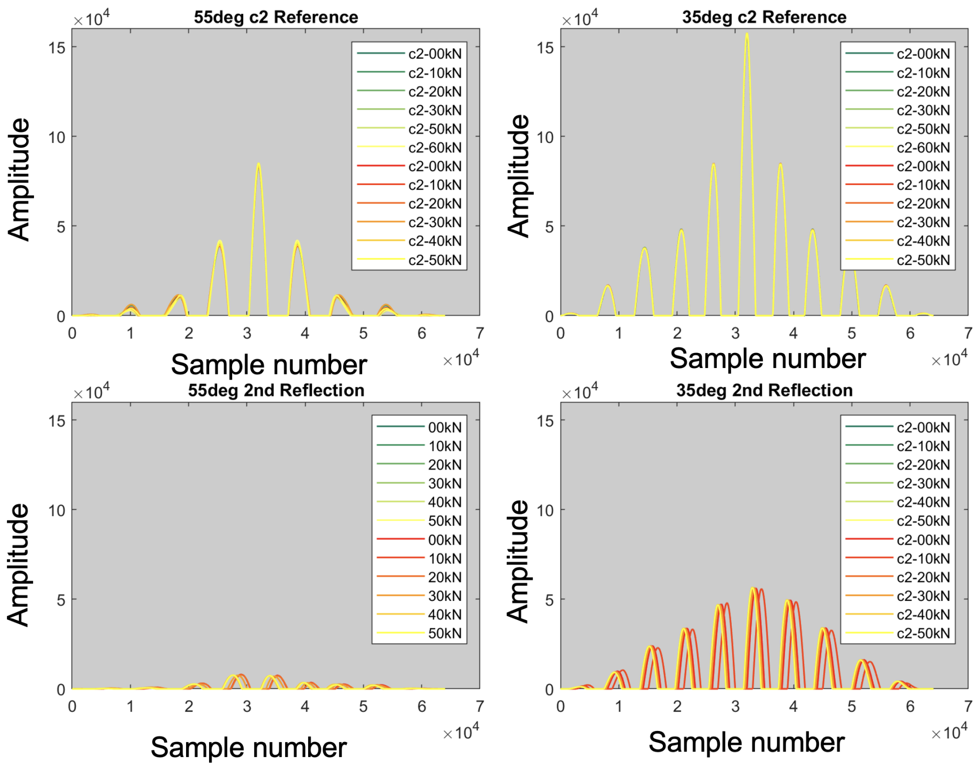

Figure 8.35: A screenshot of correlation value plots for each loading step for reference and second reflection signals, for both 35- and 55-degree signals – loading cycle 2

The peak-find model, along with the envelope model as the most promising alternative algorithms, were used to process the HSDQ data. The data are plotted at the same vertical scale to show the relative strength of the signal at each of the windows of interest. The 35-degree signals have excellent SNR. Those from the 55-degree transducers are very much lower. Peak values from the correlation data are plotted for loading cycle 1 in Figure 8.36 and for cycle 2 in Figure 8.37. Unlike data from the High Stress testing, only the 35-degree signals show alignment of the initial reference correlation maxima. The second reflection maxima from neither angle show a clear correlation with applied stress.

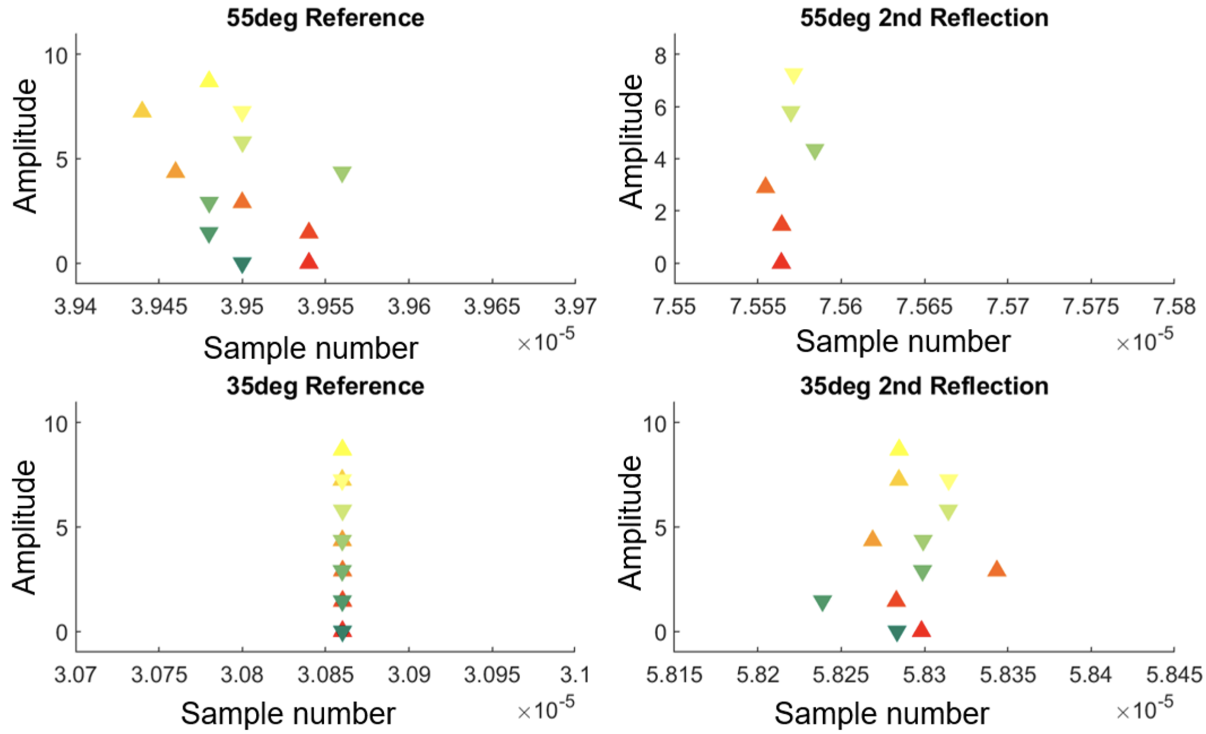

Figure 8.36: A screenshot of correlation value maxima for each loading step for reference and second reflections, for both 35- and 55-degree signals – loading cycle 1

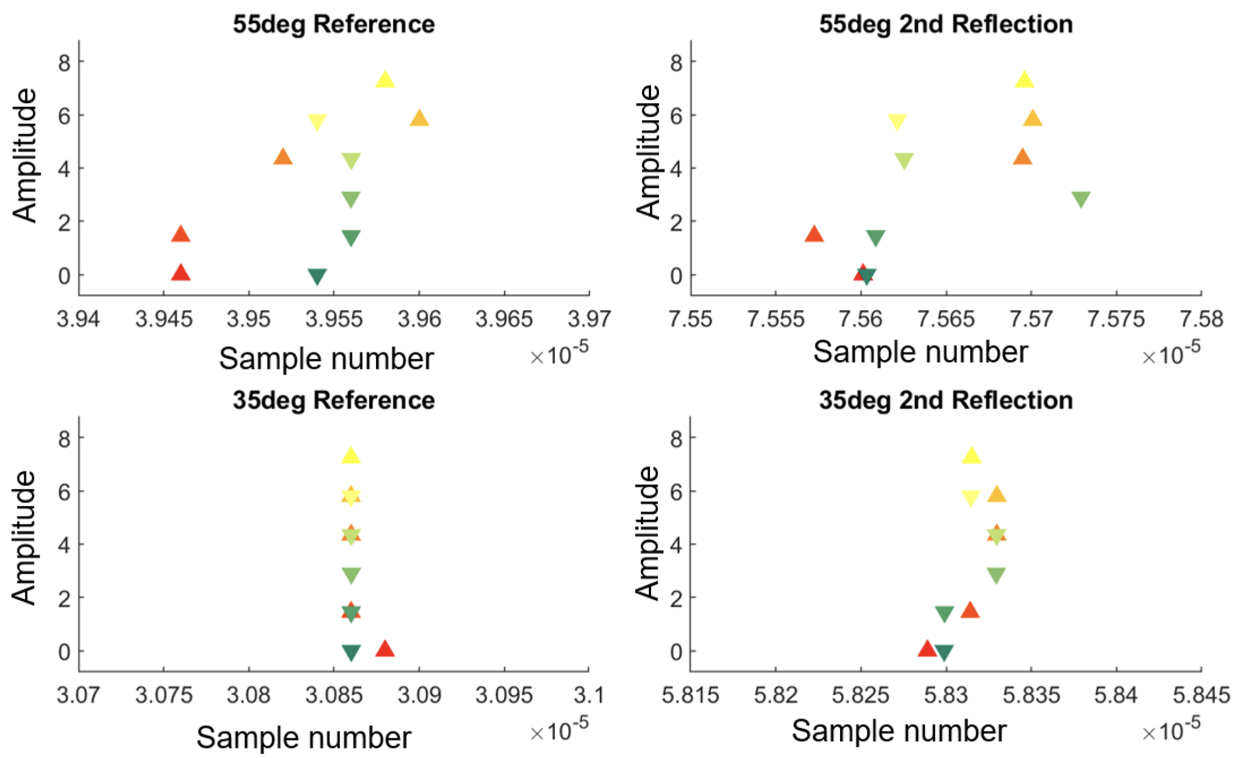

Figure 8.37: A screenshot of correlation value maxima for each loading step for reference and second reflections, for both 35- and 55-degree signals – loading cycle 2

The lack of correlation transfers directly to the ToF calculations shown for the peak find (Figure 8.38) and envelope models (Figure 8.39).

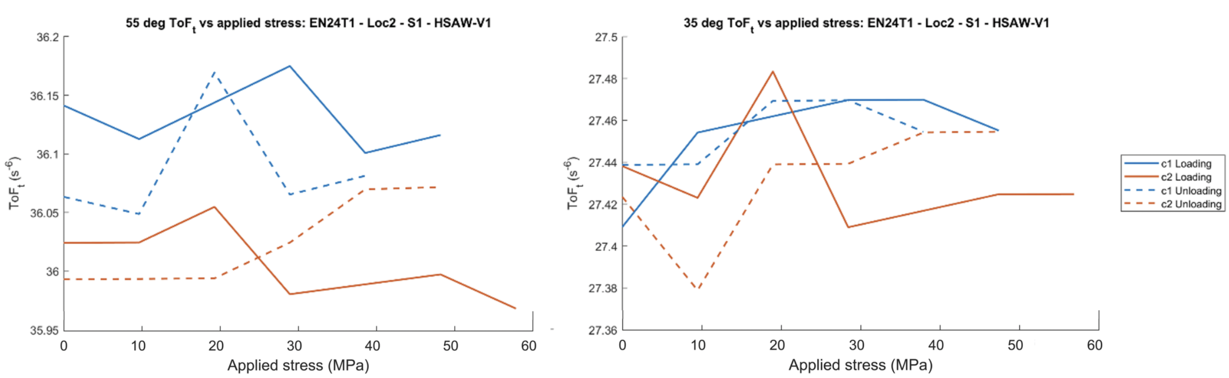

Figure 8.38: ToF vs applied stress for 35- and 55-degree signals – Peak-find model

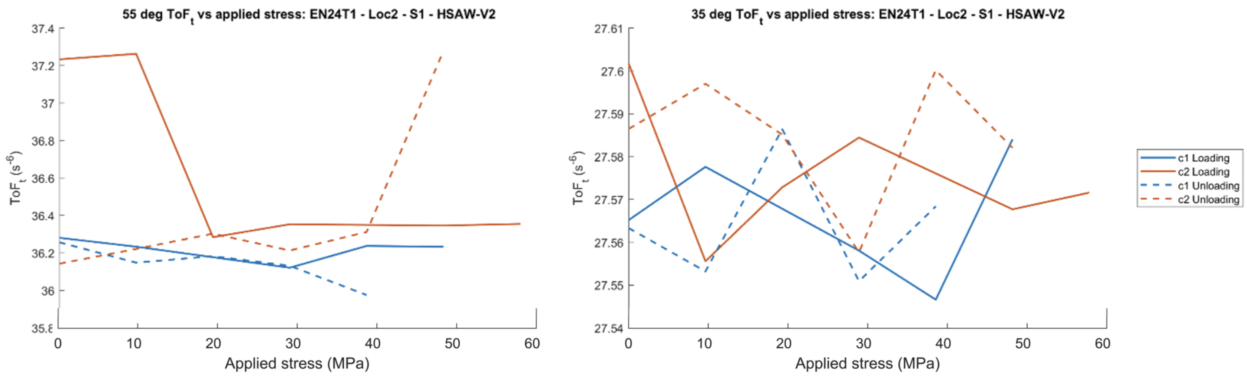

Figure 8.39: ToF vs applied stress for 35- and 55-degree signals – Envelope model

There is no consistent trend within either the 35- or 55-degree ToF data. As expected from the irregular ToF results, the stress prediction accuracy for the high-speed measurements is equally variable, shown in Figure 8.40 for the peak-find model, and Figure 8.41 for the envelope model.

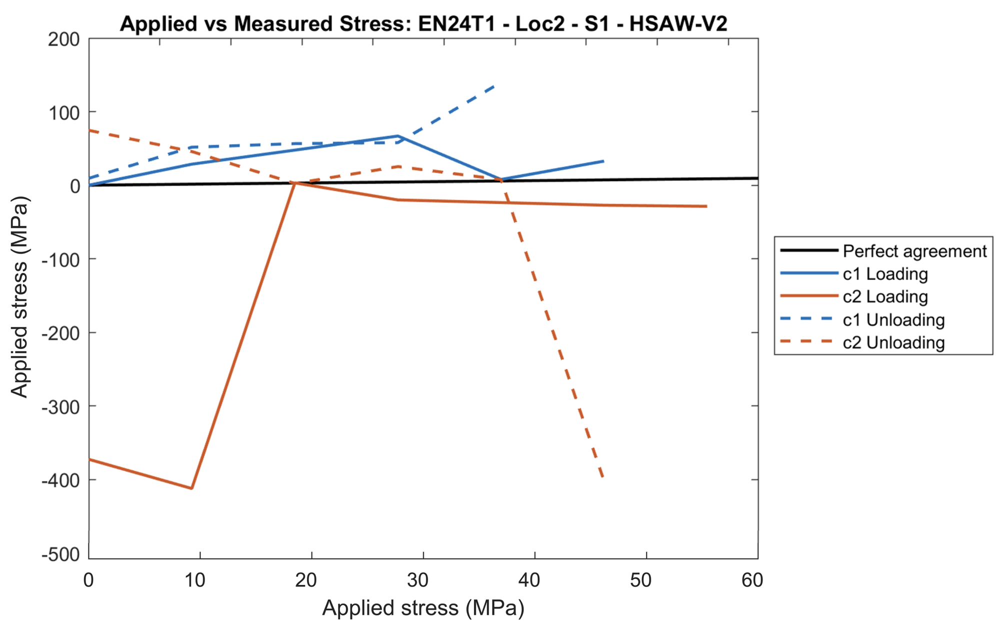

Figure 8.40: HSDQ Predicted vs applied stress – EN24T, Location 2, Set 1 peak-find processing model

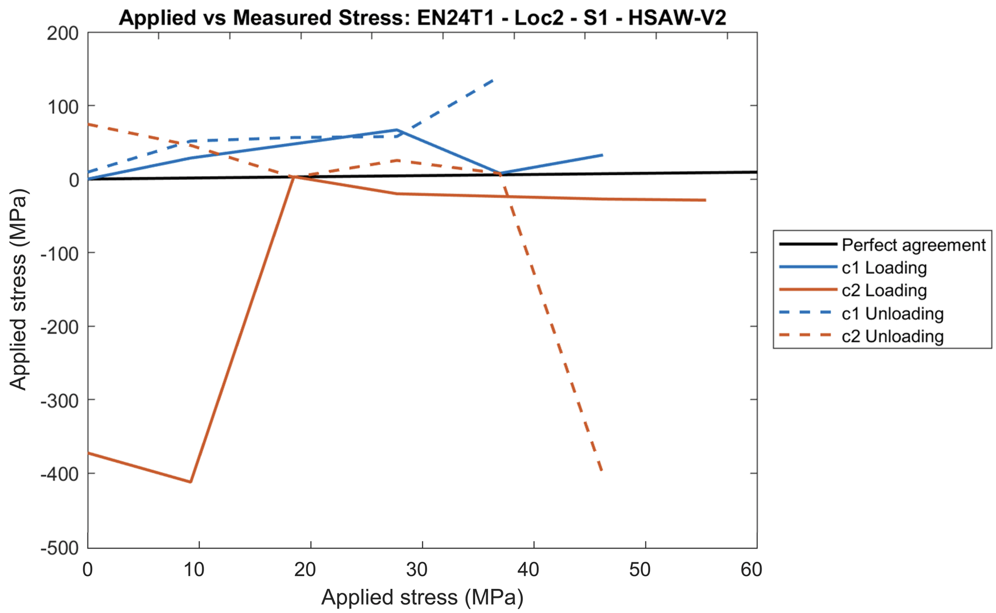

Figure 8.41: Measured vs applied stress for 35- and 55-degree signals – Envelope model

The large jumps in stress prediction in either of these plots is likely due to the inconsistency in the algorithms ability to align the 55-degree reference signal with itself (Figure 8.36 & Figure 8.37). I believe that the legacy nature of the oscilloscope, including its file system, the lack of integration into a computer controlled data capture system are all contributors to the poor results.

Chapter 9

Conclusions

Unfortunately, the primary goal of this work was not achieved - I did not manage to develop a calibration-free method for measuring thermally induced longitudinal stress in rail. This section details the progress that was achieved and the attendant conclusions.

9.1 Birefringence

Laboratory and track trials were carried out to investigate the effectiveness of the birefringence method for NRT measurement, across a total of 5 different test specimens (EN24T, R260A, R260B, R260D, R260E). Specimens were both placed in tension (laboratory) and compression (track).

The birefringence measurement was successful in returning material-specific ultrasonic constants to a higher degree of accuracy than previous empirical values. Table 9.1 shows a comparison between the empirical values and measured values that were calculated from the birefringence experiments using test platform 3.

Table 9.1: Table of calculated Lamé parameters from ultrasonic ToF data using test platform 3 in comparison to converted empirical values [85].

	Lamé values (GPa)		Third-order elastic constants		
	λ	μ	λ_1	μ_1	η_1
Empirical	$112 \pm 2.3\%$	$80.8 \pm 2.3\%$	$0.537 \pm 45\%$	$-0.129 \pm 50\%$	$-2.45 \pm 2.5\%$
Platform 3	$109 \pm 0.3\%$	$79.6 \pm 0.3\%$	$0.776 \pm 24\%$	$0.297 \pm 8\%$	$-3.43 \pm 4\%$

In the laboratory experiments, the birefringence technique was able to return a stress prediction accurate to 52 - 55MPa on R260 rail. This is nearly equivalent to entire 0 - 60MPa stress range of interest for in-service rails. Table 9.2 shows the mean of the calculated errors for both the expected vs measured constant of birefringence and the overall error induced by the zero-offset for each test specimen from the tensile testing done on test platform 4.

Table 9.2: Variation and errors for measured acoustoelastic constant and 'zero-offset' for birefringence testing of EN24T and R260 specimens

Specimen	C_{brfg}	σ_{offset} (MPa)	Error C_{brfg} (MPa)	Error σ_{offset} (MPa)	Cumulative max error (MPa)	Cumulative max error (°C)
EN42T	-1.146±7.78%	1524±165%	11.7	2506	2718	1058
R260-A	-1.197±36.8%	4141±0.42%	55.2	17.4	72.6	37.8
R260-B	-1.462±34.8%	91±774%	52.2	6897	6949	2919

The full-rail testing for the birefringence method returned more accurate and less variable results. Table 9.3 gives the average values for C_{brfg}, zero-offset and their respective error percentages, for the full rail testing and also tabulates the impact these errors have on the measurement of both stress and NRT.

Table 9.3: Variation and errors for measured acoustoelastic constant and 'zero-offset' for birefringence testing of two full rail R260 specimens and the effect of this variation on the error in stress measurement and NRT

Specimen	C_{brfg}	σ_{offset} (MPa)	Error C_{brfg} (MPa)	Error σ_{offset} (MPa)	Cumulative max error (MPa)	Cumulative NRT error (°C)
R260D-L1	-1.62±21.1%	-468±11%	18.8	51.2	70.0	29.0
R260D-L2	-1.34±36.8%	-500±26%	16.1	130.4	146.5	60.7
R260E-L1	-1.14±34.8%	-456±03%	15.8	14.5	30.3	12.5
R260E-L2	-0.98±34.8%	-388±12%	38.2	41.1	79.3	32.8

The equivalent C_{brgf} error for the on-track measurements is significantly lower and more consistent than those conducted in the laboratory, between 26 and 63 percent of the stress range of interest. The zero-offset error is also significantly reduced. The reasons for this are unclear.

As it stands, the birefringence technique has not shown the required accuracy for use in NRT measurement. It is also important to consider that the results have been corrected for zero-offset, and no consistent value or repeatable experimental process was found to eliminate this other source of error. It remains possible that a higher speed DAQ system could enable an accurate calibration value in the future.

9.2 Angled wedge

Laboratory and track trials were carried out to validate the calibration-free, angled wedge NRT measurement method across a total of 5 different test specimens (EN24T, R260A, R260B, R260D, R260E). Specimens were both placed in tension (laboratory) and compression (track). High-stress level testing was conducted on EN24T and R260 samples to simulate higher speed data acquisition and finally a high speed DAQ system was developed and tested on lower stress ranges.

Although initial problems were encountered with highly non-linear responses from the 35-degree ToF data, that specific issue was overcome by improving the experimental set-up. The 55-degree ToF data, in contrast, have proven to be the least reliable in more recent testing phases. I believe this to be a result of degradation of the sensor assemblies over the duration of the project. The signal quality and clarity, especially of the later reflections, deteriorated over time.

In addition, several other challenges were encountered, some at a very late stage in the project. The sensitivity analysis implied the presence of unknown interactions with the wedge/specimen interface and the long travel-path and the irregular wave forms were also sources of inaccuracies in ToF calculation. I believe it unlikely that these issues can be resolved simply through improvements to the algorithms at this time.

It was also noticed at a very late stage in the investigation that the signals for the angled wedge data showed signs of clipping. This was a devastating realisation for the confidence in the ToF extraction method, as it could be the single greatest contributing factor to the variance and persistent inaccuracy of the angled wedge method. Improving the reliability of the signal waveform through sensor re-instrumentation (perhaps moving back to larger sensor assemblies) to obtain more reflections from which to calculate ToF, would improve the measurement significantly, and would mitigate the potential of signal clipping.

Each stage of the project resulted in improvements to either the sensor clamp, sensor assemblies and data processing algorithms, resulting in a general trend of improved results, the measurement from the angled wedge method has not reached a sufficient reliability to record a confident accuracy value. The variance of the measurements in the best cases is an order of magnitude more than the target measurement range, and the zero-offset issue has not been successfully resolved. It is not conclusively known whether or to what extent material property variation is impacting the measurements as the reliability and resolution of the measurements has not been fine enough to see patterns in the sensitivity analyses. The sensitivity analysis was conducted with a slower digitization rate, however, so it would be of interest to troubleshoot the HSDQ system and data processing and conduct another sensitivity analysis. Table 9.4 shows a comparison of the zero-offset values for the uncorrected data from both HSDQ and high stress testing for the peak find and envelop data processing methods.

Table 9.4: Mean modulus values for zero-offset from high-speed and high-stress test phases for both peak find and envelope data processing methods

	HSDQ (MPa)	High Stress (MPa)
Peak Find	641	3213
Envelope	1276	2179

A mean of the modulus values has been presented to retain the magnitude of the error, rather than a simple mean that would have obscured the overall magnitudes due to the varying signs.

The increase in digitization rate using the HSDQ seems to have improved the zero-offset values significantly for both peak find and envelope models, though they are still variable, have varying signs, and remain an order of magnitude larger than the maximum stress of the target measurement range. The HSDQ data set was also very small and a much larger data set would be needed to both troubleshoot the accuracy issues as well as validate the zero-offset improvements

The results have shown directly that the larger range gives better accuracy, however the consistent inconsistency revealed the need for a more in-depth investigation into the data processing methodology.

Investigation as to why the results were so unpredictable lead to the development of three separate models to extract the ToF. These different methods greatly affect both variance, accuracy and repeatability of the data.

A mean of the modulus values has been presented to retain the magnitude of the error, rather than a simple mean that would have obscured the overall magnitudes due to the varying signs. The increase in digitization rate seems to have improved the zero-offset values significantly, though they are still variable, have varying signs, and remain an order of magnitude larger than the maximum stress of the target measurement range. The HSDQ data set was also very small and a much larger data set would be needed to both troubleshoot the accuracy issues as well as validate the zero-offset improvements.

Data captured in on-track testing using a somewhat rudimentary, though carefully undertaken, rail preparation method proved successful in reproducing measurements of similar accuracy and variability to those captured in the laboratory with high-accuracy ground specimens. Should the problems with the laboratory measurement be solved, and the results brought into a suitable accuracy range, I feel confident that the angled wedge measurement would be directly transferable to the track.

9.2.1 Clamping assembly manufacturing tolerance

There is a consistent problem with signal shift moving from loading to unloading and vice versa. From experimental experience, the manufacturing tolerance of some of the components was not sufficiently accurate, requiring the use of very thin shim material to ensure correct parallelism between wedges.

The clamping assembly is also made from multiple components (for cost, weight and machining considerations). It is suspected that there is a slight shift in geometry, alignment or couplant thickness at these inflection points that slightly changes the waveform, especially that of the 55-degree signals which travel a longer flight-path and are more susceptible to interference of this kind.

9.2.2 Numerical accuracy

The variance of many data sets is greater than the overall measurement. Without significant additional analysis, particularly of the R260 results, there area also to many outlier data points, most likely the result of incorrect windowing or peak selection. The removal of these would, in the opinion of the UoS team, invalidate error calculations made on a cherry-picked data set. Therefore, calculation of numerical accuracy values for this dataset is not currently meaningful.

Chapter 10

Transfer to track

10.1 Current progress

During this work, I have advanced the development of a novel measurement technology that showed some potential to return calibration-free ultrasonic measurement of rail LS. This has not shown sufficient robustness in laboratory or full-scale testing at this time.

I have also made a number of iterations and refinements to an existing prototype for measuring longitudinal rail stress using the birefringence method. This, while requiring some calibration, has delivered more reliable results in the laboratory, and has exhibited much less disruption to the measurements when trialled on full rail under compression. This is still, however, susceptible to too large an error and a lacks the required repeatability for a reliable measurement.

10.2 Future work

It is my hope that this thesis can be of service to others in future attempts at ultrasonic analysis of stress states in constrained steel structures.

To that end, I present my proposed first steps in any continuing investigations, or the tests I was not, for lack of time, skill or other resources, able to complete.

1. High-speed low-voltage testing

   Using much larger sensors and lower voltage in combination with a very fast DAQ system to attempt to overcome the combination of signal clipping and high SNR could lead to much improved accuracy, or at least increase the measurement sensitivity enough to determine the impact of varying experimental parameters such as surface roughness.

2. Solid couplant layer

   Removing the inconsistency and poor temperature stability of the glycerin-based couplant would likely lead to much improved repeatability in lab and on-track testing would eliminate the precession from zero shown in repeated loading cycles.

3. Hybrid measurement

   With more time I would have been excited to conduct more in-depth measurements with different combinations of birefringence, angled wave and surface wave modes.

The following subsections also detail some larger-scale investigations that could address gaps in fundamental knowledge that could be of use to this work and to many others in the area of ultrasonic analysis in rail.

10.3 Existing constraints

The results of the sensitivity analysis showed that while both measurements are significantly impacted by several experimental conditions, such as the parallelism or surface finish of the rail specimen, the birefringence measurement is less susceptible to error on all counts.

In light of these results this section assesses the likelihood, and comments on the prospective difficulty, of overcoming the current barriers as exposed during this work. In short, is it possible to transfer these technologies to track?

10.3.1 Contact between sensors and rail

The requirement for a portable tool capable of quick successive measurements by a track-side operative introduces the need for removable ultrasonic sensors. The non-permanent interface is complex. While there is a long history of removable ultrasonic sensors used in NDT, the type of measurement being attempted here, the required accuracy and alignment sensitivity and the incredibly high data resolution complicates this even further.

The measurement system must therefor overcome challenging variability in:

1. Condition of the couplant layer (viscosity, thickness, couplant composition)
2. Rail surface (parallelism/waviness, surface roughness, presence of rust or dirt)
3. Condition of the sensor face/piezo-electric transducer (surface wear, damage, alignment/parallelism)

The investigations conducted during the sensitivity analysis were necessarily brief. While they were informative, they were not conclusive and provided no detailed quantitative data on the impact of changing the couplant viscosity, temperature or material on the ultrasonic ToF. It is this author's opinion that there could be many years of dedicated investigation on the use of, and variability resulting from, liquid couplants alone.

10.3.1.1 Ultrasonic couplant

The current practice for transmission of shear waves through structural materials is the use of a glycerin-based coupling fluid.

User experience has shown that the couplant enables better signal transmission and a more stable zero-offset values at temperatures below 23°C. This is most likely due to the changes in viscosity at higher temperatures.

At higher temperatures there is also visual evidence of more couplant leakage from the sensor-specimen interface. This could be a significant impact on the precession of ToF values over subsequent loading cycles.

Additional investigations:

A comprehensive investigation into couplant suitability and effects on measurements is necessary to fully understand and control the zero-offset measurements. Such a study should include:

1. Exploration of all commercially available liquid couplants, seeking advice and feedback from the manufacturers
2. Feasibility investigation into use solid couplants ie. acoustic rubber
3. Exploration of semi-permanent sensor installation
   - Using heat-debondable adhesives (such as those commonly used in the automotive industry for bonding glass into car bodies)
   - Low ductility permanent adhesives (hoping to use the adhesive's brittle failure mode to remove a sensor assembly once measurements are complete)
4. Consideration of low-cost permanent installations depending on the desired measurement or sensor assembly type. Sensors could be bonded in place using:
   - Permanent adhesives
   - Friction welding

10.3.1.2 Rail web surface preparation

Currently, tensile specimens are ground flat and parallel to ensure the best quality investigation and experimental data. The sensitivity analysis has shown that the measurements are very susceptible to any miscalculation or error in flight path length, though measurements are not significantly impacted by the absolute value of the surface roughness. This indicates that the parallelism of the faces is by far the most important concern.

It is therefore reasonable to conclude that a device could be designed and manufactured to the required tolerances to conduct automated preparation of the rail web surface to achieve a high-quality surface finish with accurate dimensional tolerance of the parallelism, in both vertical and longitudinal planes, of the two sides of the web.

The surface finish requirement could be satisfied by the application of grinding wheels, liquid abrasive mixes or sandpaper. The UoS team would suggest that the clamping arrangement for whichever surface preparation mechanism is of paramount importance. The datum level of the underside of the rail foot would provide the most accurate location both for rigid clamping and accurate determination of the parallelism of the web faces. Multi-bar linkages would be required, perhaps linked together on either side, to ensure the surface preparation equipment was operating exactly in the same plane on either side of the rail web. A solution to this problem would be expensive but is currently both realistic and feasible.

Additional investigations:

A detailed design project is needed to develop a new piece of rail track machinery to complete high-tolerance surface preparation of measurement locations on rail webs.

10.3.2 Limitations in digitisation frequencies

There have been two separate DAQ systems used in this investigation. The majority of the testing was conducted using an oscilloscope from Pico Technology (model 5442D) which operates at a maximum limit of 0.5 GigaSamples per second (GS), equivalent to a time-resolution of 2ns.

The theoretical sensitivity analysis in Section 5 concluded that errors from sampling frequency would be minimal provided that adequate interpolation and averaging of signals were done during data capture and processing. In reality, a time resolution of 2ns between two orthogonally polarised signals would equates to a 40.7MPa difference in measured stress.

For birefringence measurements, this is roughly equal to the values returned for the C_{brfg} values. It follows that this could realistically be the source of inaccuracy in that measurement, though it still leaves uncertainty regarding the much larger zero-offset.

For the angled wedge technique, the 2ns time resolution has between 2 and 3 time less impact on the ToF percentage error, but a much higher overall error due to the square of the ToF terms in the numerator of the universal stress equation.

The data obtained from the short investigation conducted with a high speed DAQ was not sufficiently reliable to make a valuable comparison. I suspect that the influence of other experimental factors dominate the data variance in the angled wedge case.

A quick search revealed that the fastest commercially available DAQ system on the market the DSOX6004A, manufactured by Keysight Technologies. Capable of capturing 20 GS (equivalent to a time resolution of 0.05 ns) this system could reduce the SoS error to $\pm 0.013ms^{-1}$, equating to a potential zero-offset error of $\pm 0.5MPa$. Costing £28,000, however, would limit the accessibility of the technology to the marketplace. **Future investigations:**

An alternative would be to undertake the design development of a bespoke system-on-chip solution. Developing a bespoke system-on-chip multiplexing DAQ architecture could enable a higher sample rate acquisition and a reduced error factor.

10.3.3 Variation in acoustoelastic constants

Past investigations into an ultrasonic measurement system for determining longitudinal rail stress, such as the Debro30, have concluded in-service rails have significant variation in their acoustoelastic constants and steel quality (specifically the possibility of impurity inclusions within the rail web) originating from several sources, such as service life, age, provenance (year and site of manufacture) and variation by location along a single rail section.

There is too little data on these variables to make a serious assessment as to the potential impact of these variations, and the investigation presented in this these has failed to differentiate between these features above the overall experimental noise.

The use of a higher-speed DAQ system could potentially address the visibility of these experimental parameters and material constants.

Additional investigations:

It would be of great benefit to the rail industry to conduct a thorough analysis of acoustoelastic constants for a wide cross-section of track samples from across the rail network would provide a library of essential data for improving the measurement accuracy and calibration of the birefringence method. This would require a thorough investigation into the acoustic properties of all rail types and ages within the established rail network.

10.3.4 Calibration as a solution

Based on the results shown in Table 7.8, between 50 and 60 percent of the overall error originates from the unpredictable zero-offset. Should the zero-offset issue be resolved or stabilised, and a sufficiently quick DAQ system be used, I believe that accurate calibration is a realistic prospect for the birefringence method.

References

[1] Wikipedia, Rail transportation in the united states (2022).

[2] Wikipedia, List of common carrier freight railroads in the united states (2022).

[3] Association of American Railroads, Climate change report (2021).

[4] S. Delouya, Why doesn't the us have more passenger trains? (2023).

[5] Wikipedia, Transport in the european union (2023).

[6] Eurostat, Modal split of inland freight transport, 2020 (%, based on tonne-kilometres) (2020).

[7] W. S. Raphael Preindl, Roadmap - combined transport in light of the european green deal, International Union of Combined Road-Rail Transport (2021).

[8] Briefing, High speed railroading, The Economist (2010).

[9] US Department of Transportation, Travel trends report: Transit ridership on the rise nationwide, industry supports hundreds of thousands of jobs (2025).

[10] US Department of Transportation, 2023 national transit summaries trends (2023).

[11] US Department of Transportation, Transportation statistics annual report (2024).

[12] US Department of Transportation, Railroad update, Rail Energy Transportation Advisory Committee (2024).

[13] U.S. Bureau of Transportation Statistics, Rail freight carloads, retrieved from FRED, Federal Reserve Bank of St. Louis (2025).

[14] U.S. Bureau of Transportation Statistics, Rail freight intermodal traffic, retrieved from FRED, Federal Reserve Bank of St. Louis (2025).

[15] Eurostat, Railway freight transport statistics (2023).

[16] Office of Rail and Road, Table 1350 - rail freight market share (2025).

[17] Office of Rail and Road, Freight rail usage and performance (2024).

[18] Office of Rail and Road, Table 1230 - passenger kilometres (2025).

[19] Association of American Railroads, Railroad 101 - freight railroads fact sheet (2022).

[20] M. Andrei, Germany slashes public transit fares to reduce fuel usage, ZME Science (2022).

[21] European Commission, The European Green Deal, International Union of Combined Road-Rail Transport (2019).

[22] Wikipedia, Trans-european transport network (2023).

[23] Infrastructure: update to ten-t corridor work plans (2020).

[24] European Commission, Trans-european transport network - ten-t core network corridors (pre-brexit) (2020).

[25] E. Commission, Trans-european transport network - ten-t core network corridors (post-brexit) (2023).

[26] J. Blaze, What's the 2020 outlook for railroad capital expenditures?, Railwayage.com (2019).

[27] AMTRAK, Amtrak's vision for improving transportation across america (2021).

[28] A. Ohnsman, Amtrak buying $3.4 billion of advanced siemens trains as it overhauls rail network, Forbes.com (2021).

[29] Intergovernmental Panel on Climate Change, Climate change 2021 - the physical science basis (2021). doi:10.1017/9781009157896.

[30] E. A. Kostianaia, A. G. Kostianoy, M. A. Scheglov, A. I. Karelov, A. S. Vasileisky, Impact of regional climate change on the infrastructure and operability of railway transport, Transport and Telecommunication 22 (2021) 183–195. doi:10.2478/ttj-2021-0014.

[31] Network Rail, Challenge statement - track rail stress management (2019).

[32] Network Rail, Challenge statement - enabling transition to predict and prevent maintenance regimes (2019).

[33] D. Browne, Hs2 plans digital 'predict and prevent' maintenance, Transport Network (2022).

[34] J. Duggan, Bidding open for £275 million hs2 control centre and maintenance depot, Rail Advent (2021).

[35] A. Stansfield, C. Ciobanu, An introduction to rail thermal force calculations, Permanent Way Institution 135 (2017).

[36] F. Railroad, Track buckling prevention : Theory , safety concepts , and applications (2013).

[37] Arcadia, Modelling the impacts of climate change on cities: Economic costs of rail buckle events.

[38] G. Liu, H. Liu, A. Wei, J. Xiao, P. Wang, S. Li, A new device for stress monitoring in continuously welded rails using bi-directional strain method, Journal of Modern Transportation 26 (2018) 179–188. doi:10.1007/s40534-018-0164-z.

[39] H. He, Y. Ling, A law for the temperature-induced stress distribution in continuously welded rail, Proceedings of the Institution of Mechanical Engineers, Part F: Journal of Rail and Rapid Transit 229 (2015) 500–506. doi:10.1177/0954409713516612.

[40] A. Miri, M. Dhanasekar, D. Thambiratnam, B. Weston, T. H. Chan, Analysis of buckling failure in continuously welded railway tracks, Engineering Failure Analysis 119 (1 2021). doi:10.1016/j.engfailanal.2020.104989.

[41] S. G, K. A, P. J, K. A, S. A, Wood tie track resistance charaterization and correlations study, US Department of Transportation (1995).

[42] A. Skarova, J. Harkness, M. Keillor, D. Milne, W. Powrie, Review of factors affecting stress-free temperature in the continuous welded rail track, Energy Reports 8 (2022) 769–775. doi:10.1016/j.egyr.2022.05.046.

[43] J. Szelazek, Ultrasonic measurement of thermal stresses in continuously welded rails, NDTnet 3 (1992).

[44] K. Knopf, D. C. Rizos, Y. Qian, M. Sutton, A non-contacting system for rail neutral temperature and stress measurements: Concept development, Structural Health Monitoring 20 (2021) 84–100. doi:10.1177/1475921720923116.

[45] A. T. M, Measuring the neutral temperature in railway track during installation and use, Ph.D. thesis, Delft University of Technology (2011).

[46] E. Johnson, Measurement of forces and neutral temperatures in railway rails - an introductory study (2004).

[47] G. Kjell, E. Johnson, Measuring axial forces in rail by forced vibrations: Experiences from a full-scale laboratory experiment, Proceedings of the Institution of Mechanical Engineers, Part F: Journal of Rail and Rapid Transit 223 (2009) 241–254. doi:10.1243/09544097JRRT210.

[48] V. Damljanović, R. L. Weaver, Laser vibrometry technique for measurement of contained stress in railroad rail, Journal of Sound and Vibration 282 (2005) 341–366. doi:10.1016/j.jsv.2004.02.055.

[49] X. Zhu, F. L. di Scalea, Thermal stress measurement in continuous welded rails using the hole-drilling method, Experimental Mechanics 57 (2017) 165–178. doi:10.1007/s11340-016-0204-8.

[50] A. Nasrollahi, P. Rizzo, Numerical analysis and experimental validation of an nondestructive evaluation method to measure stress in rails, Journal of Nondestructive Evaluation, Diagnostics and Prognostics of Engineering Systems 2 (8 2019). doi:10.1115/1.4043949.

[51] G. A. Alers, A. Manzanares, Use of surface skimming sh waves to measure thermal and residual stresses in installed railroad tracks introduction, Review of Progress in Quantitative Nondestructive Evaluation 9 (1990).

[52] J. Szelazek, Monitoring of thermal stresses in continuously welded rails with ultrasonic technique, Institute of Fundamental Technological Research, Warsaw, Poland, (1998).

[53] S. Hurlebaus, Determination of longitudinal stress in rails (2011).

[54] C. Nucera, R. Phillips, F. L. di Scalea, M. Fateh, G. Carr, System for in situ measurement of neutral temperature in continuous-welded rail: Results from laboratory and field tests, Transportation Research Record: Journal of the Transportation Research Board 2374 (2013) 154–161.

[55] H. V., Structural and residual stress analysis by nondestructive methods, Amsterdam: Elsevier Science, 1997.

[56] A. Wegner, Prevention of track buckling and rail fracture by non-destructive testing of the neutral temperature in cw-rails, IHHA Spezialist Technical Session (STS) Kiruna Sweden (2007).

[57] C. Nucera, R. Phillips, F. Lanza, D. Scalea, A wayside system for in-situ measurement of rail neutral temperature by nonlinear ultrasonic guided waves (2012).

[58] X. Zhu, F. L. di Scalea, Sensitivity to axial stress of electro-mechanical impedance measurements, Experimental Mechanics 56 (2016) 1599–1610. doi:10.1007/s11340-016-0198-2.

[59] N. K. Mandal, M. Lees, Effectiveness of measuring stress-free temperature in continuously welded rails by rail creep method and rail stress modules, Engineering Failure Analysis 104 (2019) 189–202. doi:10.1016/j.engfailanal.2019.05.032.

[60] HBM, 'the fatigue life of electrical strain gauges.

[61] Y. Guo, Z. Yu, H. Shi, Effects of rail thermal stress on the dynamic response of vehicle and track, Vehicle System Dynamics 53 (2015) 30–50. doi:10.1080/00423114.2014.973420.

[62] Y. Luo, L. Li, H. Yin, A dynamic analysis of a continuous welded rail track under a longitudinal stress caused by temperature changes, Proceedings of the Institution of Mechanical Engineers, Part F: Journal of Rail and Rapid Transit 224 (2010) 91–101. doi:10.1243/09544097JRRT290.

[63] P. Šarga, F. Trebuňa, Modern trends in the field of measurement of residual stresses using hole-drilling method 4 (2016) 353–356. doi:10.12691/ajme-4-7-21.

[64] P. Šarga, F. Trebuňa, Modern trends in the field of measurement of residual stresses using hole-drilling method 4 (2016) 353–356.

[65] P. Wang, S. Zhu, G. Y. Tian, H. Wang, X. Wang, Stress measurement using magnetic barkhausen noise and metal magnetic memory testing 3 . experiment setup and typical bn signal, Stress: The International Journal on the Biology of Stress (2008) 25–28.

[66] J. W. Wilson, G. Y. Tian, V. Moorthy, B. A. Shaw, Magneto-acoustic emission and magnetic barkhausen emission for case depth measurement in en36 gear steel, IEEE Transactions on Magnetics 45 (2009) 177–183.

[67] A. Stupakov, A. Perevertov, M. Neslušan, Reading depth of the magnetic barkhausen noise. i. one-phase semi-hard ribbons (2020).

[68] D. Shu, L. Yin, J. Bu, J. Chen, X. Qi, Application of a combined metal magnetic memory-magnetic barkhausen noise technique for on-site detection of the stress-free temperature of a continuous welded rail, Proceedings of the Institution of Mechanical Engineers, Part F: Journal of Rail and Rapid Transit 230 (2016) 774–783. doi:10.1177/0954409714562874.

[69] S. Ding, P. Wang, Y. Lin, D. Zhu, Reduction of thermal effect on rail stress measurement based on magnetic barkhausen noise anisotropy, Measurement: Journal of the International Measurement Confederation 125 (2018) 92–98. doi:10.1016/j.measurement.2018.02.041.

[70] D. Read, B. Shust, Investigation of prototype rail neutral temperature measurement system, Railway Track Structures 103 (2007).

[71] PANDROL, Verse product information sheet (2002) 2.

[72] H. Du, J. A. Turner, Ultrasonic attenuation in pearlitic steel, Ultrasonics 54 (2014) 882–887. doi:10.1016/j.ultras.2013.10.017.

[73] D. Read, Advances in rail neutral temperature measurement techniques, Railway Track & Structures 106 (2010) 21.

[74] F. Djayaputra, Determination of longitudinal stress in rails, Ph.D. thesis (2010).

[75] J. Turner, Ultrasonic stress measurement, Ph.D. thesis, University of Nebraska-Lincoln.

[76] C. Esveld, Improved knowledge of cwr track, Interactive Conference on Cost Effective-ness and Safety Aspects of Railway Track, UIC/ERRI, Paris (1998) 8–9.

[77] M. S. Dersch, Vibration-based longitudinal rail stress estimation exploiting acoustic measurement and machine learning (2020).

[78] A. Aikawa, H. Sakai, K. Abe, Numerical and experimental study on measuring method of rail axial stress of continuous welded rails based on use of resonant frequency, Quarterly Report of RTRI 54 (2013) 118–125.

[79] C. Nucera, F. L. di Scalea, Nondestructive measurement of neutral temperature in continuous welded rails by nonlinear ultrasonic guided waves, Journal of the Acoustical Society of America 136 (2014) 2561–2574.

[80] A. Skarova, J. Harknessa, W. P. Matthew Keillorb, David Milnea, The verification of rail thermal stress measurement system, Periodica Polytechnica Transportation Engineering 48 (2020) 45–51.

[81] M. S. Kang, A. Azad, Y.-K. An, Neutral temperature estimation of continuous welded rails using group velocity of ultrasonic waves, e-Journal of Nondestructive Testing 27

(9 2022). doi:10.58286/27213.

[82] D. Vangi, A. Virga, A practical application of ultrasonic thermal stress monitoring in continuous welded rails, Experimental Mechanics 47 (2007) 617–623. doi:10.1007/s11340-006-9016-6.

[83] M. Hirao, H. Ogi, Advanced ultrasonic method for measuring rail axial stresses with electromagnetic acoustic transducer 5 (1994) 211–223.

[84] Y. Yang, Don't know the exact title, The University of Sheffield (2023).

[85] D. M. Egle, D. E. Bray, Measurement of acoustoelastic and third-order elastic constants for rail steel, Journal of the Acoustical Society of America 60 (1976) 741–744. doi:10.1121/1.381146.

[86] G.-Y. Li, A. L. Gower, M. Destrade, An ultrasonic method to measure stress without calibration: The angled shear wave method, The Journal of the Acoustical Society of America 148 (2020) 3963–3970.

[87] Olympus IMS, retrieved from olympus com (2021).

[88] C. H. Gür, B. O. Tuncer, Characterization of microstructural phases of steels by sound velocity measurement, Materials Characterization 55 (2005) 160 – 166.

[89] J. J. Lewandowski, A. W. Thompson, Effects of the prior austenite grain size on the ductility of fully pearlitic eutectoid steel, Metallurgical Transactions 17A (1986) 461–472.

[90] S. S. Sahay, G. Mohapatra, G. E. Totten, Overview of pearlitic rail steel: Accelerated cooling, quenching, microstructure, and mechanical properties, Journal of ASTM International (2009).

[91] S. Maya Johnson, A. Ramirez, A. Toro, Fatigue crack growth rate of two pearlitic rail steels, Engineering Fracture Mechanics 138 (03 2015). doi:10.1016/j.engfracmech.2015.03.023.

[92] Z. Abbasi, N. Tehrani, D. Ozevin, J. E. Indacochea, The influence of ferrite volume fraction on rayleigh wave propagation in a572 grade 50 steel, AIP Conference Proceedings 1806 (2017) 1–9.

[93] R. H. Bergman, R. A. Shahbender, Effect of statically applied stresses on the velocity of propagation of ultrasonic waves, Journal of Applied Physics 29 (1958) 1736–1738. doi:10.1063/1.1723035.

[94] D. R. Allen, C. M. Sayers, The measurement of residual stress in textured steel using an ultrasonic velocity combinations technique, Ultrasonics 22 (1984) 179–188.

[95] E. Schneider, Ultrasonic birefringence effect—its application for materials characterisations, Optics and Lasers in Engineering 22 (1995) 305–323. doi:https://doi.org/10.1016/0143-8166(94)00032-6.

[96] F. D. Murnaghan, Finite deformations of an elastic solid, Source: American Journal of Mathematics 59 (1937) 235–260.

[97] T. Ting, Recent developments in anisotropic elasticity, International journal of solids and structures 37 (1) (2000) 401–409.

[98] Schilke, Degradation of railway rails from a materials point of view, Chalmers University of Technology, Göteborg, Sweden (2013).

[99] H. F. Nied, P. B. Woelke, J. N. DuPont, S. Kizildemir, F. B. Fletcher, J. W. Hutchinson, Defect growth characterization in modern rail steel (2018).

[100] B. Ahn, S. S. Lee, Effect of microstructure of low carbon steels on ultrasonic attenuation, IEEE Transactions on Ultrasonics, Ferroelectrics, and Frequency Control 47 (2000) 620–629.

[101] Hanningfield, retrieved from hanningfield.com (2022).

[102] J. Sabhadiya, What is the density of steel?, Engineering Choice (2023).

[103] E. Oruklu, Y. Lu, J. Saniie, Hilbert transform pitfalls and solutions for ultrasonic nde applications, IEEE International Ultrasonics Symposium Proceedings (1995).

[104] J. M. Alexandra Collins, Deborah Coughlin, S. Kirk, The production of quick scoping reviews and rapid evidence assessments, Department for Environment & Rural Affairs (2015).

Appendix A

Literature review methodology

A.1 Evidence review methodology

This literature review was conducted using an adapted PICO methodology for rapid evidence assessments [104]. Adaptations were made to the standard PICO terminology to allow it to be fit to the specific subject area:

Population ⟶ Area of Interest

Intervention ⟶ Technology

Comparator ⟶ Failure modes & incidence

Outcomes ⟶ Outcomes from a successful technique

The primary and secondary questions used in the evidence review were:

Primary: What is the best technology for, and history, of measurements of longitudinal rail stress?

Secondary: How does failure to manage longitudinal stress impact the railway industry?

Keywords for each of the 4 PICO categories were chosen (Table A.1).

Table A.1: PICO keywords list

P	I	C	O	NOT
rail	ultrasonic	buckling	maint	residual
stress	barkhausen	derail	cost	x-ray
longitudinal	emat	de-rail	safety	xray
analysis	electromagnetic	downtime	improv	bend
thermal	strain	disruption	reduc	torsion
expansion	gauge	function	decreas	contact
neutral	verse	service		ballast
railway	vortok	pull apart		sleeper
railroad	ultrasound	pull-apart		bridge
track	shear	fail		subgrade
track	plane	reduc		rcf
road	wave	increas		fatigue
way	gage	decreas		
temperature	attenuation	rail		
manage	bulk			
steel	standing			
acousto	harmonic			
cwr	elastic			
monitor	magnet			
condition	debro			
free	nist			
stress	ripl			
measur	rail-nt			
	db			
	method			
	db-method			
	vibration			
	cross			
	section			
	cross-section			
	acousto			

A.1.1 Sources

The following searchable databases were included in the search:

Scopus wwww.scopus.com

Google Scholar wwww.googlescholar.com

StarPlus Sheffield University internal library system

The search was limited to Engineering, Materials science, Mathematics and Multidisciplinary fields and additional keywords were excluded based on a high incidence of repeating unforeseen keywords within the initial search results. The final search query used was:

(TITLE ((rail* OR rail* AND (steel OR way OR road OR track)) AND stress* AND (neutral OR longitudinal OR temperature OR manage* OR measur* OR monitor* OR analys* OR thermal OR expansion OR free OR condition))) OR (TITLE (rail* AND (ultraso* OR barkhausen OR acousto* OR emat OR electromag* OR magnet* OR attenutat* OR db-method OR (db W/2 method*) OR ripl OR nist OR debro OR ((cross* W/2 section*) W/3 vibrat*) OR (cross-section* W/3 vibrat*) OR (strain AND (gauge OR gage)) OR verse OR vortok OR (wave W/3 (shear OR elastic OR plane OR standing OR harmonic OR longitudinal OR bulk))))) OR (TITLE (rail* AND (buckl* OR fail*) AND ((climate W/3 change) OR derail* OR de-rail* OR pull-apart OR (pull AND apart) OR accident OR incident OR ((network OR service OR function) W/5 (downtime OR disrupt* OR loss))))) OR (TITLE ((rail* AND stress AND (maint* OR cost* OR reduc* OR descreas* OR improv*) OR (safety W/5 (improv* OR increas*))) (maint* OR cost*) OR (reduc* OR descreas* OR improv*) OR (safety W/5 (improv* OR increas*)))) AND NOT (TITLE ((rail* AND stress AND (maint* OR cost* OR reduc* OR descreas* OR improv*) OR (safety W/5 (improv* OR increas*))) (maint* OR cost*) OR (reduc* OR descreas* OR improv*) OR (safety W/5 (improv* OR increas*)))) AND (EXCLUDE (SUBJAREA, ”PHYS”) OR EXCLUDE (SUBJAREA,”COMP”) OR EXCLUDE (SUBJAREA, ”ENER”) OR EXCLUDE (SUBJAREA, ”SOCI”) OR EXCLUDE (SUBJAREA,”CENG”) OR EXCLUDE (SUBJAREA, ”ENVI”) OR EXCLUDE (SUBJAREA, ”BUSI”) OR EXCLUDE (SUBJAREA, ”CHEM”) OR EXCLUDE (SUBJAREA,”EART”) OR EXCLUDE (SUBJAREA, ”BIOC”) OR EXCLUDE (SUBJAREA, ”DECI”) OR EXCLUDE (SUBJAREA,”AGRI”) OR EXCLUDE (SUBJAREA, ”ARTS”) OR EXCLUDE (SUBJAREA,”MEDI”)) AND (EXCLUDE (EXACTKEYWORD,”Energy Harvesting”) OR EXCLUDE (EXACTKEYWORD,”Electric Traction”)

OR EXCLUDE (EXACTKEYWORD, ”Eddy Current Testing”) OR EXCLUDE (EXACTKEYWORD,”Automobile Suspensions”) OR EXCLUDE (EXACTKEYWORD, ”Traction Control”) OR EXCLUDE (EXACTKEYWORD, ”Fuel Injection”) OR EXCLUDE (EXACTKEYWORD, ”ELECTROMAGNETIC PROPULSION”) OR EXCLUDE (EXACTKEYWORD, ”Ship Propulsion”) OR EXCLUDE (EXACTKEYWORD, ”Magnetic Storage”) OR EXCLUDE (EXACTKEYWORD, ”Overhead Lines”) OR EXCLUDE (EXACTKEYWORD, ”Fatigue Damage”))

The first 40 pages from Google Scholar and STAR (400 results each) were scanned for inclusion. In addition, an existing library folder of rail-specific tribological and ultrasonic papers that has been developed and maintained by myself and a number of colleagues over a number of years was added to the analysis as a resource already rich in relevance to the topic of interest.

A.2 Grey literature

Grey literature was identified using three approaches

1. Asking stakeholders for relevant data sources / conversations with stakeholders
2. Reviewing the websites of key organisations for in-house publications
3. Performing a Google search with the existing keyword combinations:

A.3 Existing library

An exiting library curated by a number of University of Sheffield Tribology researchers, including Dr. Andy Hunter and Dr. Henry Brunksill, and added to myself during my time in the research group also provided a significant number of relevant papers.

A.3.1 Screening

A spreadsheet was used to organise the database outputs, automatically generating a scoring of keyword incidence in the title field. Papers receiving a PICO score >2 were passed to secondary screening.

A.3.1.1 Secondary screening

Abstracts and initial paragraphs were read for each paper in secondary screening, and scores were assigned for relevance to primary and secondary questions and robustness. A score was also assigned, where possible, as an assessment of the research methodology's limitations (Table A.3).

Papers meeting the criteria: (Robustness $\times$ Primary Relevance) + Secondary Relevance > 4 were used for evidence extraction.

After evidence extraction was complete, a final re-assessment of the relevance was conducted before synthesising the results into the review.

Final numbers of included results are detailed in Table A.2.

Table A.2: Results from academic database searches.

Database	Search returns	Duplicates	Relevant papers	Papers included
Scopus	493	5	27	5
STAR*	1003	6	24	12
Google Scholar	400	2	26	4
Tribology library	N/A	N/A	N/A	51

*Sheffield University internal library system

Table A.3: Scoring methodology for research relevance and value weighting

	Relevance (Primary)		Relevance (Secondary)		Robustness		Limitations
5	Evidence / Investigation into rail longitudinal stress (LS) measurement	4	Evidence of rail failure/buckling events over >10 years - including trends and climate linked data	3	All/most methodological criteria appropriate for the study type have been fulfilled (low risk of bias)	3	Few/insignificant identifiable limitations
4	Evidence / Investigation into rail LS measurement with lab-based experiments	3	Evidence of rail failure/buckling events over <10 years - including trends and climate linked data	2	Some methodological criteria fulfilled. Those not fulfilled are thought unlikely to alter the conclusions (risk of bias)	2	Some/somewhat significant identifiable Limitations
3	Numerical model with potential application to OR technologies for rail LS analysis	2	Evidence of rail failure/buckling events over >10 years	1	Few or no methodological criteria fulfilled. Conclusions of study thought likely/v. likely to alter (high risk of bias)	1	Many/significant identifiable limitations
2	Material properties underpinning OR technologies for rail stress analysis	1	Evidence of rail failure/buckling events over <10 years				
1	Theoretical modelling of rail stress OR defect detection methods	0	No relevance				
0	No relevance						

Appendix B

Sensitivity Analysis

B.1 Surface finish

B.1.1 Birefringence

Figure B.1 shows a schematic of a perfect and imperfect rail surface finish, and illustrates that variance in the surface profile of the material under analysis could result in differing flight paths between different transducer pairs.

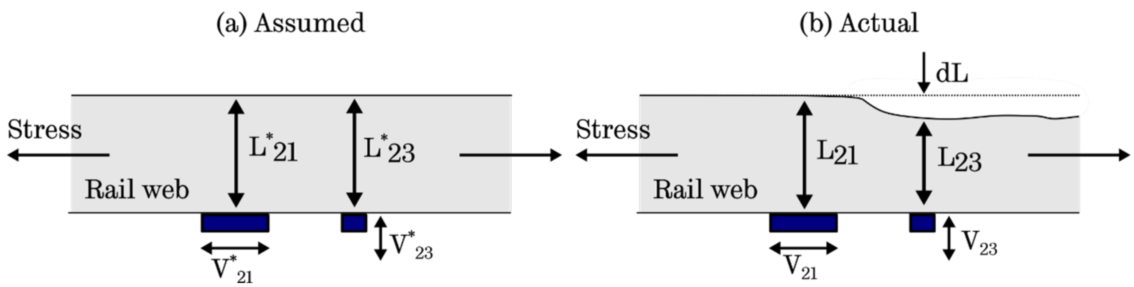

Figure B.1: The impact of variations in surface finish of the rail material on the ultrasonic flight path for (a) a perfect surface and (b) an actual, imperfect surface [Image credit: Gary Nicholas]

Where L represents flight path length, V denotes SoS and * denotes the ideal assumed case, we can describe the following simple relationships:

$$v_{21}^{*} = \frac{L_{21}^{*}}{ToF_{21}} \tag{B.1}$$

$$v_{23}^{*} = \frac{L_{23}^{*}}{ToF_{23}} \tag{B.2}$$

$$v_{21} = \frac{L_{21}}{ToF_{21}} \tag{B.3}$$

$$v_{23} = \frac{L_{23}}{ToF_{23}} \tag{B.4}$$

Subtracting the squares of equations B.1 and B.2, and B.3 and B.4 gives the following:

$${v_{21}^{*}}^{2} - {v_{23}^{*}}^{2} = \left(\frac{L_{21}^{*}}{ToF_{21}}\right)^{2} - \left(\frac{L_{23}^{*}}{ToF_{23}}\right)^{2} \tag{B.5}$$

and:

$${v_{21}}^{2} - {v_{23}}^{2} = \left(\frac{L_{21}}{ToF_{21}}\right)^{2} - \left(\frac{L_{23}}{ToF_{23}}\right)^{2} \tag{B.6}$$

Dividing B.5 by B.6 gives the stress-dependant error associated with surface finish imperfections:

$$\sigma_1^* = \frac{({v_{21}^*}^2 - {v_{23}^*}^2)}{({v_{21}}^2 - {v_{23}}^2)} \cdot \sigma_1 = \kappa_{ra-A} \cdot \sigma_1 \tag{B.7}$$

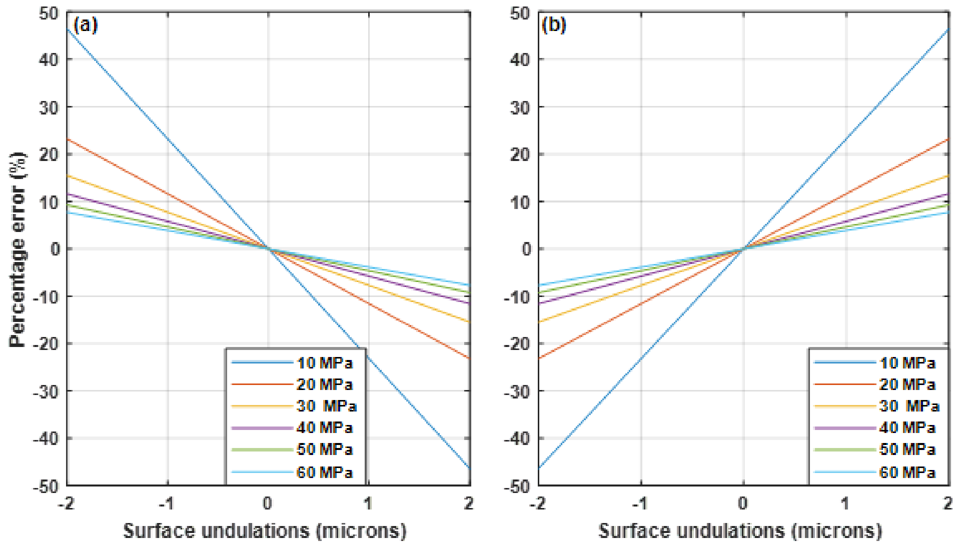

Figure B.2: The percentage error in stress measurement for the birefringence method due to unaccounted surface finish variation for different applied stress values for (a)v_{23} and (b) v_{21} [Image credit: Art Gower]

Error percentages are shown to decrease linearly with increasing applied stress.

B.1.2 Angled wedge

Figure B.3 shows a schematic of a perfect and imperfect rail surface finish, and illustrates that variance in the surface profile of the material under analysis could result in differing flight paths between the angled wedges.

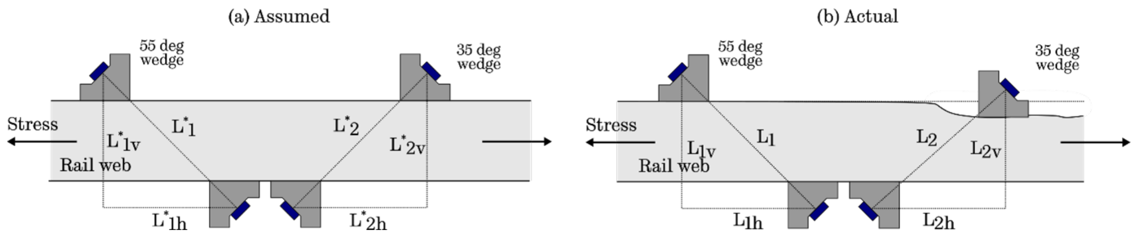

Figure B.3: The impact of variations in surface finish of the rail material on the ultrasonic flight path for (a) a perfect surface and (b) an actual, imperfect surface [Image credit: Gary Nicholas]

Where L represents flight path length (calculated trigonometrically from the vertical and horizontal lengths L_h and L_v), V denotes SoS and * denotes the ideal assumed case, we can describe the following simple relationships:

$$v_1^* = \frac{L_1^*}{ToF_1} \tag{B.8}$$

$$v_2^* = \frac{L_2^*}{ToF_2} \tag{B.9}$$

$$v_1 = \frac{L_1}{ToF_1} \tag{B.10}$$

$$v_2 = \frac{L_2}{ToF_2} \tag{B.11}$$

Subtracting the squares of B.8 anf B.9, and B.10 and B.11, gives:

$$v_1^{*2} - v_2^{*2} = \left(\frac{L_1^*}{ToF_1}\right)^2 - \left(\frac{L_2^*}{ToF_2}\right)^2 \tag{B.12}$$

and:

$$v_1{}^2 - v_2{}^2 = \left(\frac{L_1}{ToF_1}\right)^2 - \left(\frac{L_2}{ToF_2}\right)^2 \tag{B.13}$$

Dividing B.5 by B.6 gives the stress-dependant error associated with surface finish imperfections:

$$\sigma_1^* = \frac{(v_1^{*2} - v_2^{*2})}{({v_1}^2 - {v_2}^2)} \cdot \sigma_1 = \kappa_{ra-B} \cdot \sigma_1 \tag{B.14}$$

Figure B.4 shows the stress-related error percentage for the angled wedge method for different applied stress values.

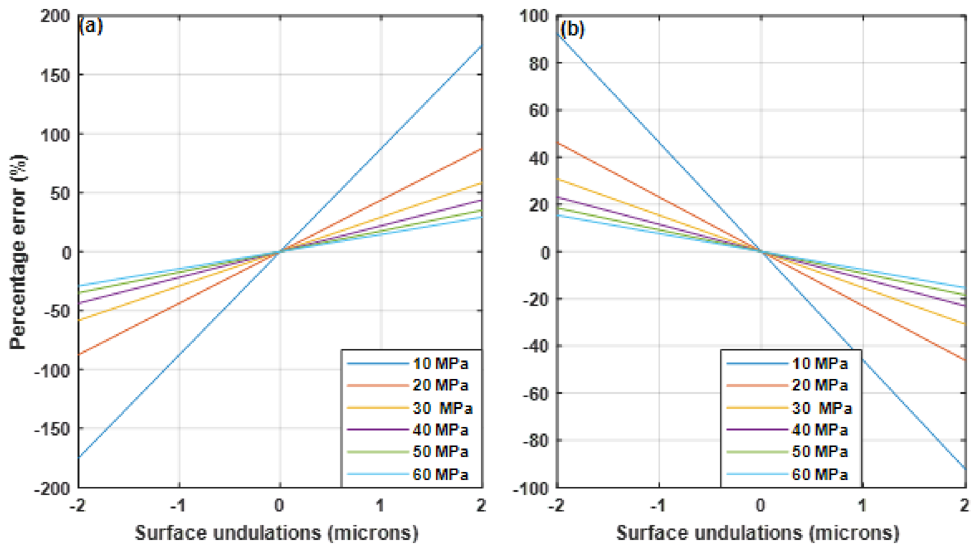

Figure B.4: The percentage error in stress measurement for the angled wedge method due to unaccounted surface finish variation for different applied stress values for (a)35° and (b) 55° wedge angles [Image credit: Art Gower]

Error percentages are higher than those shown for the birefringence method, but show the same decreasing linear trend with increasing applied stress.

B.2 Surface parallelism

B.2.1 Birefringence

Figure B.5 shows a schematic of both parallel and non-parallel surfaces for the birefringence model.

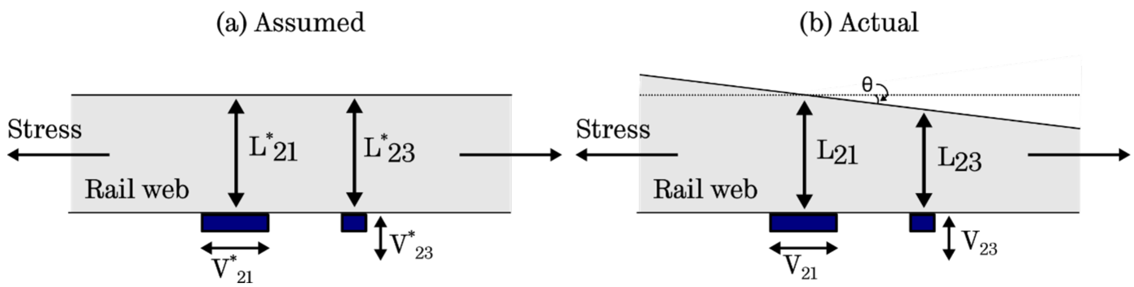

Figure B.5: The impact of non-parallel surfaces of the rail material on the ultrasonic flight path for (a) parallel surfaces and (b) non-parallel surfaces [Image credit: Gary Nicholas]

The analysis is nearly identical to that presented in subsection B.1.1, with a key difference: the path difference between L_{21} and L_{23} can be expressed as a function of the separation distance between the sensors and the angle of deviation from parallelism.

$$L_{23} = L_{21} + L_s \tan \Theta \tag{B.15}$$

which leads to the subtraction of squares identities:

$$v_{21}^{*\,2} - v_{23}^{*\,2} = \left(\frac{L_{21}^*}{ToF_{21}}\right)^2 - \left(\frac{L_{23}^*}{ToF_{23}}\right)^2 \tag{B.16}$$

and:

$$v_{21}{}^2 - v_{23}{}^2 = \left(\frac{L_{21}}{ToF_{21}}\right)^2 - \left(\frac{L_{21} + L_s \tan \Theta}{ToF_{23}}\right)^2 \tag{B.17}$$

Dividing B.5 by B.6, using a nominal value of 10mm for L_s gives the stress-dependant error associated with non parallel faces:

$$\sigma_1^* = \frac{(v_{21}^{*\,2} - v_{23}^{*\,2})}{(v_{21}{}^2 - v_{23}{}^2)} \cdot \sigma_1 = \kappa_{surface_{\Theta}-A} \cdot \sigma_1 \tag{B.18}$$

Figure B.6 shows the measurement error percentage due to non-parallel surfaces.

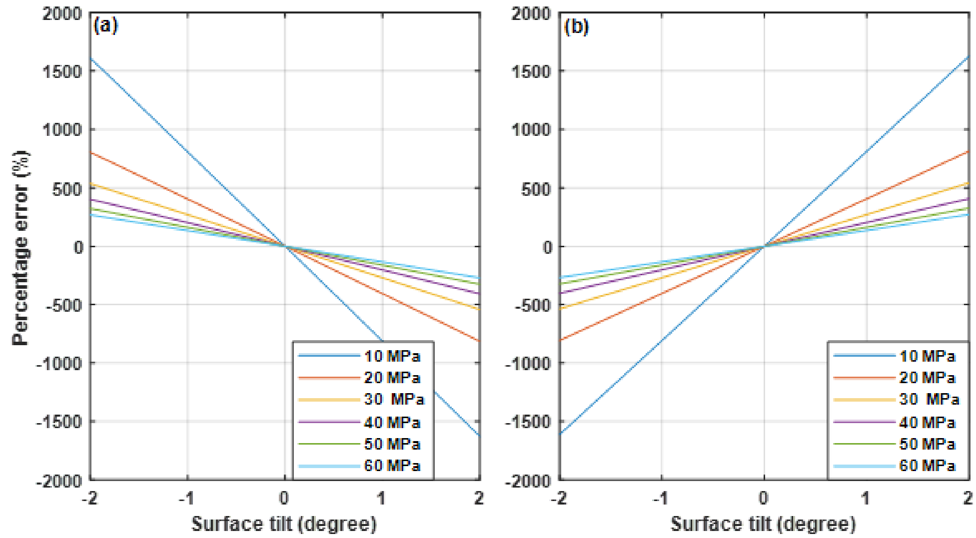

Figure B.6: The percentage error in stress measurement for the birefringence method due to unaccounted non-parallelism in specimen surfaces for different applied stress values for sensor (a) v_{23} and (b) v_{21} [Image credit: Art Gower]

There are very large errors predicted due to very slight variations in angle. The shorter the sensor separation distance, the lower the subsequent error, and highest errors are, as usual, seen at lowest applied stresses.

B.2.2 Angled wedge

A change in angle for the specimen surfaces causes a compound problem for the angled wedge method, in that it changes both he propagation angle as well as the signal flight path. The impact on the stress measurement error is so complex that the analysis presents only the impact of flight path change on the measurement accuracy.

Figure B.7 shows the measurement error in the angled wedge system due to non-parallel surfaces.

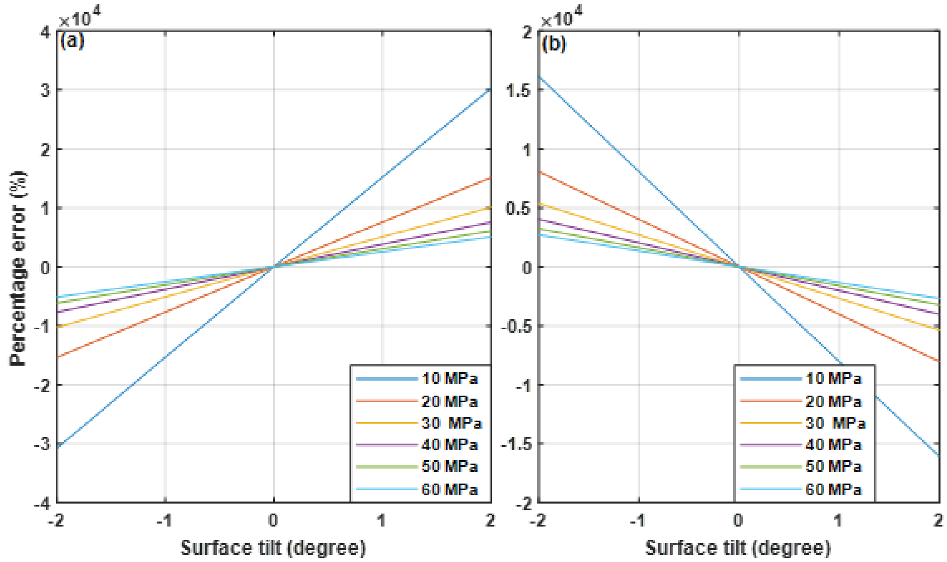

Figure B.7: The percentage error in stress measurement for the angled wedge method due to unaccounted non-parallelism in specimen surfaces for different applied stress values for (a) 35° and (b) 55° wedge angles [Image credit: Art Gower]

The predicted errors are very large indeed, with lowest applied stresses showing largest errors.

B.3 Web thickness

B.3.1 Birefringence

Figure B.8 shows schematically the deviation from expected signal paths due to any error in the measurement of the rail web thickness for the birefringence method.

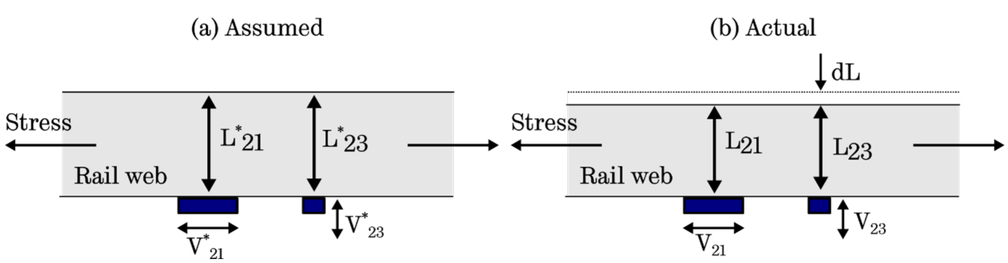

Figure B.8: Schematic showing the signal paths and deviations due to inaccurate measurement of web thickness for the birefringence method[Image credit: Gary Nicholas]

The steps to extract the error term follow the same pattern as the previous analyses, with the inclusion of the δL term in the thickness term for the idealised case.

The final identity is as follows:

$$\sigma_1^* = \frac{({v_{21}^*}^2 - {v_{23}^*}^2)}{({v_{21}}^2 - {v_{23}}^2)} \cdot \sigma_1 = \kappa_{t-A} \cdot \sigma_1 \tag{B.19}$$

By selecting a conservative estimate of ±1mm error in web thickness measurement, the plot for 10MPa applied stress is given in figure B.9

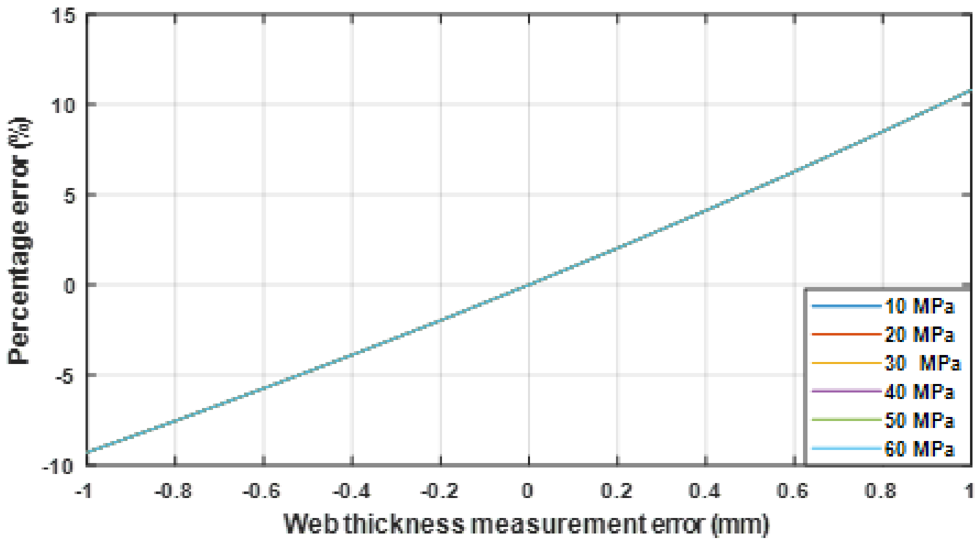

Figure B.9: A plot of the percentage error in stress measurement due to variance in the measured value for rail web thickness at 10MPa applied stress [Image credit: Art Gower]

The resulting errors are very small, especially considering the conservative error range chosen. The measurement error of the over-rail calipers ranges from 0.3mm to 0.03mm. The resulting error at ±0.03mm is 0.4%.

B.3.2 Angled wedge

Figure B.10 shows schematically the deviation from expected signal paths due to any error in the measurement of the rail web thickness for the angled wedge method.

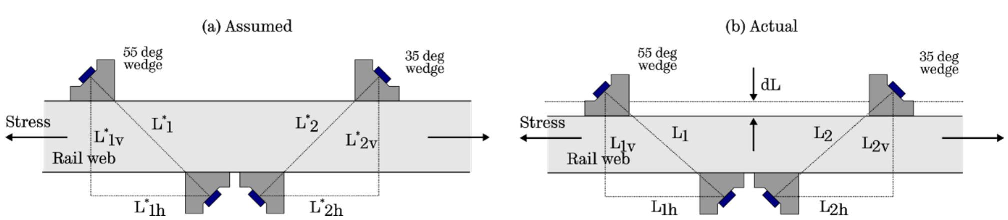

Figure B.10: Schematic showing the signal paths and deviations due to inaccurate measurement of web thickness in the angel wedge method[Image credit: Gary Nicholas]

The steps to extract the error term follow the same pattern as the previous angled wedge analyses, with the trigonometric calculation of the centre points of the transducers calculated from the vertical and horizontal distances.

The final identity is as follows:

$$\sigma_1^* = \frac{(v_1^{*2} - v_2^{*2})}{({v_1}^2 - {v_2}^2)} \cdot \sigma_1 = \kappa_{t-B} \cdot \sigma_1 \tag{B.20}$$

By again selecting a conservative estimate of ±1mm error in web thickness measurement, the plot for 10MPa applied stress is given in figure B.11

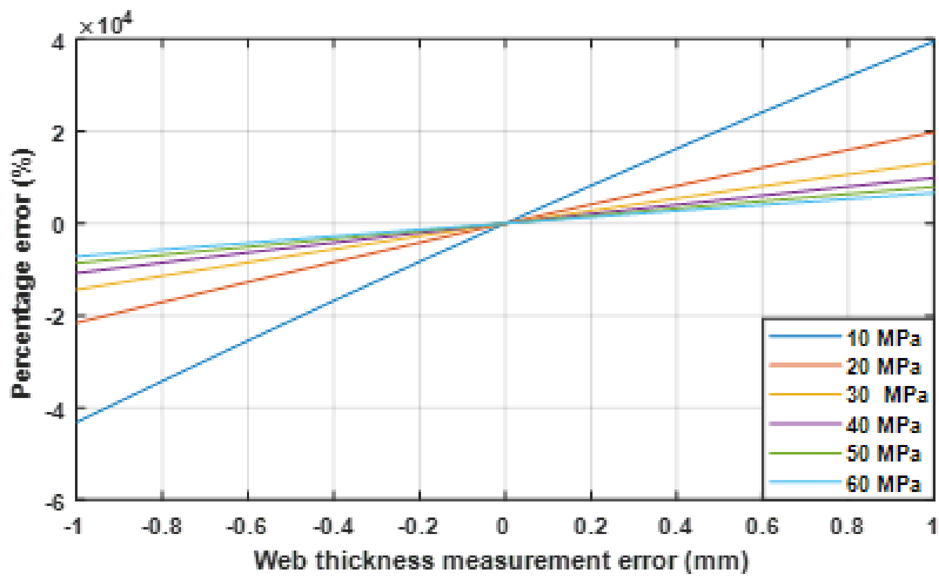

Figure B.11: A plot of the percentage error in stress measurement, using the angled wedge method, due to variance in the measured value for rail web thickness at for differing values of applied stress [Image credit: Art Gower]

The errors in this analysis are very large indeed. An achievable accuracy of ±0.03mm still leaves a 514% error in stress measurement at an applied stress of 10MPa, decreasing to 85% at 60MPa

B.4 Time resolution

B.4.1 Birefringence

The speed at which the DAQ system can capture signals determines how many samples a second and therefore has implications of the accuracy of the measurements. The error incurred is the difference between the true ToF and the point in time at which the DAQ actually captures the signal.